



**Ricardo Gil Henriques
Serra**

**Resistência à intempérie de filmes obtidos por
polimerização por plasma aplicados em aço pré-
pintado**

**Weathering resistance of thin plasma polymer films
on pre-coated steel**



**Ricardo Gil Henriques
Serra**

**Resistência à intempérie de filmes obtidos por
polimerização por plasma aplicados em aço pré-
pintado**

**Weathering resistance of thin plasma polymer films
on pre-coated steel**

Dissertação apresentada à Universidade de Aveiro para cumprimento dos requisitos necessários à obtenção do grau de Doutor em Ciência e Engenharia de Materiais, realizada sob a orientação científica do Doutor Mário Guerreiro Silva Ferreira, Professor Catedrático no Departamento de Engenharia Cerâmica e do Vidro da Universidade de Aveiro, e do Doutor Luís António Ferreira Martins Dias Carlos, Professor Catedrático no Departamento Física da Universidade de Aveiro.

Apoio financeiro da FCT, referência SFRH/BD/21541/2005, e do FSE no âmbito do III Quadro Comunitário de Apoio

o júri

presidente

Prof. Doutor José Carlos Esteves Duarte Pedro
Professor Catedrático no Dep. de Electrónica, Telecomunicações e Informática

Prof. Doutor Mário Guerreiro Silva Ferreira (orientador)
Professor Catedrático no Dep. Eng. Cerâmica e do Vidro da Universidade de Aveiro

Prof. Doutor Luís António Ferreira Martins Dias Carlos (co-orientador)
Professor Catedrático no Dep. Física da Universidade de Aveiro

Prof. Doutor Fernando Manuel Bico Marques
Professor Catedrático no Dep. Eng. Cerâmica e do Vidro da Universidade de Aveiro

Prof. Doutor Albano Augusto Cavaleiro Rodrigues de Carvalho
Professor Catedrático no Dep. Eng. Mecânica da Faculdade de Ciências e Tecnologia da Universidade de Coimbra

Prof. Doutora Alda Maria Pereira Simões
Professora Associada com Agregação no Dep. Eng. Química e Biológica do Instituto Superior Técnico

Prof. Doutor António Pedro dos Santos Lopes Castela
Professor Adjunto na Escola Superior de Tecnologia do Barreiro do Instituto Politécnico de Setúbal

agradecimentos

O autor agradece, reconhecido

aos meus orientadores, ao Professor Mário Guerreiro Silva Ferreira pelo acompanhamento e presença sempre constante na elaboração e resolução de problemas que foram surgindo ao longo trabalho realizado, e ao Professor Luís António Ferreira Martins Dias Carlos pela disponibilidade para atender as várias questões levantadas. A ambos agradeço a oportunidade, a orientação científica e pronto apoio prestado.

ao Mikhail por todo o apoio e ajuda no trabalho experimental realizado. Novas ideias e formas de teste apareceram devido à sua experiência e pensamento científico.

todo o apoio e ajuda dado por professores e colegas com quem tive o prazer e oportunidade de trabalhar são também reconhecidos, sendo que partilharam não só o seu tempo mas também o seu conhecimento. Estes foram elementos chave para levar avante as tarefas necessárias.

aos colegas de laboratório, pelo apoio e amizade.

a todos os, que sem sequer se aperceberem, contribuíram fortemente para o sucesso do trabalho.

à ECSC (Comunidade Europeia do Carvão e do Aço) pelo projecto 7210-PR/383 que deu o financiamento base para o projecto, aos parceiros do projecto pelas amostras utilizadas para o trabalho e à FCT pela bolsa de doutoramento concedida.

finalmente à minha família, pais e irmãos, pelo apoio e pela educação que me levarem a descobrir o interesse pela ciência, permitindo que tenha seguido esse caminho.

palavras-chave

Aço em banda pré-pintado, polimerização por plasma, protecção da corrosão, propriedades barreira, AFM, EIS.

resumo

O trabalho apresentado teve origem no projecto de investigação "Tailored Thin Plasma Polymers Films for Surface Engineering of Coil Coated Steel", financiado pelo Programa Europeu ECSC Steel Research.

Sistemas de aço galvanizado pré-pintado em banda à base de poliéster e poliuretano foram submetidos a um processo de polimerização por plasma onde um filme fino foi depositado de modo a modificar as propriedades de superfície. Foram usados reactores de cátodo oco, microondas e rádio frequência para a deposição do polímero fino. Os sistemas preparados foram analisados de modo a verificar a influência do processo de polimerização por plasma na alteração das propriedades barreira dos sistemas pré-pintados em banda. Foi estudado o efeito dos diferentes passos do processo de polimerização por plasma, bem como o efeito de diferentes variáveis operatórias. A mistura precursora foi variada de modo a modificar as propriedades da superfície de modo a poder vir a obter maior hidrofobicidade, maior resistência a marcas digitais, bem como maior facilidade de limpeza. Os testes foram conduzidos em solução de NaCl 0,5 M.

Para o trabalho foram usadas técnicas de análise da morfologia da superfície como Microscopia de Força Atómica e Microscopia Electrónica de Varrimento. As propriedades electroquímicas dos sistemas foram estudadas por Espectroscopia de Impedância Electroquímica. A estrutura dos filmes gerados no processo de polimerização por plasma foi caracterizada por Microscopia de Transmissão Electrónica. A modificação das propriedades ópticas devido ao processo de polimerização por plasma foi também obtida.

keywords

coil coated steel, plasma polymerization, corrosion protection, barrier properties, EIS, AFM.

abstract

The present work was originated in the project “Tailored Thin Plasma Polymers Films for Surface Engineering of Coil Coated Steel”, financed by the European Program ECSC Steel Research.

Polyurethane and polyester coil coatings modified with plasma polymer films prepared by hollow cathode, microwave and radio frequency plasma reactors were tested in order to obtain information about the influence of the process on the barrier properties of the coated systems and stability of the films obtained. The effects of the different steps on the whole process as well as the effect of different operating parameters were analysed. Different plasma precursors that could provide tailored surface properties, e.g. ultra-hydrophobic surface, anti-finger print and enhanced cleaning properties were also tested. The experiments were performed in 0.5 M NaCl solution.

The coating surface evolution was studied by means of Scanning Electronic Microscopy and Atomic Force Microscopy. Electrochemical Impedance Spectroscopy was used to study the electrochemical properties of the coating systems. Results obtained by Transmission Electronic Microscopy revealed the microstructure of the plasma polymer films applied on the top of the coil coatings. Surface optical properties modification with plasma polymerization was also investigated.

Contents

Júri	iii
Agradecimentos	iv
Resumo	v
Abstract	vi
Contents	1
Abbreviations	7
List of Figures	11
List of Tables	19
Foreword	21
Introduction	27
Section 1. Corrosion and Corrosion Control	29

1.1.	Introduction	29
1.2.	Metals and Corrosion	30
1.3.	Corrosion Control	31
1.4.	Organic Coatings	33
1.5.	Coil Coating	34
1.6.	Degradation of Painted Metals	36
Section 2. Plasma Polymerization		39
2.1.	Introduction	39
2.2.	Plasma Polymerization	40
2.3.	Mechanism of Plasma Polymerization	41
2.4.	Application of the Plasma Films	44
2.5.	Application to Coil Coatings	44
2.6.	Effect of Process Variables	45
2.6.1.	Flow Rate	45
2.6.2.	Discharge Power	45
2.6.3.	Electromagnetic Field Frequency	46
2.6.4.	Pressure	46
2.6.5.	Feed Gas	47
i.	Inert Gas	47
ii.	Oxygen Containing Gas	47
iii.	Hydrocarbons	48
iv.	Fluorocarbons	48
v.	Silicon Containing Gas	48
vi.	Metal-containing Gas	49
2.6.6.	Type of Reactors	49
i.	Internal Electrode Reactor	49
ii.	External Electrode Reactor	50
iii.	Electroless Reactor	50
iv.	Atmospheric Pressure Reactor	50
Experimental		51
Section 3. Principles of the Experimental Techniques		53
3.1.	Electrochemical Impedance Spectroscopy	54
3.1.1.	Impedance	54
3.1.2.	Validity	56
3.1.3.	Spectra Interpretation	57
i.	Single Elements	57
ii.	Simple Circuit Elements	59
iii.	Impedance of Painted Systems	60
3.1.4.	Water Uptake	63
3.2.	Scanning Electron Microscopy	65
3.3.	Energy-Dispersive X-ray Spectroscopy	65

3.4.	Transmission Electron Microscopy	66
3.5.	Atomic Force Microscopy	68
3.5.1.	Basic Principle	68
3.5.2.	Statistical Characterization	69
3.5.3.	Imaging Modes	70
i.	Contact Mode	70
ii.	Tapping Mode	71
3.6.	Colour Measurement	72
3.6.1.	Colour Vision	72
3.6.2.	The CIE XYZ Colour Space	73
3.6.3.	The CIE Chromaticity Diagram	75
Section 4. Experimental		77
4.1.	Specimens	77
4.1.1.	Coil Coatings	78
4.1.2.	Plasma Polymerization	80
i.	Microwave Plasma Reactor - M	82
ii.	Radio Frequency Plasma Reactor - R	84
iii.	Hollow Cathode Plasma Reactor - H	87
4.2.	Techniques Used	88
4.2.1.	Electrochemical Impedance Spectroscopy	88
i.	Electrochemical Cells	89
ii.	Experimental Conditions	90
4.2.2.	Scanning Electronic Microscopy	90
4.2.3.	Energy Dispersive Spectroscopy	90
4.2.4.	Transmission Electronic Microscopy	91
4.2.5.	Atomic Force Microscopy	91
4.2.6.	Colour Coordinates	92
Results		93
Section 5. Unmodified Coil Coating		95
5.1.	Introduction	95
5.2.	EIS Measurements	96
5.2.1.	Numerical Fitting of EIS Data	99
5.2.2.	Water Uptake Estimation	102
5.3.	Surface Characterisation	103
Section 6. Modified Coil Coating		107
6.1.	Introduction	107
6.2.	Microwave Plasma Reactor	108
6.2.1.	Plasma Activation Stage	108
i.	EIS Results	109
•	Numerical Fitting of EIS Data	110

•	Water Uptake	112
ii.	Surface Characterisation	113
6.2.2.	Plasma Deposition Stage	116
i.	EIS Results	116
•	Electrochemical Testing at 45° C	119
•	Numerical Fitting of EIS Data	120
•	Water Uptake	121
ii.	Plasma Polymer Films Structure	123
iii.	Surface Characterization	124
•	Surface Morphology and Composition Evolution	126
iv.	Optical Properties	127
6.3.	Radio Frequency Plasma Reactor	131
6.3.1.	Plasma Activation Stage	132
i.	EIS Results	132
•	Numerical Fitting of EIS Data	136
•	Water Uptake Estimation	138
ii.	Surface Characterization	139
•	Evolution of the Surface Properties	142
6.3.2.	Plasma Deposition Stage	145
6.3.3.	Plasma Stabilization Stage	148
6.3.4.	Characterization of the Systems Obtained in Stages 3 and 4	151
i.	Numerical Fitting of EIS Data	152
ii.	Water Uptake	154
iii.	Structure	155
iv.	Surface Characterization	157
•	Evolution of the Surface Properties	161
v.	Colour Coordinates	166
6.4.	Hollow Cathode Plasma Reactor	167
6.4.1.	EIS Results	167
i.	Numerical Fitting of EIS Data	168
ii.	Water Uptake	169
6.4.2.	Plasma Polymer Film Characterization	170
i.	Structure	170
ii.	Surface Morphology	171
	Discussion	173
	Section 7. Discussion	175
7.1.	Introduction	175
7.2.	Coil Coating	177
7.3.	Plasma Activation	179
7.3.1.	Activation Time and Carrier Gas	179
7.3.2.	Electrode Location	181

7.4.	Plasma Polymer Film Deposition	183
7.4.1.	Pressure, Oxygen Availability and Monomer	184
7.4.2.	Electrode Location and Steps Combination	187
7.4.3.	TMS Monomer	192
7.5.	Reactor Comparison	193
7.6.	Estimation of Economical Aspects	195
	Conclusions	199
	Section 8. Conclusions	201
	Section 9. Future Work	205
	• Work Started but Not Completed	205
	• Continuation of the Work	206
	References	209
	Appendix - Activation and Deposition (R)	219
	• Systems Characterization	220

Abbreviations

Abbreviation used in this works:

a	area
a.c.	alternating current
AFM	atomic force microscopy
ATR-IR	Attenuated total reflection infrared spectroscopy
β	Stern-Geary coefficient
b_a	Tafel coefficient for the anodic partial reaction
b_c	Tafel coefficient for the cathodic partial reaction
BC	before Christ
BSE	back scattered electrons
C	capacitance / capacitor
CCD	charge-coupled device
CIE	commission Internationale de l'éclairage

CPE, Q	constant phase element
d	thickness
d.c.	direct current
DOC	Dortmunder Oberflächencentrum
E	voltage / potential
e ⁻	electron
E ₀	amplitude of the signal
ϵ	dielectric constant
ϵ_0	permittivity of vacuum
ϵ_{H_2O}	dielectric constant of water
EDS	energy-dispersive X-ray spectroscopy
EEDF	electron energy distribution function
EIS	electrochemical impedance spectroscopy
f	frequency
F	Farad
h	average surface height
HDFD	heptadecafluoro-1-decen
HMDSO	hexamethyldisiloxane
I	current / response signal
L	inductor
M	metal
MPIE	Max Planck Institut für Eisenforschung
n	constant phase element exponent
ω	radial frequency
ϕ	phase
Q	constant phase element
R	resistance / resistor
R _a	arithmetic roughness
R _{sk}	surface skewness
R _t	root mean square roughness
SEM	scanning electron microscopy
SFM	scanning force microscopy
STM	scanning tunnelling microscopy
sccm	standard cubic centimetres per minute
t	time
τ	time constant
T _g	glass transition temperature
TEM	transmission electron microscopy
TMS	tetramethylsilane
v	average electron-neutral collision frequency
VOC	volatile organic compounds
W	Warburg
X	disbonded area of delamination
XPS	X-ray Photoelectron Spectroscopy
x, y	reflection colour coordinates

$\bar{X}, \bar{Y}, \bar{Z}$	colour matching functions
X, Y, Z	tristimulus
Y	admittance, luminance parameter
Z	impedance of the system / elevation profile
Z'	real part of impedance
Z''	imaginary part of impedance
Z _{mod}	modulus of impedance
Z _{0.1 Hz}	modulus of impedance at 0.1 Hz

Subscripts

0	refers to initial time
coat	refers to the coating
ct	refers to the charge transfer
dl	refers to the double layer
dl0	refers to the uncoated metal double layer
i	represents each point measured
por	refers to the pores
sol	refers to the solution
t	represents the time

List of Figures

Figure 1 Scheme of the plasma polymerization stage introduced in the coil coating production line.	22
Figure 1.1 General scheme of a coil coating production line. ³¹	36
Figure 2.1 Schematic diagram of polymer films.	41
Figure 2.2 Schematic diagram of reaction network. ⁵⁴	43
Figure 3.1 Sinusoidal current response in a linear system.	55
Figure 3.2 Argand diagram showing impedance vectors.	56
Figure 3.3 Resistor and capacitor a. Impedance expressions, represented as; b. Nyquist; and c. Bode plots, for two resistance values $R_1 = 10$ ohm and $R_2 = 1000$ ohm; and for two capacitance values $C_1 = 10^{-6}$ F and $C_2 = 10^{-9}$ F.	58

Figure 3.4 a. Expression of total impedance; b. equivalent electric circuit of series resistor and capacitor combination with representation in Nyquist; and c. Bode impedance plots, $R = 10^3$ ohm and $C = 10^{-6}$ F.	59
Figure 3.5 a. Expression of total impedance; b. equivalent electric circuit of parallel resistor and capacitor combination with representation in Nyquist; and c. Bode impedance plots, $R = 10^3$ ohm and $C = 10^{-6}$ F.	60
Figure 3.6 a. Expression of total impedance; b. equivalent electric circuit with resistor and capacitor in parallel with resistor with representation in Nyquist; and c. Bode impedance plots; $R_1 = 10^3$ ohm, $R_2 = 10^6$ ohm and $C = 10^{-6}$ F.	60
Figure 3.7 Scheme showing the equivalent electric circuits used for describing painted metal coating degradation with immersion time.	62
Figure 3.8 Block diagram of atomic force microscope technique.	69
Figure 3.9 Diagram of Munsell, Ostwald and CIE chromaticity coordinate systems.	73
Figure 3.10 Colour-matching functions \bar{X} , \bar{Y} and \bar{Z} .	74
Figure 3.11 The CIE chromaticity diagram.	76
Figure 4.1 a. Polyurethane coil coating system cross section image; and EDS maps for the b. zinc; and c. iron elements.	78
Figure 4.2 a. Polyester coil coating system cross section image; and EDS maps of the elements: b. iron; c. silicon; d. zinc; and e. titanium.	79
Figure 4.3 Scheme of the M plasma reactor.	82
Figure 4.4 Structure of the monomers used for the plasma polymerization, a. HMDSO; and b. HDFD.	83
Figure 4.5 Scheme of the R plasma reactor.	85
Figure 4.6 Scheme of the H plasma reactor.	87
Figure 4.7 Structure of the TMS monomer used for plasma polymerization.	88
Figure 4.8 a. Electrochemical cell arrangement used for EIS impedance measurements of the samples tested at ambient temperature, working area of 3.4 cm^2 ; b. container for immersion tests at 45° C ; and c. electrochemical cell arrangement used for EIS impedance measurements of the samples tested at 45° C , working area of 2.46 cm^2 .	89
Figure 5.1 Bode plot diagrams for U coil coating submitted to immersion tests in 0.5 M NaCl at: a. ambient temperature; and b. 45° C .	97
Figure 5.2 Bode and Nyquist plot diagrams for E coil coating, tests at ambient temperature.	98

Figure 5.3 Equivalent electric circuits used for numerical fitting of the EIS data obtained for the painted systems: a. undamaged system; and b. two processes.	99
Figure 5.4 Numerical fitting for unmodified E coil coating: a. immediately after immersion, $Q (C_{\text{coat}}) = 3.35 \times 10^{-10} \text{ F cm}^2 \text{ s}^{n-1}$ with $n = 0.958$, $R_{\text{por}} = 2.21 \times 10^{11} \text{ ohm cm}^2$ and b. after 130 days of immersion, $Q (C_{\text{coat}}^*) = 3.53 \times 10^{-10} \text{ F cm}^2 \text{ s}^{n-1}$ with $n = 0.965$, $R_{\text{por}}^* = 5.51 \times 10^6 \text{ ohm cm}^2$; $Q (C_{\text{coat}}) = 6.11 \times 10^{-10} \text{ F cm}^2 \text{ s}^{n-1}$ with $n = 0.481$; and $R_{\text{por}} = 1.33 \times 10^9 \text{ ohm cm}^2$. The black squares represent the EIS data and the red line the respective fitting.	100
Figure 5.5 Evolution of the C_{coat} and R_{por} estimated parameters for E and U coil coating.	101
Figure 5.6 Water uptake estimation for E and U coil coatings.	102
Figure 5.7 AFM $1 \times 1 \mu\text{m}$ images of the surface morphology evolution for: a. U coil coating and b. E coil coating, with the respective values, in nm, of R_a and h .	103
Figure 5.8 SEM images of the surface evolution of the E coil coating.	104
Figure 5.9 Composition spectra obtained by EDS technique for: a. U coil coating; and b. E coil coating. The quantification for some elements appears in the table, values in at. %.	106
Figure 6.1 Bode plots with the impedance evolution during the immersion tests of the U coil coating submitted to different plasma activation conditions in M plasma reactor: a. immediately after immersion (1 hour); and b. for the time of immersion indicated.	110
Figure 6.2 Evolution of C_{coat} and R_{por} parameters during immersion. The values came from the fitting of the impedance results for the M plasma activated U systems.	111
Figure 6.3 Water uptake evolution for the M plasma activated U systems calculated from capacitance measurements at 10 kHz, values in percentage.	112
Figure 6.4 AFM $1 \times 1 \mu\text{m}$ images with the surface morphology after the plasma activation step, systems: a. UM1aP ₁ ; b. UM1bP ₁ ; c. UM1cP ₁ ; and d. UM1dP ₁ . The R_a and h values in nm appear in the respective image.	114
Figure 6.5 AFM $1 \times 1 \mu\text{m}$ images with the surface morphology after 21 days of immersion, systems: a. UM1aP ₁ ; b. UM1bP ₁ ; c. UM1cP ₁ ; and d. UM1dP ₁ . The R_a and h values in nm appear in the respective image.	114
Figure 6.6 Composition (EDS) evolution during immersion of the plasma activated U systems using the M plasma reactor. Quantification values in at. %.	115
Figure 6.7 Bode plots with impedance evolution of U coil coating submitted to plasma polymerization process in M plasma reactor, systems: a. UM2eP ₂ ; and b. UM2eP ₃ .	117

Figure 6.8 Bode plots with impedance evolution of the U coil coating submitted to M plasma polymerization, systems: a. UM2fP ₃ ; and b. UM2gP ₂ .	118
Figure 6.9 EIS data evolution for 45° C immersion tests of the 45UM2gP ₂ system.	119
Figure 6.10 Evolution with immersion of C _{coat} and R _{por} parameters for the M plasma polymerized U systems.	121
Figure 6.11 Water uptake evolution for the plasma polymerized U systems in M plasma reactor. Results obtained from the capacitance values at 10 kHz.	122
Figure 6.12 TEM micrographs of the plasma polymer films generated using M plasma reactor, systems: a. UM2eP ₂ ; b. UM2eP ₃ ; c. UM2fP ₃ ; and d. UM2gP ₂ .	123
Figure 6.13 Surface morphology 4x4 μm images of the plasma polymer layers generated using the U coil coating obtained by AFM technique. The values in nm of R _a and h also appear in the images, systems: a. UM2eP ₂ ; b. UM2eP ₃ ; c. UM2fP ₃ ; and d. UM2gP ₂ .	125
Figure 6.14 Composition of the M plasma polymerized U systems with quantification of the fluorine and silicon elements, values in at. %.	125
Figure 6.15 AFM 4x4 μm images with the surface morphology evolution during immersion, systems: a. UM2eP ₂ ; b. UM2eP ₃ ; c. UM2fP ₃ ; and d. UM2gP ₂ . The R _a and h values in nm are in the correspondent image.	128
Figure 6.16 CIE chromaticity diagram (1931) coordinates for 2° standard observer showing the evolution during immersion of the (x,y) reflection colour coordinates for the M plasma polymerized U systems: a. UM2eP ₂ ; and b. UM2eP ₃ . Unmodified U coil coating is plotted for reference.	129
Figure 6.17 CIE chromaticity diagram (1931) coordinates for 2° standard observer showing the evolution during immersion of the (x,y) reflection colour coordinates for the M plasma polymerized U systems: a. UM2fP ₃ ; and b. UM2gP ₂ . Unmodified U coil coating is plotted for reference.	130
Figure 6.18 Evolution with immersion of reflectance spectra for the M plasma polymerized U systems: a. UM2eP ₂ ; b. UM2eP ₃ ; c. UM2fP ₃ ; and d. UM2gP ₂ .	131
Figure 6.19 Impedance evolution during immersion for the U coil coating plasma activated in the R plasma reactor: a. ambient temperature, systems UR1hP ₄ G and UR1hP ₄ P; and b. 45° C temperature, systems 45UR1hP ₄ G and 45UR1hP ₄ P.	133
Figure 6.20 Bode plots with the impedance evolution during immersion tests at ambient temperature of plasma activated E systems in R plasma reactor, systems: a. ER1hP ₄ G; and b. ER1hP ₄ P.	135
Figure 6.21 Nyquist plots with the impedance evolution during immersion tests at ambient temperature of E coil coating plasma activated in R plasma reactor: a.	

ER1hP ₄ G; and b. ER1hP ₄ P systems. Legend colours are similar to Bode plots of Figure 6.20.	135
Figure 6.22 Evolution of: a., b. C_{coat} ; and c., d. R_{por} parameters for the plasma activated U and E systems, prepared using the two electrode locations. The C_{coat} graphs have different scale adapted to the different magnitude of the results.	137
Figure 6.23 Water uptake plot for the plasma activated E and U systems, prepared using the R plasma reactor.	138
Figure 6.24 Surface morphology AFM 1x1 μm images for the plasma activated U systems using R plasma reactor, systems: a. UR1hP ₄ P; and b. UR1hP ₄ G. The values in nm of R_a and h appear in the respective image.	139
Figure 6.25 Composition and element content quantification of U coil coating after the plasma activation step, quantification values in at.%.	140
Figure 6.26 Surface morphology SEM micrographs for the plasma activated E systems using R plasma reactor, systems: a. ER1hP ₄ P; and b. ER1hP ₄ G.	141
Figure 6.27 Composition and element content quantification of the plasma activated E systems using the R plasma reactor, quantification values in at. %.	141
Figure 6.28 Surface morphology AFM 1x1 μm images for the evolution during immersion tests of the plasma activated U systems using R plasma reactor, systems: a. UR1hP ₄ G; and b. UR1hP ₄ P. The values in nm of R_a and h are in the respective image.	142
Figure 6.29 Surface morphology images, obtained with SEM, showing the surface evolution during immersion of the plasma activated E systems using R plasma reactor, systems: a. ER1hP ₄ G; and b. ER1hP ₄ P.	144
Figure 6.30 Bode plots with evolution of impedance during immersion for the systems: a. UR3eP ₅ G; and b. UR3eP ₅ P.	146
Figure 6.31 Bode plots with the impedance values obtained during the immersion tests of the systems: a. ER3eP ₅ P; and b. ER3eP ₅ G.	148
Figure 6.32 Bode plots for immersion tests at 45° C of R plasma polymerization using U coil coating, systems: a. 45UR4iP ₄ P; and b. 45UR4iP ₄ G.	149
Figure 6.33 Bode plots obtained during the immersion tests for the systems: a. ER4iP ₄ P; and b. ER4iP ₄ G.	151
Figure 6.34 Evolution of the estimated parameters for the R plasma polymerization using U and E systems: a., c. C_{coat} values; and b., d. R_{por} values. The C_{coat} graphs have different scales adapted to the respective magnitude of the results.	153
Figure 6.35 Water uptake plot for the plasma polymerized E and U systems using the R plasma reactor stage 3 and 4.	154
Figure 6.36 TEM micrographs of the plasma polymer films prepared in the R plasma reactor, systems: a. UR4iP ₄ P; and b. ER3eP ₅ G.	156

Figure 6.37 AFM 4x4 μm images with the surface morphology for the systems: a. UR3eP ₅ G; b. UR3eP ₅ P; c. UR4iP ₄ G; and d. UR4iP ₄ P. The values in nm of R_a and h are in the respective image.	157
Figure 6.38 Surface composition spectra of the R plasma polymerized U systems, quantification values in at. %.	158
Figure 6.39 Surface morphology of the R plasma polymerized E systems: a. ER3eP ₅ G; b. ER3eP ₅ P; c. ER4iP ₄ G; and d. ER4iP ₄ P.	159
Figure 6.40 Surface composition of the plasma polymerized E systems performed in the R plasma reactor, quantification values in at. %.	160
Figure 6.41 AFM 1x1 μm images of the surface morphology evolution during immersion for the plasma polymerized U systems using the R plasma reactor: a. UR3eP ₅ G; b. UR3eP ₅ P; c. UR4iP ₄ G; and d. UR4iP ₄ P. The values in nm of R_a and h appear in the respective image.	162
Figure 6.42 Surface morphology evolution during immersion tests for plasma polymerization of E systems using the R plasma reactor: a. ER3eP ₅ G; b. ER3eP ₅ P; c. ER4iP ₄ G; and d. ER4iP ₄ P.	164
Figure 6.43 CIE chromaticity diagram (1931) coordinate for 2° standard observer showing the (x,y) reflection colour coordinate for the plasma polymerized systems using the R plasma reactor.	167
Figure 6.44 Impedance values evolution during immersion for the system UH2kP ₆ .	168
Figure 6.45 Evolution of C_{coat} and R_{por} parameters during immersion obtained by fitting the impedance results for the system UH2kP ₆ .	169
Figure 6.46 Water uptake evolution during immersion obtained from capacitance measurements, for the system UH2kP ₆ .	170
Figure 6.47 TEM cross-section micrograph of the system UH2kP ₆ .	170
Figure 6.48 AFM 1x1 μm images with the surface morphology evolution during immersion, for the system UH2kP ₆ , with the values in nm of R_a and h .	171
Figure 7.1 Evolution of the $ Z _{0.1 \text{ Hz}}$ values during immersion tests for the unmodified E and U coil coatings.	178
Figure 7.2 Degradation mechanism scheme for the unmodified coil coatings; a. U; and b. E.	178
Figure 7.3 $ Z _{0.1 \text{ Hz}}$ evolution during immersion of the plasma activated systems using the M plasma reactor.	179
Figure 7.4 Degradation scheme of the plasma activation with argon, system UM1dP ₁ .	180
Figure 7.5 Degradation mechanism scheme for plasma activation with oxygen of the U systems.	181

Figure 7.6 $ Z _{0.1 \text{ Hz}}$ evolution during immersion of the plasma activated systems using the R plasma reactor.	182
Figure 7.7 Degradation mechanism scheme for R plasma activation of E systems with oxygen.	183
Figure 7.8 Evolution of the $ Z _{0.1 \text{ Hz}}$ during immersion for the plasma polymerization performed in M plasma reactor.	184
Figure 7.9 Degradation mechanism of the M plasma polymerization with HMDSO and oxygen.	185
Figure 7.10 Degradation mechanism of the M plasma polymerized U system using HMDSO and argon precursor mixture.	186
Figure 7.11 Evolution of the $ Z _{0.1 \text{ Hz}}$ values during immersion for the plasma polymerized systems in R plasma reactor, using: a. U coil coating; and b. E coil coating.	188
Figure 7.12 Degradation mechanism for the plasma polymerized E systems in the R plasma reactor using HMDSO and oxygen precursor mixture.	189
Figure 7.13 Degradation mechanism for the plasma polymerized U systems using the R plasma reactor with HMDSO and oxygen precursor mixture.	191
Figure 7.14 Evolution of $ Z _{0.1 \text{ Hz}}$ values for the system UH2kP ₆ .	192
Figure 7.15 Evolution of $ Z _{0.1 \text{ Hz}}$ for the plasma polymerization performed using HMDSO or TMS monomers: M vs. R vs. H plasma reactors.	194
Figure a Water uptake plot for the plasma polymerized U systems using the R plasma reactor.	220
Figure b AFM 1x1 μm images with the surface morphology evolution during immersion for the systems a. UR2jP5P and b. UR2jP5G. The Ra and h values in nm are in the correspondent image.	222

List of Tables

Table 2.1 Elementary processes occurring during the plasma polymerization. ⁵⁴	42
Table 3.1 Electrical impedance elements and respective impedance expressions.	58
Table 4.1 Labels attributed to the combination of plasma steps.	80
Table 4.2 Labels attributed to the reactor time of the process, carrier gas and monomer.	81
Table 4.3 Labels attributed to the reactor pressure.	81
Table 4.4 Description of the plasma activation step and tested variables, together with the respective labels attributed to each system.	83

Table 4.5 Description of the plasma polymerization step performed in the M plasma reactor with the respective conditions used, together with the labels attributed to the systems prepared.	84
Table 4.6 Description of the plasma polymerization steps performed in the R plasma reactor with the plasma polymerization conditions used.	86
Table 4.7 Samples prepared at G and P electrode location of R plasma reactor, with the respective label correspondence.	86
Table 4.8 Plasma polymerization conditions used in the H plasma reactor, with the respective label attributed.	88
Table 6.1 Composition evolution during immersion tests for fluorine and silicon elements of the M plasma polymerized U systems, values in at. %.	127
Table 6.2 Elements content evolution during immersion of the plasma activated U systems, values in at. %.	143
Table 6.3 Elements content evolution during immersion of plasma activated E systems, values in at. %.	143
Table 6.4 Composition evolution during immersion tests for the plasma polymerized U systems, values in at. %.	163
Table 6.5 Composition evolution during immersion of the plasma polymerized E systems prepared in the R plasma reactor using the two electrode locations, values in at. %.	166
Table 6.6 Surface composition evolution for the UH2kP ₆ system, quantification values in at. %.	172
Table 7.1 Estimated cost for the plasma deposition step using TMS monomer.	197
Table 7.2 Estimated cost for the plasma deposition step using HMDSO monomer.	197
Table a Systems prepared at G and P electrode location of R plasma reactor, with the respective label correspondence.	220
Table b Composition evolution during the immersion tests of the systems UR2jP5G and UR2jP5P.	221

Foreword

The coil coating industry is looking for solutions to improve specific properties of the coil coated material without significant loss of formability and corrosion protection. Some of these properties include anti-fingerprint and easy to clean surfaces together with anti-wear and colour control. The deposition of thin films by plasma polymerization on the top of the organic coatings can be an effective and attractive way to modify the surface properties of coated systems. The procedure can be optimized to tailor the final surface properties maintaining the rest of the coil coating properties.

The aim of the project *Tailored thin plasma polymers for surface engineering of coil coated steel* (ECSC project 7210-PR/383), ¹ in which this work is included, was to verify the applicability of thin plasma polymer films to tailor the surface

properties of coil coated steel by adding one extra stage to the production line, as shown in Figure 1.

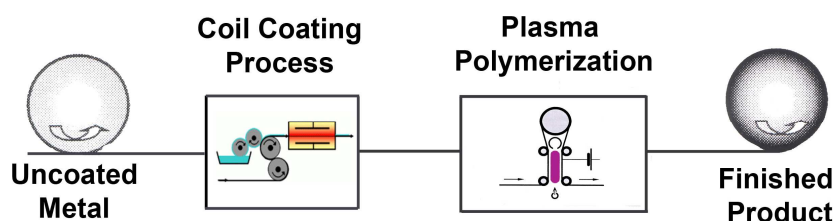


Figure 1 Scheme of the plasma polymerization stage introduced in the coil coating production line.

To develop optimal final paint systems it is necessary a good understanding of the degradation of the polymers, metallic corrosion, micromechanical properties and adhesion of plasma polymers to organic coatings. Other adjustable properties, such as high wear resistance, ultra hydrophobicity and ultra hydrophilicity, also require a good understanding of the chemical structure and morphology of the plasma polymer coating. The stability of these properties over a long service life is mandatory.

The plasma polymerization process is performed inside a vacuum chamber where a glow discharge initiates the polymerization. The excited electrons created by the glow discharge ionize the monomer molecules shattering them into reactive radicals that condense and polymerize on the substrate, creating a hard and dense coating. The glow discharges in the present study took place in microwave and radio frequency reactors.

This work studies the influence of reactor conditions, precursor mixtures and polymerization steps on the film properties. In particular, study of the structure, composition, morphology, colour, immersion stability and barrier properties of the plasma polymer films. The influence of the plasma polymerization process on the properties of the whole system (coil coating with plasma polymer on the top of it) was also analysed. This was accomplished using different types of spectroscopy, microscopy and electrochemical tests. The collected experimental data permitted to obtain information concerning the degradation and mechanisms of the coating protection.

This text is organised in four main parts: Introduction, Experimental, Results and their Discussion. Part one is an introduction divided in two sections: In the first, Section 1, common corrosion protection strategies are presented, focusing the protection given by organic coatings. The second, Section 2, gives

some insights about the plasma polymerization process, parameters, reactions, feed gas and type of reactors. State of the art concerning the application of plasma polymer films is also presented.

The experimental part appears divided in two sections. Principles about the techniques used appear in Section 3 and Section 4 describes the samples and the set-ups used for testing, along with operational parameters specific for each technique.

In the third part, in Section 5 and 6, the results are presented and in Section 7 they are discussed. Section 5 contains the results obtained with the unmodified coil coated galvanised steel. Their analysis permits to understand the coil coating behaviour and to collect reference values for the whole system performance. Then, Section 6 presents the results for the same systems after the surface modification by plasma polymerization process. Here, the characterization of the plasma polymer film and the whole system properties are studied. Section 7 discusses the experimental results and performs a correlation between the several parameters studied in the course of the experimental work.

Two complementary parts, general conclusions and suggestions for future work appear in Section 8 and 9, respectively.

“Je n'ai fait celle-ci [lettre] plus longue que parce que je n'ai pas eu le loisir de la
faire plus courte.”

Blaise Pascal, Les Provinciales, Seizième lettre, 4 décembre **1656** 865

Introduction

Section 1. Corrosion and Corrosion Control

1.1. Introduction

Materials are present in everyday life since the beginning of human history. Initially natural materials, like stone, wood and animal or vegetable fibres, were used to improve their comfort. Because of constant research, new materials have been created and introduced to the civilization. *Materials science* searches the basic knowledge about composition, structure, properties and processing of materials while *materials engineering* concerns the use of that knowledge to convert the materials into usable products. ²

Processed materials can be divided into three main classes: metallic, polymeric and ceramic materials. ³ The science and engineering of materials relies on material parameters, which describe them: *composition, structure, properties, processing* and

performance. The materials *composition* refers to their constituent elements. The *structure* of a material refers to the internal arrangement of its components. The *properties* appear related with the response to specific imposed stimulus, independent of the material shape and size. The properties subdivide in six categories: *mechanical*, *electrical*, *thermal*, *magnetic*, *optical* and *deteriorative*. The materials *structure* is dependent of how it is *processed* and the *performance* is a function of its properties.

One of the goals of materials engineering is the proper selection of materials for a specific use. The decision for a given material comes from a compromise between required properties, dictated by the service conditions, the expected service time and cost of the finished product.^{3;4}

1.2. Metals and Corrosion

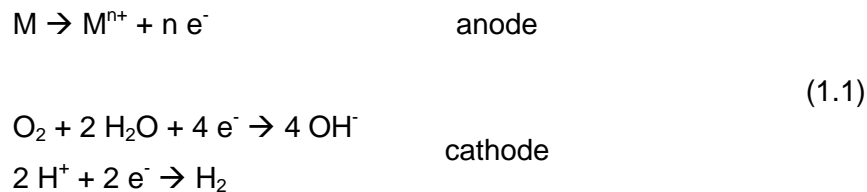
Metals are inorganic substances composed of one or more metallic elements, which may also contain some non-metallic elements. Crystalline structure with atoms arranged in orderly manner is characteristic of metals. In general, they are good thermal and electric conductors, relatively strong and ductile at room temperatures and maintain good strength at high temperature.²

Process metallurgy is one of the oldest applied sciences. Its history can be traced back to earlier than 6000 BC. Currently there are 86 known metals, but until the 17th century, only 12 of these metals had been discovered. The first known metal was gold before 6000 BC, then copper 4200 BC, silver 4000 BC, followed by lead 3500 BC, tin 1750 BC, iron 1500 BC and mercury 750 BC, then arsenic, antimony, zinc and bismuth in the 13th and 14th centuries, while platinum was discovered in the 16th century.

Metals (and metal alloys) possess high structural strength per unit mass, making them useful structural materials. Metal alloys can be engineered to have high resistance to shear, torque and deformation. The strength and resilience of metals has led to their frequent use in building and bridge construction, as well as vehicles, appliances, tools, pipes and railroad tracks.

Metals are extracted from the earth by means of mining. The extracted ores in natural form are in combined state, i.e. oxidized state as carbamates, oxides, sulphides, etc. In this form, they are at their lower energy state. The transformation to the metallic form requires large amounts of energy in order to reduce the extracted ores. The formed metals are, therefore, thermodynamically unstable and tend to oxidise to the previous native and more stable state - by corrosion process. Metallic corrosion is at low temperature of electrochemistry nature, in which metallic ions leave the metal and form compounds in the presence of water and gases.^{2;5-9}

Due to the thermodynamic nature the metallic oxidation, the corrosion process cannot be eliminated, but can be controlled and reduced. All metals and alloys have different tendency to corrode in a particular environment. Usually oxidants present in the environment are sufficient to initiate corrosive processes on most metals. The metal oxidizes forming ions and the oxidant is reduced. The corrosion of a given metal (M) involves usually an anode and a cathode and the reactions present are very often: ^{2;8-10}



The electrons (e^{-}) are able to move in the metal to the cathode area where they react. The solid corrosion products can precipitate at the metal surface. ^{2;8}

The electrochemical corrosion of metallic substrates causes economic costs estimated to be around 2 to 4% of the gross domestic product of a country. ⁹ To these direct costs can be added the cost of temporary shut down of manufacturing plants, with the consequent loss of production. Together with the economic costs, there is the catastrophic failure of public and industrial infrastructures, which can lead to loss of human lives.

1.3. Corrosion Control

Frequently, corrosion can be prevented or minimized by proper selection of materials (not necessarily a metal) and by a careful design of structures. ²⁻⁴ Metals corrode differently in different environments, thus the best choice depends on the environment conditions prevailing during service life. ^{2;8;11;12} A structure projected to avoid direct contact with aggressive agents, points of water accumulation or galvanic contact of different metals will have an extended life, compared to similar structures conceived without such preoccupations. ¹¹

A second approach relies in changing the service environment. Examples are lowering the temperature, removal of oxygen (e.g. with oxygen scavengers in the aqueous phase) and oxidizers, decrease of the concentration of aggressive species present and controlling humidity in the air (atmospheric corrosion only becomes meaningful above 70% relative humidity). ¹¹

Another way of environment modification is with corrosion inhibitors. These are added in small concentrations to decrease the corrosion rate. They inhibit either anodic processes, cathodic processes or both, decreasing the corrosion rate. Corrosion inhibitors include inorganic compounds (e.g. chromates and phosphates) and organic compounds (wide range of saturated, unsaturated, cyclic and aromatic with ionic end groups). Contamination of the environment is a concern since many inhibitors are toxic. Their primary use is in closed systems where the corrosive environment is contained for long periods or re-circulated. The method makes the system less sensitive to scratches or defects compared to coatings, since the inhibitor is available whenever the metal becomes exposed.¹¹

Some metals and alloys exhibit passivation given the right conditions. In this process, a protective surface layer of oxide occurs rendering the metal surface passive, which prevents further reactions. The reaction initially is quite rapid until the protective layer forms. Examples are aluminium, nickel, titanium and chromium together with alloys of these elements.^{2;4;11}

The anodic protection, based in the application of careful controlled anodic currents to promote the passivation of the metal, is only possible with passivating metals and in particular environments. The technique brings some concerns because it relies in modifications of the kinetics/mechanism of the process, which is related with the environment. Environmental changes could lead to mechanism variation and corrosion, typically localized corrosion, may become possible.¹¹

For large steel structures, e.g. naval ships, off shore structures, pipelines, buried tanks and reservoirs, the common procedure is the cathodic protection. This controls the corrosion in the metal surface by making it the cathode of a huge electrochemical cell. For effective protection, the potential of the steel surface is polarized (pushed) to more negative values until only the cathodic reaction becomes possible. At this potential, the oxidation is thermodynamically impossible. There are two main ways to apply the cathodic protection. One is the impressed current technique, which uses anodes connected to a direct current (d.c.) power source (alternating current with a.c. power rectifier) being the structure to be protected the cathode of the electrochemical cell. The second way is the use of sacrificial anodes, where metals with potential more negative than steel oxidize and provide the current needed for the steel polarization. Usually galvanic protection is combined with painting of the structures, to minimize the metal area that is exposed to the environment needing protection, thus saving energy and anodes.^{6;11;13;14}

Surface treatments for protection of the metallic structures are other approach to the corrosion protection. The basic idea is to provide a barrier of material between the aggressive environment and the structural materials. The conversion coatings chemically react with the metal surface to create a physical surface that allows better paint adhesion. They also act as a buffer between the coating and the substrate, reducing the corrosion

rate and the effects of sudden temperature changes. Typical examples are conversion coatings based in phosphates and chromates.

Artificially increase of the natural oxide layer enhances the protection - metals anodization. The process consists in a specialized electrolytic surface finish for aluminium in order to grow the natural passive oxide layer.¹¹ The process improves the hardness of the surface and corrosion resistance, increases paint adhesion, provides electrical insulation and imparts decorative characteristics.

Sol-gel films were recently introduced in the fields of materials science and ceramic engineering. The process consists in a wet-chemical technique starting with typical precursors (metal alkoxides and metal chlorides), which undergo hydrolysis and polycondensation reactions. These are also used as pre-treatment before painting, promoting adhesion and offering extra corrosion protection.

Metallic coatings, like hot dip galvanized steel, provide barrier and, upon its preferential corrosion, ensure cathodic protection if some localised defect allows access of corrosion agents to the metal. Organic coatings rely in similar barrier effect, however, without the cathodic protection.^{11;15;16}

Special surface treatments (e.g. physical vapour deposition, chemical vapour deposition, ion implantation) also could protect metals from corrosion. Apart from that, the thin films are used for the modification of other surface properties: gloss, hardness, electrical or thermal conductivity and wear resistance.

1.4. Organic Coatings

The most common method to control the corrosion process is the application of organic coatings. Advantages like low cost, easy applicability, together with effective corrosion protection ensure increase of their application. Another reason for the success of organic coatings is their high variety of properties and application, since many surfaces are painted for aesthetical reasons.^{17;18}

Paints are not a new invention. Wood and metal have been painted with organic or inorganic pigments to improve their aesthetic appearance and their environmental stability.¹⁹ The development of corrosion protection coatings followed the industrial revolution and development of metallic structures. Usually mechanical strength and fracture toughness are provided by the substrate and the coating provides protection against the environmental degradation processes, including corrosion, wear and erosion, and biological attack.²⁰

Several constituents compose the organic coatings: binder, solvent, pigments and additives. Binders are responsible for film continuity and adhesion to the substrate. They constitute the matrix where all other constituents are integrated forming a composite material. Nowadays binders are mainly synthetic polymeric resins made from petroleum derivatives but natural oils are also an option. The film properties depend of the binder. The solvent dissolves or disperses (water based paints) the binder giving it enough fluidity for application. Pigments are insoluble solids dispersed in a vehicle, which remain suspended in the binder after film formation. They provide colour, opacity and sometimes, anticorrosion properties. The additives are materials introduced in low quantities to modify the film properties during processing, application and polymerization or during service life, e.g. catalysts, stabilizers, dispersants, wetting agents, surface adhesion promoters and rheology.^{20;21}

There are several mechanisms of corrosion protection that organic coatings provide: (i) barrier between the substrate and the environment, reducing the flux of O₂, H₂O and ions from the environment; (ii) high resistance between anodes and cathodes when corrosion takes place, slowing down the reaction rates; (iii) resistance to corrosion products, originating concentration polarization (iv) cathodic/sacrificial protection (e.g. zinc rich coatings); (v) inhibitive/passivation protection, i.e. coatings formulated with inhibitive pigments or additives. The first three mechanisms rely in the film capability of blocking some corrosion process while the last two mechanisms are designated “active”, and take place when physical damage occurs.^{7;11}

Nowadays, the paint industry is passing through significant changes to comply new restrictive laws. Due to these new regulations, the most effective components used for decades, which had outstanding performance, were banned since they are dangerous for the environment and for human health. Typical examples are volatile organic compounds (VOC), pigments using chromium and lead and additives containing mercury.²²⁻²⁵

1.5. Coil Coating

One of the fundamental forms used in metalworking nowadays is metal sheet. Car bodies, airplane wings, medical tables, roofs for building, among others are all constructed from this form of material. Metal sheet is available as flat pieces or in coiled format. The coils production consists in running a continuous sheet of metal through a roll slitter.⁹

Pre-painted metals - *coil coating* - were introduced in the 1940's, as advanced metal anticorrosive paint technology.²⁶ It relies on the simple fact that it is easier to prepare and paint a flat surface than an irregular shape. The process is one of the most advanced techniques to apply continuously a thin organic coating, of uniform quality and excellent

service performance, on a metal sheet just after metal fabrication. Later the coil coated metal sheets are submitted to shaping forming the desired products. The technology of coil coating has several advantages: ^{9;12;18;25;26-36}

- Productivity gains: pre-painted metal sheet allows many manufacturing industries to cut their own painting lines saving in space and time.
- Process cost reduction: for the same amount of painted metal less paint is needed, since the application is precise and with high control of thickness decreasing losses. Energy savings are also possible with efficient curing and automatization of the process.
- Quality increase: achieved by control of steps, uniform cleaning and surface preparation followed by painting with constant and reproducible properties and thickness.
- Environmental gains: a close painting circuit means no losses of paint and capture of solvents, which are then regenerated or incinerated. Any other atmospheric or water pollutants are also treated.

Coil coatings, however, also have some disadvantages. Only companies with enough volume of production can take advantage of the process. Not all type of final products can use the pre-coated metal, due to shape or function. Welding of pre-painted metals shows problems and has limited application. In the cut-edges, loss of adhesion and corrosion initiation is a concern. Since the paint is already applied when the metal sheet is formed to their final shape, the mechanical forces can affect the paint forming cracks and other defects.

The most common metallic substrates used are aluminium and steel. Steel is frequently electro or hot dip galvanised for extra protection, thus ensuring an important performance improvement. A schematic coil coating production line is in Figure 1.1.

For the coil coating process, the metal substrate is delivered in coils weighting from 5-6 tonnes for aluminium to 36 tonnes for steel, having up to 1.4 m wide and 3.6 km long. The metal coil is positioned at the beginning of the line and unwound at a constant speed, as fast as 100 m/min. ³⁶ Two strip accumulators, found at the beginning and at the end of the line, enable the work to be continuous allowing new coils to be added and finished coils removed by a metal stitching process, without stopping or slowing down the production line.

The metal sheet is sequentially cleaned, pre-treated and painted under strict control of the parameters, ensuring uniformity of the process. Afterwards, the sheet enters a painting chamber where special rotating rubber roller applicators paint either one or both sides. The sheet enters a furnace where the organic coating film cures. Several layers can be applied.

The system achieves protection before subsequent formability processes. Finally, a winding machine re-rolls the painted sheet to complete the coil coating production. Coil coatings show consistent quality, excellent formability, long durability, good corrosion and weathering resistance.¹⁵

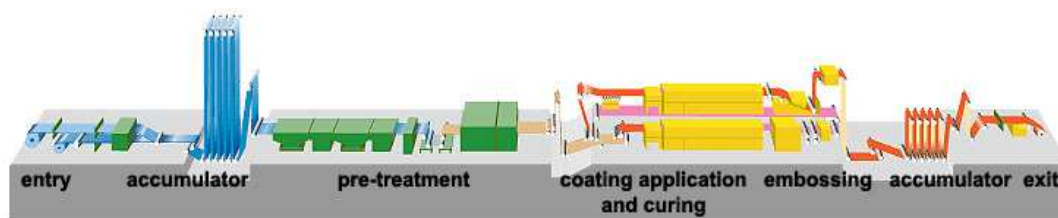


Figure 1.1 General scheme of a coil coating production line.³¹

1.6. Degradation of Painted Metals

Although paints offer a significant enhancement to the life of coated steel, they do eventually fail in some fashion. Coated metals fail when the coating no longer prevents the corrosion reactions from occurring. This leads to appearance changes of the coating until an unsatisfactory level or, at later level, to a decrease of the mechanical performance of the system below its original design specifications.^{7;16;37}

In painted galvanised steel panels, the cathodic protection of the zinc layer is also present and initially only slow white corrosion products appear, even in the most aggressive environments. When the zinc-containing metallic coating locally wears off completely, together with complete leach out of pigments, the system protection disappears. At this point orange-reddish corrosion points form due to attack of the base steel.

Generally, several paint degradation processes take place simultaneously that ultimately form blisters or flaking of the paint.

Ultraviolet attack is a possible degradation process in which polymer chains become destroyed, changing the paint colour and decreasing the gloss. Chemical agents attack (solvents, acids and bases), together with mechanical aggressions (like scratches and abrasion effects), are possible external processes. The temperature of the working environment can provoke different contraction or dilatation of the substrate and of the paint.

These processes lead to the formation of blisters and delaminating areas, reducing the adhesion of the paint to the substrate. The metallic corrosion usual occurs associated with

these processes. Several types of corrosion processes may occur in the metal-paint interface:

- Blisters form in areas where the paint loose adherence to the substrate. Water, oxygen and ions absorption across the paint is common (since no coating system in use stops completely their transport), permitting the dissolution of ionic species present in the interfacial area or from the paint matrix. As consequence, the adherence decreases and blisters are formed.
- Anodic delamination, which occurs when the metal anodic area is dissolved provoking separation of the paint from the substrate. This is more common in aluminium. In steel occurs when anodic potentials are imposed and in galvanised steel when the zinc layer dissolves leaving a space between the paint and the steel substrate.
- Filiform corrosion takes place in high humidity environments when the substrate (usually steel, aluminium or magnesium) is contaminated with soluble salts. This shows the formation of threadlike filaments in the paint/substrate interface emanating from one or more sources in semi-random directions. The filaments are fine tunnels composed of corrosion products underneath the bulged and cracked coating.
- Cathodic delamination occurs when the paint is detached in the metal cathodic zone. This is more common when cathodic protection is combined with paints. In this cathodic area the pH is higher due to $\text{OH}^-_{(\text{aq.})}$ resulting from the cathodic reaction. In strong alkaline environments, (pH of 10 to 14) dissolution of the interfacial oxide film can occur or reaction with the polymer groups binding to the substrate. In any of these cases, interruption of the paint substrate binding occur leading to adhesion decrease.

Given enough time, the failure of the metal coated systems is catastrophic. Generally, the failure results from macroscopic defects originated by initial microscopic physical defects that, in turn, are the result of chemical variations occurring in the coating system during exposition to working conditions in which they are placed.³⁸

Section 2. Plasma Polymerization

2.1. Introduction

Several works have reported that the coil coating systems confer excellent protective properties to the metallic substrates against corrosion.^{18;25;36} There is, however, a constant development of industry with new demands for products, which bring the painted systems to new environments, where the coating systems have to work protecting the metallic substrates.^{39;40} These new environments are also becoming more aggressive, demanding better performance from the paint systems used. In general, special properties with regard to chemical resistance, hydrophilicity, roughness, crystallinity, conductivity, lubricity and scratch resistance are required for the success of these applications. For these reasons,

surface modification techniques that can tailor the coil coating surface have become an important part of industrial objectives.⁴¹

Surface tailoring modifies the chemical and physical properties of substrates surfaces, without affecting the bulk properties. Common surface modification techniques include treatments by corona, flame, photons, plasmas, electron beams, ion beams and x-rays. These surface treatments are applied to achieve several purposes. The modification can include the incorporation of specific elements (oxygen, nitrogen, fluorine atoms, etc.) or moieties (hydroxyl, carbonyl, carboxylate, etc.), in the surface for specific interactions with other functional groups. Surface crosslinking and removal of weak boundary layers contaminants, surface morphology variation by increasing or decreasing crystallinity and roughness are also achievable.^{41;42}

2.2. Plasma Polymerization

Tonks and Langmuir first used the term plasma in 1929 to describe a collection of charged particles.^{43;44} Lord Rayleigh in 1906 already described the collective behaviour of charged particles due to the long range of the Coulomb forces, during the analysis of electron oscillations in the Thomson's model of the atom.⁴⁵ *Plasma* is a gas containing charged and neutral species, including electrons, positive ions, negative ions, radicals, atoms and molecules. The average electron voltage ranges between 1 and 10 eV, the electron density varies from 10^9 to 10^{12} cm^{-3} and the degree of ionization can be as low as 10^{-6} or as high as 0.3.⁴¹

The plasma can be used to modify chemically and physically the surface properties of a chosen substrate modifying only the topmost layers, typically of several hundred Angstroms. The depth of surface modification mainly depends on the power level and plasma treatment time. The modified layer has different (generally desired) properties from the bulk material, which retains the original properties. The process is rapid, clean and environmental friendly, providing chemically mild and mechanical non-destructive means of altering the surface properties, targeting improved surface characteristics. This is very convenient for activation or modification of polymer surfaces.^{41;42;46-50}

The most appropriate term to describe the plasma deposition process is *luminous chemical vapour deposition*, but the phenomenon is known as *plasma polymerization* or *plasma chemical vapour deposition*.⁵¹ The excited atoms emit photons and create the *glow*. The *plasma glow* or *luminous gas phase* creates the environment from which material deposition occurs.^{42;52} Since remaining positive ions also flow towards the cathode, the most intense glow in the reactor is at the cathode. The space between cathode and anode, containing electrons, ions and radicals, is electrically neutral and

represents the *plasma glow discharge*. This process takes place in low pressure and low temperature plasma.⁵³

The plasma polymerization may also be named *chemical glow discharge*, since the polymer is deposited as a thin film on the substrate surface at the immediate environment of a glow discharge of the constituent gaseous monomers. The condition for the process is the presence of chain-producing atoms such as carbon, silicon or sulphur, in the working gas. This permits wider range of starting materials, including monomers usually not considered in conventional polymerization. In contrast with conventional polymers, plasma polymers consist of branched and irregular chains randomly terminated, which are three-dimensional and amorphous with highly crosslinked network, showing chemically and physically stable characteristics.^{41;46;47;54-56}

The stoichiometric composition of the plasma deposited polymer can differ significantly from the starting monomer. This characteristic is related with the highly decomposed molecules reacting with ions and electrons. This is also the reason of the higher density with branched and irregular chains, when compared with the conventional polymers produced from the same monomers. The process parameters control the structure preservation and crosslinking gradients. To preserve the monomer structure in the plasma polymer films the power input should be limited with operation at high pressure. This limits the residence time of the monomer in the plasma avoiding ionic bombardment. Layer crosslinking gradients increase the degree of crosslinking over the layer thickness, which results in denser and disordered structure.^{41;47;48;52;54;57-60}

The schematic diagram of Figure 2.1 shows the difference between conventional polymers and polymers produced by plasma polymerization procedure.

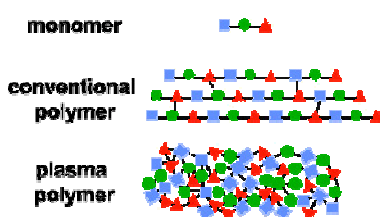


Figure 2.1 Schematic diagram of polymer films.

2.3. Mechanism of Plasma Polymerization

Under plasma conditions, the monomer molecules undergo fragmentation, forming free reactive radicals. The combination and recombination of these radicals generate higher

molecular weight compounds. The mechanism of the plasma polymerization for organic compounds is, therefore, *the free radical mechanism* with ionization. The mechanism is grouped in five generic processes: initiation, adsorption, propagation, termination and re-initiation. The equations of Table 2.1 list the elementary reactions responsible by the plasma polymerization.⁵⁴

Table 2.1 Elementary processes occurring during the plasma polymerization.⁵⁴

a - initiation	b - adsorption
$e^- + M_g \rightarrow 2R_g + e^-$ $e^- + M_g \rightarrow M_g^* + 2H \text{ (or } H_2) + e^-$ $M_g \xrightarrow{(e^-, hv)} 2R_g$	$M_g + S \Leftrightarrow M_g$ $R_g + S \Leftrightarrow R$
c - propagation	d - termination
$R_g \text{ (or } H) + M_g \rightarrow R_g^*$ $R_s + M_g \rightarrow R_s^*$ $R_s + M_s \rightarrow R_s^*$	$R_g \text{ (or } H) + R_g^* \rightarrow P_g$ $R_g + R_s^* \rightarrow P_s$ $R_s + R_s^* \rightarrow P_s$
e - re-initiation	
$e^- + P_g \rightarrow R_g + R_g^* + e^-$ $H + P_g \rightarrow R_g + H_2$ $P_s \xrightarrow{(e^-, hv)} R_s + R_s^*$	

Legend:

M – monomer

R – free radical

H – hydrogen atom

S – substrate

P – polymer film

* – depletion of one hydrogen atom

h – Planck constant, 6.626×10^{-34} J s

v – electromagnetic wave

g – gas

s – surface

- *Initiation* corresponds to free radicals formation in the gas phase by collision of energetic free electrons with the monomer molecules. This produces hydrogen and monomer depleted of one hydrogen atom. The hydrogen atoms formed can produce further free radicals by either hydrogen abstraction or addition to an unsaturated monomer.
- *Adsorption* of both monomer and gas phase free radicals occur at the surface of the substrate in contact with the plasma.

- *Propagation* of chain growth occurs both in the gas phase and on the surface of the depositing polymer film. The reaction may occur either with the original monomer fed to the plasma or with the unsaturated products formed by electron molecule collision.
- *Termination* of chain growth also occurs both in the gas phase and at the polymer surface. In the gas phase, the free radicals are lost by reaction with hydrogen atoms and other free radicals. At the polymer, radicals are lost by reactions involving gaseous atomic hydrogen, gas phase free radicals and absorbed free radicals.
- *Re-initiation* processes occur when the chain fragments formed by the recombination of free radicals reconvert into radicals. This is possible by reactions in gas phase, via electron collision and in the polymer surface, by impact of charged particles or photon absorption. Hydrogen transfer reactions may also induce *re-initiation* in gas phase and on the polymer surface.

The free radicals are the primary species propagating chain growth, both in the gas phase and on the surface of the deposited polymer. These species form in the gas phase through the collision of free electrons with monomer molecules and on the surface of the growing polymer film through the impact of ions and electrons. Surface free radicals are also produced through the adsorption of a part of the radicals formed in the gas phase.⁵⁴

The major plasma polymer deposition occurs in the substrate surface that makes contact with the glow. The growth mechanism is rapid step growth polymerization with the creation of chemically reactive species. Subsequent growth of the polymer film occurs by the reaction of surface free radicals with either gas phase free radicals or unsaturated monomer.^{41;48;51;52;54;61;62}

A general reaction scheme is presented in Figure 2.2. The scheme suggests that the monomer converts into reactive and nonreactive products through processes occurring in the plasma (reaction pathways 2 and 4) as well as entering into polymer formation (reaction pathway 1).

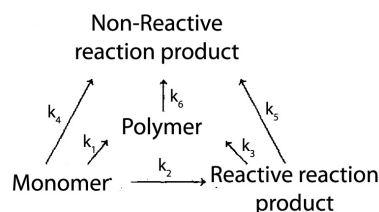


Figure 2.2 Schematic diagram of reaction network.⁵⁴

The reactive products may further contribute to polymer deposition (reaction pathway 3) or be converted to non-reactive products (reaction pathway 5). The degradation of the polymer to form non-reactive products (reaction pathway 6) is also considered.⁵⁴

2.4. Application of the Plasma Films

The applications of plasma polymer films include hydrophobic or water repellent films,^{42;46;53;63-69} modification of membrane surfaces,⁷⁰ cellulose and paper,^{71;72} electrical conductive layers, scratch resistance coatings, optical filters, protective coatings,^{39;53;73-79} chemical barrier coatings and compatibility between two polymers.^{41;42;46-48;53;66;80-84} More specific developments are production of graded refractive index,⁸⁵⁻⁸⁸ scratch resistant and antireflection layers,⁸⁹⁻⁹² dielectric coatings,^{41;42;48} chemical inertness films,⁹³⁻⁹⁵ encapsulations and development of protective and biocompatible materials.⁹⁶⁻¹⁰¹

The plasma polymerization process presents a wide range of properties and accurate process control that leads to reproducible modifications and feasibility to scale up reactors and processes to industrial dimensions.^{40;41;46;47;102;103} Three-dimensional objects are more difficult to be plasma polymerized by the fact that power input may not be uniform over the entire substrate surface. The generated films have composition that can vary from inorganic silica to teflon-like polymers.⁴⁸

2.5. Application to Coil Coatings

Two main technological developments promote the application of plasma polymerization for continuous deposition. The first is a hollow cathode reactor designed for a continuous high rate deposition of plasma polymers on metal sheet. In this case, parasitic deposition on reactor walls can be avoided. The second concerns barrier discharges and microwave discharges that lead to plasma polymer deposition at atmospheric pressure, current pressures range from 0.1 mbar to 1 bar. The use of vacuum technology for plasma polymerization is avoidable in the near future.^{39;104;105}

The application of the plasma polymerization process to coating systems can have, however, significant influence on their protection properties.¹⁰⁶ This influence mainly relates with the severe process conditions necessary for the plasma generation in the reactor. The possible ways of failure increase the necessity of improved weathering stability of the plasma film since the long term corrosion protection is directly dependent of the ability of the plasma layer to resist against the environment. Cohesion and adhesion

between the coil coating and the top layers has a great influence on this weathering stability.¹⁰⁷

The weathering resistance is determined by the surface, chemical and physical properties of the substrate and coating layers.⁴¹ The mechanical properties are determined by the physical properties of the matrix material, by the interaction between the layers and by the functional groups of the surface. The chemical and physical properties are the key factors for the coating system performance.

2.6. Effect of Process Variables

The quality of the plasma polymer films is dependent and controlled by the process parameters, such as monomer flow rate, system pressure, discharge power, geometry of the system, reactivity of the starting monomer, electromagnetic field frequency, that also permit a wide choice of final properties.^{47;48;52;58;108}

2.6.1. Flow Rate

Keeping constant the other parameters (power, pressure, etc.), the deposition rate rises monotonically with the increasing flow rate, because the polymerization rate is limited by the supply of fresh feed gases. However, at high flow rates the deposition rate decreases because the residence time of the feed gases decreases and even activated species may be prevented from reaching the substrate by being drawn away and pumped out. A maximum occurs when the competing processes are balanced.⁴⁷

2.6.2. Discharge Power

With pressure and flow rate held constant, the deposition rate increases with power (power density) at first and then becomes independent of power at high values.⁴⁷ The minimum power necessary for the plasma polymerization of a given monomer differs significantly from one to another, because the discharge power needed to initiate glow discharge varies from one monomer to another.^{48;52}

The plasma is a direct consequence of the gas ionisation due to an increase of the applied voltage between the two parallel plate electrodes. This will eventually lead to an abrupt increase in current due to breakdown of the gases between the electrodes. The power

input employed in plasma polymerization initiates and sustains the plasma, and leads to fragmentation of the monomer. Increase of power will result in an increased density of energetic electrons and in an increased bombardment of the electrode by energetic ions. The crosslinking in plasma polymer increases with the intensity and energy of bombarding ions.^{48;52}

2.6.3. Electromagnetic Field Frequency

The frequency of the applied electromagnetic field used for producing the plasma is one of the major variables that influences the properties of the plasma polymerized thin films. Some of these effects result from changes in the shape of the electron energy distribution function (EEDF) which, under certain pressure conditions, can be frequency dependent. The shape of the EEDF as well as its average energy depends on the ratio ν/ω (ν is the effective average electron-neutral collision frequency for momentum transfer and $\omega=2\pi f$ is the wave angular frequency) in gases where the electron-neutral collision cross section depends on the electron energy. This theory predicts a significant difference depending on whether the plasma operates in the microwave domain or in the radio frequency domain. In the microwave domain, i.e. for frequencies such that the ratio ν/ω tends towards zero, the EEDF tends toward a Maxwellian distribution, whereas in the radio frequency domain ($\nu/\omega > 1$), it is non-Maxwellian with a comparatively smaller energetic tail but a relatively larger population of low-energy electrons and a slightly higher average energy. These differences in the EEDF reflect on the population density of excited species and because of the highly energetic tail of the Maxwellian EEDF, the higher levels should be more densely populated. This explains why microwave plasma contains more electrons and ions than radio frequency plasma, and for the same given absorbed power density in microwave (2.45 GHz) plasma, deposition rates tend to be at least an order of magnitude greater than in radio frequency plasmas.¹¹⁰

2.6.4. Pressure

The effect of pressure during the plasma polymerization includes the effect of the residence time, which increases with increasing pressure, and the effect on average electron energy.⁴⁷ The atoms in vacuum travel in straight lines, however, if there is residual gas in the chamber, the atoms will collide with the gas and disperse in all directions losing some energy as heat. At higher pressures, the collisions will cause atoms to condense in air before reaching the substrate surface, giving rise to powder deposits.⁴⁸

The requirements for the formation of plasma polymers are low mean pathway, long residence time, and relatively high electron energy, therefore, the plasma polymerization occurs easier at higher pressure, even if increased pressure can result in the inhomogeneity in deposition rate distribution. Plasma polymerization at higher pressure leads to the deposition of nanoparticles with diameters ranging from 20 to 90 nm, which are incorporated in the growing film. During the formation of the first layer, these nanoparticles adsorb on the surface and lead to interfacial nanoscopic voids. Subsequently, the roughness of the growing film increases with its thickness. This leads to the formation of an increased number of diffusion pathways.⁴⁰ Therefore, most operations of plasma polymerization occur at pressures below 1.333 mbar (1 Torr) in order to obtain a more homogeneous film and to increase interaction of plasma with the surface. The deposition rate rises at first and tends to saturate at increased pressure, power and flow rate being held constant.⁴⁷

2.6.5. Feed Gas

The plasma polymerization processes of gas plasmas can be classified as cleaning and etching, surface reactions and plasma polymerization depending on the feed gas and plasma conditions.

i. Inert Gas

Inert gas plasmas are used for pre-treatment of the substrates for cleaning and adhesion purposes, applied before reactive gases. Helium, neon, and argon are the three inert gases used in plasma technology. Due to the relatively lower cost, argon is by far the most common inert gas used. The treatments use low-power plasma of noble gases for periods typically from 1 second to several minutes. This exposure is sufficient to abstract hydrogen and to form free radicals at or near the surface, which then interact to form crosslinks and unsaturated groups with chain scission. The plasma also removes low-molecular-weight species or converts them to a high molecular weight by crosslinking reactions. As a result, the weak boundary layer formed by the low molecular weight species is removed and, consequently, greater adhesive strengths are observed.^{41;110}

ii. Oxygen Containing Gas

Oxygen and oxygen-containing plasmas modify the polymer surfaces, reacting with a wide range of polymers, producing a variety of oxygen functional groups, including C-O, C=O,

O-C-O, C-O-O, and CO₃ at the surface. In oxygen plasma, two processes occur simultaneously: etching of the polymer surface, through the reactions of atomic oxygen with the surface carbon atoms giving volatile products, and the formation of oxygen functional groups at the substrate surface, through reactions between the active species from the plasma and the surface atoms.⁴¹

iii. Hydrocarbons

Hydrocarbons used in plasma polymerization may not contain conventionally polymerizable groups. Ethane, methane and cyclohexane can be used at a slower rate than acetylene, ethylene and benzene. These starting feed gases can be divided by three subclasses: (1) triple bond containing structures (including benzene), (2) cyclic and double bond containing structures, and (3) saturated structures. These three subclasses differ in deposition rate for similar molecular weight feed gases under identical conditions.⁴⁷

Chains containing polar groups form a more polar plasma polymer than those from hydrocarbons alone. Feed gases as pyridine, vinyl pyridine, and allyl-amine are included here. Additionally, the use of N₂ and/or H₂O as a co-feed gas with a hydrocarbon can form a hydrophilic plasma polymer.

iv. Fluorocarbons

Fluor polymer films have unique properties such as good thermal stability, chemical resistance, low dielectric constant, low coefficient of friction, low surface energy, and high impact strength offering the possibility of making adherent highly fluorinated coatings.⁴² Super-hydrophobic fluorocarbon coatings with ribbon-like morphology are possible from pulsed radio frequency discharges. Plasma etching in microelectronics applications occurs and the choice of plasma conditions and fluorocarbon decide whether etching or deposition occurs. The choice of functional groups attached to fluorocarbon monomers is severely limited.^{41;47}

v. Silicon Containing Gas

Silicon containing feed gas includes various linear and cyclic siloxanes and silazanes, as well as silanes. The plasma polymers obtained from organosilicon monomers have excellent thermal and chemical resistance and outstanding electrical, optical, and biomedical properties.^{41;47;48}

The various organosilicon precursors include silanes (Si), disilanes (SiSi), disiloxanes (SiOSi), disilazanes (SiNHSi), and disilthianes (SiSSi).⁴¹ These functional groups add to

the substrate surfaces via plasma polymerization. Most used monomers include tetramethylsilane, vinyltrimethylsilane, hexamethyldisiloxane and hexamethyldisilazane containing Si, H, C, O or N atoms.⁴⁸

Hexamethyldisiloxane is a normal choice of industry because it is a non-toxic material and no harmful materials are produced during processing. This monomer also offers flexible Si-O-Si bond in the backbone and shows resistance to water permeation, characteristic of polysiloxane films.^{48;53}

vi. Metal-containing Gas

Metal containing plasma polymers films are produced using volatile organometallic compounds as feed gases or by the use of atomic metal (from an evaporation source or sputtering) in combination with conventional feed gases.⁴⁷

2.6.6. Type of Reactors

The most widely used reactor configurations for plasma polymerization are divided in classes: (i) internal electrode reactor; (ii) external electrode reactor; and (iii) electrodeless microwave or high frequency reactor. There are also developments for (iv) atmospheric pressure reactors.⁴⁷

i. Internal Electrode Reactor

Reactors with internal electrodes have several names, e.g. flat bed, parallel plates, planar, diode, etc. Their main features are power supply, coupling system, vacuum chamber, radio frequency driven electrode, grounded electrode and one or more substrate holders. The radio frequency power supply couples to the system by a blocking capacitor (capacitive coupling) or direct dc coupling. In the first case, the driven electrode potential oscillates around a cathodic self-bias potential, which can be very negative. The appropriate working conditions and apparatus geometry significantly influence the extent of ion bombardment on the substrate as well as electron energy distribution and active species production. The internal electrode arrangements use ac 1 to 50 KHz and radio frequency fields for plasma excitation. The vacuum chambers are either of glass or of conductive materials, such as metal, to have better shielding from external sources. A metallic shield for the cathode surrounding the electrode highly improves the glow confinement inside the interelectronic space. The electrode material and area affect the extent of sputtering on the target.⁴⁷

ii. External Electrode Reactor

External electrode reactors can be capacitive or inductive coupled with power transmitted from the power supply to the gas by a capacitor and a coil respectively. Insulating tubular reactors are used, recurring to glass, quartz, or alumina for reactor materials. Inductively coupled tubular reactors, when operating at low pressure (lower than 1.3 mbar), are not uniformly coupled to the power supply, however, coupling uniformly increases with increasing working pressure.⁴⁷

Many experimental arrangements exist, each differing in power supplies, reactor geometries, and sample positions. The working frequencies range from 13.56 to 35 MHz, and the tube geometry and sample position varies from upstream to downstream of gas flow in order to obtain different polymer composition and properties.⁴⁷

iii. Electroless Reactor

In electroless reactors, impurities formed cannot be sputtered off and become incorporated into the growing films as in the reactor electrodes. The systems are microwave powered characterized by tubular or Pyrex reactors with a resonant cavity coupled with a power supply typically in the region of the 2.45 GHz. The plasma is generated in the resonant cavity and the polymer is collected outside the glow region.⁴⁷

The deposition of the film cannot occur in the discharge region and instead occurs by introducing the feed gas into the downstream area of the carrier gas excited in the plasma zone so that the substrate is placed far away from the gas inlet.⁴⁷

iv. Atmospheric Pressure Reactor

Most plasma polymerization of polymer thin films has been performed at low pressure (less than a few bar) in order to form uniform films. Atmospheric pressure glow plasma system appears to reduce the cost of the apparatus and to simplify the experimental operations. For stable plasma glow at atmospheric pressure is used: an ac power source with frequency greater than 1 kHz, an insulating plate on the lower electrode and metal-plate upper electrode with the insulating plate set on its bottom. This reactor can treat not only dielectric plates but also metallic plates. The atmospheric pressure plasma polymerization method provides a promising application for large-scale system production of polymer thin films.⁴⁷

Experimental

Section 3. Principles of the Experimental Techniques

Organic coatings are tested for various purposes: to control the quality of the coatings, to develop new coating materials, to select the best coating for a particular environment, to study the fundamental properties of coatings and their operating modes, etc. The tests may be physical, testing the primary properties of coatings; accelerated, performed by increasing the temperature and concentration of the corrosive species; atmospheric, exposed at different environmental conditions of earth; or electrochemical, since even painted metals corrode by an electrochemical process. Different forms of microscopy and spectroscopy are also useful for these types of studies to obtain the structure and composition of the systems. Electrochemical tests are used when the corrosion of the painted metals is of interest.¹¹²

The main techniques employed in this work were Electrochemical Impedance Spectroscopy (EIS), Scanning Electron Microscopy (SEM), Energy-dispersive X-ray spectroscopy (EDS), Transmission Electron Microscopy (TEM), Atomic Force Microscopy

(AFM) and colour measurements. Some introductory notions about the techniques appear in this section.

3.1. Electrochemical Impedance Spectroscopy

The application of electrochemical impedance spectroscopy (EIS) to study the degradation of polymer coated metals became very common nowadays. The technique permits to obtain several parameters in a single measurement, which are related with the coating and to the corrosion process. Moreover, it is a non-destructive technique and using a small amplitude perturbation does not modify the processes occurring. In addition, permits to test the same sample during long immersion periods.¹¹²⁻¹¹⁷

The technique permits to obtain the electrochemical properties of the coated systems by studying the impedance as a function of the frequency of an applied ac wave. It is one of the most used techniques to study the degradation of coated systems, also common for corrosion studies and electrochemistry for materials characterization.¹¹⁸⁻¹²⁰

3.1.1. Impedance

The electrical resistance is the ability of a circuit element to resist the flow of electrical current. The Ohm's law defines resistance in terms of the ratio between applied voltage, E , and current, I :

$$R = E/I \quad (3.1)$$

The ideal resistor follows Ohm's law at all current and voltage levels.¹¹⁸⁻¹²⁰ The real systems correspond to electric circuits with different elements and with a more complex behaviour and, instead of resistance, impedance is needed to correctly describe the circuit performance. An electrochemical cell could be considered as equivalent to an electric circuit. The impedance measurement is normally done by applying an a.c. sinusoidal potential excitation to the cell and measuring the current through it. The response to the potential is an a.c. current signal. The excitation signal used is small so that the cell response is considered pseudo-linear. In a linear (or pseudo-linear) system, the current response to a sinusoidal potential will be a sinusoid at the same frequency but shifted in phase (ϕ), Figure 3.1.

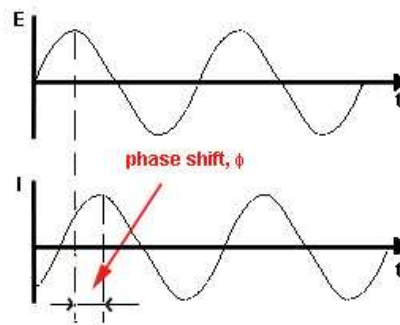


Figure 3.1 Sinusoidal current response in a linear system.

The excitation signal as a function of time has the form:

$$E_t = E_0 \sin(\omega t) \quad (3.2)$$

where E_t is the potential at time t , E_0 is the amplitude of the signal and ω is the radial or angular frequency. The ω and f are related by $\omega = 2\pi f$, with f in Hz. In a linear system, the response signal, I_t , is shifted in phase:

$$I_t = I_0 \sin(\omega t + \phi) \quad (3.3)$$

Using an expression analogous to Ohm's Law leads to the impedance of the system expressed in terms of magnitude, Z_0 and phase shift, ϕ :

$$Z = \frac{E_t}{I_t} = \frac{E_0 \sin(\omega t)}{I_0 \sin(\omega t + \phi)} = Z_0 \frac{\sin(\omega t)}{\sin(\omega t + \phi)} \quad (3.4)$$

Introducing the complex notation enables the impedance relationships to be presented as Argand diagrams, like the one shown in Figure 3.2, where both cartesian (Z' , Z'') and polar coordinates (Z_{mod} , ϕ) are presented. The former leads to the complex plane plot or Nyquist impedance spectrum, where the real impedance, Z' , is plotted against the imaginary impedance, Z'' , and the latter to the Bode spectrum where both the logarithmic of modulus of impedance, Z_{mod} , and the phase angle, ϕ , are plotted as a function of the logarithmic of frequency. ^{112;121}

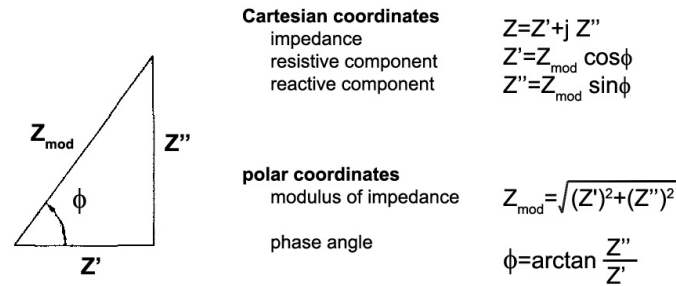


Figure 3.2 Argand diagram showing impedance vectors.

Using the Euler's relationship, $e^{j\phi} = \cos\phi + j \sin\phi$ and with $j = \sqrt{-1}$ it is possible to re-write equation 3.4 and express it as a complex number:

$$Z = \frac{E_0 e^{j\omega t}}{I_0 e^{j(\omega t + \phi)}} = Z_{\text{mod}} e^{-j\phi} \quad (3.5)$$

$$Z = Z' + j Z'' = Z_{\text{mod}} \cos\phi + j Z_{\text{mod}} \sin\phi$$

The real part of impedance is characteristic of irreversible processes like energy dissipation and transport at large distances, while the imaginary part characterizes reversible processes like energy storage from polarization and magnetization processes.

The use of Bode plots has some advantages. All measured points appear equally scattered while in the Nyquist the majority of the points are located at both ends of the spectrum. Labelling of the curves in a Nyquist plot with frequency marks can be quite cumbersome. In Bode plots, resistive and capacitive regions are clearly distinguished and together with the information provided by the frequency dependence of the phase angle, which is a very sensitive indicator of small changes in the spectra, a quick analysis of spectrum is possible. Processes that have different time constants can be easily observed due to the logarithmic scale used in Bode plots.

3.1.2. Validity

The EIS measurements have to fulfil some criteria to be valid:

- **Causality**, the response of the system must be due only to the perturbation applied and does not contain significant components from other sources;

- *Linearity*, impedance is independent of the magnitude of the perturbation;
- *Stability*, the system has to return to its original state after removal of the perturbation;
- *Finiteness*, the transfer function must be finite valued at $\omega \rightarrow 0$ and $\omega \rightarrow \infty$ and must be continuous and finite-valued at all intermediate frequencies.

Some authors use the Kramers-Kronig transforms to check the validity of an impedance data set, obtained for a linear system over a wide range of frequencies. Application to electrochemical and corrosion systems was performed. The equations show that the real component of the impedance can be calculated from the imaginary component and vice versa.^{122,123}

3.1.3. Spectra Interpretation

The most common way to analyse EIS spectra nowadays is by fitting the impedance data to an equivalent electrical circuit, which is representative of the processes taking place in the system under investigation.¹¹²






As stated before, the electrochemical system can be described by passive electrical circuits. Each circuit element relates to one independent electrochemical property or process and each element has a defined value obtained from the impedance response.

i. Single Elements

The most important circuit elements used in corrosion studies appear in Table 3.1. The respective impedance equations are also shown.

The resistor, R , corresponds most frequently to the resistance of solution or oxide layers or to the charge transfer resistance associated to the corrosion process and the capacitor, C , is normally associated with oxide layers or the double layer capacitance. The Warburg element, W , is used to model linear semi-infinite diffusion, which occurs when the diffusion layer has infinite thickness. The constant phase element (CPE), Q , is a general element which can represent a variety of elements such as inductance ($n = -1$), resistance ($n = 0$), Warburg ($n = 0.5$), capacitance ($n = 1$) or non-ideal dielectric behaviour ($-1 \leq n \leq 1$). It can account for a distribution of relaxation times over the surface of the electrode or for non-uniform diffusion, whose electrical analogue is an inhomogeneously distributed RC transmission line. Usually, Q replaces C , the pure capacitive response seldom found in real systems.¹¹²

Table 3.1 Electrical impedance elements and respective impedance expressions.

element	symbol	impedance expression
resistor, R		R
capacitor, C		$\frac{1}{j\omega C}$
inductor, L		$j\omega L$
Warburg, W		$W = \sigma \omega^{-1/2} - j\sigma \omega^{-1/2}$, where $\sigma = \frac{RT}{n^2 F^2 \sqrt{2}} \left[\frac{1}{C_{H_8^{2+}} (D_{H_8^{2+}})^{1/2}} + \frac{1}{C_{H_8} (D_{H_8})^{1/2}} \right]$
CPE, Q		$\frac{1}{Y_0(j\omega)^n}$

Y_0 is the frequency independent admittance.

In Figure 3.3 the Nyquist (**b**) and Bode diagrams (**c**) are shown for two resistors ($R_1=10$ ohm and $R_2=1000$ ohm) and for two capacitors ($C_1=10^{-6}$ Farads (F) and $C_2=10^{-9}$ F), together with their expressions (**a**) for real and imaginary components of the impedance.

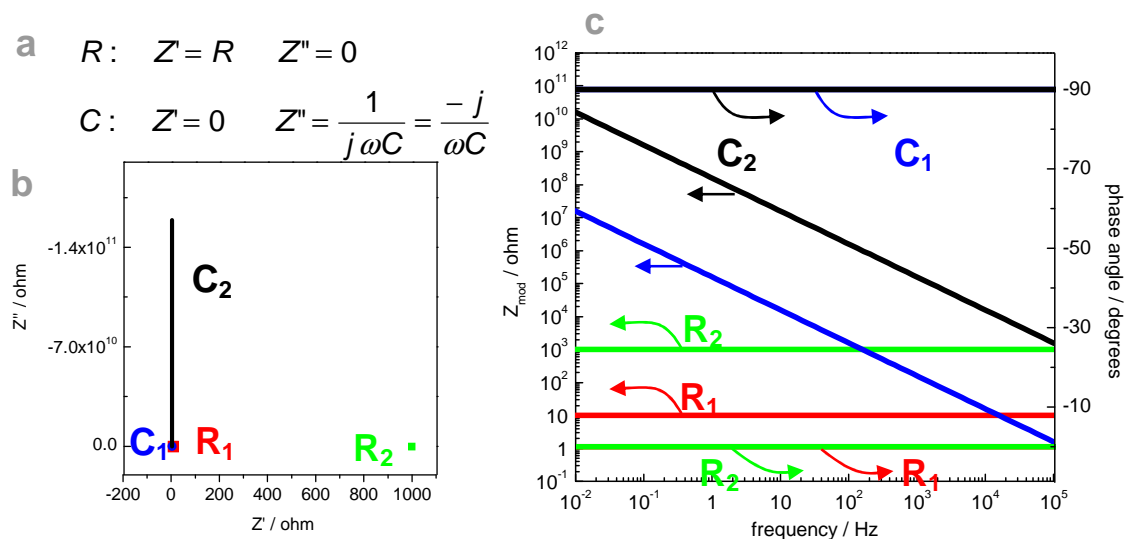


Figure 3.3 Resistor and capacitor **a**. Impedance expressions, represented as; **b**. Nyquist; and **c**. Bode plots, for two resistance values $R_1 = 10$ ohm and $R_2 = 1000$ ohm; and for two capacitance values $C_1 = 10^{-6}$ F and $C_2 = 10^{-9}$ F.

In the Nyquist plot, the representation of a pure resistor is a single point in the Z' axis (R_1 and R_2). On a Bode plot, it is a straight line parallel to the frequency axis (R_1 and R_2). The horizontal line shows that the impedance is independent of frequency and has no reactive components. The phase angle is zero at all frequencies. ¹²⁴

The Nyquist plot for a pure capacitor is a vertical line (C_1 and C_2), indicating that the resistive component, Z' , is zero, and that the reactive component, Z'' , is inversely related to frequency. The Bode plot for the capacitor is a straight line of slope -1 on Z_{mod} versus frequency, indicating that the modulus is inversely related to frequency, and phase angle value of -90 degrees at all frequencies (C_1 and C_2 , blue and black lines).

ii. Simple Circuit Elements

A combination of resistor (R) and capacitor (C) elements in series, Figure 3.4, gives a different plot than the combination of the same R and C elements in parallel, Figure 3.5. Adding a second R in series with the latter circuit, Figure 3.6, produces a conjugation of the previous plots. The total impedance expressions of each circuit appear with the respective plots. The circuits follow the Kirchhoff's laws and the total impedance (Z) of a circuit with two elements, with impedances Z_1 and Z_2 , is:

$$Z = Z_1 + Z_2 \text{ for elements in series, and} \quad (3.6)$$

$$Z = \frac{Z_1 Z_2}{Z_1 + Z_2} \text{ for elements in parallel} \quad (3.7)$$

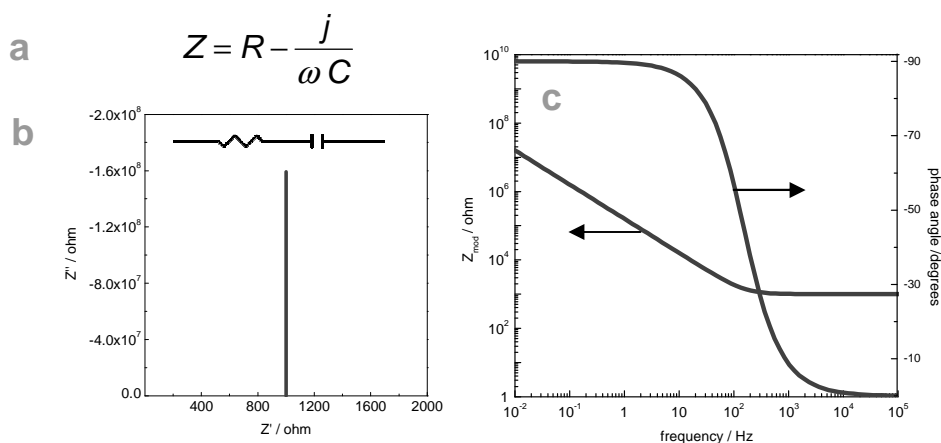


Figure 3.4 a. Expression of total impedance; **b.** equivalent electric circuit of series resistor and capacitor combination with representation in Nyquist; and **c.** Bode impedance plots, $R = 10^3$ ohm and $C = 10^{-6}$ F.

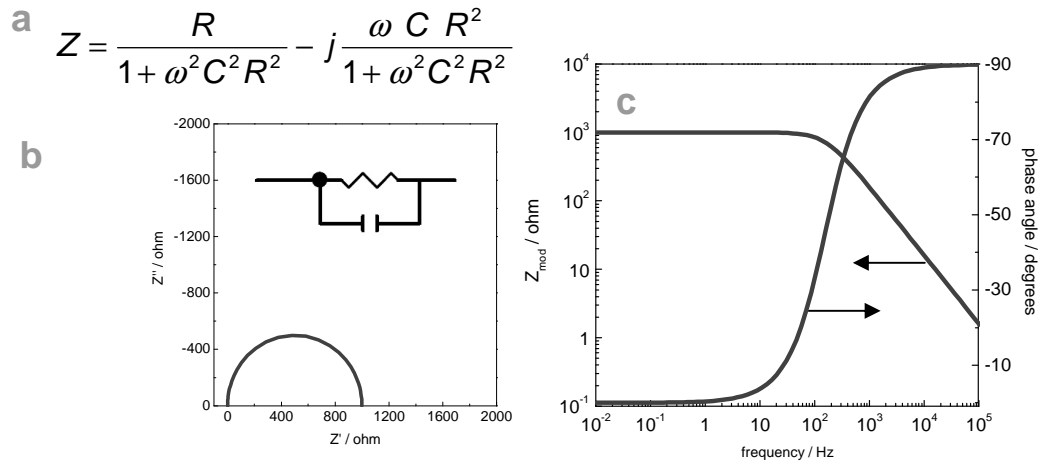


Figure 3.5 a. Expression of total impedance; **b.** equivalent electric circuit of parallel resistor and capacitor combination with representation in Nyquist; and **c.** Bode impedance plots, $R = 10^3$ ohm and $C = 10^{-6}$ F.

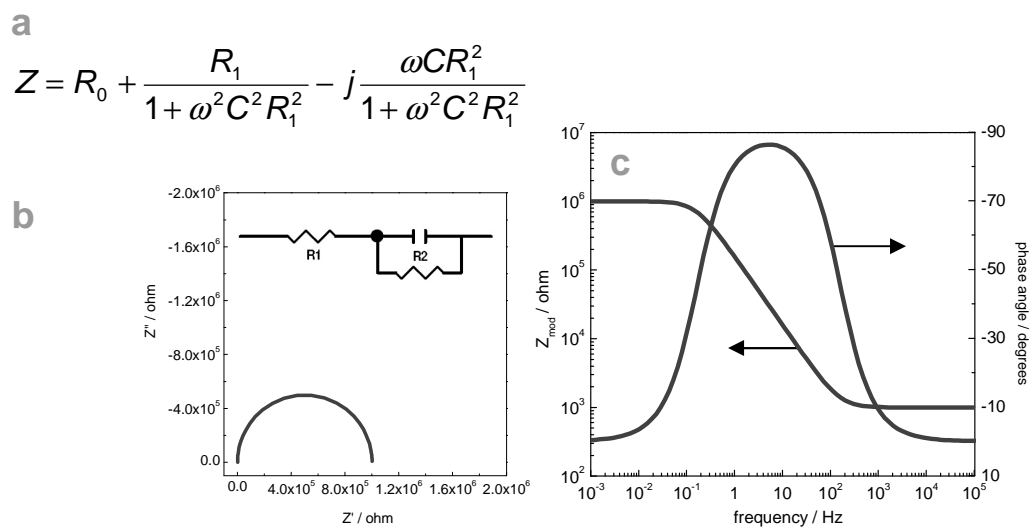


Figure 3.6 a. Expression of total impedance; **b.** equivalent electric circuit with resistor and capacitor in parallel with resistor with representation in Nyquist; and **c.** Bode impedance plots; $R_1 = 10^3$ ohm, $R_2 = 10^6$ ohm and $C = 10^{-6}$ F.

iii. Impedance of Painted Systems

The impedance plots of a painted system correspond to different equivalent circuits depending on the state of the paint. An important parameter for description of a process is

the time constant, τ , which is the time taken by the system to relax to the new steady state after an a.c. perturbation, is given by:

$$\tau = R C \quad (3.8)$$

Here R and C are the resistance and capacitance associated to the process. In the frequency domain, fast processes (with small τ) occur at high frequencies while slow processes (with high τ) occur at low frequencies. The frequency around which a process occurs may be ascertained by:

$$f = \frac{1}{2\pi\tau} \quad (3.9)$$

Thus, dipolar properties may be studied at high frequencies, bulk properties at intermediate frequencies and surface properties at low frequencies. The best way to extract information from EIS spectra is to fit the data to equivalent circuits, using computer assisted non-linear numerical methods.

The fitting can be done choosing the appropriate circuit, with different elements and values, all being able to adjust to the experimental values. The choice between different circuits occurs by matching the elements with the present physical or chemical processes. Usually, the simplest circuit is the chosen one when several fit correctly the system. The model for degradation and corrosion of painted metals is represented in Figure 3.7.¹²¹

Protective and intact coatings display very high barrier properties and the equivalent circuit is like that of a capacitor (C_{coat}). The solution resistance (R_{sol}) is too low when compared with the system impedance values. The electric response is like that of RC circuit in series, Figure 3.7a.^{15;112;113;125-127}

As the exposure time goes on, the amount of permeating water, oxygen and ionic species increase the paint coating conductivity, becoming measurable the film ionic resistance (R_{por}) which adds up in parallel to the C_{coat} . The signal obtained is that of an RC circuit in parallel, similar to the one shown in Figure 3.7b. The R_{por} corresponds to paths of lower resistance short-circuiting the organic coating.

Once the permeating species reach the metallic substrate, the corrosion processes may start, causing the emergence of a second time constant, due to the relaxation of the electrochemical double-layer capacitance (C_{dl}) and the charge transfer resistance (R_{ct}) proper of a faradaic process. The two new elements related with the corrosion process are added to the equivalent electric circuit, Figure 3.7c. Evolution of the painted system with time corresponds usually to C_{coat} increase and R_{por} and R_{ct} decrease.

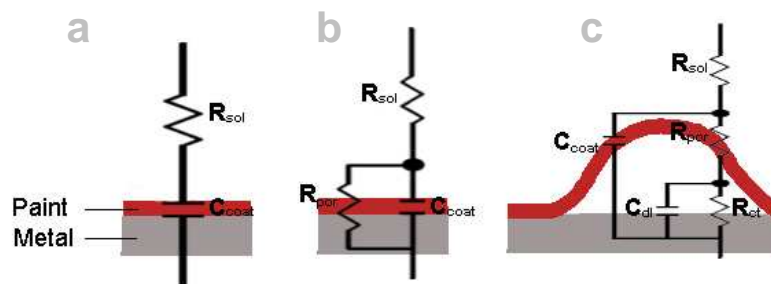


Figure 3.7 Scheme showing the equivalent electric circuits used for describing painted metal coating degradation with immersion time.

Description of the passive elements used in the circuits:

- The R_{sol} is the uncompensated solution resistance between the reference electrode and the working electrode. The internal electric resistance of the electrodes and wires also counts for this value, but is usually very low and negligible. It is also referred as solution or electrolyte resistance. The R_{sol} value increases with electrode distance and with the decrease of solution conductivity.
- The C_{coat} refers to a capacitor, where one of the plates is the coating/solution interface and the other the coating/metal interface. The capacitance of the coating is given by:

$$C = \frac{\varepsilon \varepsilon_0 a}{d} \quad (3.10)$$

where ε is the relative permittivity of the coating, ε_0 is the permittivity of vacuum ($8.86 \times 10^{-12} \text{ F.m}^{-1}$), a is the area of the coating and d is its thickness. The ε of most coatings are in the range 2 to 5, while for water is equal to 80 at 25°C. The entry of water into the coating increases C and, therefore, C can be a measure of the water uptake into the coating.

- The R_{por} , also called pore resistance of the coating, results from the penetration of charges across the film (ions). This may occur through real (microscopic) pores and/or virtual pores defined by regions in the polymer of low crosslinking and therefore high transport. The magnitude of R_{por} , at a given time, is indicative of the degradation state of the paint film, caused by the ions ingress via pathways through the film and ions produced in the degradation process out of the system.
- The C_{dl} is the capacity of the electric double layer formed in the metal/solution interface. For painted metals is assumed that only when direct contact of solution with metal appears it can be measured giving a measure of the area over which the coating has been disbonded. The area of delamination may be calculated from:

$$X = \frac{C_{dl}}{C_{dl0}} \quad (3.11)$$

where $C_{dl,0}$ is the double-layer capacitance of the uncoated metal.

- The R_{ct} is the most appropriate parameter for monitoring the protective properties of the coating as the corrosion rate, i_{corr} , of the underlying metal can be estimated from the Stern-Geary equation:

$$i_{corr} = \frac{\beta}{R_{ct}}, \text{ where } \beta = \frac{b_a b_c}{2.3 (b_a b_c)} \quad (3.12)$$

where b_a and b_c are the Tafel coefficients for the anodic and cathodic partial reactions.¹⁰⁹

When there is no water or ions within the metal/organic coating interface, neither electric double-layer formation, nor faradaic reactions occur, the only information that can be obtained from impedance spectra is related to the dielectric properties of the organic coating.^{32;39;40}

3.1.4. Water Uptake

As already described, upon exposure of organic coatings to the testing solution the film absorbs solution. The rate of water absorption by the organic coatings has significant importance from the point of view of the corrosion protective properties, since the corrosion process can only start after water reaches the metallic substrate.

The degree of water uptake depends on the structure and composition of the polymer. The water absorption can be estimated by measuring the capacitance of the coatings, since a notable increase in the coating capacitance occurs because the dielectric constant of water (approximately 80 at room temperature) is much larger than that of a typical organic coating (2 to 5).¹¹⁹

A simple method of calculating the amount of water absorbed by the coating from the capacitance data is by using the empirical formula derived by Brasher and Kingsbury for the volume fraction of absorbed water, ϕ .^{112;128;129}

$$\phi = \frac{\log \left(\frac{C_t}{C_0} \right)}{\log \epsilon_{H_2O}} \quad (3.13)$$

where C_t is the capacitance at a specific time of immersion, C_0 is the initial capacitance before water uptake, and ϵ_{H_2O} is the dielectric constant of water.

In this analysis, it is assumed that:

- The increase of the coating capacitance is only due to the ingress of water;
- There is no swelling of the film;
- The distribution of water in the film is uniform and with a low volume fraction.

Other models were described for water uptake estimation. The Brasher and Kingsbury's equation was compared with five mixture formulas derived from the theory of the dielectric properties of heterogeneous materials.^{129;130} Those equations are all based on the theoretical model of an inner component of spheres randomly distributed in an outer continuous media, which is too simple to be applied to water in paint films.

To estimate the amount of water absorbed by a paint film on metal, the empirical equation given by Brasher and Kingsbury gives better agreement with gravimetry than the mixture equations.^{129;130}

Two other models were proposed, one for thin films - the discrete model - and another one used for thicker films - the continuous model.^{129;131} These determine the ratio ϕ/ϕ_{∞} , where ϕ represents the mass uptake of water in volume fraction and ϕ_{∞} the equilibrium volume fraction. The first model assumes that the organic film behaves electrically like a capacitor in parallel with a resistance, while for the second model the film is divided in thin layers, assuming that they behave like a finite series of RC circuits, where each layer corresponds to an RC circuit. In these models, the absolute amount of water into the films is not determined only the diffusion coefficients are obtained.

Water uptake estimations taking into consideration the swelling of the film^{129;132} and the non-Fickian behaviour of the water uptake process into the film^{129;133} were also published. The dielectric changes in the film are measured using constant phase elements^{129;134} and also using the concept of dielectric relaxation and the capacitance with Cole–Cole depression.^{129;133} Other authors^{129;135;136;137} refer that water absorption by the coating leads to solid phase structural changes and, consequently, to modification of their mechanical and electric properties. A method for the estimation of this altered dielectric constant considering the glass transition temperature was also proposed.^{129;137}

Recently a model assuming that the film is composed by three phases, solid (coating), liquid (solution) and gaseous (air), insoluble among them, their electrical properties and ionic forces constant throughout the thickness and the water uptake model and electrical properties of the film described as a finite series of RC circuits throughout the film thickness was proposed.¹³⁸⁻¹⁴⁰ With these assumptions, the dielectric constant of the film can be given by the average of the dielectric properties for each component. For a more realistic estimation of the water uptake values, i.e. better correlation with the gravimetry results, a new model was created.¹²⁹ In this case, the tortuosity of micropores inside the film is taken into consideration, defined as the ratio between the distance that a species has to travel to get through the film and the film thickness. For both models, their authors claim better correlation with gravimetric results, although until now were only published the results for a few paint systems.

3.2. Scanning Electron Microscopy

The scanning electron microscopy (SEM) uses a high-energy beam of electrons in a raster pattern to scan the sample surface, forming an image. The electrons interact with the surface atoms producing signals that are influenced by the surface topography, composition and electrical conductivity.¹⁴¹⁻¹⁴³

The types of signals produced by SEM include secondary electrons, back scattered electrons (BSE), characteristic x-rays, light (cathodoluminescence) and transmitted electrons. These types of signal all require specialized detectors for their collection. The signals result from interactions of the electron beam with atoms at or near the surface. In the standard detection mode, secondary electron imaging, the SEM can produce very high-resolution images of the surface, revealing details about 1 to 5 nm in size. Due to the way these images are created, SEM micrographs have a very large depth of field yielding a characteristic three-dimensional appearance, useful for understanding the surface morphology. A wide range of magnifications is possible, ranging from 25x (equivalent to that of a powerful hand-lens) to 250000x, which is 250 times the magnification limit of the best light microscopes. The BSE constitute a beam of electrons reflected from the sample by elastic scattering. BSE often have application in analytical SEM along with the spectra made from the characteristic x-rays. Because the intensity of the BSE signal appears strongly related to the atomic number of the specimen, the images can provide information about the distribution of different elements in the sample. Characteristic x-rays are emitted when the electron beam removes an inner shell electron from the sample, causing a higher energy electron to fill the shell releasing energy. These characteristic x-rays permit to identify the composition and measure the abundance of elements in the sample (see 3.3).

The specimens must be electrically conductive for conventional imaging, at least at the surface, and electrically grounded to prevent the accumulation of electrostatic charge at the surface. Metallic objects preparation for SEM just needs cleaning and mounting on a specimen holder. Nonconductive specimens tend to charge when scanned by the electron beam, especially in secondary electron imaging mode, which causes several image artifacts. Therefore, they are previously coated with an ultrathin layer of electrically conducting material, deposited on the sample either by low vacuum sputtering or by high vacuum evaporation.

3.3. Energy-Dispersive X-ray Spectroscopy

Energy dispersive X-ray spectroscopy (EDS or EDX) is an analytical technique used for the elemental analysis of a sample. It relies on the investigation of a sample through interactions between electromagnetic radiation and matter. It recurs to x-rays emitted by the surface in response to being hit with a high-energy beam of electrons. The characterization capabilities are due to the fundamental principle that each element has a

unique atomic structure, allowing characteristic x-rays of an element to be identified uniquely.¹⁴¹⁻¹⁴³

To stimulate the emission of characteristic x-rays from a specimen, a high energy beam of electrons or a beam of x-rays, is focused into the sample under study. The sample atoms in fundamental state have the electrons in discrete energy levels or electron shells bound to the nucleus. The incident beam excites an electron from an inner shell, ejecting it while creating an electron hole that will be occupied by a higher-energy electron from an outer shell. The difference in energy between the higher-energy shell and the lower energy shell may be released in the form of an x-ray. The number and energy of x-rays emitted from a specimen can be measured by an energy dispersive spectrometer. Since the energy of the x-rays is characteristic of the difference in energy between the two shells and of the atomic structure of the element from which they were emitted, the elemental composition of the specimen can be determined.

There are four primary components of the EDS setup: the beam source; the X-ray detector; the pulse processor; and the analyzer. A number of freestanding EDS systems exist. However, EDS systems are most commonly found coupled with scanning electron microscopy (SEM-EDX). Scanning electron microscopy is equipped with a cathode and magnetic lenses to create and focus a beam of electrons. A detector converts the x-ray energy into voltage signal and this information passes to a pulse processor, which measures the signals and passes them onto an analyzer for data display and analysis.

The accuracy of the EDS spectrum can be affected by many variables. Windows in front of the SiLi detector can absorb low-energy x-rays and the presence of oxygen, carbon, boron cannot be detected. The peaks size depends on the voltage of the EDS. Raising the voltage on the SEM will shift the spectrum to the larger energies making higher-energy peaks larger while making smaller the peaks with lower energy. Many elements have overlapping peaks. The accuracy of the spectrum can also be affected by the nature of the sample. Any atom in the sample that is sufficiently excited by the incoming beam can generate x-rays. These x-rays emit in any direction, and so may not all escape the sample. The likelihood of an x-ray escaping the specimen, and thus being available to detection and measurement depends on the energy of the x-ray and the amount and density of material it has to pass through. This can result in reduced accuracy in inhomogeneous and rough samples.

3.4. Transmission Electron Microscopy

Transmission electron microscopy (TEM) is a microscopic technique where a beam of electrons transmits across an ultra thin specimen, interacting with the specimen as it passes through it. An image forms from the electrons transmitted through the specimen. Magnification and focus by an objective lens permits imaging on a screen, usually fluorescent screen, in a monitor or on a layer of photographic film. Nowadays a sensor

such as a charge-coupled device (CCD) camera is also used. Max Knoll and Ernst Ruska built the first TEM in 1931, developing the first TEM with resolving power greater than that of light in 1933 and introducing the first commercial TEM in 1939.¹⁴⁴⁻¹⁴⁶

The TEM has application in both materials science and biological sciences. In both cases, the specimens must be very thin and able to withstand the high vacuum present inside the instrument. The electrons are usually generated in an electron microscope by thermionic emission process from a tungsten filament or alternatively by field emission. Acceleration occurs due to an electric potential and focus by electrostatic and electromagnetic lenses onto the sample. The transmitted beam contains information about electron density, phase and periodicity, used to form an image.

A TEM system is composed of several components: a vacuum system in which the electrons travel; an electron emission source for generation of the electron beam; a series of electromagnetic lenses; and electrostatic plates. The latter two allow the operator to guide and manipulate the beam as required.

In order to allow for uninterrupted passage of electrons, the TEM must be evacuated to low pressures, typically on the order of 10^{-4} to 10^{-8} kPa. This allows the voltage difference between the cathode and the ground without generating an arc, reducing the collision of electrons with gas atoms to negligible levels. Poor vacuum is the cause of several problems, from deposition of gas inside the TEM onto the specimen through a process known as electron beam induced deposition, to in more severe cases damage of the cathode from an electrical discharge. Vacuum problems owing to specimen sublimation are limited by the use of a cold trap to adsorb sublimated gases in the vicinity of the specimen.

The system emission source may be a tungsten filament or a lanthanum hexaboride (LaB_6) source. Connecting this source to high voltage source, it will begin to emit electrons into the vacuum. The upper lenses of the TEM allow for the formation of the electron probe to the desired size and location for later interaction with the sample.¹⁴⁷

The sample preparation for imaging in TEM can be a complex procedure, mainly because the specimens are typically nanometres thick and the electron beam has to interact readily with the sample. The preparation of specimens is specific to the material under analysis and the desired specimen information. For biological specimens, the maximum specimen thickness is approximately 1 micrometer.

To withstand the instrument vacuum, biological specimens are typically held at liquid nitrogen temperatures after embedding in vitreous ice, or fixed using a negative staining material such as uranyl acetate or by plastic embedding. In materials science and metallurgy, the specimens tend to be naturally resistant to the vacuum conditions, but they must still be prepared as a thin foil, or etched to make some portion of the specimen thin enough for the beam to pass through.

Constraints on the thickness of the material may be limited by the scattering cross-section of the atoms from which the material is composed. Materials that have dimensions small enough to be electron transparent, such as powders or nanotubes, can be quickly

prepared by the deposition of a dilute sample containing the specimen onto support grids or films.

For other materials, a common strategy is to use a microtome, which is a mechanical instrument used to cut specimens into transparent thin sections for microscopic examination. Microtome use steel, glass or diamond blades depending upon the specimen being sliced and the desired thickness of the sections being cut.

Steel blades are used to prepare sections of animal or plant tissues for light microscopy histology. Glass knives are used to slice sections for light microscopy and to slice very thin sections for electron microscopy. Industrial grade diamond knives are used to slice hard materials for both light microscopy and for electron microscopy. Gem quality diamond knives are used for slicing thin sections for electron microscopy.

3.5. Atomic Force Microscopy

The atomic force microscopy (AFM) and scanning force microscopy (SFM) are very high-resolution type of scanning probe microscopy, with demonstrated resolution of fractions of a nanometre, more than 1000 times better than the optical diffraction limit.¹⁴⁸

Gerd Binnig and Heinrich Rohrer developed the precursor of the AFM, the scanning tunnelling microscopy (STM), in the early 1980s, being Binnig, Quate and Gerber the first to build one AFM in 1986. The AFM is one of the foremost tools for imaging, measuring and manipulating matter at the nanoscale. The information is gathered by "feeling" the sample surface with a mechanical probe. The scanning is performed using piezoelectric elements that accurately and precisely move on command enabling very precise scanning area.

3.5.1. Basic Principle

The system consists of a microscale cantilever with a sharp tip (probe) at its end used to scan the specimen surface. The cantilever is typically silicon or silicon nitride with a tip radius of curvature on the order of nanometres. When the tip approaches to the proximity of the sample surface, forces between the tip and the sample lead to a deflection of the cantilever according to Hooke's law. Depending on the situation, forces that are measured in AFM include mechanical contact forces, Van der Waals forces, capillary forces, chemical binding, electrostatic forces, magnetic forces, Casimir forces, solvation forces, etc. In addition to force, other quantities may simultaneously be measured using specialised types of probes (scanning thermal microscopy, photothermal microspectroscopy, etc.). Typically, the deflection is measured using a laser spot reflected

from the top of the cantilever into an array of photodiodes. Other methods that are used include optical interferometry, capacitive sensing and piezoresistive AFM cantilevers. The cantilevers are fabricated with piezoresistive elements that act as a strain gauge. Using a Wheatstone bridge, strain in the AFM cantilever due to deflection can be measured, but this method is not as sensitive as laser deflection or interferometry.

In Figure 3.8 appears a schematic representing the general arrangement of one AFM system. The resulting map of the area $s=f(x,y)$ represents the topography of the sample.

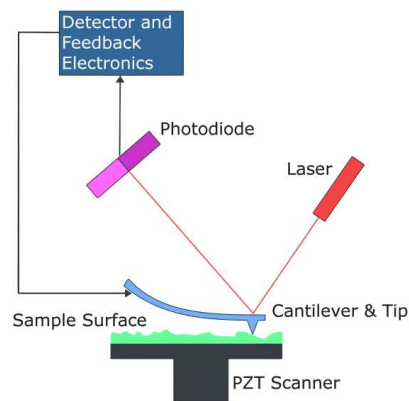


Figure 3.8 Block diagram of atomic force microscope technique.

In most systems, a feedback mechanism is employed to adjust the tip-to-sample distance to maintain a constant force between the tip and the sample, to avoid collision with the surface damaging it. The sample, or the probe, depending on the arrangement, is mounted on a piezoelectric tube, which can move in the z direction for maintaining a constant force, and the x and y directions for scanning the sample. Alternatively a 'tripod' configuration of three piezo crystals may be employed, with each responsible for scanning in the x, y and z directions. This eliminates some of the distortion effects seen with a tube scanner.

3.5.2. Statistical Characterization

Mathematical tools permit to extract quantitative information on surface roughness from AFM topography images. The common parameters used to describe the roughness are the root mean square roughness (R_r), the arithmetic roughness (R_a) and the average surface height (h).¹⁴⁹⁻¹⁵¹

These parameters are determined using the following equations, where Z_i is the elevation profile acquired at each point i , and N the number of points of the square array:

$$h = \frac{\sum_i^N z_i}{N} \quad (3.14)$$

$$R_t = \sqrt{\frac{1}{N} \sum_{i=0}^N (z_i - h)^2} \quad (3.15)$$

$$R_a = \frac{1}{N} \sum_{i=1}^N |z_i - h| \quad (3.16)$$

Another parameter, the surface skewness (R_{sk}), verifies the third momentum of the height distribution. The values are positive when the surface has peaks above the flatter average while negative values refer to porous surfaces. Surfaces that are more random have skewness closer to zero and R_{sk} higher than 1.5 (positive or negative) indicate that the surface does not have a simple shape. The determination of the surface skewness used the following equation:

$$R_{sk} = \frac{1}{NR_t^3} \sum_{i=1}^N (z_i - h)^3 \quad (3.17)$$

3.5.3. Imaging Modes

The AFM operation uses a number of modes depending on the application. In general, possible imaging modes are static (contact) modes and a variety of dynamic (or non-contact) modes.

i. Contact Mode

The primary modes of operation are static (contact) mode and dynamic mode. In the static mode operation, the static tip deflection is used as a feedback signal. Because the measurement of a static signal is prone to noise and drift, low stiffness cantilevers boost the deflection signal. However, close to the surface of the sample, attractive forces can be quite strong, causing the tip to 'snap-in' to the surface. Thus, static mode AFM occurs in contact, where the overall force is repulsive, consequently, called *contact mode*. In contact

mode, the force between the tip and the surface is kept constant during scanning by maintaining a constant deflection.

In the dynamic mode, the cantilever is externally oscillated at or close to its fundamental resonance frequency or a harmonic. Tip-sample interaction forces modify the oscillation amplitude, phase and resonance frequency. These changes in oscillation with respect to the external reference oscillation provide information about the sample's characteristics. Schemes for dynamic mode operation include frequency modulation and the more common amplitude modulation. In frequency modulation, changes in the oscillation frequency provide information about tip-sample interactions. Frequency measurement is very sensitive and thus the frequency modulation mode allows for the use of very stiff cantilevers. Stiff cantilevers provide stability very close to the surface and, as a result, this technique was the first AFM technique to provide true atomic resolution in ultra-high vacuum conditions.

In amplitude modulation, changes in the oscillation amplitude or phase provide the feedback signal for imaging, used to discriminate between different types of materials on the surface. Amplitude modulation operation occurs either in the non-contact or in the intermittent contact regime. In ambient conditions, most samples develop a liquid meniscus layer. Because of this, keeping the probe tip close enough to the sample, so that short-range forces become detectable, while preventing the tip from sticking to the surface, presents a major hurdle for the non-contact dynamic mode in ambient conditions. Development of the dynamic contact mode (intermittent contact or tapping mode) bypasses this problem.¹⁵² In dynamic contact mode, the cantilever oscillation is such that modulation of the separation distance between the cantilever tip and the sample surface occurs.

Using amplitude modulation in the non-contact regime forms images with atomic resolution, recurring to very stiff cantilevers and small amplitudes in an ultra-high vacuum environment.

ii. Tapping Mode

In tapping mode, the cantilever oscillates up and down at near its resonance frequency by a small piezoelectric element, mounted in the AFM tip holder. The amplitude of this oscillation is greater than 10 nm, typically 100 to 200 nm. Interaction of forces acting on the cantilever when the tip comes close to the surface, e.g. Van der Waals force or dipole-dipole interaction, electrostatic forces, etc, cause the amplitude of this oscillation to decrease as the tip gets closer to the sample. An electronic servo uses the piezoelectric actuator to control the height of the cantilever above the sample. The servo adjusts the height to maintain the cantilever oscillation amplitude as the cantilever passes over the sample. A tapping AFM image appears by imaging the force of the oscillating contacts of the tip with the sample surface. Tapping mode is gentle enough even for the visualization of supported lipid bilayers or adsorbed single polymer molecules under liquid medium. At

the application of proper scanning parameters, the conformation of single molecules remains unchanged for hours.¹⁵³

3.6. Colour Measurement

The perception of colour is a psychophysical phenomenon, and the measurement of colour must be defined in such a way that the results correlate accurately with what the visual sensation of colour is to a normal human observer.¹⁵⁸

The visible light consists of the electromagnetic spectra with wavelength between 400 (blue) and 700 nm (red). Colorimetry is the science and technology used to physically quantify and describe the human colour perception. The basis for colorimetry was established by the Commission Internationale de l'éclairage (CIE) in 1931 based on visual experiments. Even though limitations are well recognized, the CIE system of colorimetry remains the only internationally accepted metric for colour measurement. All the official colour-related international standards and specifications use the CIE System.¹⁵⁹

3.6.1. Colour Vision

Isaac Newton studied colour and one of his contributions was the idea that light is made up of a mixture of light containing all wavelengths of the visible spectrum. He demonstrated this fact with experiments on the dispersion of light in glass prisms in 1704.¹⁶⁰ He realized that some colours (magenta, purple) are spectral colours.

Thomas Young suggested in 1802 that the eye has three different kinds of colour receptors, corresponding roughly with the red, green, and blue primary colours.¹⁶¹ This is useful in matching a wide range of visual colours by additive colour mixing. Two complementary theories of colour vision arise, the trichromatic theory and the opponent process theory. The trichromatic theory, or Young-Helmholtz theory, proposed in the 19th century by Thomas Young and Hermann von Helmholtz, states that the retina's three types of cones are preferentially sensitive to blue, green, and red. Ewald Hering proposed the opponent process theory in 1872, which states that the visual system interprets colour in an antagonistic way: red vs. green, blue vs. yellow, black vs. white.

Nowadays, both theories are correct and describe different stages in visual physiology. The first theory was correct since the human eye really does contain red, green and blue sensors and the second was also right since the RGB signals do not explain all the spectral colours without being converted to opponent signals: red-green, yellow-blue and black-white.^{162;163}

The three different types of colour sensitive cones from the human eye response are described in terms of *hue*, *saturation* and *intensity*. *Intensity* reflects light intensity converted into brightness value and reflectivity of an object. The *intensity* values are not directly proportional to light intensity but they are proportional to the logarithm of that intensity. *Hue* corresponds to the colour reflected from or transmitted through an object. In common use is identified by the name of the colour, such as red, orange, or green. *Saturation* is the strength or purity of colour, how much light of different frequencies appears mixed in with a *hue*.

The response of the eye is also described in terms of three "tristimulus values". The tristimulus values of a colour are the amounts of three primary colours in a three-component additive colour model needed to match that test colour. Any specific method for associating tristimulus values with each colour refers to a colour space.

The colour space uses different coordinate systems. The Figure 3.9 presents some of the most common systems, Munsell, Ostwald and CIE.

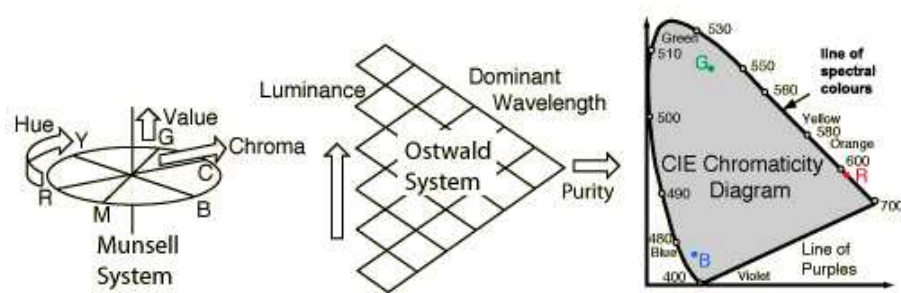


Figure 3.9 Diagram of Munsell, Ostwald and CIE chromaticity coordinate systems.

The three systems describe the colour space using different parameters. The Munsell system uses hue, value, and chroma and the Ostwald system uses dominant wavelength, purity, and luminance. The more precise CIE system uses a parameter Y to measure brightness and parameters x and y to specify the chromaticity, which covers the properties hue and saturation on a two dimensional chromaticity diagram. The CIE 1931 colour space shows the tristimulus values, denoted X , Y , and Z .¹⁶⁴

3.6.2. The CIE XYZ Colour Space

CIE XYZ system consists on direct measurements of human visual perception. The CIE system characterizes colours by a luminance parameter Y and two colour coordinates x

and y , which specify the point on the chromaticity diagram. ¹⁶⁵ The parameters are based on the spectral power distribution of the light emitted from a coloured object and are factored by sensitivity curves which have been measured for the human eye. For this it was defined a set of three colour-matching functions, called \bar{X} , \bar{Y} and \bar{Z} , defined as shown on Figure 3.10.

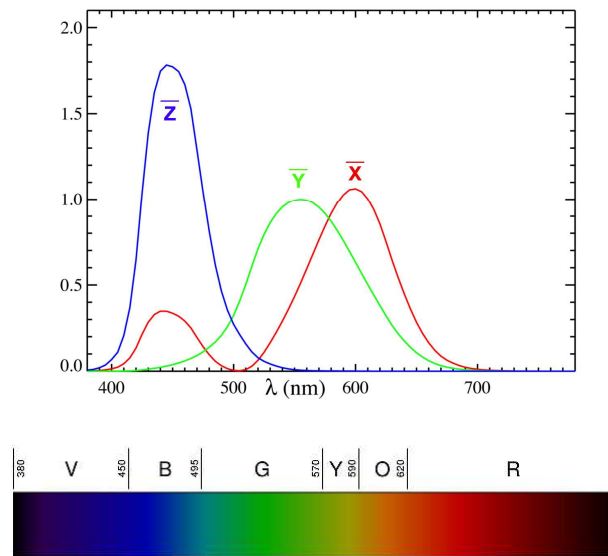


Figure 3.10 Colour-matching functions \bar{X} , \bar{Y} and \bar{Z} .

These consist of the spectral sensitivity curves of three linear light detectors that yield the CIE XYZ tristimulus values X , Y and Z . The tabulated numerical values of these functions are known collectively as the CIE standard observer. ¹⁶⁶

The human eye colour sensors respond to different ranges of wavelengths then a full plot of all visible colours is a three-dimensional figure. The area under each curve is X , Y and Z . Converting the three dimensional colour space into a two dimensional colour space is done by removing the intensity, and by dividing each value by the total intensity of $X + Y + Z$, as shown by the equations 3.17:

$$\begin{aligned}
 x &= \frac{X}{X + Y + Z} \\
 y &= \frac{Y}{X + Y + Z}
 \end{aligned}
 \tag{3.18}$$

$$z = \frac{Z}{X + Y + Z} = 1 - x - y$$

The derived colour space specified by x , y , and Y is known as the CIE xyY colour space and is widely used to specify colours in practice.

The X and Z tristimulus values appear back from the chromaticity values, x and y , and the Y tristimulus value:

$$\begin{aligned} X &= \frac{Y}{y}x \\ Z &= \frac{Y}{y}(1 - x - y) \end{aligned} \tag{3.19}$$

3.6.3. The CIE Chromaticity Diagram

The Figure 3.11 shows the related chromaticity diagram. The outer curved boundary is the spectral locus, with wavelengths shown in nanometres. The chromaticity diagram is a tool to specify how the human eye will experience light with a given spectrum. Specify colours of objects do not arise since the chromaticity observed while looking at an object depends on the light source as well. Mathematically, x and y are projective coordinates and the colours of the chromaticity diagram occupy a region of the real projective plane.

The chromaticity diagram illustrates a number of interesting properties of the CIE XYZ colour space:

- The diagram represents all of the chromaticity visible to the average person - the gamut of human vision. The name of the curved edge of the gamut is the spectral locus and corresponds to monochromatic light, with wavelengths listed in nanometres. The name of the straight edge on the lower part of the gamut is the line of purples. These colours, although they are on the border of the gamut, have no counterpart in monochromatic light. Less saturated colours appear in the interior of the figure with white at the centre.
- All visible chromaticity correspond to non-negative values of x , y , and z (and therefore, to non-negative values of X , Y , and Z).
- If one chooses any two points on the chromaticity diagram, all colours formed by mixing these two colours lie between those two points, on a straight line connecting them. It follows that the gamut of colours must be convex in shape. All colours

formed by mixing three sources appear inside the triangle formed by the source points on the chromaticity diagram (and so on for multiple sources).

- An equal mixture of two equally bright colours will not generally lie on the midpoint of that line segment. Generally, a distance on the xy chromaticity diagram does not correspond to the degree of difference between two colours.
- Given three real sources, these sources cannot cover the gamut of human vision. Geometrically stated, there are no three points within the gamut that form a triangle that includes the entire gamut; or more simply, the gamut of human vision is not a triangle.
- Light with a flat energy spectrum corresponds to the point $(x,y) = (1/3,1/3)$.

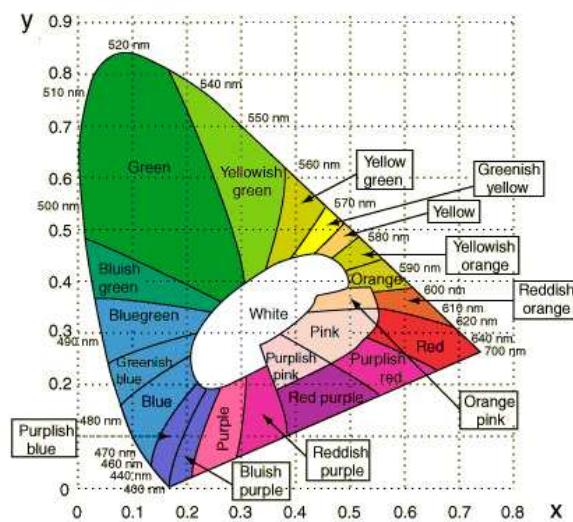


Figure 3.11 The CIE chromaticity diagram.

Section 4. Experimental

4.1. Specimens

The specimens used in this work were coil coated electro-galvanized steel with a fine stone finish supplied by Voestalpine Stahl GmbH, Austria. The plasma polymerization occurred at Max Planck Institut für Eisenforschung (MPIE) in Germany, at the former Corus (now Corus Tata) in the United Kingdom and at Dortmunder Oberflächencentrum (DOC) in Germany. The samples preparation and characterization were done under the project #7210-PR/383 of European Research Fund for Coal and Steel programme, in which those organizations and the University of Aveiro were partners.

4.1.1. Coil Coatings

As substrate for the coil coating process, DC05 steel ¹⁶⁷ with 0.6 mm thickness was used, with a zinc layer with nominal thickness of 7.5 μm , electro deposited on both sides.

Two coil coating paint systems were used, one polyurethane based and the other polyester based both used in the automotive industry. The cross section images and respective composition maps, obtained by SEM coupled with EDS, are shown in the Figure 4.1 and Figure 4.2, where is possible to distinguish the different coating layers, numbered in the figures. Number **1** represents the steel and number **2** the zinc layer. The primer (layer **3**) was deposited on the top of the zinc layer. It is 13 to 15 μm thick for polyurethane and 5 μm for polyester.

In Figure 4.1**a**, the polyurethane based system shows three more layers: layer **4** is the basecoat; layer **5** is the clearcoat; layer **6** is the topcoat. The thickness of the whole paint is 60 μm .

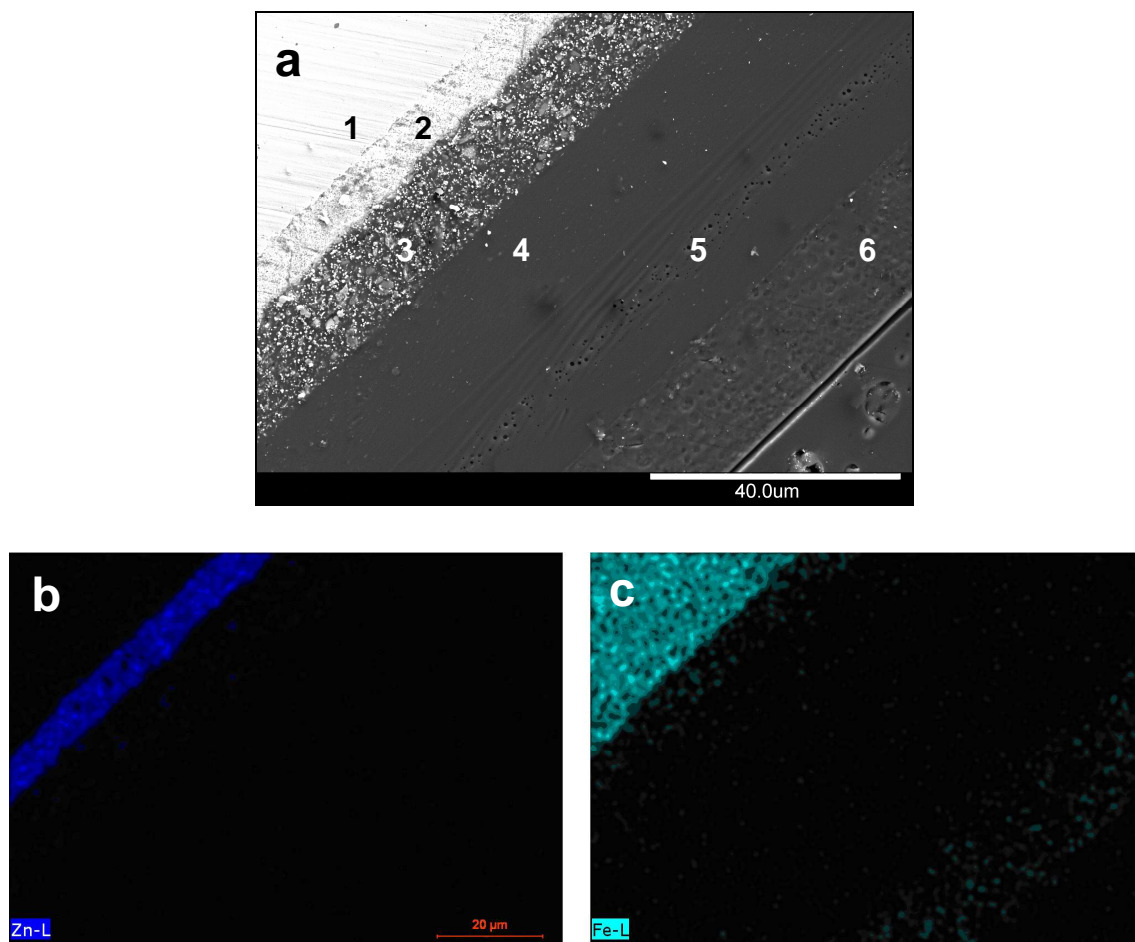


Figure 4.1 a. Polyurethane coil coating system cross section image; and EDS maps for the **b.** zinc; and **c.** iron elements.

For the polyester based system, Figure 4.2a, only one more layer was applied in the top of the primer. This is a silicon based layer filled with titanium based pigments, layer 4. The SEM and EDS maps show that the particles are not homogeneously distributed, appearing areas without the titanium based pigments (like zone 5), corroborated by the EDS titanium map in Figure 4.2e. The thickness of the whole paint is in this case 30 μm .

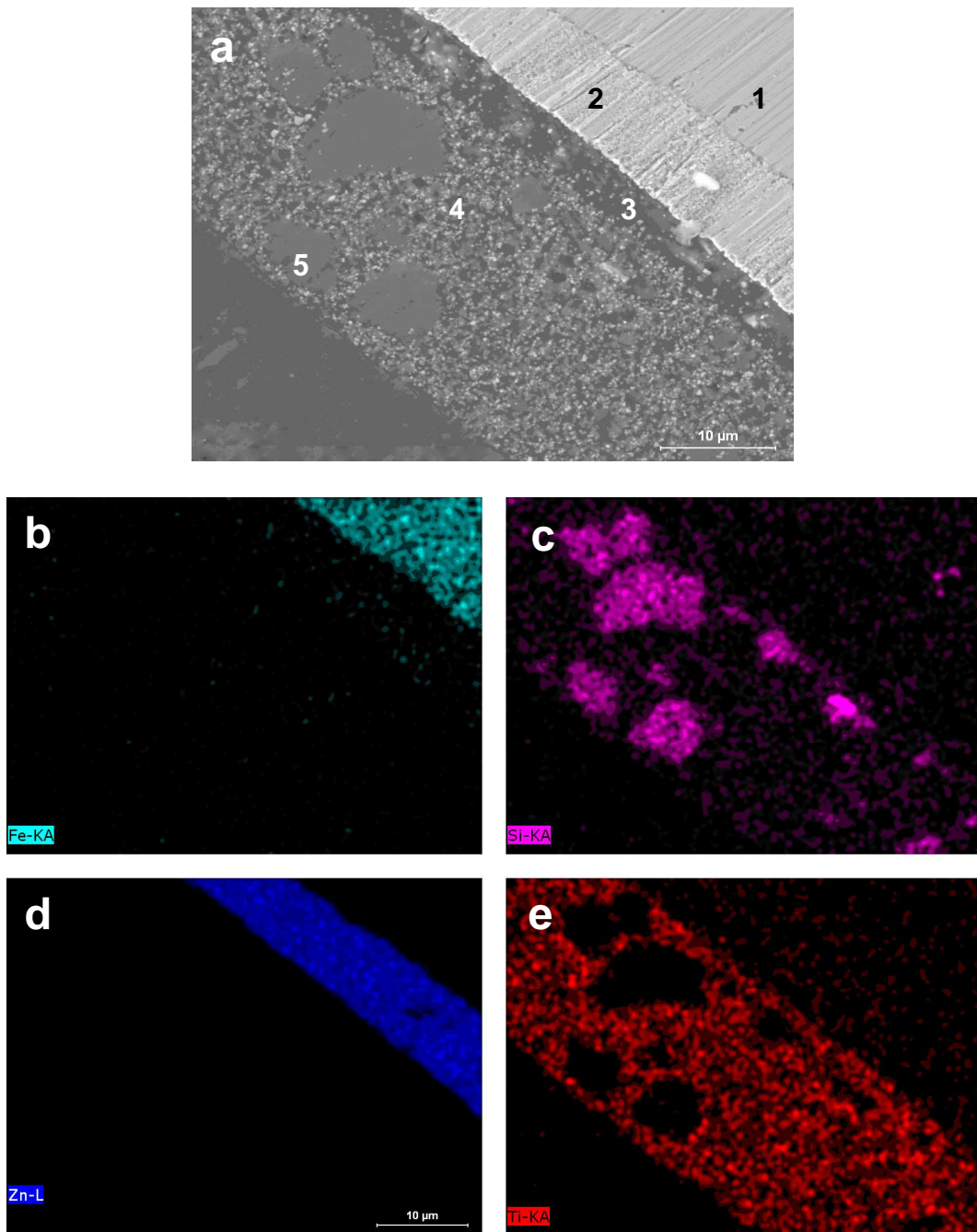


Figure 4.2 a. Polyester coil coating system cross section image; and EDS maps of the elements: **b.** iron; **c.** silicon; **d.** zinc; and **e.** titanium.

4.1.2. Plasma Polymerization

The samples treated by plasma polymerization procedure were prepared using the two coil coatings painted systems previously described, three plasma reactors, several combinations of plasma polymerization steps and different experimental conditions. A labelling system was used for reference of each combination tested. Each letter or digit of the label refers to a specific variable studied in the following order: (coil coating) (plasma reactor) (step combination) (reactor precursor mixture) (pressure).

For the two coil coatings used, **U** label refers to polyurethane system and **E** to polyester system. The plasma reactors also received a label: **M** for microwave, **R** for radio frequency and **H** for hollow cathode.

The complete plasma polymerization process recurs to several steps, *plasma activation*, *plasma deposition* and *plasma stabilization*. The steps occur in sequence during normal plasma polymerization process.

The *plasma activation* step consists in cleaning and activation of the coil coating surface, and was performed by feeding the plasma reactor with the carrier gas under plasma conditions. The plasma activation using argon leads to abstraction of hydrogen with formation of free radicals at the surface. The oxidation reactions occur, with formation of C-O bonds on the surface, for plasma activation with oxygen. Point 2.6.5 describes in more detail the role of each gas.^{46;168}

The *plasma deposition* step consists in the generation and deposition of the plasma polymer film. The step starts with the introduction of the gaseous precursor mixture in the plasma reactor, which undergoes fragmentation reactions of radicals with subsequent combination and recombination of these radicals to form the plasma polymer film. Description of the plasma polymerization mechanism appears in more detail in point 2.3.

The addition of a *plasma stabilization* step, also using the carrier gas in plasma conditions, occurs to stabilize the surface of the formed plasma polymer layer. The process uses conditions similar to the ones used during the plasma activation step and with similar surface reactions occurring, but in this case in the surface of the plasma polymer film.

In this work were used several combination of steps, that were called stages. A summary of the labels used for each combination of steps (stages) used appear in Table 4.1.

Table 4.1 Labels attributed to the combination of plasma steps.

label for the stage	plasma polymerization step		
	activation	deposition	stabilization
1	X		
2	X	X	
3	X	X	X
4		X	X

Thus, **1** refers to plasma activation step alone, **2** to the combination of plasma activation step with plasma deposition step, **3** refers to the combination of plasma activation step, plasma deposition step and plasma stabilization step, and **4** refers to the combination of plasma deposition step and plasma stabilization step

For each combination of process duration, carrier gas employed and precursor mixture used was attributed a letter, from **a** to **k**. Table 4.2 shows the used combinations.

Table 4.2 Labels attributed to the reactor time of the process, carrier gas and monomer.

plasma polymerization step					label
activation		deposition	stabilization ⁽²⁾		
duration (seconds)	gas	monomer	duration (seconds)	gas	
5	oxygen	-	-	-	a
70	oxygen	-	-	-	b
140	oxygen	-	-	-	c
140	argon	-	-	-	d
70 or 300 ⁽¹⁾	oxygen	HMDSO	60	oxygen	e
70	argon	HMDSO	-	-	f
70	argon	HMDSO, HDFD	-	-	g
300	oxygen	-	-	-	h
300	-	HMDSO	60	oxygen	i
2	oxygen	TMS	-	-	k

¹ 70 seconds for **M** plasma reactor and 300 seconds for **R** plasma reactor.

² Applied only during the plasma polymerization process performed in the **R** plasma reactor.

The pressure inside the reactor in which the plasma polymerization process occurs receives the label **P_x**, where the index **x** depends on the respective pressure used. The different pressures used appear in Table 4.3.

Table 4.3 Labels attributed to the reactor pressure.

label	P₁	P₂	P₃	P₄	P₅	P₆
pressure (mbar)	0.2	0.1	0.05	0.07	0.03	0.17

As an example, the label **UM1aP₁** is used when:

U	M	1	a	P₁
coil coating	plasma reactor	stage	reactor conditions	pressure in the reactor

When the immersion tests are carried out at 45° C the **45** prefix is used before the type of coil coating.

i. Microwave Plasma Reactor - **M**

In this work, the plasma polymerization with **M** plasma reactor took place in MPIE facilities, using the **U** coil coating. The deposition of the plasma polymer films occurred in a chamber with a linear microwave power source using a frequency of 2.46 GHz, shown schematically in Figure 4.3. The vacuum chamber and the samples were grounded. According with point 2.6.6 the setup corresponds to the electroless plasma reactor.

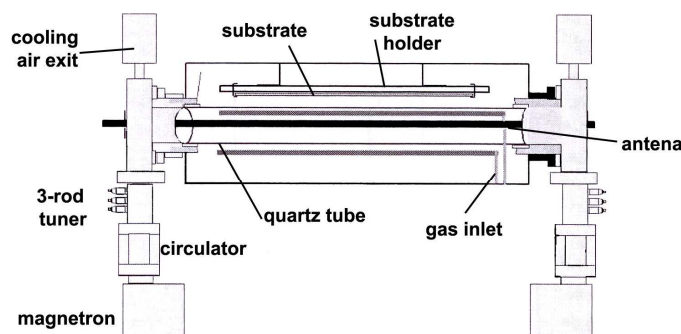


Figure 4.3 Scheme of the **M** plasma reactor.

During the plasma polymerization process, the samples were plasma cleaned and plasma activated for about 70 seconds at 400 W. After this step, the introduction of the desired precursor mixture occurs in the chamber, with the pressure adjusted to the desired conditions. The plasma initiates and reaches equilibrium during several minutes, with the sample far from the deposition zone. The specimen moves over the plasma at 0.5 to 1 mm s⁻¹. The deposition time was 140 seconds. During deposition, the specimen temperature reached 50° C, measured with a thermocouple. The control of the film thickness occurs through the plasma deposition time.

The chemical structure of the plasma polymer film deposited from atmospheres containing hexamethyldisiloxane (HMDSO) and oxygen depends on their ratio. An increasing

HMDSO/O₂ ratio leads to the increase of Si-O-Si groups and to the decrease of the carbon containing groups. Thereby, the nature of the films can vary from organic to inorganic.^{91;169}

In this work, the flow rates were chosen so that the ratio between oxygen and the monomer HMDSO equalled 20. The adjusted overall pressure varied between 0.05 and 0.2 mbar. Under these conditions, deposition of silica-like films occurs. The pressure decrease occurred with variation of both flow rates by a factor of three. Adjustment of the morphology of the film is obtained by changing the plasma power and deposition pressure. Experiments of deposition with HMDSO and argon precursor mixture were also performed along with the introduction of the heptadecafluoro-1-decene (HDFD) monomer combined with HMDSO and argon. Figure 4.4 shows the structure of the monomers used for the plasma polymerization process.

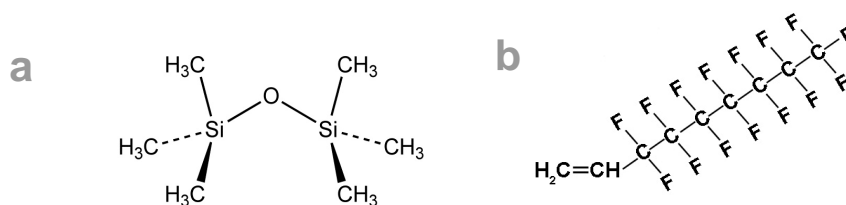


Figure 4.4 Structure of the monomers used for the plasma polymerization, **a.** HMDSO; and **b.** HDFD.

In this work, two stages of the **M** plasma polymerization were studied, the plasma activation of the coil coating surface only (stage **1**, accordingly with Table 4.1), and the combination of this plasma activation step with the plasma deposition step, performed in sequence (stage **2**). Only the plasma deposition step is worthless for the industrial process and for this reason not performed.

The Table 4.4 shows the conditions used for stage **1**. In the table are also the labels for the plasma activated systems, which are used along this text.

Table 4.4 Description of the plasma activation step and tested variables, together with the respective labels attributed to each system.

step	description	conditions	label
plasma activation	clean and activation of the coil coating surface with the carrier gas at 0.2 mbar (P ₁) and 400 W power	5 seconds with O ₂	a
		70 seconds with O ₂	b
		140 seconds with O ₂	c
		140 seconds with Ar	d
	1		UM1aP ₁
			UM1bP ₁
			UM1cP ₁
			UM1dP ₁

The plasma activation procedure occurs just before deposition of the plasma polymer film, being performed with the coil coating surface directly exposed to the plasma conditions. For this reason, degradation of the coil coating barrier properties may occur.

The experimental parameters used for the stage **2** together with the respective labels attributed to each system generated that are used along this text, appear in Table 4.5.

In this case, the plasma activation step, performed before the plasma deposition step, had the duration of 70 seconds with the other conditions similar to the ones shown in Table 4.4.

Table 4.5 Description of the plasma polymerization step performed in the **M** plasma reactor with the respective conditions used, together with the labels attributed to the systems prepared.

step	description	precursor mixture	pressure (mbar)	label
plasma deposition	deposition of the plasma polymer film at 400 W power during 140 seconds, coil coating speed 0.5 to 1 mm/s	HMDSO and O ₂ e	0.1 P ₂	UM2eP₂
		HMDSO and O ₂ e	0.05 P ₃	UM2eP₃
		HMDSO and Ar f	0.05 P ₃	UM2fP₃
		HMDSO, HDFD and Ar g	0.1 P ₂	UM2gP₂ ⁽²⁾

¹ Although the parameters here indicated correspond to the step of plasma deposition, the label **2** corresponds to two steps performed in sequence, plasma activation and plasma deposition.

² When tested at 45° C these systems label receives the **45** prefix.

ii. Radio Frequency Plasma Reactor - **R**

The plasma polymerization using the **R** plasma reactor took place in Corus facilities. Surface modification, using HMDSO and oxygen precursor mixture, were performed on **U** and **E** coil coatings. The plasma polymerization conditions were maintained constant throughout the experiments performed in this plasma reactor.

For the plasma generation was used a glow discharge from a radio frequency capacitive coupling reactor at 13.56 MHz of frequency. The Figure 4.5 shows a schematic of the plasma discharge reactor. In this case, according with point 2.6.6, the plasma reactor setup corresponds to external electrode plasma reactor.

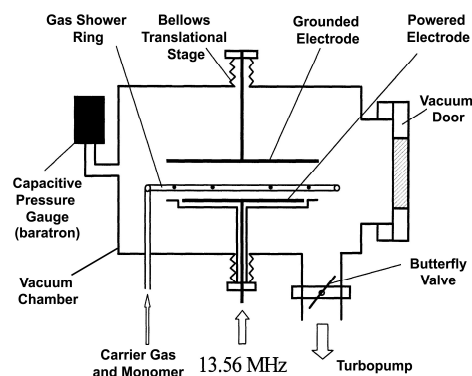


Figure 4.5 Scheme of the R plasma reactor.

The vacuum chamber was made of stainless steel with a volume of 21 litres. The process used a classical configuration of capacitive discharge, where the plasma is generated between two fixed electrodes because of the potential difference between them. The samples can be prepared by attaching them alternately onto one of the two possible electrodes. The bottom powered electrode (**P**) has 160 mm in diameter while the upper grounded electrode (**G**) has 200 mm. The largest samples produced were of size 160 x 105 mm for the **G** and 160 x 125 mm for the **P**. In the chosen configuration, the plasma polymerization occurs simultaneously in the two electrodes locations.

The regulation of the carrier gas flow occurs via a mass flow controller. The monomer flow control occurs through its partial pressure, by regulating the metering valve of the monomer line. The monomer and carrier gas enter the plasma chamber via the gas shower ring. The **P** electrode location is constrained within the chamber just below the gas shower ring for distribution of the monomer and carrier gas. The **G** electrode location can shift vertically using bellows on a translation stage. All samples were prepared with a fixed electrode gap of 75 mm between the **P** and **G** electrodes. Introduction of the gas mixture of oxygen and HMDSO into the chamber starts the plasma polymerization procedure.

Table 4.6 shows a resume describing each step where the conditions of plasma polymerization are also summarised.

In this work, to understand the influence of the plasma polymerization process on the coil coating, preparation of samples using different step combination occurs. First was tested only the plasma activation step performed on the coil coating surface. This stage receives the label **1** according to Table 4.1 and label **h** according to Table 4.2. The full plasma polymerization process (plasma activation, plasma deposition and plasma stabilization combination of steps) was then tested, label **3** and **e**. Finally, testing of the plasma deposition and plasma stabilization steps, performed without the initial plasma activation step occurs, i.e. the deposition of the plasma polymer film followed by plasma stabilization, receiving the label **4** and **i**.

Table 4.6 Description of the plasma polymerization steps performed in the **R** plasma reactor with the plasma polymerization conditions used.

step	description
plasma activation	clean and activation of the coil coating surface with O ₂ plasma at 0.07 mbar of pressure and 20 W power, during 300 seconds
plasma deposition	deposition of the plasma polymer film, HMDSO and O ₂ precursor mixture, with ratio 1:19 at total pressure of 0.03 mbar and 100 W power, during 80 seconds
plasma stabilization	stabilization of the plasma polymer surface with O ₂ plasma at 0.07 mbar and 20 W power, during 60 seconds

The **U** and **E** coil coatings, treated by the plasma polymerization procedure at both **P** and **G** electrode locations, used similar conditions and stages.

When the radio frequency plasma reactor was used, the electrode location of the specimens receive the letter **G** or **P** correspondent to grounded or powered electrode, respectively, which is added to the end of the label. The labels attributed to each prepared system, which are used along the text, appear in Table 4.7.

Table 4.7 Samples prepared at **G** and **P** electrode location of **R** plasma reactor, with the respective label correspondence.

coil coating	stage	activation time or precursor mixture	pressure (mbar)	label
polyurethane U ⁽¹⁾	plasma activation 1	300 seconds with O ₂ h	0.07 P ₄	UR1hP₄G ⁽¹⁾ UR1hP₄P ⁽¹⁾
	plasma deposition 3 ⁽²⁾	HMDSO and O ₂ e	0.03 P ₅	UR3eP₅G UR3eP₅P
	plasma stabilization 4 ⁽³⁾	60 seconds with O ₂ i	0.07 P ₄	UR4iP₄G ⁽¹⁾ UR4iP₄P ⁽¹⁾
polyester E	plasma activation 1	300 seconds with O ₂ h	0.07 P ₄	ER1hP₄G ER1hP₄P
	plasma deposition 3 ⁽²⁾	HMDSO and O ₂ e	0.03 P ₅	ER3eP₅G ER3eP₅P
	plasma stabilization 4 ⁽³⁾	60 seconds with O ₂ i	0.07 P ₄	ER4iP₄G ER4iP₄P

¹ When tested at 45° C, these systems receive the **45** prefix.

² Although the parameters indicated correspond to the step of plasma deposition, the label **3** corresponds to the combination of the three steps: plasma activation, plasma deposition and plasma stabilization performed in sequence.

³ Although the parameters indicated correspond to the step of plasma stabilization, the label **4** corresponds to the combination of the two steps: plasma deposition and plasma stabilization performed in sequence.

iii. Hollow Cathode Plasma Reactor - H

The plasma polymerization using the **H** plasma reactor took place in DOC facilities, treating the surface of the **U** coil coating. The process is especially designed for continuous deposition of plasma polymer films on plain sheets. The setup corresponds to internal electrode plasma reactor, according with point 2.6.6.

The sheet to be coated confines nearly completely the reaction zone and at the same time forms the cathode. This process has the advantage of high deposition rate and minimises the amount of parasitic deposition in the chamber walls. A large area, high density hollow cathode glow discharge is used for precursor gas activation and plasma generation. The precursor gas is activated close to the metal surface with a gas pressure of about 0.17 mbar, where parasitic formation of solid material by volume reactions is almost completely prevented.

For continuous deposition, the metal sheet forms a loop generating between their parallel legs a hollow cathode with a spacing of a few centimetres, shown schematically in Figure 4.6. For static deposition, a set-up with two parallel metal substrates forming the hollow cathode is used. The advantage of the static set-up deposition is a faster exchange of samples and thus an easier and faster coating development.

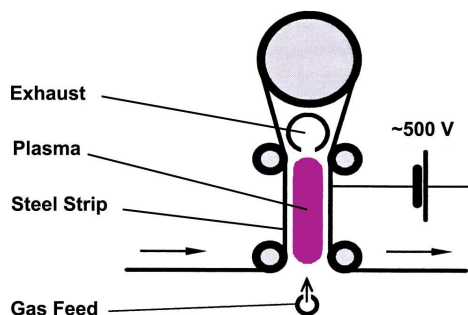


Figure 4.6 Scheme of the **H** plasma reactor.

The plasma polymerization occurs in a cylindrical vacuum chamber with an inner diameter of 2 m and a depth of 1 m, which was suitable for both static and dynamic set-ups for deposition on the sheets. Mass flow controllers control the monomer tetramethylsilane (TMS) flow. The achievement of different surface chemical properties is possible, by modification of the plasma polymerization parameters.^{170;171} The structure of the TMS monomer appears in Figure 4.7.

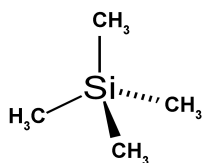


Figure 4.7 Structure of the TMS monomer used for plasma polymerization.

In the dynamic setup (scheme shown), are used sheets of up to 300 mm width and 0.3 mm thickness. In the static case, sheets of 750 mm length and 140 mm width are used, with an exposed area of 2 x (275 x 140) mm² to the plasma discharge. The coating deposition occurred at 0.17 mbar with 0.3 kW. The Table 4.8 shows the plasma polymerization conditions used in the **H** plasma reactor, with the respective label attributed that is used along the text.

Table 4.8 Plasma polymerization conditions used in the **H** plasma reactor, with the respective label attributed.

step	stage	conditions	label
plasma activation	2	clean and activation of the coil coating surface with mixture of argon and oxygen gases at 300 W and 40 kHz during 2 seconds	UH2kP₆
plasma deposition		deposition of the plasma polymer film at 0.17 mbar using TMS, argon and oxygen precursor mixture at 300 W and 40 kHz during 3 seconds	

4.2. Techniques Used

4.2.1. Electrochemical Impedance Spectroscopy

The measurements performed with Gamry FAS2 Femtostat with PCI4 Controller board, took place inside a Faraday cage to minimise the external electrical noise interference.

The measurements were carried out at the frequency range of 100 kHz down to 10 mHz with 7 points per frequency decade. The spectra were recorded at open circuit potential with a sinusoidal perturbation of 10 mV root mean square. The impedance data were analysed using the Gamry Echem Analyst software. At least two measurements for each condition were taken to verify their reproducibility.

The water uptake estimation recurs to the Brasher and Kingsbury's equation,¹²⁸ which procedure is described in point 3.1.4. The value of capacitance used was obtained from separate impedance measurements performed at 10 kHz, using specimens identical to the ones used for the EIS measurements.

Extrapolation of the initial value of the coating capacitance, C_0 in equation 3.13, arises from the values of capacitance determined at the initial stages of immersion.¹¹²

This model was chosen for its simplicity or adequate response compared with other models. Moreover, the results published in literature are mainly obtained with the Brasher and Kingsbury's equation. This one was the reason why the model of Castela et al.¹³⁸⁻¹⁴⁰ was not used, since they were only tested for few systems. One of the recent models proposed,¹²⁹ although also claim better correlation with the gravimetric results, requires parameters that are unknown.

i. Electrochemical Cells

The electrochemical cell used consisted of a three-electrode arrangement, with a XR110 saturated calomel reference electrode ($\text{Hg}|\text{Hg}_2\text{Cl}_2, \text{KCl}_{\text{sat}}$) from Radiometer Analytical, France, a M241Pt platinum foil counter electrode, also from Radiometer Analytical, and the exposed sample area as working electrode.

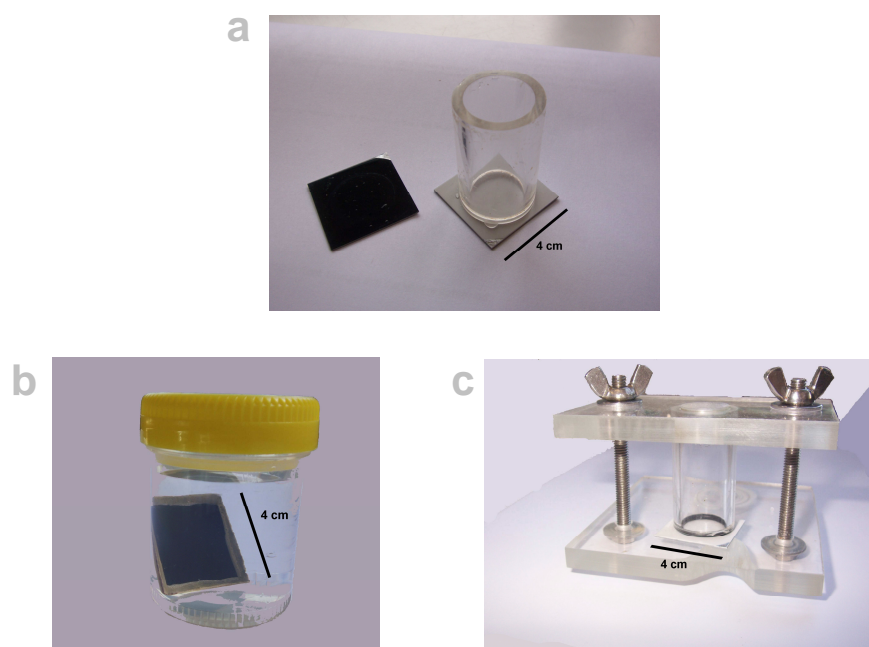


Figure 4.8 a. Electrochemical cell arrangement used for EIS impedance measurements of the samples tested at ambient temperature, working area of 3.4 cm^2 ; b. container for immersion tests at 45° C ; and c. electrochemical cell arrangement used for EIS impedance measurements of the samples tested at 45° C , working area of 2.46 cm^2 .

For ambient temperature tests, polymethyl methacrylate (PMMA) tubes were glued to the sample surface with two component epoxy glue, araldite[®] rapid. The tubes were used both for area limiting and as reservoirs of the testing medium, Figure 4.8a, with working area of 3.4 cm².

For higher temperature testing, the immersion of the sample took place inside a closed plastic container filled with the testing medium, Figure 4.8b. The specimen edges were protected with beeswax to prevent filiform degradation. The plastic containers were then placed in bath with controlled temperature at 45° C. For the EIS measurement, the specimen was cooled during 1 hour until room temperature was reached before the measurement. The electrochemical cell arrangement was similar to the one used for ambient testing, but using an o-ring for limiting of the working area to 2.46 cm², Figure 4.8c.

ii. Experimental Conditions

The test medium used during the work was an aqueous solution of sodium chloride (from Reidel-de Haën[®], p.a. purity), prepared with distilled water (resistivity of 1x10⁵ Ω cm). The concentration used was 0.5 M with pH 7.

Storing of the prepared cells occurs at room temperature in contact with air, protected from direct sun light and from dust. For long term tests, reposition of lost solution was done when needed. There was no variation of pH during the testing period.

4.2.2. Scanning Electronic Microscopy

The Scanning Electron Microscopy (SEM) consists of a Hitachi S-4100 system, with beam energy of 25.0 kV. The plasma polymer surfaces were mounted in the holder using conductive carbon glue and were coated with carbon to avoid surface charging, which would affect the secondary electrons imaging. During the measurements, tilting of the samples at 30 degrees occurs to increase the information about the surface morphology.

4.2.3. Energy Dispersive Spectroscopy

Energy Dispersive Spectroscopy (EDS) was used coupled with the SEM, using SiLi Röntec system UHV dewar detector, to obtain the surface composition. The respective composition evolution with immersion was obtained by EDS measurements after different immersion times.

The quantitative analysis used the Röntec software supplied with the equipment. During the elemental quantification, the software does not consider the carbon element proportion (considers the carbon value equal to zero), since for reduction of surface charging effect during the SEM imaging a surface layer of this element was sputtered in the samples surface, as described in point 4.2.2.

The sample preparation was the same as for SEM imaging. The measurements occurred in the same sample after the SEM imaging procedure, using an adjacent area.

4.2.4. Transmission Electronic Microscopy

Transmission Electron Microscopy (TEM), performed on Hitachi H9000-NA system with beam energy of 300 keV, revealed the structure of the plasma polymer films. Preparation of the samples for TEM imaging used an ultramicrotome from Leica with a diamond knife from Diatome[®] with 45° and 3 mm edge.

The sections of plasma polymerized coil coating system, obtained by detaching them from the metallic substrate using a spatula tool, were embedded in epoxy resin (from Agar scientific) and the cross-section prepared by ultramicrotomy. Several sections were obtained with thickness around 30 nm, were collected onto a nickel grid and stored in a grid box until observation.

The polyurethane coil coating has high thickness but is carbon based. Carbon element is transparent under TEM imaging. The technique offers no information in this case.

The polyester coil coating also has high thickness and its composition contains silicon and titanium elements. These elements provide strong contrast under TEM, offering high detail of the polyester coil coating structure.

The plasma polymer films generated are silicon based layers. The atomic weight of this element provides enough contrast for imaging by TEM, providing information about the plasma polymer films structure. The amorphous structure and the low thickness, however, made difficult to find the film. Deposition of a thin gold layer, around 3 to 4 nm, on the surface help to overcome the problem. The gold has higher elementary weight that gives higher contrast, appearing immediately under the electron beam. This was used to correctly positioning and focus of the electron beam.

4.2.5. Atomic Force Microscopy

Atomic force microscopy (AFM) verifies the surface morphology modification after the plasma process and provides information about the surface morphology evolution of the plasma polymer layers during immersion.

Two AFM systems were available, a Digital Instruments with NanoScope III controller and a Pico LE AFM microscope from Scientec. In the first system, the samples have a size limit less than 1 cm of side due to the microscope geometry arrangement. In the second apparatus, the samples measured can have up to 4 by 4 cm. This case was used for measurements for different immersion times on the same sample.

The AFM examinations used heavily doped silicon probes with tip radius of 5 to 6 nm. The probes were model ACT from AppNano, USA and the cantilever length was 125 μm , with resonant frequency of 300 kHz and spring constant of 50 N/m. The scans are performed in air at non-contact mode in order to prevent any damage of the film surface. On each scan recording of the topography, amplitude and phase angle was done.

The root mean square roughness (R_t), the arithmetic roughness (R_a) and the average height (h) were calculated from the topography maps, using standard software (Pico scan software version 5.3.3 from Veeco, WSxM version 5.0 from Nanotec Electronica SL¹⁷² and Gwyddion version 2.17). The surface parameters were obtained from the software, arising from the equations of point 3.5.2.

The images received a mean plane correction in order to reduce waviness due to scanner bow and variations of the film thickness. Then, they receive a line wise levelling to reduce possible line-by-line repetition errors.

The R_a and R_t parameters have similar behaviour. For simplicity, on this work, only the values of R_a and h appear in the respective images. The surface roughness corresponds to pores when the surface skewness (R_{sk}) is negative. In this case, the R_{sk} negative values appear in the images, otherwise they are omitted.

4.2.6. Colour Coordinates

The colour measurements use a telescope optical probe, Nikon Top 100 DTS140-111 from Instrument Systems GmbH. The light source was a tungsten lamp, model LS100-130 from the same company, coupled with a power supply model ES030-10 from Delta Elektronika. The width of the collecting reflection was set to 0.5 mm at 45 degrees angle using a commercial standard mirror as reference.

The Commission Internationale d'Eclairage (CIE) reflection (x,y) colour coordinates for 2° standard observer were estimated using IS SpecWin software for the plasma polymerized coil coating systems. Measurements performed along the immersion test permit to obtain the colour variation of the systems during tests.

Results

Section 5. Unmodified Coil Coating

5.1. Introduction

The coil coatings were analysed using the experimental techniques, the testing procedures and conditions previously described in points 4.1 and 4.2.

For the study of the coil coating degradation, the samples were submitted to immersion tests using 0.5M NaCl solution, which simulates natural aggressive conditions. The impedance response of the systems and respective impedance evolution with testing time was one of the procedures used to rank the coating systems.

Monitoring of the surface morphology and composition evolution during the immersion tests was performed. These results also produce parameters, which permit to assess the

surface properties, described in point 3.5.2. The surface results correlated with the impedance evolution makes easier to understand the degradation mechanism involved.

The results, obtained for the unmodified coil coating, serve as reference to compare the performance variation after the plasma polymerization process performed the coil coatings. Two different types of coil coatings are tested: polyurethane (**U**) based and polyester (**E**).

5.2. EIS Measurements

The coil coating upon contact with the environment behaves like a barrier to water and ions. The protection mechanism corresponds to hold these species away from the metallic substrate. The EIS technique offers characteristic responses attributed to the several degradation stages of the systems during immersion, as described in section 3.1.3.iii. Defects already present in the coating system, formed during the coil coating preparation or during handling of the samples, also influence the EIS response.

The Bode plots obtained for the **U** coil coating appear in Figure 5.1. Part **a** represents the system impedance evolution during immersion in 0.5 M NaCl solution, at ambient temperature. Impedance data for accelerated immersion tests performed at 45° C, using identical testing solution, are in Figure 5.1**b**.

The impedance in the two set of plots is different because of the different testing conditions. Higher temperature tests accelerate the degradation and the impedance response reflects exactly this difference.^{173;174} However, no changes on the degradation mechanism occur with the raising of testing temperature - the impedance spectra curve format remains unchanged with acceleration of the degradation.

Initial immersion (1 hour), has similar impedance values for both testing temperatures. Capacitive behaviour for the full frequency range tested arises, with very high impedance value in the low frequency part of the spectra, above 100 Gohm cm². The value is attributed to homogenous and defect free surfaces, representative of high performance paint systems.^{112;113;125}

At ambient temperature testing for the **U** coil coating, plots **a**, no variation of the impedance during immersion occurs. The impedance value obtained after 10 months of immersion is still higher than 100 Gohm cm² for full frequency range tested. The phase angle is also demonstrative of the system stability and during immersion remains constant near -90 degrees. This assures that the capacitive behaviour of the coil coating remains.

The results for continuous immersion tests performed in the corrosive environment at ambient temperature for the coil coatings cannot be defined as an accelerated test, since the time required to produce changes on the system response is too long.¹⁷⁵ In order to accelerate the degradation of the coil coating, introduction of high temperature testing was done. The results obtained during the testing at 45° C, using similar electrolyte solution, appear in part **b** of Figure 5.1.

The increase of the testing temperature accelerates the degradation processes but the results show that failure of the system is still far from occurring, even after 11 months of higher temperature immersion. The low frequency impedance value obtained, in this case, after 11 months is higher than 10 Gohm cm². These values represent a decrease of one order of magnitude from the initial value. The decrease of low frequency impedance is the consequence of a resistive part, appearing after 7 months of immersion.

The resistance values relate inversely to the average area of the conductive pathways present in the paint film, hence, higher resistive part appears due to the increase, in number and in size, of pores and pathways in the paint. Consequent water and ions ingress in the pores appear in the impedance response and correlates with decrease of the coating barrier properties.^{112;113;125}

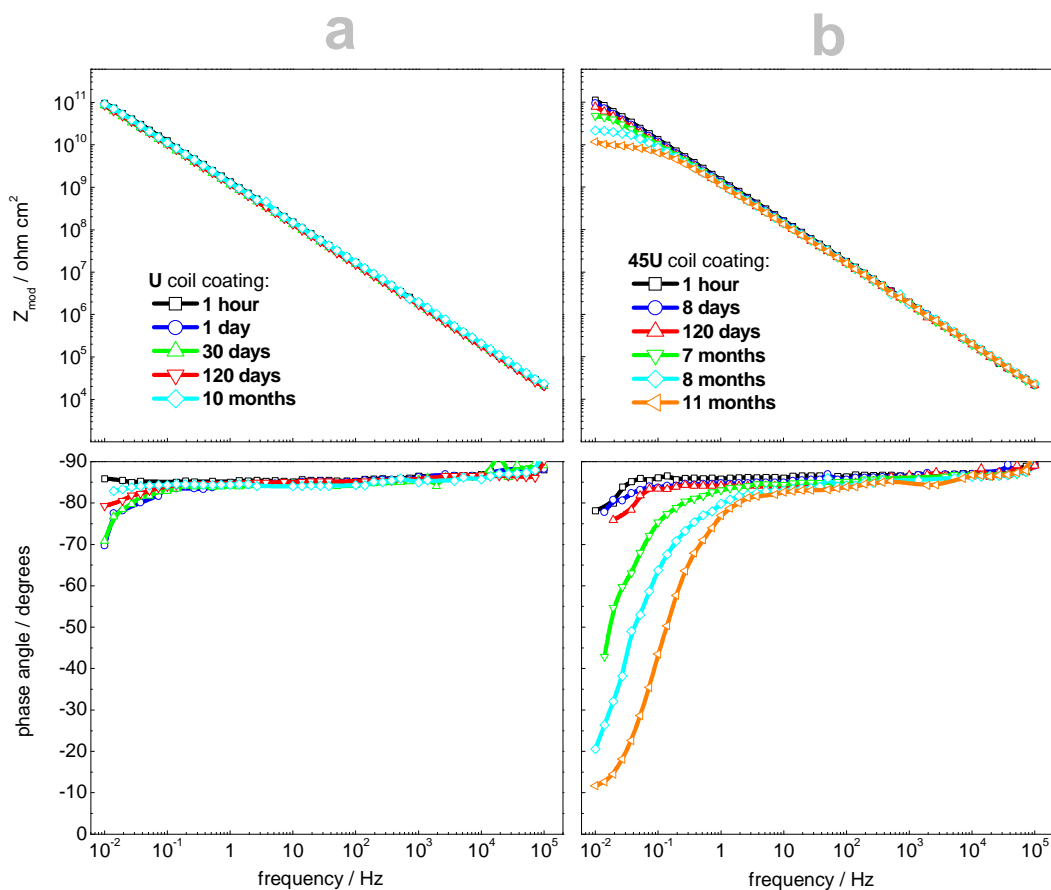


Figure 5.1 Bode plot diagrams for **U** coil coating submitted to immersion tests in 0.5 M NaCl at: **a.** ambient temperature; and **b.** 45° C.

Increase of testing time shows continuous decrease of the low frequency impedance value, attributed to the increase of coating degradation. However, after 11 months of

testing at 45° C the impedance value obtained is representative of a paint system that still confers protection to the metallic substrate.

The **E** coil coating testing was performed at ambient temperature, the results appear in Figure 5.2. In the Nyquist plot, the impedance evolution is easier to see, hence the impedance results also appear using that representation.

The impedance at low frequency after 1 hour of immersion is slightly above 10 Gohm cm². This is one order of magnitude lower than for **U** coil coating. The value is still high and representative of high performance coating systems, where pure capacitive behaviour appears for the full frequency range tested.^{112;113;125} These results suggest initial lower stability of the **E** coil coating, when compared with the **U** coil coating.

The continuous impedance decrease during immersion corresponds to coating degradation during immersion of the **E** coil coating. The low frequency impedance value decrease shows association with increasing number of pores and holidays in the coating. Water and ions enter into the coating by diffusion processes, first, filling up the holidays and pores, already present in the coating system. The absorption process continues during immersion and leads to the formation of other pathways and pores through the coating, which raises the absorption rate.^{112;113;125}

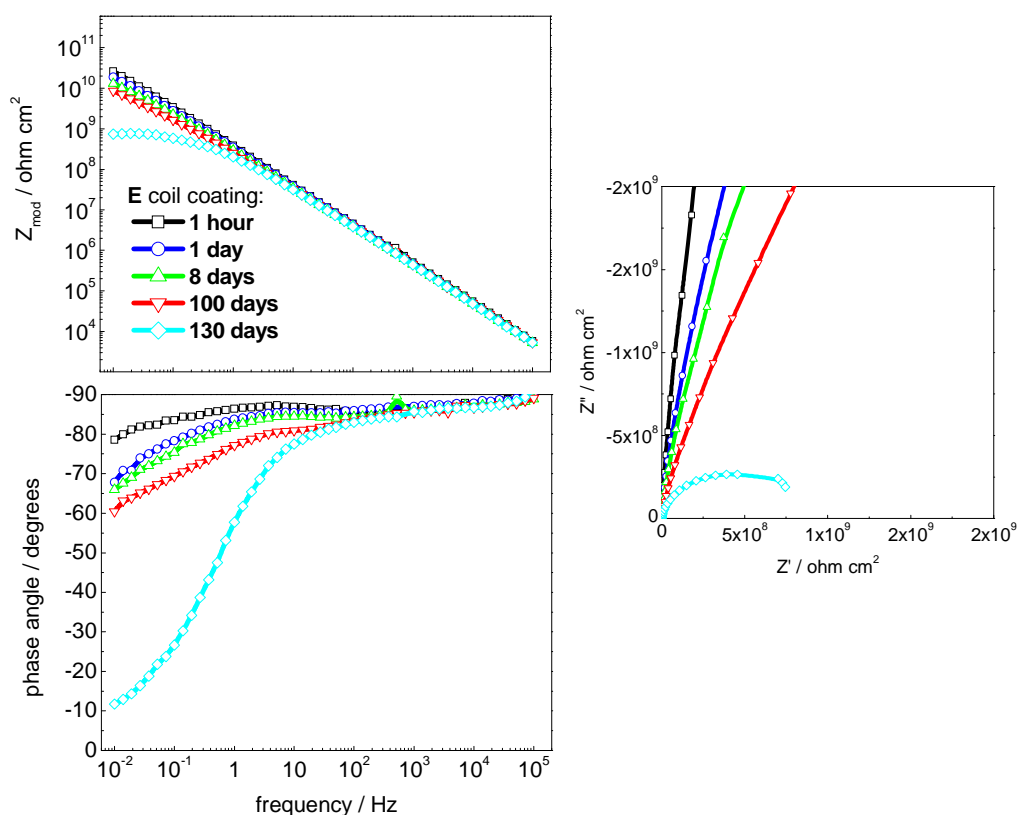


Figure 5.2 Bode and Nyquist plot diagrams for **E** coil coating, tests at ambient temperature.

These absorption processes during immersion lead to the appearing of a low frequency resistive part. The presence of the resistive part and the strong decrease of the low frequency impedance value represent a decrease of the system performance. The results after 130 days of immersion show that the coating still stands, with low frequency impedance value under 1 Gohm cm², however, suggest that the metallic surface was reached by water. The quasi semi circle formed in the Nyquist plot reinforces that the solution is in contact with the metallic substrate surface.

For longer immersion, development of the system degradation will eventually lead to corrosion processes. The coil coating systems used have a zinc layer, as galvanised steel is used, which when exposed to the aggressive environment still protects the underlying metal by cathodic protection. The protection of the zinc layer initially forms only slow white corrosion products that also confer protection. ^{15;112;113;176}

5.2.1. Numerical Fitting of EIS Data

Fitting the EIS data using equivalent circuits allows the estimation of the degradation rate of the barrier properties for the systems under study. The equivalent electric circuits used for fitting the impedance results appear in Figure 5.3.

The **U** coil coating shows only one process occurring during the immersion tests and the fittings were always performed using equivalent circuit **a** of Figure 5.3. The **E** coil coating, on the other hand, shows the presence of second high frequency process and, for correct fitting, is used the equivalent circuit **b** of Figure 5.3. The equivalent circuit parameters obtained from fitting are the resistance of the solution (R_{sol}), the pore resistance of the coating (R_{por}), and the coating capacitance (C_{coat}).



Figure 5.3 Equivalent electric circuits used for numerical fitting of the EIS data obtained for the painted systems: **a.** undamaged system; and **b.** two processes.

The data concerning the coating capacitance and pore resistance evolution show relation with the diffusion of solution into the coating. The chloride and sodium ions are very small, and for this reason, are able to diffuse through the coating. Later, the chloride ions

together with water and oxygen are responsible by the beginning of active corrosion processes when they reach the substrate.^{32;121;174}

The C_{coat}^* and R_{por}^* parameters used for the equivalent electric circuit **b** are attributed to detours from ideal behaviour. The possible reasons for the deviations have been attributed to rugosity of the electrodes, non homogeneous materials or distribution of relaxation times of the surface processes.^{131;177-182} According to MacDonald and Franceschetti¹⁸² the existence of a second time constant could be associated to different anionic and cationic mobilities inside the film in immersion. Identical finding was reached by Castela when studying a film of polyvinyl chloride - plastisol in 0.5 M NaF solution.¹⁸³

Figure 5.4 presents the impedance results and the respective fitting results for the unmodified **E** coil coating. For the fitting, the constant phase element (Q) replaced the capacitance element (C), to account inhomogeneities of the surface in the electrochemical EIS experiments.^{184;185} The numerical fitting presented confirms that the circuits used are adequate.

Initially, Figure 5.4a, one time constant is obtained and circuit **a** of Figure 5.3 is used. This provides R_{sol} , C_{coat} and R_{por} parameters. After 130 days of immersion in part **b** is noticed an accentuated impedance drop together with the formation of a second time constant at high frequencies. The two time constants demand fitting using the equivalent circuit **b** of Figure 5.3. Here, are obtained the C_{coat}^* and R_{por}^* , mentioned above (appearing at high frequency in the spectrum), together with C_{coat} and R_{por} , attributed to the coating degradation process (appearing at low frequency).¹⁷⁷⁻¹⁸²

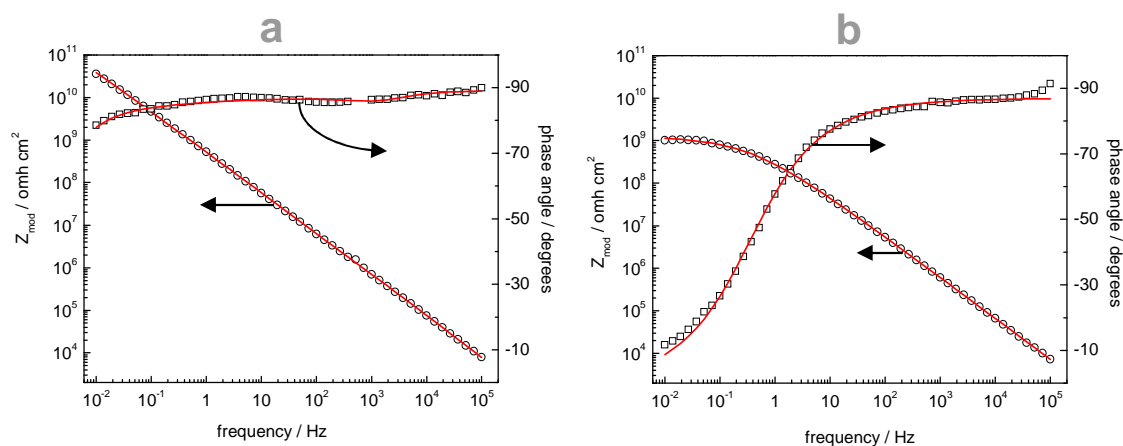


Figure 5.4 Numerical fitting for unmodified **E** coil coating: **a.** immediately after immersion, Q ($C_{\text{coat}}=3.35 \times 10^{-10} \text{ F cm}^2 \text{ s}^{n-1}$ with $n=0.958$, $R_{\text{por}}=2.21 \times 10^{11} \text{ ohm cm}^2$ and **b.** after 130 days of immersion, Q ($C_{\text{coat}}^*=3.53 \times 10^{-10} \text{ F cm}^2 \text{ s}^{n-1}$ with $n=0.965$, $R_{\text{por}}^*=5.51 \times 10^6 \text{ ohm cm}^2$; Q ($C_{\text{coat}}=6.11 \times 10^{-10} \text{ F cm}^2 \text{ s}^{n-1}$ with $n=0.481$; and $R_{\text{por}}=1.33 \times 10^9 \text{ ohm cm}^2$. The black squares represent the EIS data and the red line the respective fitting.

The low frequency impedance value obtained and the curve format of the Nyquist plots of Figure 5.2 show that active corrosion processes are not occurring. Active corrosion processes would form another time constant at low frequency and the fitting would demand an equivalent circuit similar to the one of Figure 3.7c.¹²¹

For the present analysis, the fittings results plotted refer only to C_{coat} and R_{por} parameters, since these are the representative parameters of the systems barrier properties evolution, although in the **E** systems the fitting also estimate the R_{por}^* and C_{coat}^* parameters corresponding to a high frequency process.

The estimated parameters, C_{coat} and R_{por} for the unmodified coil coatings, obtained from the equivalent circuits, appear in the Figure 5.5. The results reflect the evolution of the **E** and **U** coil coating and in the latter case the effect of the temperature of testing.^{32;39;40}

The lowest C_{coat} value is the one from the **U** coil coating. This can be partially related with the higher paint thickness, since this parameter inversely relates with the C_{coat} (higher thickness lower C_{coat}). However, the increase verified should also be due to higher intake of solution by the **E** system. The C_{coat} stable behaviour is associated with the higher barrier effect, as a result in lower amount of absorbed water and electrolyte. Increase of testing temperature for **45U** coil coating shows an increase of C_{coat} value and confirms that the increase of temperature is responsible by acceleration of the processes leading to an increase of system degradation.

The R_{por} evolution leads to identical conclusion. The value for **U** coil coating is the highest, corresponding to lower degradation. When the testing occurs at higher temperature, **45U** line, lower R_{por} value arises. The moment where the **45U** system performance starts to decrease is noticed when the R_{por} value starts to show a continuous decrease trend. For this system, this occurs after around 150 days of immersion.

The Figure 5.5 shows that the **E** coil coating has even higher C_{coat} value than **45U** system. This represents higher amount of water and ions absorption. The R_{por} value is also lower than R_{por} value for **45U** system, with strong drop occurring sooner, after 100 days of immersion. In this case, the R_{por} drop shows that water and ions reach the metallic surface.

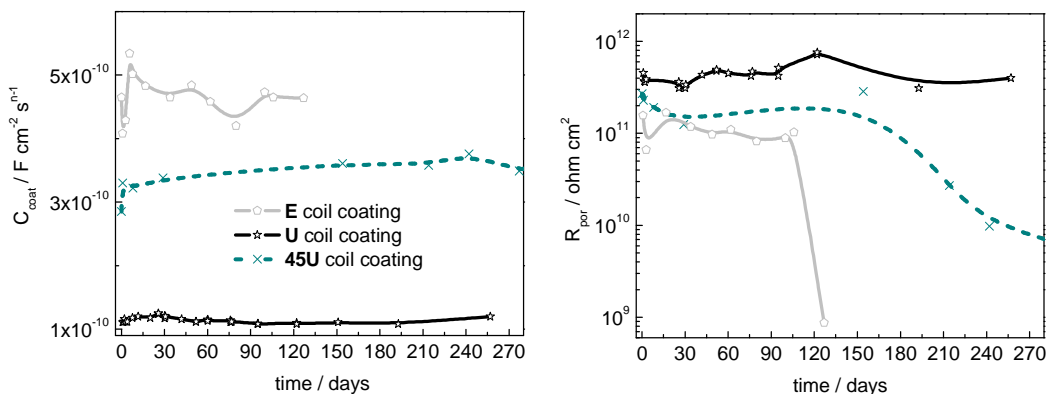


Figure 5.5 Evolution of the C_{coat} and R_{por} estimated parameters for **E** and **U** coil coating.

5.2.2. Water Uptake Estimation

The value of the coating capacitance permit to estimate the water uptake rate, using the empirical relation of Brasher and Kingsbury, ¹²⁸ eq. 3.13, following the procedure described in section 3.1.4. The water uptake plots for the coil coatings appear in Figure 5.6. The capacitance measurements were performed at 10 kHz. The signal obtained at this frequency corresponds only to the coating capacitance. The signal due to corrosion processes appears at lower frequencies, from 10 to 0.01 Hz, and after long immersion period. ¹¹²

The water uptake immediately after immersion confirms the difference in performance for the two coil coatings. For initial stages of immersion, the water uptake rate is fast in both coil coating, **U** and **E**. This is characteristic behaviour of organic coatings attributed to initial fast filling up with water of surface holidays and pores present in the coating. After some time the water absorption rate decreases and the amount of water absorbed becomes constant. ^{112;128;129}

For the **U** coil coating, the saturation occurs after 1 day of immersion, while for **E** coil coating the saturation occurs after three more days, i.e. 4 days of immersion.

The saturation level reached is also dependent of the coil coating used. The **E** coil coating shows more than twice the amount of water absorbed by the **U** coil coating, which confirms the higher performance of the **U** coil coating (lower percentage of absorbed water is attributed to better barrier properties). The **U** coil coating has more stable saturation plateau with increase of immersion time, while the **E** coil coating saturation plateau continues slowly to rise.

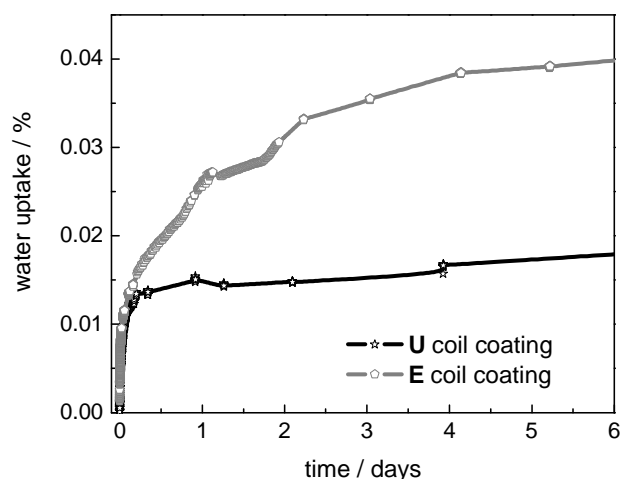


Figure 5.6 Water uptake estimation for **E** and **U** coil coatings.

5.3. Surface Characterisation

The Figure 5.7 presents the AFM images with the surface morphology of the two coil coatings. In the top of each image, in gray, is the respective time of immersion until the AFM measurement and in each image is the calculated arithmetic roughness (R_a) and average surface height (h) values, calculated accordingly to the description in point 4.2.5. The AFM images with the 0 days label represent the coil coating surface morphology before any testing.

The surface morphology is different for the two coil coatings. The evolution during the immersion tests is also dependent of the coil coating.

The surface morphology of **U** coil coating, Figure 5.7a, is non-uniform. During immersion, non-uniform surface morphology continues to appear. The R_a and h parameters have a small variation during immersion, attributed to differences of the surface morphology for different areas of measurement, which may lead to the small variation of the parameters.

The **E** coil coating AFM images, Figure 5.7b, show surface morphology with surface defects, even before testing. During immersion tests, increment of the surface defects occurs, both in size and in number. The R_a and h values evolution during immersion confirms that surface variation occurs.

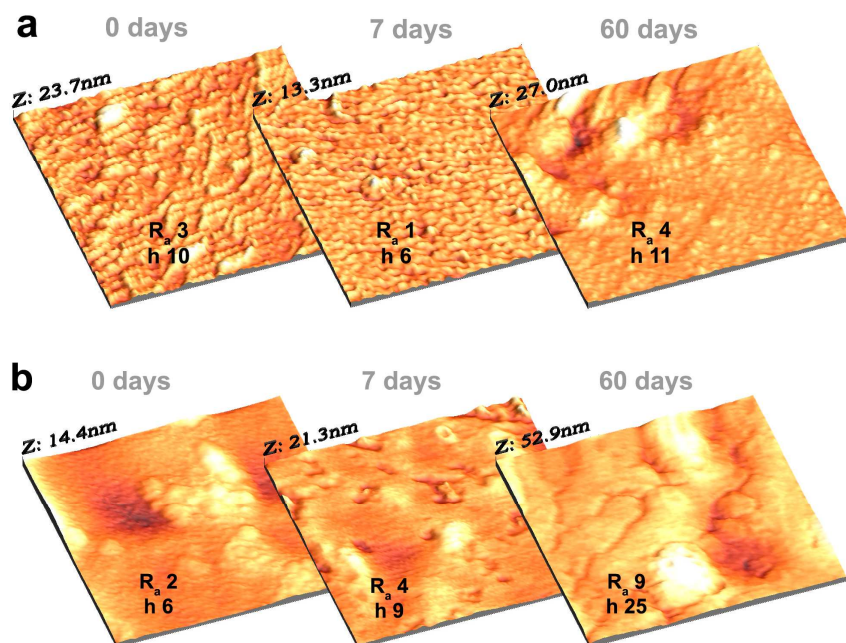


Figure 5.7 AFM 1x1 μm images of the surface morphology evolution for: **a.** **U** coil coating and **b.** **E** coil coating, with the respective values, in nm, of R_a and h .

The SEM images of Figure 5.8 show the surface morphology of **E** coil coating at lower magnification. The AFM images cover $1 \times 1 \mu\text{m}$ scan, while the SEM covers $10 \times 7 \mu\text{m}$. Here, it is possible to see pores with $3 \mu\text{m}$ diameter in the surface even before the immersion tests. Several particles appear in the images with 300 nm of diameter, which EDS reveal to be titanium containing. These are titanium dioxide charges added to the formulation of the **E** coil coating. Their higher elemental weight is responsible by the colour difference in the micrographs.

Variation of the surface morphology during immersion occurs, noticed in the pores walls. They become less sharp during the immersion tests and show the formation of deposits inside and around the pore walls. These deposits arise from paint components reaction with the testing solution. This may be responsible by the impedance instability verified during immersion tests and when occurs in the internal pores can block them. This blocking process prevents, or at least delays, further water uptake processes through the pores or pathways until a new pathway forms or dissolution of the blocking products occurs.

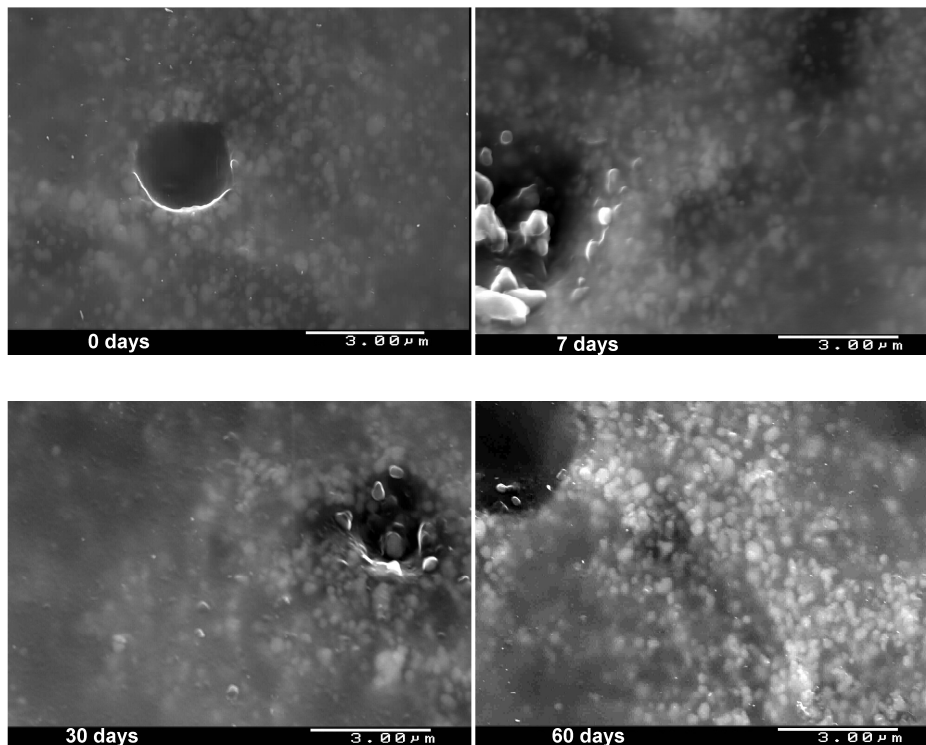


Figure 5.8 SEM images of the surface evolution of the **E** coil coating.

The **E** coil coating surface characterization using the SEM technique shows better results, compared with the surface morphology results obtained from AFM images, offering more

information about the system surface. It is, however, impossible to calculate surface parameters from the micrographs. The **U** coil coating, on the other hand, is less stable when under the SEM electron beam. The beam energy in this case has enough energy to burn and melt the **U** coil coating.

In the rest of this work, the SEM technique was used only for surface morphology characterisation of **E** coil coating and the AFM technique for the **U** coil coating. In this latter case, R_a and h values are calculated and given in the respective AFM images as in Figure 5.7.

The coil coating composition was obtained by EDS technique. The composition evolution for the two coil coating systems used was obtained performing EDS measurements after exposition of the coating systems for different immersion periods, Figure 5.9 shown in the next page. Quantification of the principal elements was done and the results appear in the table, values in at. %. The quantification procedure does not consider the carbon element content (the carbon at. % is considered zero) since a surface layer of carbon element was used for decrease of the surface charging effect, as described in 4.2.3.

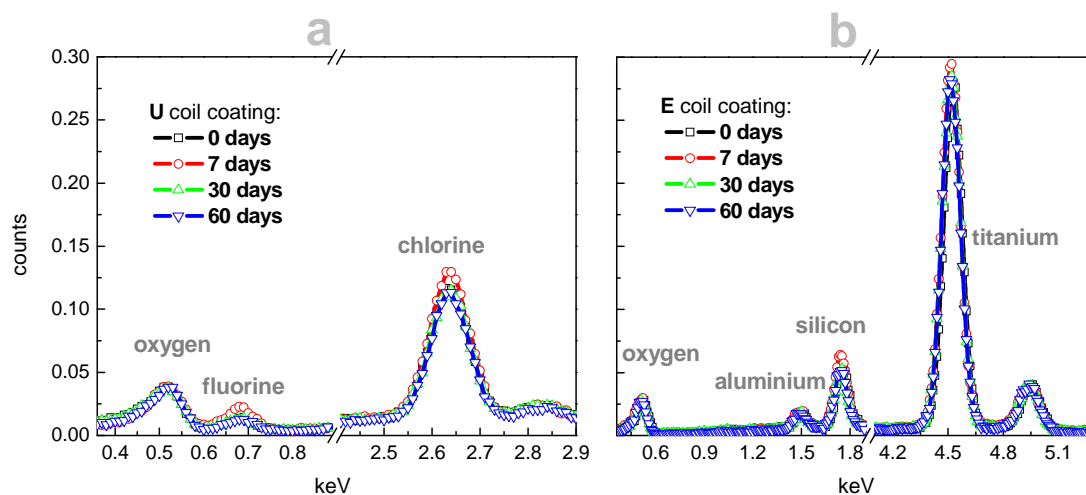
The principal elements obtained for the **U** coil coating were fluorine, chlorine, oxygen and carbon. EDS cannot correctly quantify the last two elements, due to their low elemental weight and external interference sources. Carbon element comes from covering the surface in order to reduce the surface charging effect, while oxygen can enter to the specimen chamber from the environment. For this reason, the software considers the carbon element proportion equal to zero, as referred in point 4.2.3.

For the **U** coil coating, the composition remains practically unchanged during immersion for both the fluorine and chlorine peaks, which are the representative elements of the **U** coil coating. The quantification values for these elements suggest that the systems have high stability during long immersion periods, since no variation of the element content appears.

The **E** coil coating shows different composition. Here titanium, silicon and aluminium are the representative elements. Oxygen and carbon elements are also obtained, but due to external interferences as mentioned.

The spectra show constant peaks during the immersion tests. The elemental composition, obtained by quantification of the spectra appears in the table and corroborates the stability of the **E** system showing constant values.

The results obtained for the unmodified coil coatings show that these systems have high performance against the testing conditions. The **U** coil coating shows outstanding stability during very long immersion in aggressive testing conditions. For the **E** coil coating some degradation takes place during the testing but the chemical composition does not change during the period shown.



time (days)	U coil coating		E coil coating		
	fluorine	chlorine	aluminium	silicon	titanium
0	56	3	1	3	24
7	43	3	1	3	24
30	41	3	1	3	25
60	52	3	1	3	27

Figure 5.9 Composition spectra obtained by EDS technique for: **a.** U coil coating; and **b.** E coil coating. The quantification for some elements appears in the table, values in at. %.

Section 6. Modified Coil Coating

6.1. Introduction

The results obtained for the plasma polymerized coil coating systems are presented in this section. The systems correspond to the same base coil coatings tested in Section 5 after the surface modification obtained with partial or total plasma polymerization process. The main objective was the study of the influence of the plasma polymerization process on the properties of the coil coating. The new surface properties and stability of the plasma treated surface in 0.5 M NaCl solution were analysed.

The modified coil coatings were analysed using the same set of techniques, experimental procedures and experimental conditions also used for the unmodified coil coatings, with the objective of comparing the behaviour of the systems before and after the plasma polymerization modification.

The results for the modified coil coating appear divided accordingly to the different reactors used for the plasma polymerization process. First appears the results for microwave (**M**) plasma reactor, point 6.2, followed by radio frequency (**R**) plasma reactor, point 6.3, and, finally, hollow cathode (**H**) plasma reactor, point 6.4. For each reactor, different process variables are studied for optimization of the respective plasma polymerization process.

The results and analysis are done through this chapter and then discussed in Section 7.

6.2. Microwave Plasma Reactor

Microwave plasmas are preferred for remote processing because of their very high plasma density and high dissociation rate. However, they do not present satisfactory scalability and homogeneity for continuous applications. Additionally, in linear geometries the deposition of film on the microwave coupling window cannot be totally avoided, even when a remote process is used.¹⁸⁶

Point 4.1.2.i describes the plasma polymerization conditions used during the process, together with the respective labels attributed to each system prepared. To identify the influence of the plasma polymerization conditions on the coil coating properties the results for each stage appear in different sections.

First, the study of the plasma activation step is presented in point 6.2.1. The step occurs with the coil coating surface directly exposed to the plasma activation conditions where degradation may occur. Special attention is dedicated to the study of the **U** coil coating barrier properties degradation. In this stage, only introduction of the carrier gas occurs, oxygen or argon, without the monomer.

Then, in point 6.2.2, follows the study of the stage **2**, plasma activation and plasma deposition combination of steps performed in sequence, where deposition of the plasma polymer film occurs. In this case, the barrier properties are also object of study, together with characterization of the plasma polymer film, such as structure, surface morphology and composition. The study of the optical properties of the surface appears at the end of the section.

6.2.1. Plasma Activation Stage

For **M** plasma reactor, the plasma activation uses different times for the plasma treatment conjugated with two carrier gases, oxygen and argon. The conditions used are those indicated in Table 4.4. The step consists of cleaning the surface of the coil coating and enhancement of the adhesion between the coil coating and the plasma polymer film, deposited in the next step.

i. EIS Results

The impedance results, obtained by EIS during immersion, for the **U** coil coating after the plasma activation performed in **M** plasma reactor in the different operating conditions, appear in Figure 6.1.

The results after 1 hour immersion (part **a**) show that all the plasma activated systems have identical low frequency impedance values that are also identical to the values obtained for the unmodified **U** coil coating. The low frequency impedance value is higher than 10 Gohm cm² in all cases, showing capacitive behaviour for almost the full frequency range tested. The capacitive response assigns for the coating capacitance and the impedance values correspond to high performance systems.^{112;113;125}

A very small resistive response in the low frequency part of the spectra is visible initially for the plasma activated **M** systems. This low frequency resistive response is easier to see in the phase angle plot, which also shows that longer plasma activation forms larger resistive part.

The unmodified **U** coil coating maintains constant capacitive behaviour, without any noticeable variation after 10 months of testing, as already shown in point 5.2. The evolution of the impedance spectra during immersion of the plasma activated systems shows that influence on the barrier properties occurred, Figure 6.1**b**.

In this case, significant decrease of the low frequency impedance occurs after less than 1 month of immersion. The values obtained are dependent both of the gas used and of the time of plasma activation. The results evidence coating degradation provoked during the plasma activation, allowing water and ions to enter into the coating by diffusion processes.

The system **UM1dP₁** presents the lowest decrease of the low frequency impedance value, which could be due to the lowest influence of the **M** plasma activation step on the barrier properties. The curve format of the phase angle plot suggests that the system still offers high barrier effect, showing that the water and ions are not yet in contact with the metallic substrate. After 24 days of immersion, the low frequency impedance value decreased almost one order of magnitude, to 10 Gohm cm². This impedance value is still high suggesting that active corrosion processes are not present. The results confirm that the plasma activation with argon carrier gas has already some influence to the barrier properties of the **U** coil coating, which leads to an increase of the amount of water and ions absorbed, compared with the unmodified **U** coil coating.^{112;113;125}

The **M** plasma activation using oxygen carrier gas shows two orders of magnitude decrease of the low frequency impedance, reaching 1 Gohm cm². The coating performance depends of the time of oxygen plasma activation. The systems **UM1aP₁** and **UM1bP₁**, plasma activation during 5 and 70 seconds, show coincident resistive response after 26 and 22 days of immersion, respectively. Longer oxygen plasma activation, system **UM1cP₁**, shows even slightly lower impedance at low frequency, after only 18 days of immersion. The curve format of the phase angle, in this case, suggests that water and ions are reaching the metallic substrate, forming continuous electrical contact. This

corresponds to higher degree of degradation occurring during the plasma activation stage using oxygen in the **M** plasma reactor.

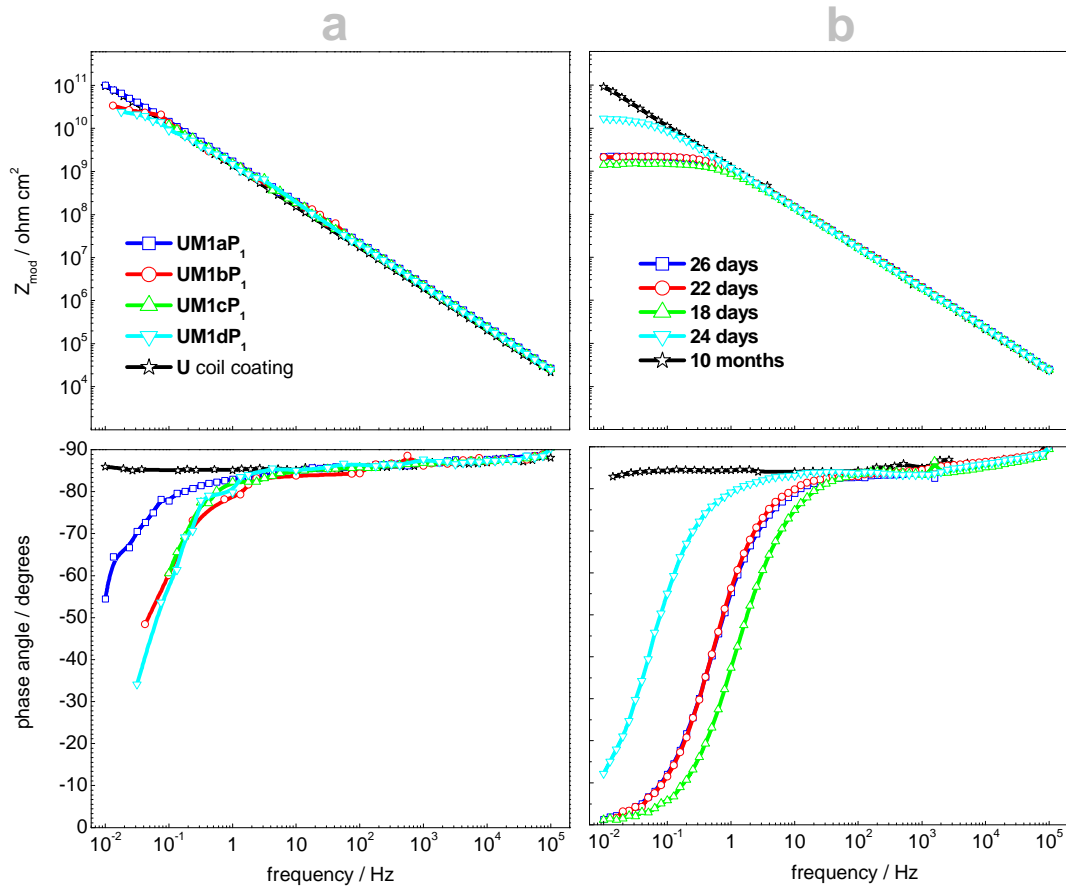


Figure 6.1 Bode plots with the impedance evolution during the immersion tests of the **U** coil coating submitted to different plasma activation conditions in **M** plasma reactor: **a.** immediately after immersion (1 hour); and **b.** for the time of immersion indicated.

- Numerical Fitting of EIS Data

Further information concerning the systems evolution is given by numerical fitting of the impedance results, using equivalent circuits. The parameters extracted have relation with the degradation processes occurring in the coating system. The fitting was done according to the procedure described in point 5.2.1, using the equivalent circuit of Figure 5.3a.

The C_{coat} and R_{por} parameters obtained as function of immersion time appear in Figure 6.2. The evolution is dependent of the carrier gas used and of the duration of the plasma

activation stage. The unmodified **U** coil coating parameters are also plotted and the results used as reference.

The unmodified **U** coil coating is stable, showing the lowest variation of both C_{coat} and R_{por} values during immersion. The results of Section 5 already showed that the unmodified **U** coil coating have very high performance when exposed to the chosen testing conditions.

Plasma activation of the **U** coil coating with argon, system **UM1dP₁**, shows the highest increase of C_{coat} . This parameter directly relates with the quantity of water absorbed by the coating, suggesting that the system has the highest water uptake.^{112;128;129} The R_{por} parameter for the same system shows the lowest decrease, which could indicate the lowest decrease of performance. The results obtained are unexpected and seem to be opposite between them. The high C_{coat} parameter suggests higher absorption rates, which corresponds to faster degradation, while the high R_{por} parameter is indicative of better performance.^{32;39;40}

The oxygen plasma activated **U** systems, **UM1aP₁**, **UM1bP₁** and **UM1cP₁**, have initially lower increase of C_{coat} compared with argon plasma activation, **UM1dP₁**. During immersion, the values of C_{coat} for the oxygen plasma activation continue to rise and approach that of system **UM1dP₁**. The longer the oxygen activation time the higher the value of the capacitance. The R_{por} parameter for these systems shows higher decrease than for system **UM1dP₁**. This suggests higher negative influence of the plasma activation step when performed with oxygen since the higher decrease of R_{por} corresponds to higher influence on the barrier properties. The R_{por} values of the plasma activated **U** systems using oxygen tend to similar values after 10 days of immersion. In this case, the results agree, suggesting stronger degradation for longer plasma activation with oxygen.

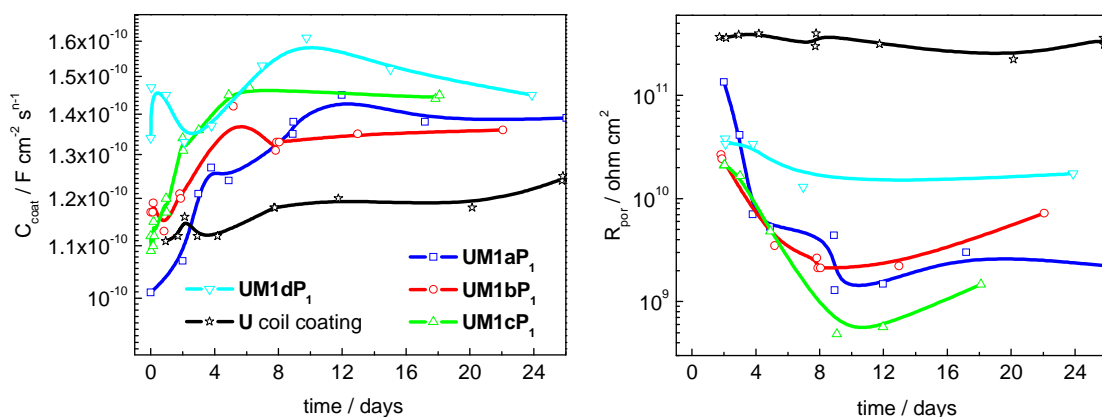


Figure 6.2 Evolution of C_{coat} and R_{por} parameters during immersion. The values came from the fitting of the impedance results for the **M** plasma activated **U** systems.

- Water Uptake

The variation of the coating capacitance value during the first 2 or 3 days of immersion permits to obtain the water uptake values of the coating for the plasma activated systems using the relationship of Brasher and Kingsbury.¹²⁸ The estimation uses eq. 3.13 following the procedure described in section 3.1.4. The results for the **M** plasma activated systems are in Figure 6.3.

All the systems, unmodified **U** coil coating included, show very fast initial water uptake, which is characteristic behaviour of organic coatings. The initial amount of absorbed water, corresponding to the saturation level, is very low for all the systems, which suggests high barrier effect of these coating systems.^{112;128;129}

The coating saturation level appears dependent of the plasma activation time and carrier gas used. The unmodified **U** coil coating has the lowest and most stable water saturation level, which corroborates the negative influence of the plasma activation step.

Unexpected result appears again for argon plasma activation, system **UM1dP**₁. The system has the highest initial saturation value, which then remains constant during immersion. These results agree with the C_{coat} values for longer immersion times, obtained from the impedance spectra.

The plasma activation using argon, system **UM1dP**₁, leads to the removal of hydrogen and low molecular weight molecules from the surface. This changes the surface of the coating, which upon contact with the testing solution may react again.^{110;111} These processes may be responsible by the interference in the C_{coat} values noticed.

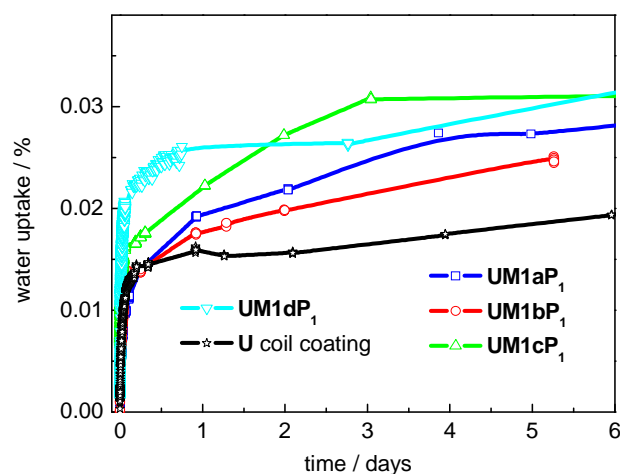


Figure 6.3 Water uptake evolution for the **M** plasma activated **U** systems calculated from capacitance measurements at 10 kHz, values in percentage.

In the case of **M** plasma activation using oxygen carrier gas, the systems after the initial water uptake, continue to absorb water during longer immersion, showing unstable saturation level. The longer the time of oxygen plasma activation the higher the water saturation level. This behaviour agrees with impedance results, which showed that longer plasma activation with oxygen leads to the highest C_{coat} values.

After 2 days of immersion, the system **UM1cP₁** already shows the highest saturation level. For lower plasma activation time, systems **UM1bP₁** and **UM1aP₂**, similar water uptake values appear also with similar raising trend.

The EIS results suggest that longer **M** plasma activation using oxygen has higher influence to the **U** coil coating barrier properties. The impedance results also show that **M** plasma activation with oxygen show higher influence than **M** plasma activation with argon, even the oxygen plasma activation during 5 seconds compared with 140 seconds of argon plasma activation, systems **UM1aP₁** and **UM1dP₁** respectively.

ii. Surface Characterisation

AFM measurements analysed the surface morphology variation occurring after the plasma activation step performed in the **M** plasma reactor using the **U** coil coating. The images of Figure 6.4 represent the surface morphology of the plasma activated systems before any test, i.e. the systems surface after the plasma activation before immersion testing. The R_a and h parameters, obtained using the procedure described in point 4.2.5 from the AFM measurements, appear in the respective images.

The images show that the systems have similar initial surface morphology, however suggesting that some differences occurred during the plasma activation.

The system **UM1aP₁**, 5 seconds of oxygen **M** plasma activation shown in image **a** of Figure 6.4, already present a small variation of surface morphology when compared with the unmodified **U** coil coating, shown in Figure 5.7a. The negative value of R_{sk} is indication that the surface morphology contains pores, as described in point 3.5.2.¹⁴⁹⁻¹⁵¹ These are formed due to the plasma activation step.

Increase of the time of **M** plasma activation with oxygen, system **UM1bP₁** and **UM1cP₁** of image **b** and **c** respectively, show similar variation of the surface roughness. The R_a and h values for these systems also slightly increase continuing to show negative R_{sk} , suggesting that the surface pores also form after longer time of oxygen plasma activation.

The surface morphology variation of the system **UM1dP₁**, argon activation during 140 seconds in image **d** of Figure 6.4, shows R_a and h values comparable with the system **UM1aP₁** but without the negative R_{sk} , meaning that surface pores are not formed. This suggests that perhaps a uniform thinning of the surface take place.

Measurements performed after 21 days of immersion for the same systems, show their surface morphology evolution during immersion. The images appear in Figure 6.5, with the values in nm of R_a and h in the respective images.

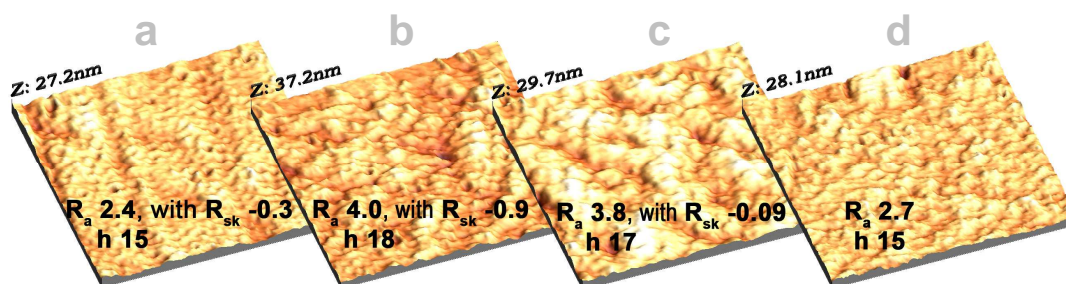


Figure 6.4 AFM 1x1 μm images with the surface morphology after the plasma activation step, systems: **a. UM1aP₁**; **b. UM1bP₁**; **c. UM1cP₁**; and **d. UM1dP₁**. The R_a and h values in nm appear in the respective image.

The surface morphology of the plasma activated systems is relatively stable during immersion. The oxygen plasma activated **U** systems continue to show negative R_{sk} , indicating that the surface pores formed are maintained during immersion. The exception is the system **UM1bP₁**, oxygen plasma activation during 70 seconds in image **b**. The R_{sk} is positive and higher than 1.5 after immersion, which suggests that the system has no “simple shape” according to point 3.5.2.¹⁴⁹⁻¹⁵¹

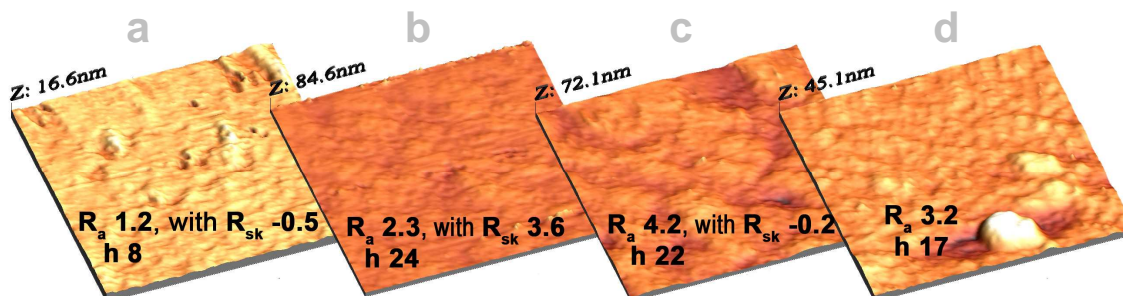
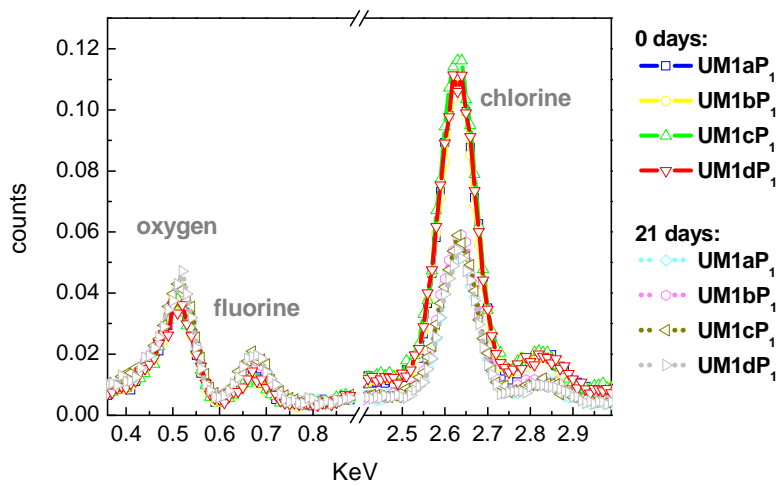


Figure 6.5 AFM 1x1 μm images with the surface morphology after 21 days of immersion, systems: **a. UM1aP₁**; **b. UM1bP₁**; **c. UM1cP₁**; and **d. UM1dP₁**. The R_a and h values in nm appear in the respective image.

The surface composition evolution during immersion of the **M** activated **U** coil coating was obtained with EDS and the results appear in the Figure 6.6. Quantification of the systems representative elements was performed and the values are in the table of the same figure. The quantification procedure does not consider the carbon element content (the carbon content is considered zero) since a surface layer of carbon element was used to decrease the surface charging effect, as described in 4.2.3.

After the plasma activation, the composition of the systems **UM1aP₁**, **UM1bP₁**, **UM1cP₁** and **UM1dP₁** show increase of the amount of fluorine and chlorine elements, compared with unmodified **U** coil coating.

After 21 days of immersion, the content of the chlorine element obtained for the plasma activated systems is closer to unmodified **U** coil coating. This represents a strong decrease of content compared with the unmodified specimens. The chlorine composition variation obtained is identical for all the plasma activated systems. For the unmodified **U** coil coating, a constant chlorine value during immersion is obtained.



time (days)	element	U	UM1aP ₁	UM1bP ₁	UM1cP ₁	UM1dP ₁
0	fluorine	56	85	67	82	95
	chlorine	2.9	4.9	5.0	5.0	4.7
21	fluorine	53	44	44	43	44
	chlorine	2.9	2.8	3.0	2.7	2.7

Figure 6.6 Composition (EDS) evolution during immersion of the plasma activated **U** systems using the **M** plasma reactor. Quantification values in at. %.

The surface results corroborate that the **M** plasma activation with oxygen has higher influence than **M** plasma activation with argon. Longer plasma activation using oxygen leads to higher influence on the **U** coil coating surface properties. These results directly relate with the impedance results obtained with oxygen plasma activation. Argon plasma activation unexpected behaviour is also explained, since the composition variation observed corroborates that surface modification, which can be responsible for the C_{coat} interference noticed.

6.2.2. Plasma Deposition Stage

After the plasma activation, the deposition of the plasma polymer film took place. The two steps occur in sequence, by adding in the deposition step the carrier gas and the monomer, forming the precursor mixture. The plasma polymerization conditions used for each step appear summarized in point 4.1.2.i.

In the **M** plasma reactor, the plasma polymerization was performed using several precursor mixtures and with different conditions. These appear described in Table 4.5 where the labels attributed to each system prepared are also shown.

i. EIS Results

The impedance evolution for the systems **UM2eP₂** and **UM2eP₃** during immersion in 0.5 M NaCl appear in the spectra of Figure 6.7. In this case, the precursor mixture is maintained constant, HMDSO and oxygen, being analysed the influence of the pressure reduction during the plasma polymerization procedure, from 0.1 to 0.05 mbar (**P₂** to **P₃**) plots **a** and **b**, respectively.

The spectra show for initial stages of immersion (1 hour line), pure capacitive behaviour for the two systems, with low frequency impedance values higher than 100 Gohm cm². These are comparable to the value obtained for the unmodified **U** coil coating, shown in Figure 5.1, and represent coating systems with very high performance.^{112;113;125}

Evolution of the systems impedance during immersion shows the formation of a low frequency resistive part, attributed to coating degradation. The low frequency impedance values decrease progressively during immersion, suggesting continuous degradation of the coating barrier properties.^{112;113;125}

The system **UM2eP₂** shows faster appearing of the resistive part at low frequency, which suggests faster degradation, plot **a**. After 1 day of immersion, there are already signs of the low frequency resistive part. The low frequency impedance value shows continuous decrease during immersion. This is a response to the continuous absorption of water and ions in pores and pathways. After 100 days (3.5 months) of immersion, the system low frequency impedance approaches 1 Gohm cm². This represents a decrease of two orders of magnitude. Impedance values of this magnitude are indicative of coating systems still without active corrosion processes. However, the curve format suggests that the water is reaching the metallic substrate, forming continuous connection between testing media and the metallic substrate.

Reduction of pressure from **P₂** to **P₃**, system **UM2eP₃** in **b** plot, also shows the resistive part formation at low frequencies. In this case, the decrease of the low frequency values is slower. After 140 days (4.5 months) of immersion one order of magnitude decrease is obtained, 10 Gohm cm² (which is one order of magnitude higher than the value obtained for the system **UM2eP₂** after 100 days of immersion).

The results suggest better performance of the system **UM2eP₃** when compared with the system **UM2eP₂** during testing. Degradation of the system **UM2eP₃** still occurs but the barrier effect is maintained. In this case, neither active corrosion processes are occurring nor is the water at the metal/coating interface.

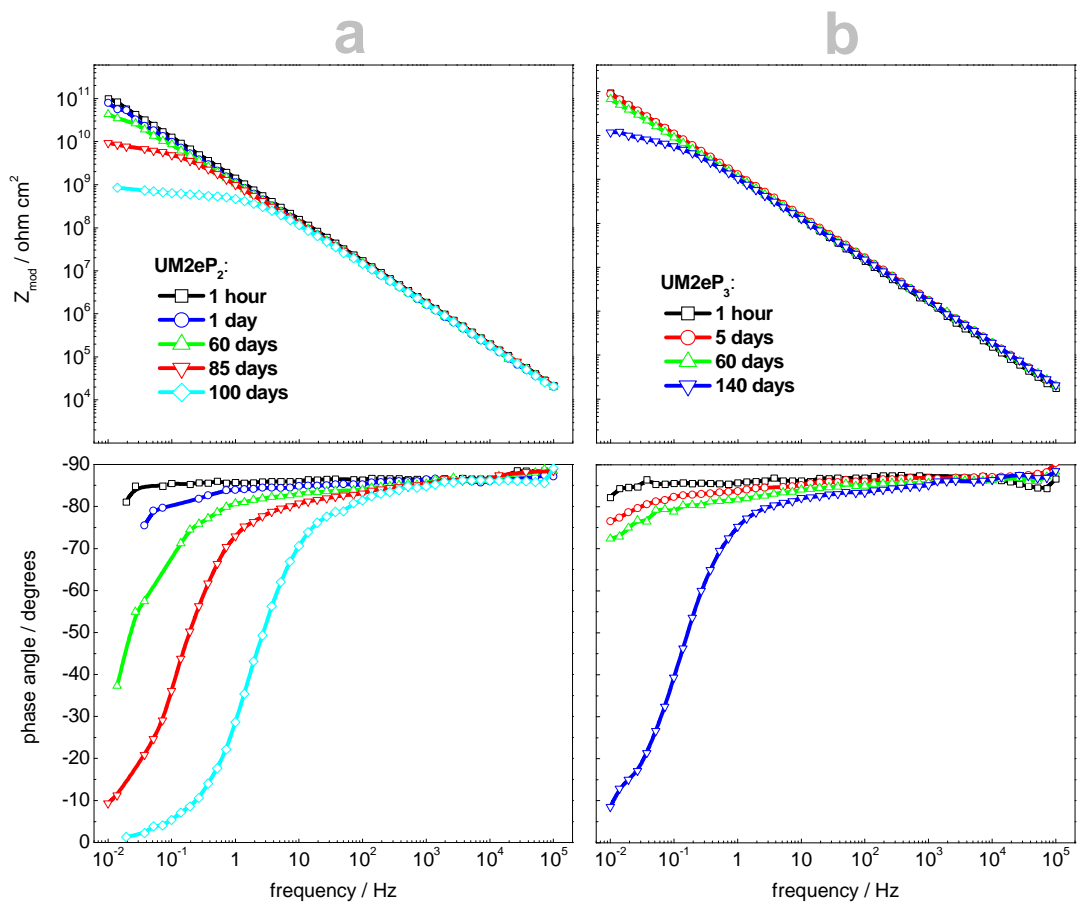


Figure 6.7 Bode plots with impedance evolution of **U** coil coating submitted to plasma polymerization process in **M** plasma reactor, systems: **a. UM2eP₂**; and **b. UM2eP₃**.

In the spectra of Figure 6.8 appears the impedance evolution of the plasma polymerized systems prepared using argon carrier gas. Plot **a** shows the system **UM2fP₃** impedance evolution. This system was prepared to test the absence of oxygen availability during the plasma polymerization, testing this influence in the final properties. The plot **b** shows the system **UM2gP₂** impedance evolution. In this case, the precursor mixture was modified by adding HDFD monomer to the precursor mixture. Hydrophobic surface properties are related to this precursor mixture.¹⁸⁷ The systems were prepared using 0.05 and 0.1 mbar pressures, respectively for the plasma polymerization procedure.

Initial results show no difference of impedance value for the two systems compared with the unmodified **U** coil coating, point 5.2. The behaviour is pure capacitive with low frequency impedance values higher than 100 Gohm cm^2 . Values of this magnitude correspond to coating systems with very high performance.^{112;113;125}

The evolution of the data during immersion shows only very slight decrease of the low frequency impedance value, to just less than 100 Gohm cm^2 . This appears after more than 8 months of immersion (230 and 250 days respectively in the plots). The behaviour is still pure capacitive for almost the full frequency range tested, with only very small resistive low frequency part visible in the phase angle plot. The results indicate that the systems barrier effect remain, without variation of performance during the immersion tests.

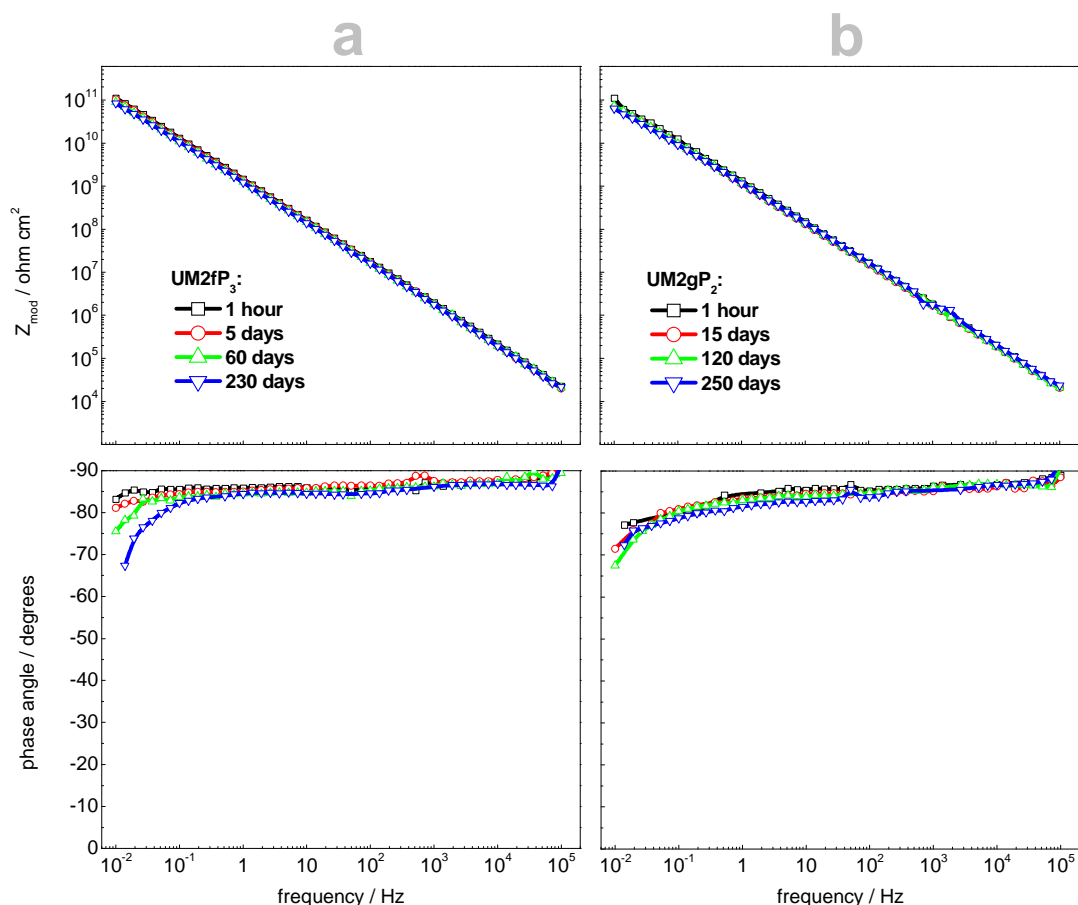


Figure 6.8 Bode plots with impedance evolution of the **U** coil coating submitted to **M** plasma polymerization, systems: **a. UM2fP₃**; and **b. UM2gP₂**.

- Electrochemical Testing at 45° C

The system **UM2gP₂** has very high impedance and to obtain faster results was tested at higher temperature in order to accelerate the degradation processes, obtaining more information about the degradation mechanism.^{173;174} The tests were performed at 45° C and the results appear in Figure 6.9, receiving the label **45UM2gP₂**.

For the initial immersion (1 hour) the results are identical to the ambient temperature results. The low frequency impedance value is higher than 100 Gohm cm², with pure capacitive behaviour for full frequency range tested.

In this case, during the tests, degradation arises, noticed by the formation of the resistive part at low frequency. This is associated with continuous decrease of the low frequency impedance value. After 1 day of immersion, the resistive part becomes visible. The degradation proceeds during immersion, easier to see in the phase angle plot. The low frequency impedance value decreases and after 120 days of immersion is 30 Gohm cm².

After 160 days of immersion two orders of magnitude decrease of the initial low frequency impedance value appears, 2 Gohm cm². At this immersion time, the curve format suggests that the water reached the metallic substrate, indicative of the presence of continuous pathways over the coating.

These pathways are responsible for an increase of the degradation rate and after 12 months (1 year) of testing, a decrease of three orders of magnitude of the low frequency impedance appears, reaching 100 Mohm cm². This suggests that active corrosion processes will occur soon.^{112;113;125}

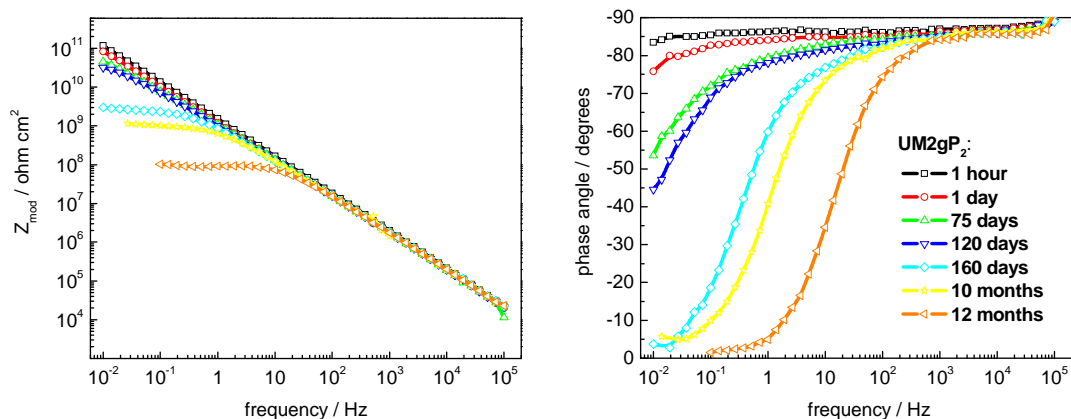


Figure 6.9 EIS data evolution for 45° C immersion tests of the **45UM2gP₂** system.

The degradation only occurs after long period of immersion at 45° C, attributed again to the system high performance (good resistance to the severe testing conditions). However, the decrease is stronger than for the unmodified **U** coil coating tested under similar conditions, Figure 5.1. This suggests that the barrier properties were affected during the plasma polymerization procedure, offering now lower protection than for the untreated **U** coil coating.

- Numerical Fitting of EIS Data

The impedance results were numerical fitted using equivalent electrical circuits. The C_{coat} and R_{por} parameters permit to extract quantitative information about the degradation process occurring during the immersion tests. The fitting procedure appears described in more detail in point 5.2.1. The data shows that the degradation corresponds only to one process occurring and consequently the fitting was performed with the equivalent circuit **a** of Figure 5.3, one time constant process.

In Figure 6.10, appear the C_{coat} and R_{por} parameters evolution during immersion for the **M** plasma polymerized **U** systems. The values obtained for unmodified **U** coil coating also appear in the figure being used as reference.

The unmodified **U** coil coating shows stable behaviour of the C_{coat} and R_{por} parameters during immersion. The C_{coat} presents the lowest value, because of the lowest water volume absorbed. The R_{por} value is initially similar for all the systems, but unmodified **U** coil coating maintains this initial value stable during further immersion. The results correspond to undamaged and high performance paint system,^{32;39;40} as was already described in point 5.2.

The **U** systems modified with the plasma polymerization process using **M** plasma reactor have higher, compared with unmodified **U** coil coating, initial C_{coat} values, but similar initial R_{por} values.

The system with the highest C_{coat} is the **UM2eP₂**, which value is maintained almost stable during immersion. The R_{por} value on the other hand is the lowest. After 30 days of immersion, the R_{por} value decreases three orders of magnitude remaining then stable at that value. These results represent coating systems with low barrier properties and are associated with fast decrease of system performance.

Decrease of operating pressure from **P₂** to **P₃**, system **UM2eP₃** has a positive effect to the C_{coat} parameter. However, after 30 days the values start to increase even overtaking the value of the system prepared at **P₂**. The R_{por} parameter shows smaller variation during immersion. The impedance results of Figure 6.7b agree with the estimated parameters suggesting that system degradation occurs during immersion, but with higher degradation occurring for the system **UM2eP₂** than for the system **UM2eP₃**.

Replacing oxygen carrier by argon, system **UM2fP₃**, yields the highest gain of performance. In this case, both parameters are stable during immersion. The C_{coat} is

slightly higher than unmodified **U** coil coating, but the lowest of the **M** plasma polymerized systems, while R_{por} is practically identical to unmodified **U** coil coating.

The **UM2gP₂** system also yields stable parameters, but in this case, C_{coat} and R_{por} values are higher and lower, respectively, than the **UM2fP₃** system. This difference can be related with the operating pressure used during the plasma polymerization, 0.1 mbar (**P₂**) instead of 0.05 mbar (**P₃**). This parameter already showed to have influence on the systems long term stability in the case of the systems **UM2eP₂** and **UM2eP₃**. However, both systems have very high performance agreeing with the impedance results of Figure 6.7.

The C_{coat} and R_{por} parameters of the system **45UM2gP₂** for the tests at higher temperature also appear in Figure 6.10. Faster degradation related with the increase of the temperature of testing occurs. The C_{coat} is coincident initially with the value of system **UM2eP₂**, the highest value obtained. During further immersion, the value remains constant, showing a small increase after 60 days of immersion. The R_{por} shows immediately lower value related with the faster degradation processes verified. After 80 days of immersion, the values also suffer accentuated drop attributed to water reaching the metallic substrate and correspondent degradation of the barrier properties.

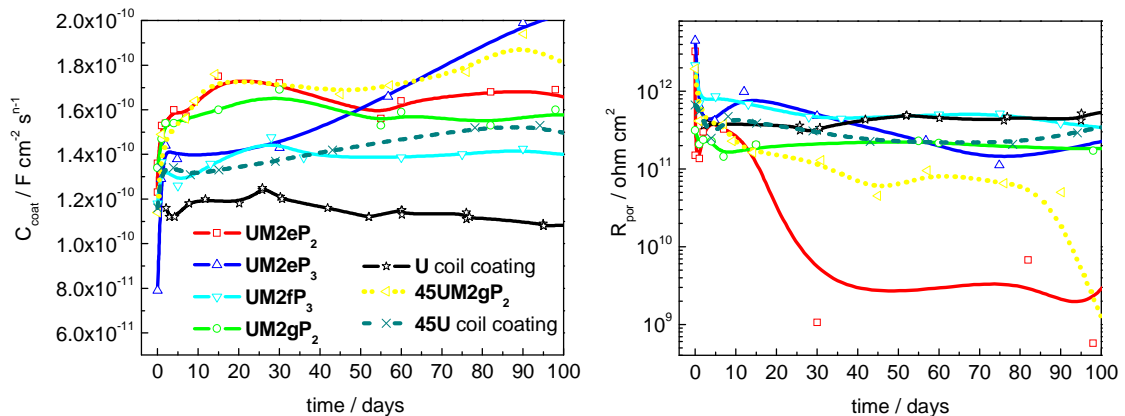


Figure 6.10 Evolution with immersion of C_{coat} and R_{por} parameters for the **M** plasma polymerized **U** systems.

- Water Uptake

The variation of capacitance value at 10 kHz related with the water absorption permits to obtain the water uptake values for the plasma polymerized **U** systems using the relationship of Brasher and Kingsbury.¹²⁸ The estimation uses eq. 3.13 and follows the procedure described in section 3.1.4. The water uptake results appear in Figure 6.11.

Initial fast water uptake appears for all the **M** plasma polymerized systems.^{112;128;129} The highest saturation level appears for the systems **UM2eP₂** and **UM2eP₃**, systems prepared with the oxygen carrier gas. For these two systems, the saturation level continues to rise during immersion.

The system **UM2eP₂** prepared at 0.1 mbar has higher water saturation than the system **UM2eP₃** prepared at 0.05 mbar. However, the increase rate trend is similar in these two systems. The behaviour agrees with impedance data, which indicates that degradation of the systems properties occurs during the plasma polymerization and that the pressure reduction increases the paint system performance.

Replacing the oxygen carrier gas with argon brings changes to the systems water uptake behaviour. The system **UM2fP₃** shows the closest water saturation level to unmodified **U** coil coating, just slightly above, also with similar variation during immersion. The **UM2gP₂** system also shows stable water uptake during immersion, however, with a small increase trend. The saturation level is higher than for **UM2fP₃** system. The increase of the water saturation level and instable behaviour can be related with the higher pressure used during the plasma deposition, since this parameter showed already to be responsible for stronger coil coating degradation during the plasma polymerization process (system **UM2eP₂**).

The results obtained by EIS for the **M** plasma polymerized systems also suggest that a relation between the systems performance and the carrier gas used during the plasma polymerization exists. The two systems prepared with oxygen gas, systems **UM2eP₂** and **UM2eP₃**, have poorer performance during testing than the two systems prepared using argon gas, systems **UM2fP₃** and **UM2gP₂**. These last two systems show virtually no variation of performance during immersion effectively protecting the metallic substrate from corrosion processes. The characterization of the systems helps to understand the degradation mechanism occurring.

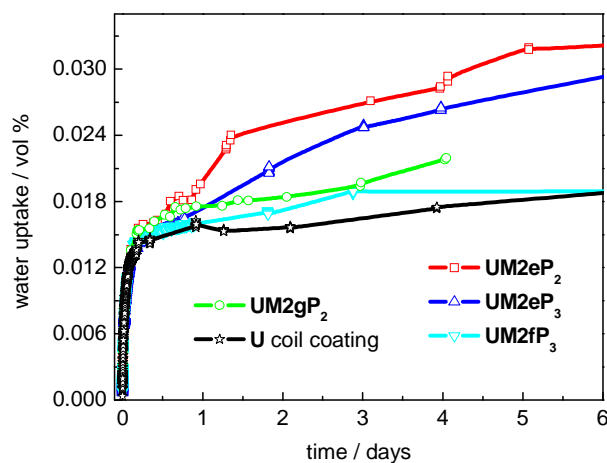


Figure 6.11 Water uptake evolution for the plasma polymerized **U** systems in **M** plasma reactor. Results obtained from the capacitance values at 10 kHz.

ii. Plasma Polymer Films Structure

The plasma polymer films are silicon based layers. The silicon element has enough elemental weight to give contrast when imaged with TEM technique. The procedure described in point 4.2.4 was used for the sample preparation and imaging.

The micrographs of the plasma polymer film are in Figure 6.12. The grey band next to the thin black line represents the plasma polymer film. The black line is a deposited gold layer, used to facilitate the TEM observation.

The structure is dependent of the carrier gas used, oxygen or argon. The plasma polymer films generated using the oxygen carrier gas, systems **UM2eP₂** and **UM2eP₃**, have individualized particles, forming particulate and amorphous structure. Between the particles are visible pathways, which offer direct access to water and ions until the coil coating surface. The plasma polymer films generated using argon carrier gas, systems **UM2fP₃** and **UM2gP₂**, have homogeneous, amorphous and compact structure without any visible pathway in the plasma polymer layer.

X-ray diffraction performed while imaging the samples by TEM show pattern consistent with amorphous structure. Similar result occurs for all the plasma polymer films.

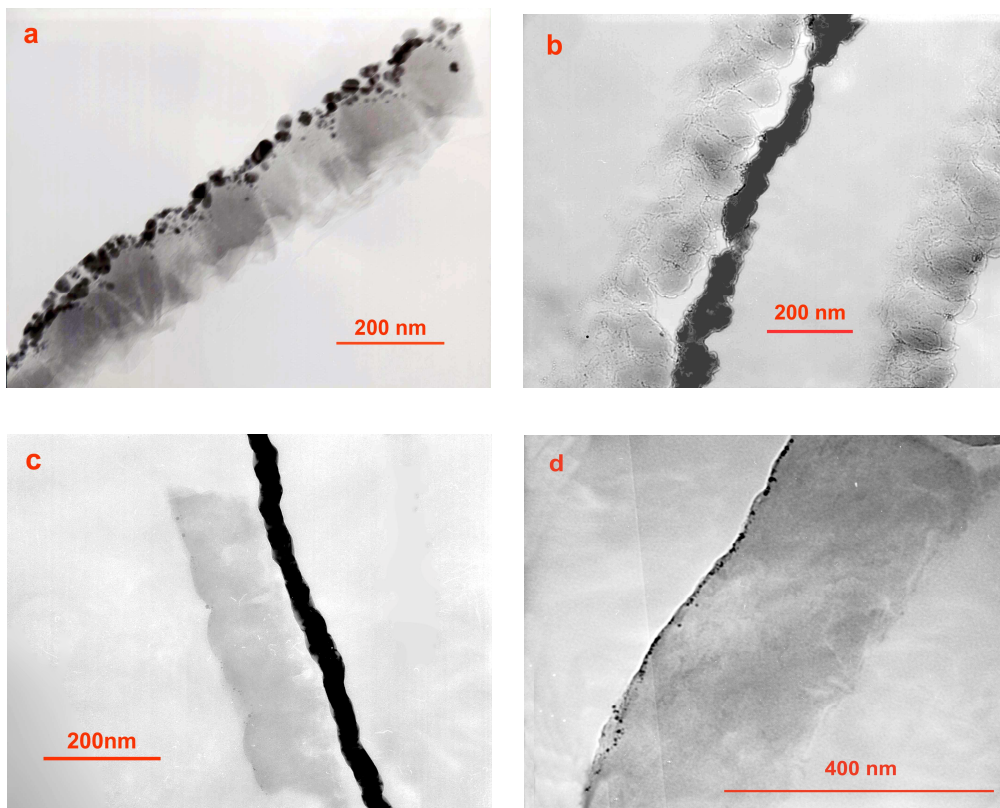


Figure 6.12 TEM micrographs of the plasma polymer films generated using **M** plasma reactor, systems: **a. UM2eP₂**; **b. UM2eP₃**; **c. UM2fP₃**; and **d. UM2gP₂**.

There is also a direct relation between film thickness, the operating pressure and the precursor mixture used. The system **UM2eP₂** shows film thickness of 180 nm, which reduces to 170 nm for the system **UM2eP₃**. This is associated with the decrease of plasma polymerization pressure. The thickness of the system **UM2fP₃**, which was prepared at lower pressure and with argon carrier, is 150 nm. The system **UM2gP₂**, with precursor modification using HFDF monomer, shows an increase of thickness to about 300 nm. For the two systems prepared with argon carrier gas, no particulate structure appears.

iii. Surface Characterization

The surface morphology of the **M** plasma polymerized **U** systems, obtained by AFM technique, appears in Figure 6.13. These images represent the systems' surface morphology after the plasma polymerization process, i.e. the surface morphology of the plasma polymer film before any immersion testing. EDS determined the surface composition of the same systems, the results appear in Figure 6.14. The table has the elements quantification content determined by EDS, values in at. %.

The surface images show that the surface morphology is different for the plasma polymer films, being possible to establish a relation between the surface morphology and the modification to the plasma polymerization conditions. The systems composition is also dependent of the modifications performed to the process of **M** plasma polymerization.

Particulate surface morphology is clearly visible for the system **UM2eP₂**, figure **a**. The particles have 180 nm diameter, which agrees with the size of the particles obtained by TEM structural images. The silicon element content for this system is the highest.

Pressure reduction during the polymerization, system **UM2eP₃** in figure **b**, shows identical particulate surface morphology, but the particle diameter is smaller, near 170 nm, which also agrees with the TEM structural results. The silicon element content shows a significant decrease while fluorine element proportion presents a small increase. The pressure reduction occurs associated with the decrease of the amount of precursor monomer feed into the reactor, as described in point 4.1.2.i, what explains the silicon content decrease with decrease of pressure.

Replacing oxygen carrier by argon, system **UM2fP₃** on figure **c**, still shows similar particulate surface morphology. The structure images by TEM of this system did not show individualized particles, but the surface morphology shows that they are present and have 150 nm diameter. The silicon proportion has a slight increase relatively to previous system and the fluorine element shows stronger increase.

The surface particles have relation with the thickness found for the plasma polymer films on the TEM micrographs. In these three systems, the fluorine element comes only from the **U** coil coating, since the monomer used has no fluorine in its composition. The increase of fluorine content noticed can be related with the decrease of thickness, from 180 to 170 and finally to 150 nm. The silicon based plasma polymer film mask this element and the thinner

the film formed the higher the amount of fluorine signal, obtained from the underneath **U** coil coating.

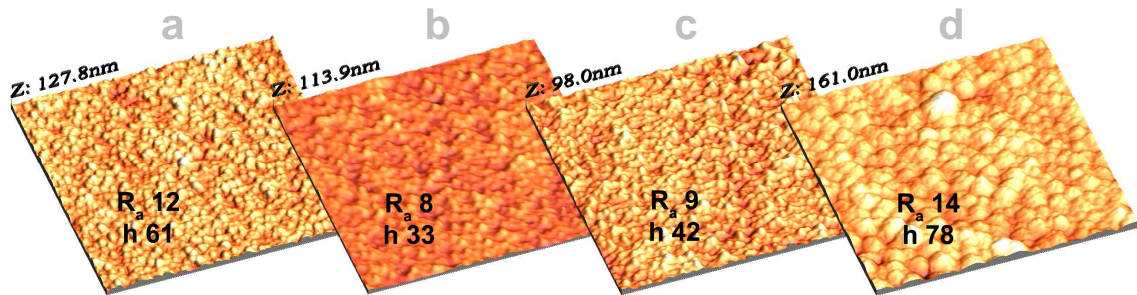
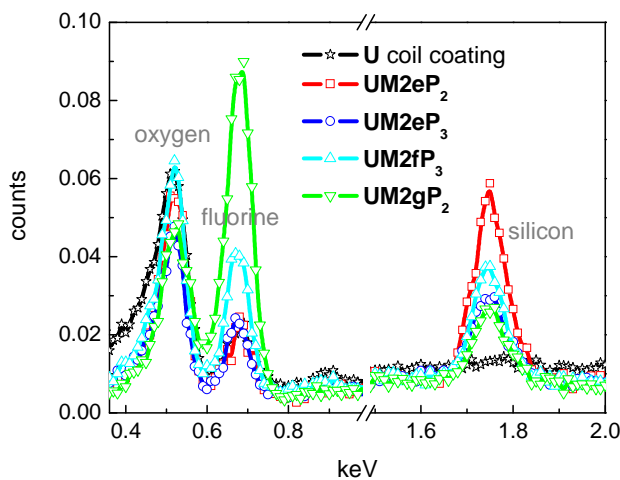


Figure 6.13 Surface morphology 4x4 μm images of the plasma polymer layers generated using the **U** coil coating obtained by AFM technique. The values in nm of R_a and h also appear in the images, systems: **a.** UM2eP_2 ; **b.** UM2eP_3 ; **c.** UM2fP_3 ; and **d.** UM2gP_2 .

The addition of HDFD monomer, system UM2gP_2 figure **d**, formed compact plasma polymer film. The surface morphology continues to be particulate. The image suggests that the particles are not individualized but agglomerated. The agglomerates diameter, around 370 nm, agrees with the plasma polymer layer thickness verified by TEM. The precursor mixture used has fluorine in its composition, which is immediately shown on EDS spectra, where strong increase of this element content appears. The silicon proportion is similar to previous systems.



element content		
system	fluorine	silicon
UM2eP_2	38	3.3
UM2eP_3	46	0.8
UM2fP_3	52	1.0
UM2gP_2	75	1.0
U	56	-

Figure 6.14 Composition of the **M** plasma polymerized **U** systems with quantification of the fluorine and silicon elements, values in at. %.

- Surface Morphology and Composition Evolution

The surface morphology evolution during immersion of the plasma polymer films obtained by AFM measurements appears in Figure 6.15, shown in page 128. These images show the systems surfaces after submitted to the immersion tests. The labels on top of each image represent the duration of immersion tests until the AFM measurement. The surface composition, collected by EDS for the plasma polymerized systems submitted to immersion, permits to know the systems composition evolution during immersion. The quantification of fluorine and silicon elements appears in the Table 6.1.

Of particular interest is the silicon content, which is the representative element of the plasma polymer layer. The fluorine element also has importance, since appears masked by the silicon based plasma polymer layer, meaning that an increase of fluorine element represents dissolution of the plasma polymer layer with decrease of the masking effect.

For the system **UM2eP₂**, variation of the surface morphology and elemental composition occurs during immersion. After *1 day* of immersion, decrease to half the initial content of the silicon element occurs. The surface morphology after *2 days* of immersion also changes and shows semi dissolved particulate surface morphology, AFM image **a**. The R_a and h values show variation as result of the surface morphology modification. New surface morphology appears again after *7 days* of immersion. The R_a and h values agree showing new variation of the values. The EDS results after the same immersion period show only vestigial silicon content. This suggests that complete removal of the plasma polymer layer occurs, leaving the activated coil coating surface exposed. Further immersion leads to a new surface morphology variation and after *60 days* of immersion the R_a and h values change once more. This new variation corresponds to further coil coating surface degradation during immersion. The R_{por} evolution of Figure 6.10 shows that higher degradation starts after *15 days* of immersion, which relates with the noticed dissolution of the plasma polymer film.

Reduction of the pressure to 0.05 mbar, system **UM2eP₃** in AFM figure **b**, also shows modification of surface morphology during the immersion tests. In this case, after *7 days* of immersion the particulate surface morphology is still present. The silicon element content decrease suggests, however, that some changes in composition already occurred. Further immersion, until *30* and *60 days* of immersion, shows that the particulate surface morphology is disappearing. The silicon element proportion decreases until vestigial values. In this case, negative R_{sk} values are obtained after *30* and *60 days* of immersion. These results suggest again removal of the plasma polymer film. The negative R_{sk} values are attributed to the reappearing of the plasma activated surface due to dissolution of the plasma polymer film (after the plasma activation step negative R_{sk} values are also obtained, Figure 6.5). This represents surface morphology with pores. The R_{por} evolution of Figure 6.10, in his case, presents slow but continuous decrease because of the dissolution of the plasma polymer film.

Replacement of oxygen carrier gas by argon gas, system **UM2fP₃** in AFM image **c**, shows stable surface morphology during immersion. In this case, even after *60 days* of

immersion, particulate surface morphology still appears with small variation of the R_a and h values, corroborating the system stability. The silicon and fluorine content stability validates these findings.

The system **UM2gP₂**, prepared with addition of HDFD monomer to the precursor mixture, also preserves the surface morphology during immersion, AFM Figure 6.15d. In this case, both silicon and fluorine elements are representative elements of the plasma polymer film, since HDFD has fluorine element in its composition. Both maintain constant proportion during immersion, corroborating the system stability. Particulate surface morphology continues to be present after 140 days of immersion.

The surface results suggest that a relation with the carrier gas used for the plasma polymerization process exists. The systems **UM2eP₂** and **UM2eP₃** results show strong signs of degradation, even suggesting complete dissolution of the plasma polymer layer during testing. The other two, systems **UM2fP₃** and **UM2gP₂**, are much more stable during immersion tests, which suggest higher performance against the testing environment and long term protection.

These results agree with the impedance data, where higher and faster degradation during immersion occurred for the plasma polymerized systems using oxygen carrier gas, systems **UM2eP₂** and **UM2eP₃**. The systems prepared with argon carrier, systems **UM2fP₃** and **UM2gP₂**, maintain high performance during immersion.

Table 6.1 Composition evolution during immersion tests for fluorine and silicon elements of the **M** plasma polymerized **U** systems, values in at. %.

time (days)	UM2eP₂		UM2eP₃		UM2fP₃		UM2gP₂	
	fluorine	silicon	fluorine	silicon	fluorine	silicon	fluorine	silicon
0	38	3.3	46	0.8	52	1.0	75	1.0
1	40	1.8	--	--	--	--	82	0.8
7	61	0.2	38	0.1	39	1.2	74	0.9
30	48	0.2	47	0.09	41	1.2	79	0.8

iv. Optical Properties

The CIE (x,y) surface reflection colour coordinates were obtained for the plasma polymerized **U** systems, using the procedure described in point 4.2.6. The results are presented in the CIE chromaticity diagrams (1931) for 2^o standard observer. The colour coordinates evolution during immersion tests, obtained performing measurements after different immersion periods, appear in Figure 6.16 and in Figure 6.17.

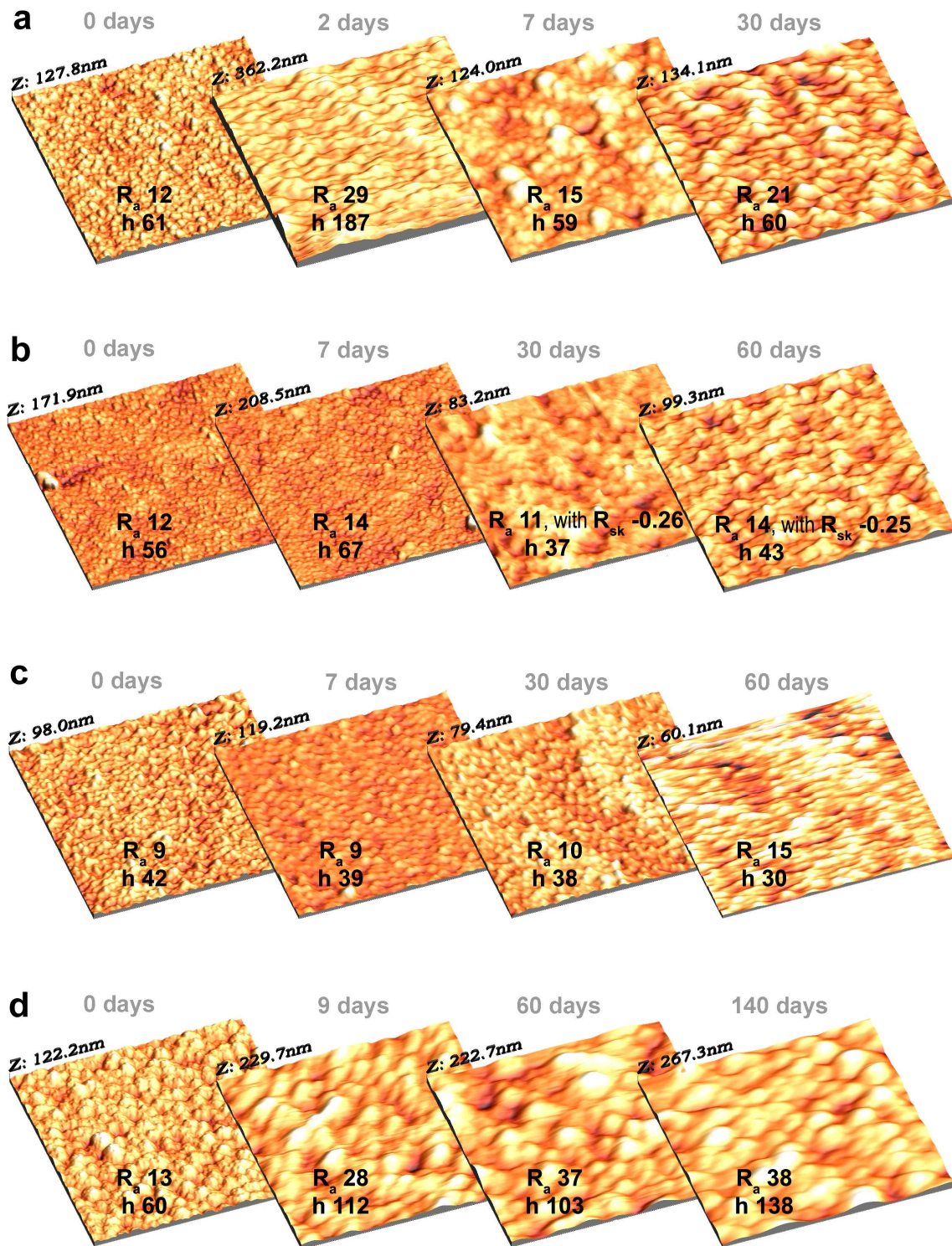


Figure 6.15 AFM $4 \times 4 \mu\text{m}$ images with the surface morphology evolution during immersion, systems: **a.** UM2eP_2 ; **b.** UM2eP_3 ; **c.** UM2fP_3 ; and **d.** UM2gP_2 . The R_a and h values in nm are in the correspondent image.

The CIE (x,y) colour coordinates for the unmodified **U** coil coating is also plotted for reference purposes. The colour coordinates for the unmodified **U** coil coating appears in the centre of the CIE lab 1931 diagram, the white area, showing no variation during immersion.

The stability of the reflection colour coordinates depends of the plasma polymerization conditions. The oxygen carrier gas generates the systems with the highest variation of surface colour. From the system **UM2eP₂** to **UM2eP₃**, pressure reduction, positive effect to the surface colour stability occurs. This is shown on the diagrams **a** and **b** of Figure 6.16, respectively for the two systems.

The system **UM2eP₂**, diagram **a** of Figure 6.16, shows fast and stronger variation of the colour coordinates. Initially, they appear in the orange part of the diagram, but after two days of immersion shift to the blue-green part. Increase of immersion time takes the colour to the yellow part, until strong shift to the blue part of the diagram occurs after 50 days of immersion. Longer immersion leads the colour coordinates further to the blue part.

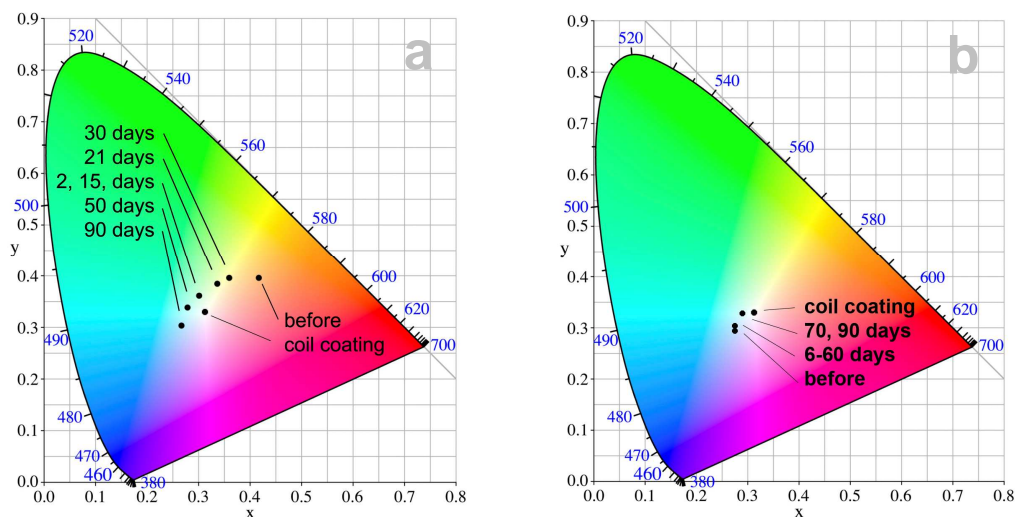


Figure 6.16 CIE chromaticity diagram (1931) coordinates for 2° standard observer showing the evolution during immersion of the (x,y) reflection colour coordinates for the **M** plasma polymerized **U** systems: **a. UM2eP₂**; and **b. UM2eP₃**. Unmodified **U** coil coating is plotted for reference.

The initial colour coordinates for the system **UM2eP₃**, diagram **b** of Figure 6.16, appear in the blue part of the diagram. During immersion, small shift occurs to lighter blue part. After 70 days of immersion, significant variation of colour coordinate occurred, approaching the unmodified **U** coil coating colour coordinate.

The system **UM2fP₃**, diagram **a** of Figure 6.17, shows a mixed behaviour of colour coordinates evolution. The initial colour coordinates appear in the orange zone of the diagram, which is similar to the system **UM2eP₂**. Immersion tests lead to a shift to the white area of the diagram, which is similar to the system **UM2eP₃**. After this initial shift, occurring after 7 days of immersion, the colour coordinates are stable during further immersion.

The colour coordinates for the system **UM2gP₂** show the most stable behaviour, diagram **b** of Figure 6.17. Initial colour coordinates appear in the green zone, which is maintained constant during further immersion.

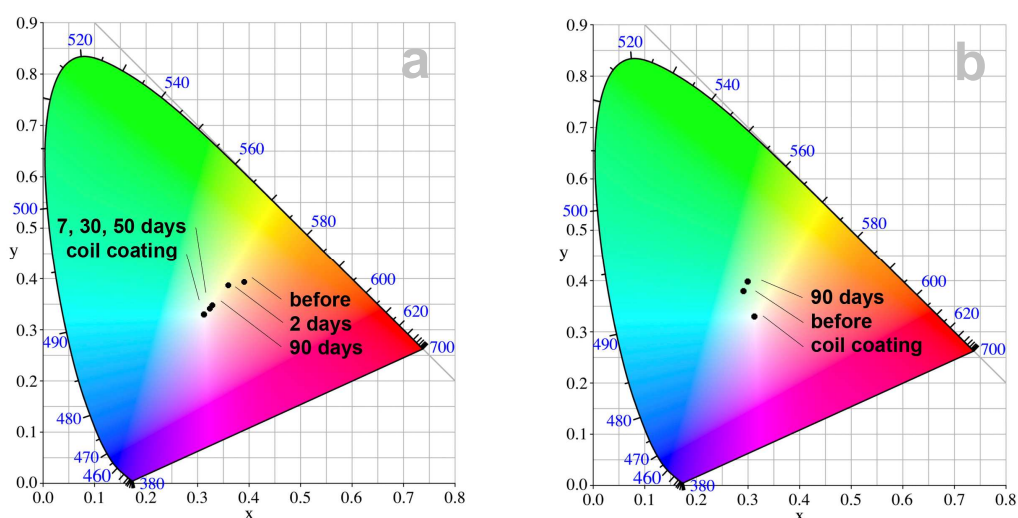


Figure 6.17 CIE chromaticity diagram (1931) coordinates for 2° standard observer showing the evolution during immersion of the (x,y) reflection colour coordinates for the **M** plasma polymerized **U** systems: **a. UM2fP₃**; and **b. UM2gP₂**. Unmodified **U** coil coating is plotted for reference.

The evolution of the reflection spectra of the systems prepared by plasma polymerization, used for colour coordinates calculation, are in Figure 6.18. There are some differences between the systems related with the plasma polymerization conditions.

The two systems **UM2eP₂** and **UM2eP₃** have similar reflection spectra, higher reflection at low wavelengths and absorption for high wavelength, spectra **a** and **b**. The pressure reduction leads to a shift of the reflection peak to lower wavelength.

Replacing oxygen carrier by argon, system **UM2fP₃** in spectrum **c**, brings bigger variation to the reflection spectrum. Here, at low wavelengths, the absorption is higher but after the 540 nm mark, the reflection appears constant.

The addition of HDFD monomer, system **UM2fP₂** in spectrum **d**, shows again different reflection spectra. The spectra show one central peak appearing with maximum near the 540 nm and two minimum at 460 and 650 nm. Two more peaks are noticed, one at lower wavelength and the other at higher. Their maxima are in the limit of the measured wavelength range, making it impossible to obtain their values.

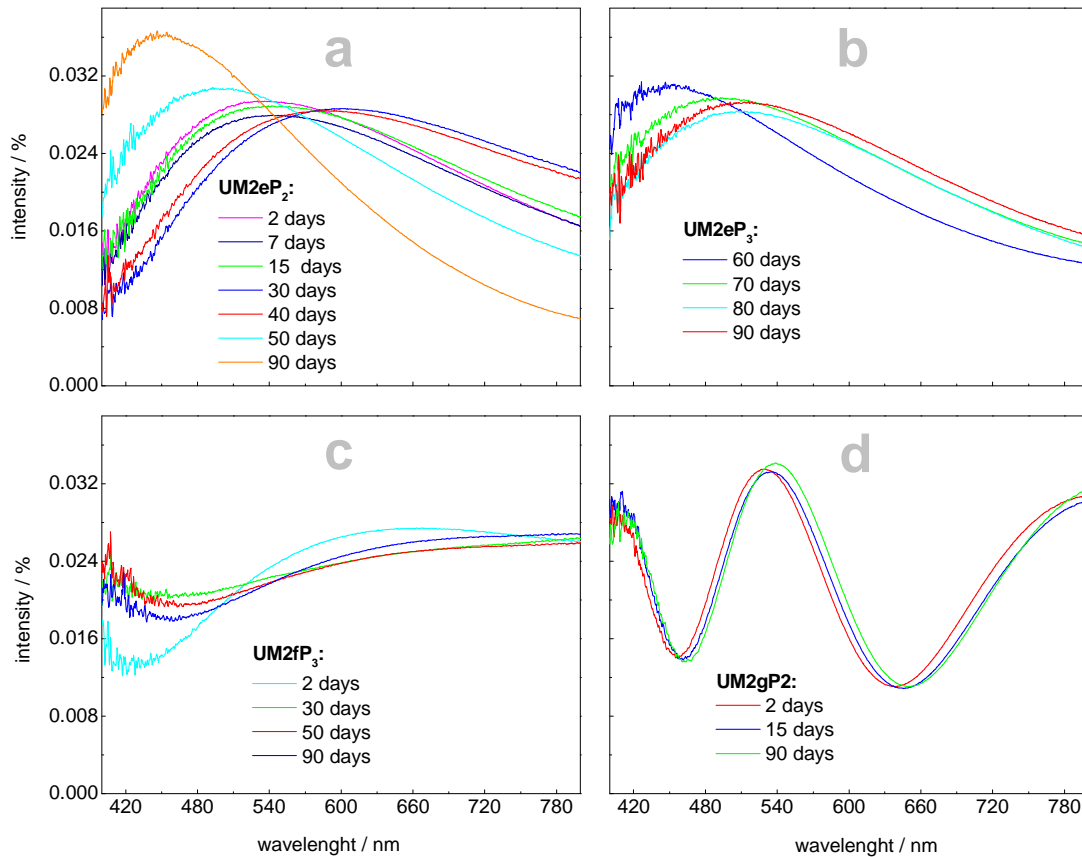


Figure 6.18 Evolution with immersion of reflectance spectra for the **M** plasma polymerized **U** systems: **a. UM2eP₂**; **b. UM2eP₃**; **c. UM2fP₃**; and **d. UM2gP₂**.

6.3. Radio Frequency Plasma Reactor

The radio frequency plasma reactor provides continuous deposition and, depending on the geometry arrangement, avoids parasitic deposition on the chamber walls.¹⁸⁶

Description of the plasma polymerization conditions used in this reactor is given in point 4.1.2.ii. The respective labels, attributed to each system prepared, appear in Table 4.7. For

easier presentation of the results and study the influence of the plasma polymerization conditions on the coil coating properties, the results for each stage appear in different sections.

Point 6.3.1 studies only the plasma activation step, where special attention is given to the coil coating barrier properties degradation. The step occurs with the coil coating surface directly exposed to the plasma activation conditions and degradation may occur. The coil coating barrier properties and their variation due to the plasma activation conditions are the properties analysed.

Then, appears the study of the systems submitted to the plasma polymerization using stages **3** and **4**. The EIS results appear in point 6.3.2 and 6.3.3, respectively for each stage. In point 6.3.4 is the characterization tests, which appear together for the two stages for easier comparison. Its content refers to the analysis of the systems barrier properties, the structure of the plasma polymer film, the surface morphology, the composition and the results of the surface colour reflection.

6.3.1. Plasma Activation Stage

The plasma activation step with oxygen gas, using the conditions described in Table 4.6, consists in cleaning the surface of the coil coating to obtain adhesion enhancement between the coil coating and the plasma polymer film, generated in the second step. Formation of C-O bonds on the surface occurs during the step, as described in point 2.6.5.^{46;168} The labels attributed to each prepared system appear in Table 4.7.

i. EIS Results

The impedance results, of the plasma activated **U** and **E** systems, obtained by the EIS technique, permit to verify the influence of the plasma activation step on the coil coating barrier properties. The specimens were placed either in **P** or **G** electrodes of the reactor.

Figure 6.19 shows the Bode plots with the impedance evolution during immersion in 0.5 M NaCl solution for the plasma activated **U** systems, using the two electrodes locations in the **R** plasma reactor. Two testing temperatures were used. Bode plots **a** present the results for testing at ambient temperature and Bode plots **b** the results for testing at 45° C.

The impedance values after immersion (1 hour) are identical. Capacitive behaviour for the full frequency range tested appears, with impedance values at low frequency higher than 100 Gohm cm². This represents coating systems with high performance,^{112;113;125} similar to the unmodified **U** coil coating, shown in Figure 5.1.

Further immersion at ambient temperature, Bode plots **a**, shows the formation of a resistive part at low frequencies, easier to see in phase angle plot. This behaviour

suggests water and ions absorption by the system. After 20 days of immersion, the resistive part is visible for system **UR1hP₄G**. After 140 days (near 5 months) of immersion, stronger decrease occurs for this same system. At this time, the low frequency impedance shows near one order of magnitude decrease to 20 Gohm cm².

The system **UR1hP₄P** also has low frequency impedance decrease, but the formation of the resistive part takes longer immersion time. In this case, the degradation is slower and only after 150 days of immersion is the value similar to the system **UR1hP₄G** after only 20 days, just under 100 Gohm cm². Impedance values of this magnitude represent coating systems that still offer excellent barrier properties. ^{112;113;125}

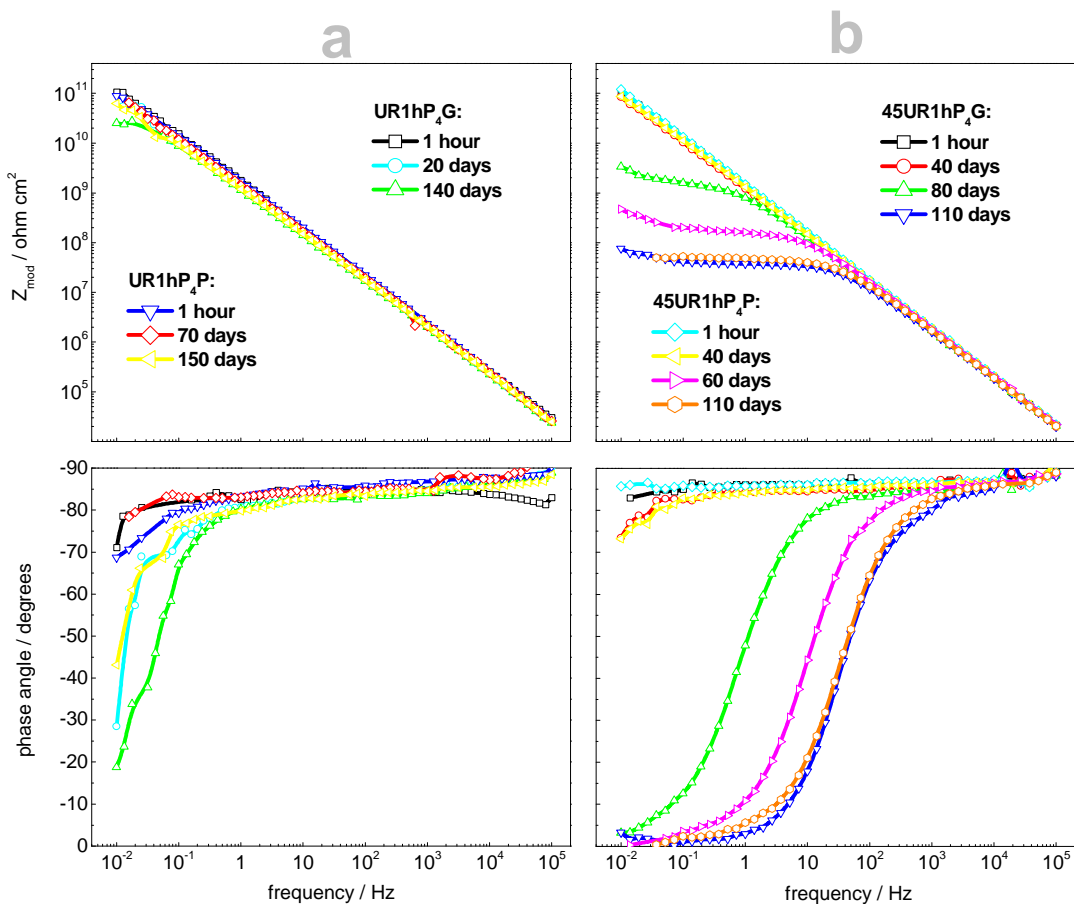


Figure 6.19 Impedance evolution during immersion for the **U** coil coating plasma activated in the **R** plasma reactor: **a.** ambient temperature, systems **UR1hP₄G** and **UR1hP₄P**; and **b.** 45° C temperature, systems **45UR1hP₄G** and **45UR1hP₄P**.

Testing of the **R** plasma activated systems at higher temperature appears in Bode plots **b** of Figure 6.19. The tests at higher temperature accelerate the systems evolution gathering

more information about the degradation process.^{173;174} The influence of the different testing conditions is visible in the impedance response.

At higher temperature, the low frequency resistive part after 40 days in both systems is still almost invisible. The low frequency impedance is still at 100 Gohm.cm². Strong decrease of performance occurs after 60 days for the system **45UR1hP₄P**, associated with low frequency impedance value of 800 Mohm cm². The system **45UR1hP₄G** also shows strong degradation after 80 days but with higher impedance value at low frequency, 6 Gohm cm². The low frequency impedance value is still relatively high but the format of the phase angle spectra suggests that water and ions is in contact with the metallic substrate.

After 110 days of immersion, both systems have coincident low frequency impedance value, with three orders of magnitude decrease to 100 Mohm cm². This represents similar degree of degradation. For longer time of immersion, further degradation of the coated systems is expected.^{112;113;125}

Thus, the higher temperature tests showed faster degradation occurred, as expected and better differentiation among the systems evolution with time.

The impedance results for the **E** coil coating submitted to the plasma activation stage, using the **R** plasma reactor, appear in Figure 6.20 as Bode plots and in Figure 6.21 as Nyquist plots. The results refer to the two electrode locations of the **R** plasma reactor, systems **ER1hP₄G** and **ER1hP₄P**, prepared with similar conditions. The Nyquist plot representation is presented because in this case the evolution is easier to see with this representation.

For the initial immersion (1 hour), the plasma activated **E** systems have low frequency impedance value higher than 10 Gohm cm², but already showing the low frequency resistive part. This represents high performance systems but already showing some degradation.^{112;113;125} This impedance value is similar to the value obtained for unmodified **E** coil coating, shown in Figure 5.2.

During immersion, the systems have decrease of low frequency impedance value, similar to the unmodified **E** coil coating. This evolution appears dependent of the electrode used.

The system **ER1hP₄P**, plots **b**, has a decrease of the low frequency impedance smaller than unmodified **E** coil coating, reaching 3 Gohm cm² after 200 days of immersion, one order of magnitude decrease. The system **ER1hP₄G**, plots **a**, on the other hand, shows much faster degradation and after 12 days of immersion, already shows similar low frequency impedance value to system **ER1hP₄P** after the 200 days of immersion, 3 Gohm cm². After 17 days, the decrease is more accentuated and the low frequency reaches 1 Gohm cm².

After the 17 days of immersion, in the Nyquist plot of Figure 6.21, formation of a quasi-complete semi-circle appears for the system **ER1hP₄G**, which reinforces that water and ions have direct contact with the metallic substrate. The unmodified **E** coil coating also forms quasi-complete semi circle, but took 130 days of immersion testing to form it, Nyquist plot of Figure 5.2.^{112;113;125}

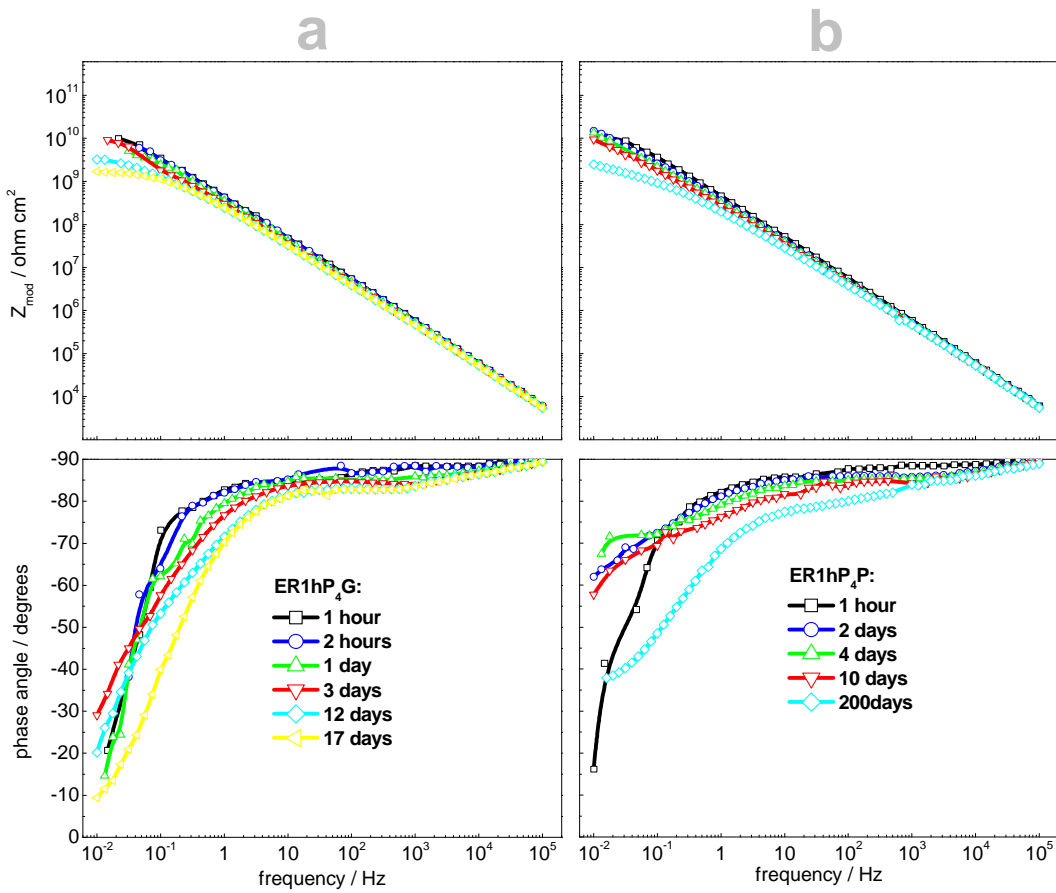


Figure 6.20 Bode plots with the impedance evolution during immersion tests at ambient temperature of plasma activated E systems in R plasma reactor, systems: **a. ER1hP₄G**; and **b. ER1hP₄P**.

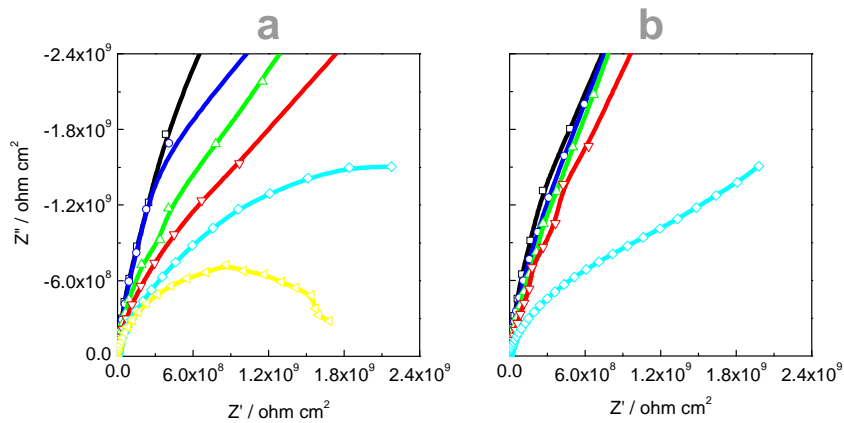


Figure 6.21 Nyquist plots with the impedance evolution during immersion tests at ambient temperature of E coil coating plasma activated in R plasma reactor: **a. ER1hP₄G**; and **b. ER1hP₄P** systems. Legend colours are similar to Bode plots of Figure 6.20.

- Numerical Fitting of EIS Data

The numerical fitted values offer quantitative information about the systems evolution during immersion. The results obtained reflect the behaviour of the plasma activated systems during immersion and are related with the degradation processes occurring in the systems.^{32;39;40}

The estimated parameters C_{coat} and R_{por} , obtained for the plasma activated **U** and **E** systems, appear in the Figure 6.22. The plasma activated **E** systems show two time constants, similar to unmodified **E** coil coating. This process appears at high frequencies and corresponds to detours from ideal behaviour during the measurements.^{131;177-182} In this case, the **b** equivalent circuit of Figure 5.3 is used. Further description of the procedure appears in point 5.2.1. For plasma activated **U** systems equivalent circuit **a**, in the same figure, is used, correspondent to the only process occurring.

Figure 6.22a shows that the systems **45UR1hP₄G** and **45UR1hP₄P**, tested at higher temperature, have higher C_{coat} parameter, since the increase of testing temperature increases the speed of the absorption process. The values have a continuous increase trend during immersion. These values are lower than for the plasma activated **E** systems, Figure 6.22b. The systems **UR1hP₄G** and **UR1hP₄P**, tested at ambient temperature, have the lowest values (although higher than unmodified **U** coil coating), with similar variation to unmodified **U** coil coating until 60 days of immersion. After that period, both start to show similar increase trend of the C_{coat} values of the systems tested at higher temperature.

The C_{coat} values of the system **UR1hP₄P** are the second lowest, only **U** coil coating shows lower values. The system **45UR1hP₄P** has practically identical evolution to the **45U** coil coating. For both testing temperatures, higher C_{coat} values appear for the plasma activation performed in the **G** electrode, systems **UR1hP₄G** and **45UR1hP₄G** than for the systems at **P** electrode. This suggests higher influence of the plasma activation stage performed in **G** electrode.

The R_{por} values for the plasma activated **U** systems, Figure 6.22c, are initially identical for both testing temperatures, except the system **UR1hP₄G**, which has R_{por} value identical to the value of **45U** coil coating. The plasma activated **U** systems tested at 45° C have a drop of R_{por} values after 40 days of immersion. The drop relates with the verified degradation of the barrier properties and is similar for both systems **45UR1hP₄G** and **45UR1hP₄P**. From this point, with further immersion, they show very strong decrease. After 60 days of immersion for the systems **45UR1hP₄G** and 80 days for the system **45UR1hP₄P**, four orders of magnitude decrease occur.

For the plasma activated **E** systems, both plasma activation locations have strong initial increase of C_{coat} during immersion but the values are lower than for the unmodified **E** coil coating, Figure 6.22b. During immersion, the values continue to increase, but remain always lower than for the unmodified **E** coil coating. Initially **ER1hP₄G** system has higher instability initially, but during immersion, the value is lower than for the system **ER1hP₄P**.

The R_{por} values for the plasma activated **E** systems appear in Figure 6.22d. The values are near one order of magnitude lower than for plasma activate **U** systems, similar to unmodified coil coatings shown in Figure 5.5. The values are also dependent of the reactor location for the plasma activation. Plasma activation performed in the **P** electrode, system **ER1hP₄P**, has similar R_{por} values to unmodified **E** coil coating, but with higher initial instability. The system activated using the **G** electrode, system **ER1hP₄G**, shows R_{por} values one more order of magnitude lower, associated with continues decrease during immersion. This represents, in principle, poorer performance after the plasma activation using the **G** electrode location.

The plasma polymerized **E** systems have lower C_{coat} parameter that is attributed to slower water absorption rate than for the unmodified **E** coil coating, suggesting that the degradation during immersion is smaller. However, the R_{por} evolution suggests better performance for the unmodified **E** coil coating, which is backed up by the impedance results.^{32;39;40} These two parameters show inverse results. This was already noticed after the plasma activation (stage 1) of the **U** coil coating, point 6.2.1.i, and was attributed to the surface modification of the coil coating. Similar process must occur here.

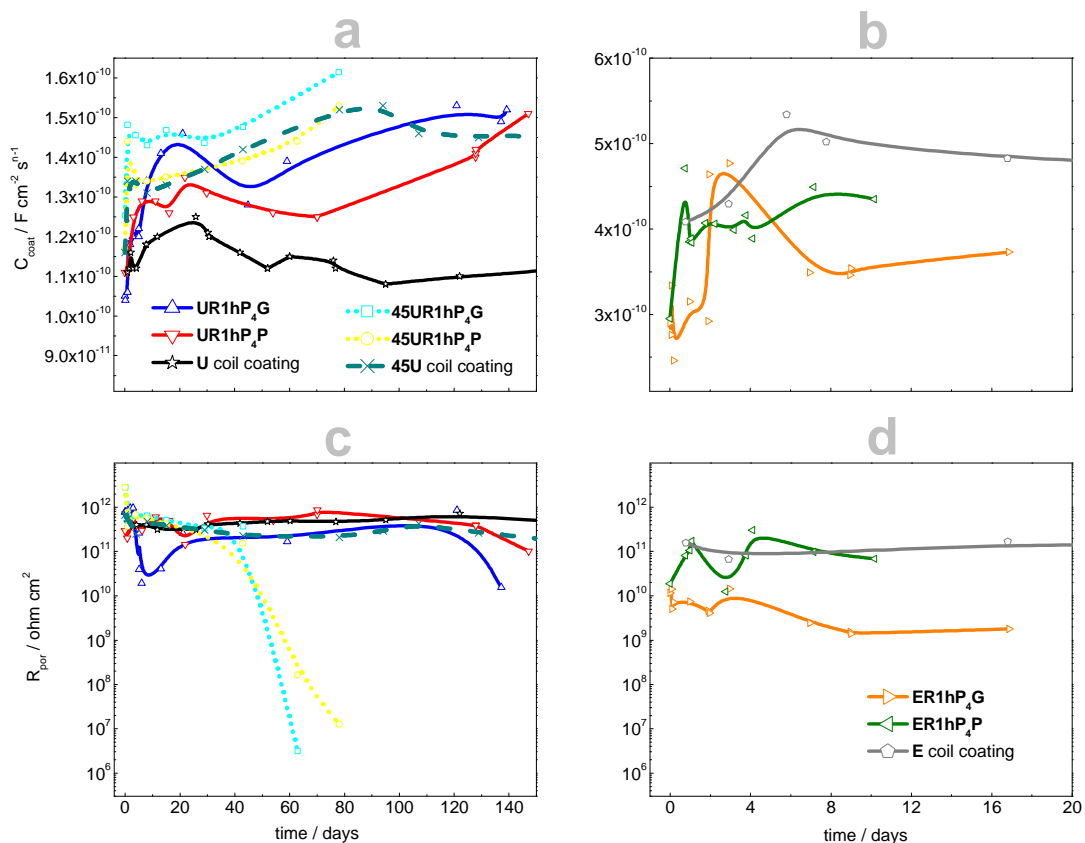


Figure 6.22 Evolution of: **a.**, **b.** C_{coat} ; and **c.**, **d.** R_{por} parameters for the plasma activated **U** and **E** systems, prepared using the two electrode locations. The C_{coat} graphs have different scale adapted to the different magnitude of the results.

- Water Uptake Estimation

The value of the capacitance of the coating systems permits to estimate the water uptake rate using the empirical relation of Brasher and Kingsbury.¹²⁸ The calculations of the water uptake use eq. 3.13, following the procedure described in section 3.1.4. The water uptake plots, for plasma activated **U** and **E** systems using the **R** plasma reactor, are in Figure 6.23, where the unmodified systems also appear for reference.

All the systems, unmodified coil coatings and plasma activated, have similar very fast water uptake for initial immersion periods. This is characteristic behaviour of the organic coatings.^{112;128;129} The water saturation level reached is, however, dependent of the coil coating used. The plasma activated **U** systems show about half water saturation level compared with plasma activated **E** systems. The saturation level also shows differences associated with the electrode used in the **R** plasma reactor.

For the plasma activated **U** systems, slightly higher saturation level than **U** coil coating is verified, being the **UR1hP₄P** the system with the highest saturation level. During immersion, the saturation levels remain stable at that value.

The plasma activated **E** systems water uptake presents continuous increase trend. The absorption rate decreases after 3 to 4 days of immersion, when they reach the water saturation plateau. This saturation level is just above for **ER1hP₄G** system, and slightly lower for **ER1hP₄P** system, when compared with the unmodified **E** coil coating.

The higher amount of absorbed water suggests higher degree of degradation, since for starting of corrosion processes water is necessary at the metal coating interface.^{112;128;129}

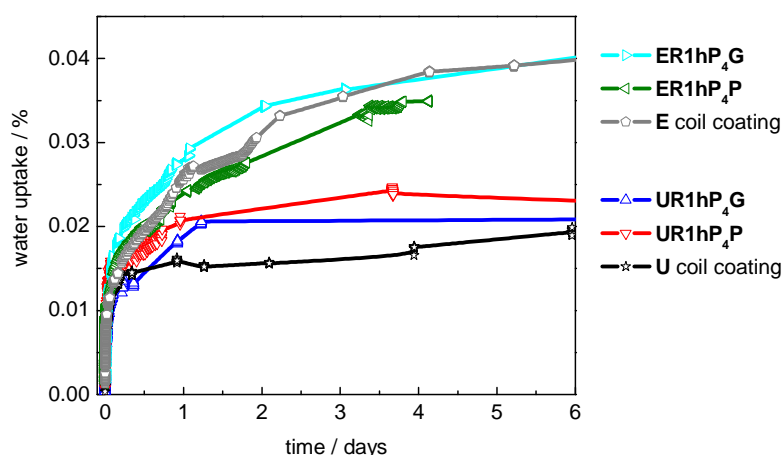


Figure 6.23 Water uptake plot for the plasma activated **E** and **U** systems, prepared using the **R** plasma reactor.

The plasma activation stage performed in the **P** electrode of the **R** plasma reactor using **E** systems shows improvement of the systems barrier properties. On the other hand, similar procedure but using **G** electrode shows faster degradation. When the **U** system is used, both electrodes lead to degradation of the barrier properties.

These results presented suggest that higher influence during the plasma activation step on the coil coating barrier properties occurs in the **G** electrode location. The surface characterization helps to understand the degradation process.

ii. Surface Characterization

The plasma activation stage introduces variation on the surface morphology of the coil coating. AFM was used to study the surface variation for the plasma activated **U** systems while SEM was used for the plasma activated **E** systems. The use of these techniques permits to observe the different features, as done in point 5.3 for the unmodified coil coatings.

The surface morphology results of Figure 6.24, for the **U** coil coating submitted to the plasma activation stage in the **R** plasma reactor, have the R_a and h parameters obtained from the AFM images, calculated using the procedure indicated in point 4.2.5. EDS permits to obtain the surface composition for the same systems. Quantification of the elements content is in the Figure 6.25, with the values in at. %.

The images present similar surface morphology after the plasma activation step performed in the two electrode locations of the **R** plasma reactor, but different from the unmodified **U** coil coating of Figure 5.7. The R_a and h values corroborate the surface variation, showing negative R_{sk} values. These negative values suggest the formation of surface pores due to the conditions used during the plasma activation step. The surface variation is a little higher in the **G** electrode location.

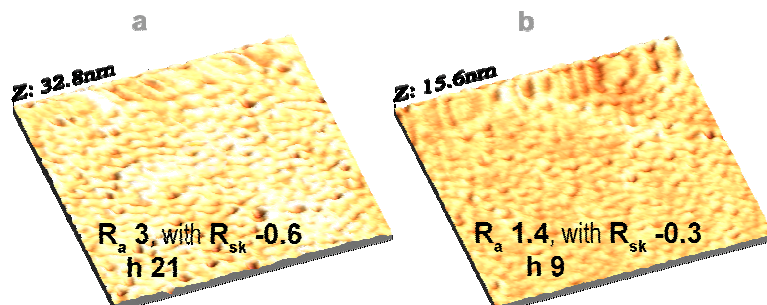


Figure 6.24 Surface morphology AFM 1x1 μm images for the plasma activated **U** systems using **R** plasma reactor, systems: **a. UR1hP4P**; and **b. UR1hP4G**. The values in nm of R_a and h appear in the respective image.

The surface composition, EDS spectra of Figure 6.25, shows the presence of fluorine and chlorine elements. The elements content variation after the plasma activation step is dependent of the reactor electrode location, using as reference the content values of the unmodified **U** coil coating of point 5.3.

For the system **UR1hP₄P** a decrease of fluorine and chlorine elements proportion occurs, while for the system **UR1hP₄G** only the chlorine element content changes. These variations suggest that the influence on the system **UR1hP₄P** is stronger. However, the EDS technique degree of uncertainty is relatively high, especially for low elemental weight elements like fluorine, and the variation of content verified is low.

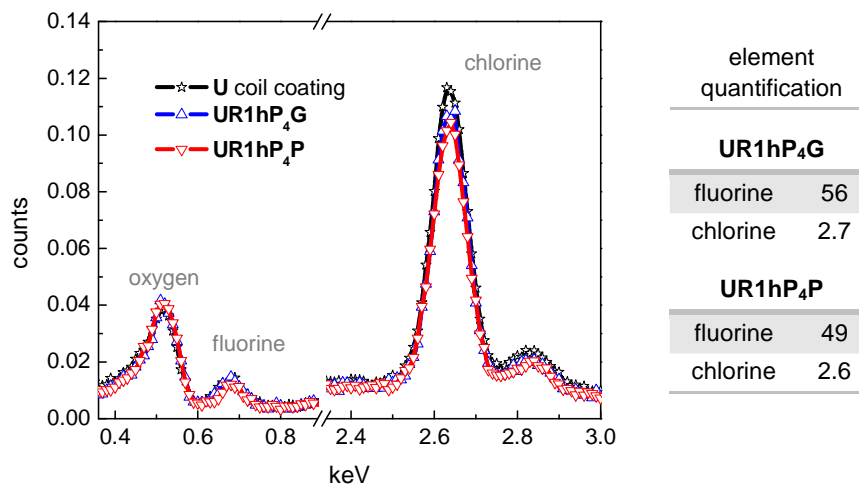


Figure 6.25 Composition and element content quantification of **U** coil coating after the plasma activation step, quantification values in at.%.

The SEM micrographs of Figure 6.26 show the respective surface morphology, for the systems **ER1hP₄G** and **ER1hP₄P** before testing. The surface composition obtained with EDS for the same systems appears in Figure 6.27. The quantification of the elements content appears in the table of the same figure, values in at. %.

In both micrographs appear small pores in the surface. These ones result from the influence of the plasma activation stage. Surface pores also are visible for the plasma activated **U** systems (negative R_{sk}). The titanium based particles continue to appear in both systems, circles with 300 nm diameter, showing no variation compared with unmodified **E** coil coating.

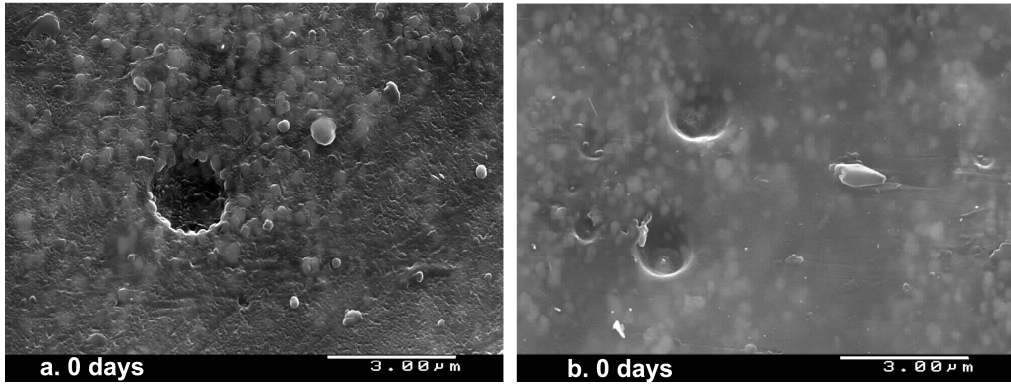


Figure 6.26 Surface morphology SEM micrographs for the plasma activated **E** systems using **R** plasma reactor, systems: **a. ER1hP₄P**; and **b. ER1hP₄G**.

The EDS spectrum of Figure 6.27 for the plasma activated **E** systems shows the presence of oxygen, aluminium, silicon and titanium elements. The elements proportion remains almost constant, compared with the composition of the unmodified **E** coil coating shown in Figure 5.9. Between the two systems **ER1hP₄G** and **ER1hP₄P**, no significant variation of elements content is also noticed.

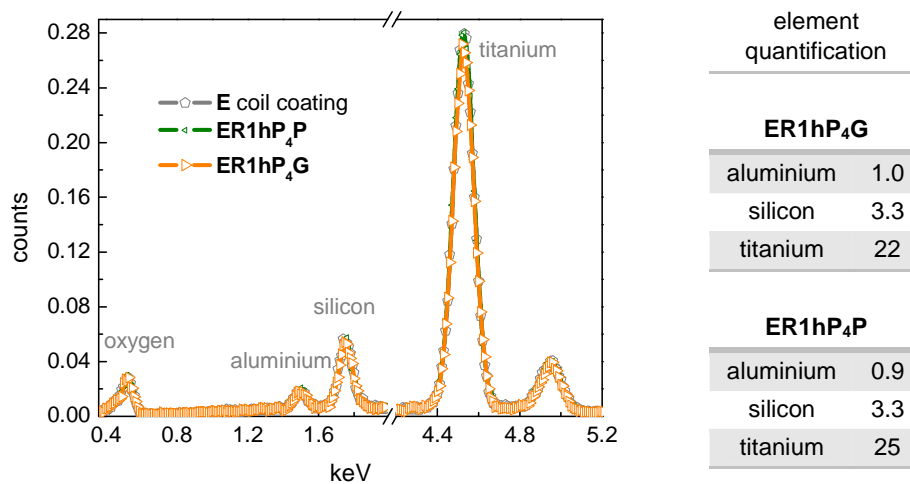


Figure 6.27 Composition and element content quantification of the plasma activated **E** systems using the **R** plasma reactor, quantification values in at. %.

- Evolution of the Surface Properties

The influence of the step of plasma activation on the systems stability during immersion tests using 0.5 M NaCl solution was analysed. The AFM images with the surface morphology evolution for the plasma activated **U** systems, after different times of immersion appear in Figure 6.28.

The surface morphology evolution during immersion of the plasma activated **U** systems is similar for both locations of **R** plasma reactor, **P** and **G** electrodes. Only the R_a and h parameters variation permit to differentiate the evolution.

The system **UR1hP₄G**, image **a**, shows negative R_{sk} until 30 days of immersion. This suggests that the pores are still present in the surface until this time of immersion. After 60 days of immersion, the R_{sk} changes, becoming positive, suggesting disappearing of the surface pores. For the system **UR1hP₄P**, image **b**, the R_{sk} changes more rapidly and after 30 days is already positive. A possible reason for disappearing of the surface pores is some swelling process related with the water uptake by the coating, leading to stabilization of the surface.

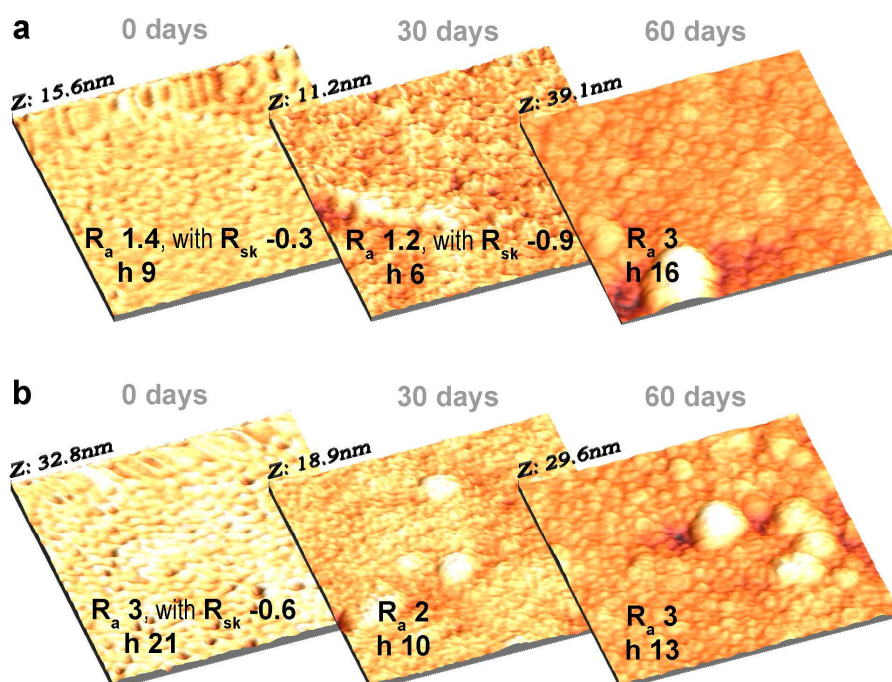


Figure 6.28 Surface morphology AFM 1x1 μm images for the evolution during immersion tests of the plasma activated **U** systems using **R** plasma reactor, systems: **a.** **UR1hP₄G**; and **b.** **UR1hP₄P**. The values in nm of R_a and h are in the respective image.

The elemental composition evolution during immersion was collected for the plasma activated **U** systems prepared in the **R** plasma reactor using the two electrode location, **G** and **P**. The correspondent element content calculated is shown in Table 6.2.

The composition does not change substantially during the immersion tests and there is no noticeable variation between the two electrode locations.

Table 6.2 Elements content evolution during immersion of the plasma activated **U** systems, values in at. %.

time (days)	UR1hP₄G		UR1hP₄P	
	fluorine	chlorine	fluorine	chlorine
0	56	2.7	49	2.6
7	54	3.0	58	2.8
30	42	3.0	45	2.9

For the plasma activated **E** systems, the SEM micrographs show the evolution of the surface morphology during immersion. The micrographs are shown in Figure 6.29, in the next page. The elemental composition evolution during immersion for the same systems, collected using EDS, appears in Table 6.3. The images show that the surface morphology evolution is dependent of the plasma reactor electrode location used.

The system **ER1hP₄P**, Figure 6.29b, has higher signs of surface degradation already noticed after 7 days of immersion with the variation of the existing surface pores. Their walls become less sharp and deposits form in the edges. The system **ER1hP₄G** also shows degradation, Figure 6.29a. After 7 days of immersion, the smooth surface disappears, but at lower extent than for the system **ER1hP₄P**.

Table 6.3 Elements content evolution during immersion of plasma activated **E** systems, values in at. %.

time (days)	ER1hP₄G			ER1hP₄P		
	aluminium	silicon	titanium	aluminium	silicon	titanium
0	1.0	3.3	22	0.9	3.3	25
7	1.0	3.6	27	1.0	3.4	24
30	0.9	3.2	27	1.0	3.6	26

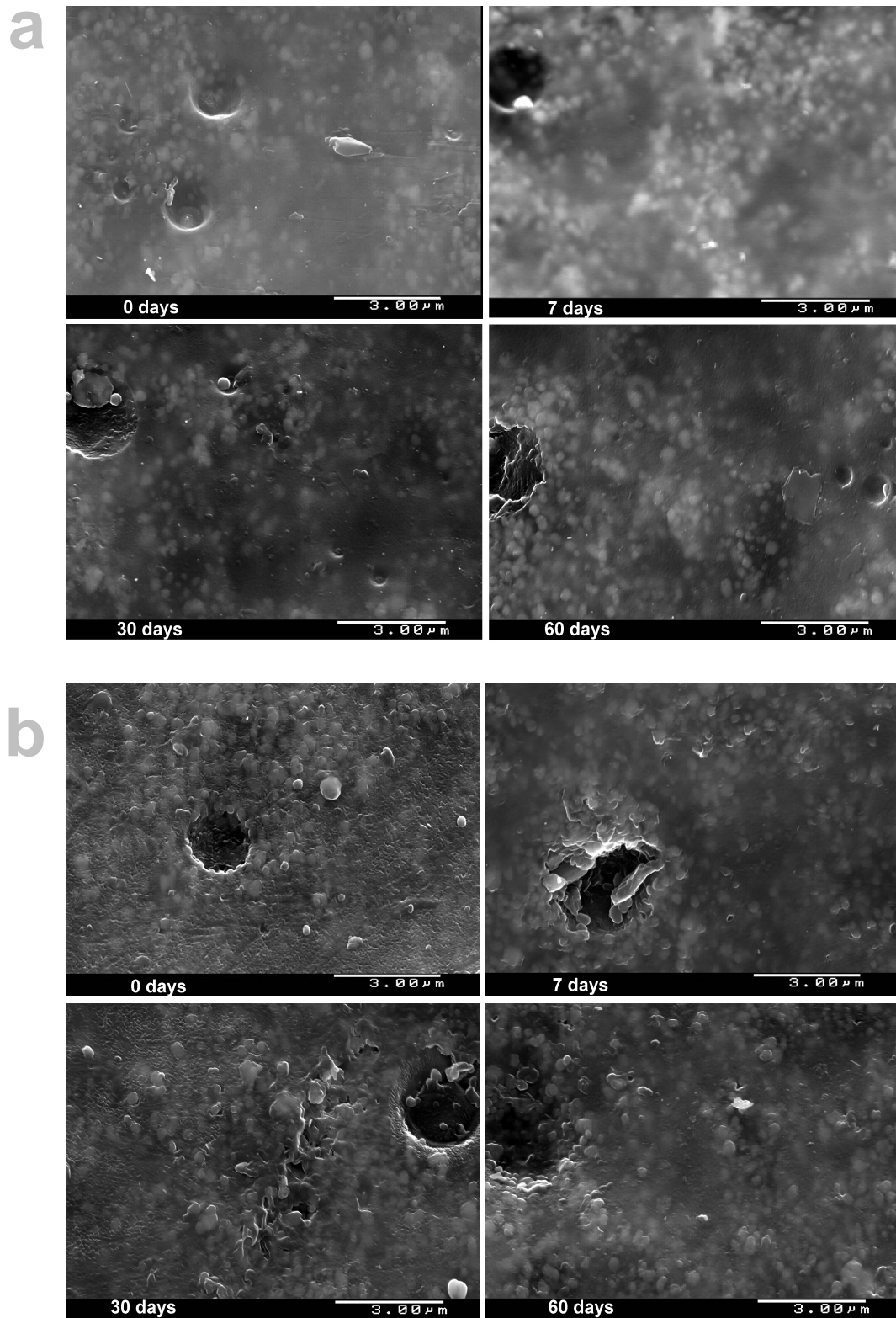


Figure 6.29 Surface morphology images, obtained with SEM, showing the surface evolution during immersion of the plasma activated E systems using R plasma reactor, systems: **a.** ER1hP₄G; and **b.** ER1hP₄P.

After longer immersion, 30 and 60 days, both systems show signs of surface cracks and, in addition, some areas show partial removal of a surface layer. The system **ER1hP₄P** shows only scratch like surface features, while **ER1hP₄G** has complete parts of the surface layer detached and deposited in adjacent areas of the defect.

The elemental analysis of the plasma activated **E** systems, Table 6.3, shows that the elements content variation during immersion is negligible in both electrode locations. The elements maintain constant content, similar to unmodified **E** coil coating, Figure 5.9.

The surface morphology results show that plasma activation performed in the **G** electrode leads to higher influence to the coil coating properties. However, the variation noticed is almost negligible. This occurs in the two coil coatings used, corroborating the impedance results.

6.3.2. Plasma Deposition Stage

In the **R** plasma reactor, the plasma deposition used HMDSO with oxygen carrier gas as precursor mixture. In this point, appear the results for the systems treated with the three steps performed in sequence, plasma activation, plasma deposition and plasma stabilization (stage **3**). The procedure is described with more detail in point 4.1.2.ii. The process was performed using the two coil coatings, **U** and **E** coil coatings, at the two electrode locations of the **R** plasma reactor. The labels attributed to the systems prepared appear in Table 4.7.

The EIS results in 0.5 M NaCl performed at ambient temperature for the systems prepared using the stage **3** appear in Figure 6.30.

After immersion (1 hour), the systems **UR3eP₅G** and **UR3eP₅P** show pure capacitive behaviour for the full frequency range tested. The low frequency impedance values are higher than 100 Gohm cm², which is identical to the values obtained for unmodified **U** coil coating shown in point 5.2. Impedance values of this magnitude represent coating systems with high barrier effect against the absorption of water and ions, from the testing solution.^{112;113;125} The evolution of the systems is dependent of the electrode used for the plasma polymerization.

The phase angle plots of the system **UR3eP₅G**, Figure 6.30a, shows a small low frequency resistive part after 30 days of immersion. After 110 days (near 4 months), the resistive part is further developed with low frequency impedance decreasing to under 100 Gohm cm². This is attributed to degradation of the system barrier properties related with the absorption of water and ions from the testing environment. The low frequency impedance continues to decrease and after 130 days (more than 4 months), two orders of magnitude decrease is obtained, to 3 Gohm cm². Further immersion, until 190 days (6 months) show further degradation, with low frequency impedance value just above 1 Gohm cm².

Values of this magnitude represent paint systems that still confer barrier effect, protecting the underlying metal from the aggressive environment. However, the curve format suggests that the metallic substrate is in contact with the testing solution. ^{112;113;125}

For the system **UR3eP₅P**, Figure 6.30b, the degradation of the barrier properties starts sooner. After 30 days of immersion, the low frequency impedance value is already similar to the value obtained for the system **UR3eP₅G** after 110 days of immersion, also showing the low frequency resistive part. At 70 days, the low frequency impedance value is lower than 1 Gohm cm², only reached after 190 days for the system **UR3eP₅G**. The curve format at this time already suggests that water and ions are in contact with the metallic substrate.

The low frequency impedance of the system **UR3eP₅P** continues to decrease, reaching lower values than for system **UR3eP₅G**. After 120 days (4 months) of immersion, the value is three orders of magnitude lower than initially, just above 100 Mohm cm². This behaviour corresponds to strong degradation of the system barrier properties. ^{112;113;125}

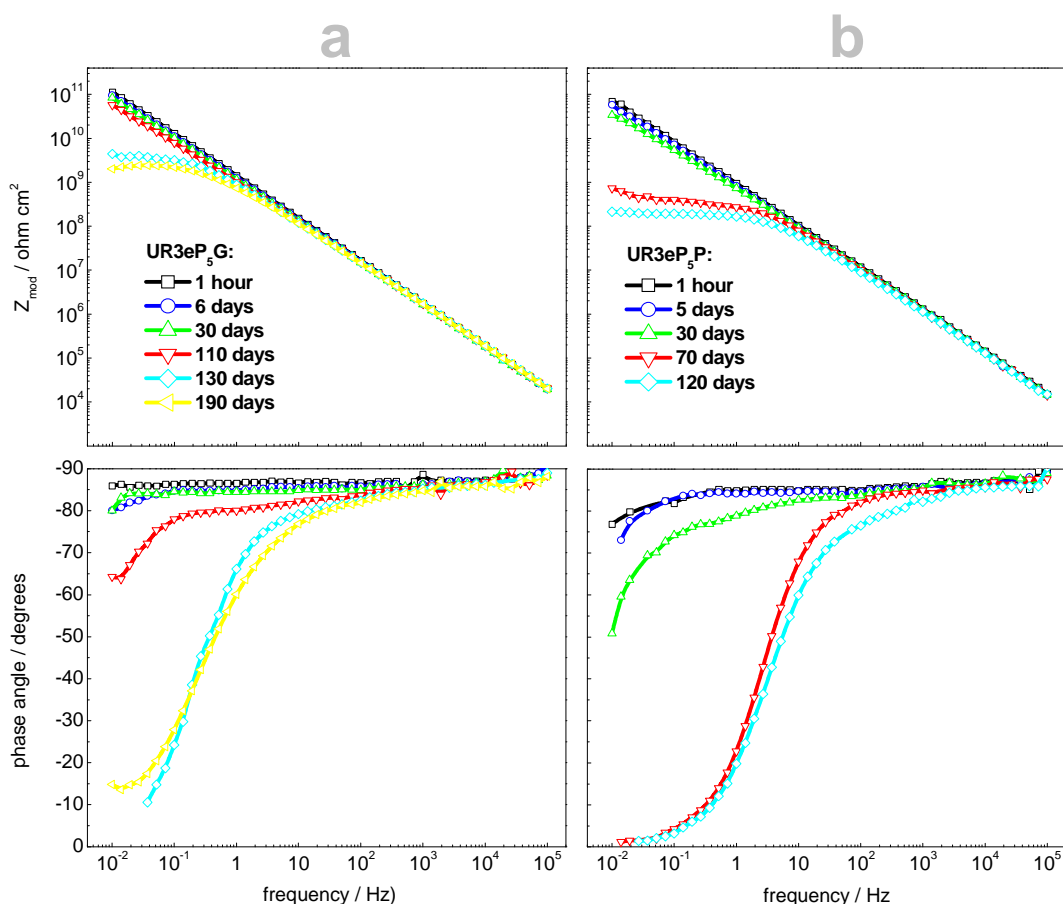


Figure 6.30 Bode plots with evolution of impedance during immersion for the systems: **a. UR3eP₅G**; and **b. UR3eP₅P**.

Similar plasma polymerization process, stage **3**, was performed with the **E** coil coating. The impedance results for these systems, measured during immersion, appear in Figure 6.31b.

The system **ER3eP₅G** immediately after immersion (1 hour) shows low frequency impedance value higher than 10 Gohm cm², similar to unmodified **E** coil coating in Figure 5.2, with capacitive behaviour for the full frequency range tested. Values of this magnitude together with the capacitive behaviour are representative of coating systems with high barrier properties.^{112;113;125} Similar to unmodified **E** coil coating this value is one order of magnitude lower than for **U** coil coating, point 5.2.

Low frequency resistive part appears during immersion for this system, **ER3eP₅G**. After 14 days of immersion, the resistive part is already visible, easier to see in the phase angle plot. The low frequency impedance value at this time of immersion is still near the 10 Gohm cm². Further immersion leads to continuous degradation and after 150 days (5 months) of immersion the low frequency impedance value is close to 1 Gohm cm². This corresponds to one order of magnitude decrease but suggests, together with the curve format, that the barrier effect is still high.^{112;113;125}

This low frequency impedance value obtained after the 150 days of immersion for the system **ER3eP₅G** is higher than for **E** coil coating after 130 days of immersion, Figure 5.2. This is an indication that the system performance increased with the plasma polymerization procedure performed in the **G** electrode location.

The system **ER3eP₅P**, Figure 6.31a, shows after immersion (1 hour) the low frequency resistive part with low frequency impedance value of 1 Gohm cm², one order of magnitude lower when compared with unmodified **E** coil coating. This already corresponds to coating systems with lower barrier properties.

During immersion, the low frequency impedance of the system **ER3eP₅P** shows very fast decrease and after 9 hours of immersion is already near 100 Mohm cm², associated with the formation of a second time constant at low frequency. After 16 days of immersion, further decrease of the low frequency impedance values occurs, reaching less than 100 Mohm cm².

The low frequency impedance value and the second time constant imply that the paint system suffers strong degradation during the plasma polymerization and does not offer good barrier properties against the environment anymore. This degradation suggests that the metallic substrate is in direct contact with water and aggressive ions with corrosion already occurring.^{112;113;125}

The coil coating systems used have a zinc layer, which when exposed to the aggressive environment still protects the underlying metal by cathodic protection process. The cathodic protection of the zinc layer initially forms only slow white corrosion products, even in the most aggressive environments. This behaviour prevents the impedance value of the system **ER3eP₅P** of decreasing faster.^{15;112;113}

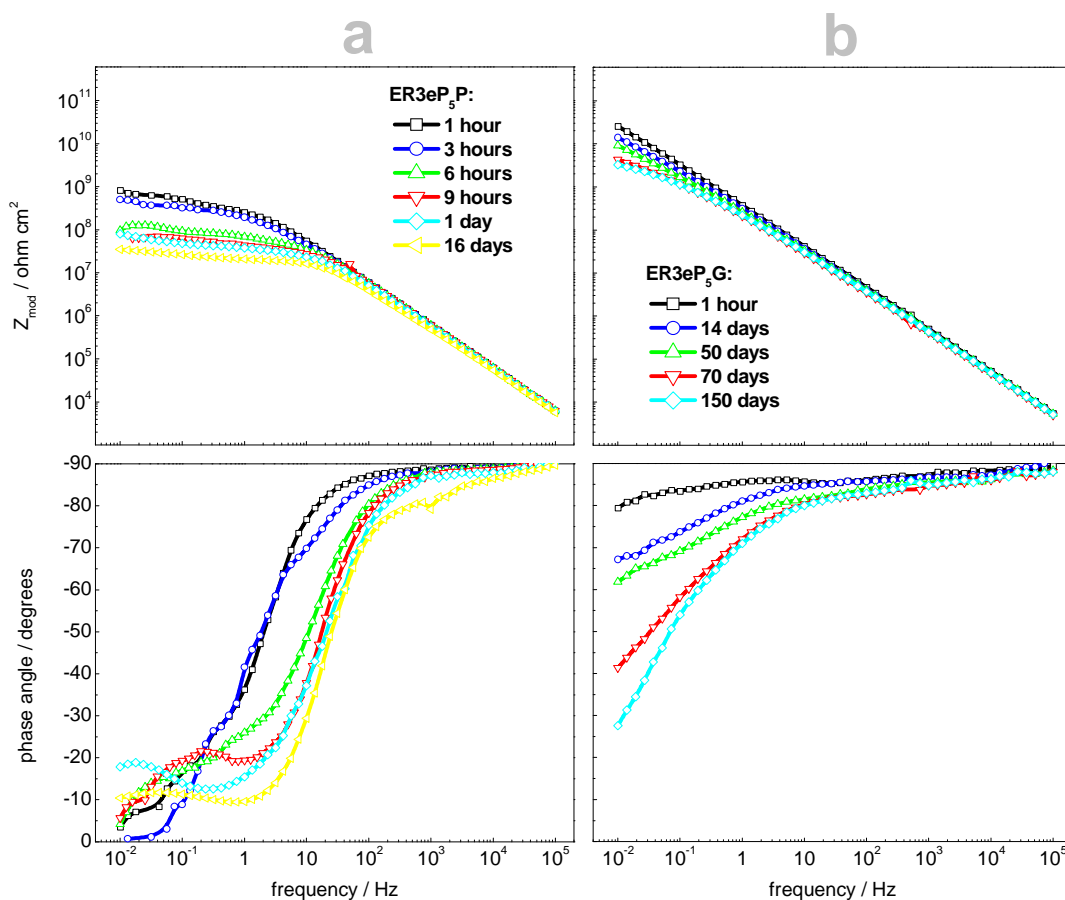


Figure 6.31 Bode plots with the impedance values obtained during the immersion tests of the systems: **a. ER3eP₅P**; and **b. ER3eP₅G**.

6.3.3. Plasma Stabilization Stage

In this point, appear the results for the systems treated with the plasma deposition step followed by the plasma stabilization step, label **4**. The plasma activation step did not take place. The procedure occurred in the two coil coatings, **U** and **E** coil coatings, at the two electrode locations of the **R** plasma reactor. The labels attributed to the prepared systems appear in Table 4.7.

The impedance spectra using the two electrode locations of the **R** plasma reactor appear in Figure 6.32 and Figure 6.33. The figures have the results obtained during the immersion tests with 0.5 M NaCl, performed at 45° C for the **U** systems and at ambient temperature for the **E** systems. The results for the plasma polymerized **U** systems refer only to measurements at 45 °C due to logistic problems during the ambient temperature measurements.

The systems **45UR4iP₄P** and **45UR4iP₄G** have initially (1 hour), pure capacitive behaviour for the full frequency range tested, Figure 6.32. The behaviour is identical to unmodified **U** coil coating shown in Figure 5.1. The initial low frequency impedance is higher than 100 Gohm cm², corresponding to undamaged and high performance paint systems with excellent barrier properties.^{112;113;125}

The immersion tests at 45° C accelerate the systems degradation and the capacitive behaviour disappears shortly after the beginning of the immersion tests.^{173;174} A relation between the degradation of the barrier properties and the electrode location can be observed.

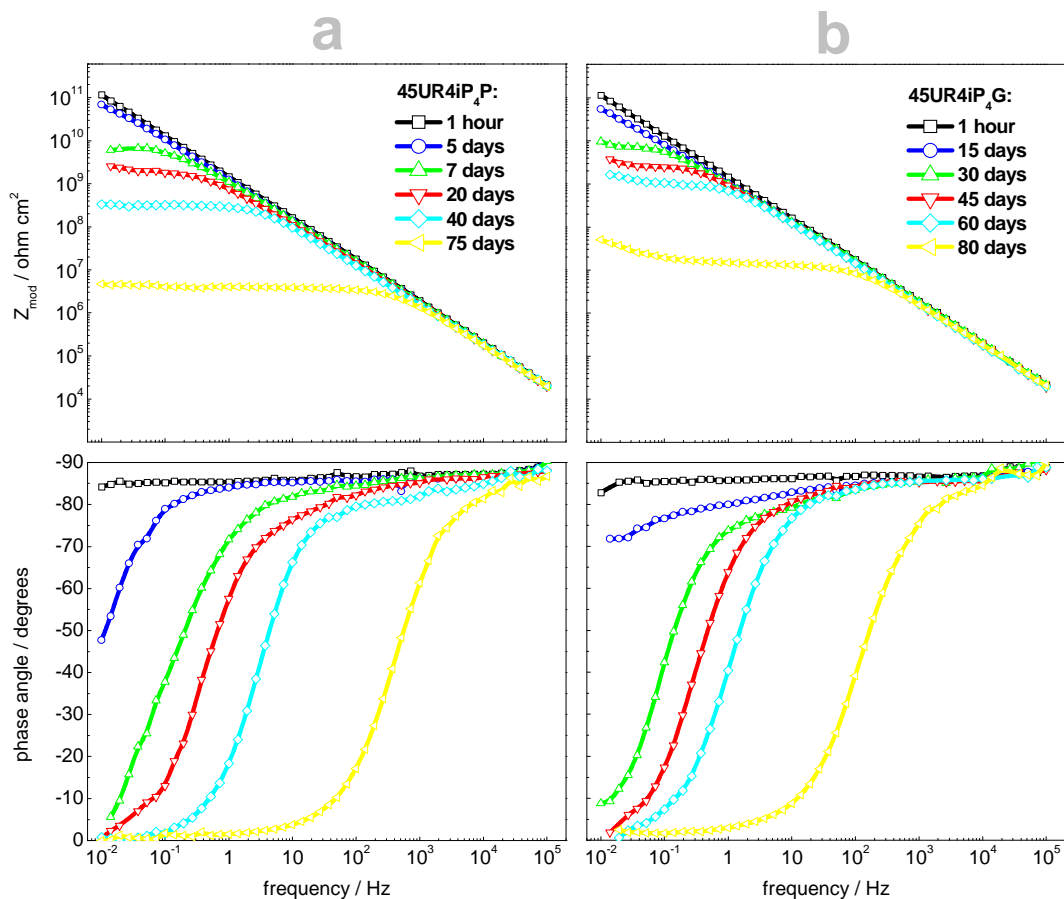


Figure 6.32 Bode plots for immersion tests at 45° C of R plasma polymerization using **U** coil coating, systems: **a. 45UR4iP₄P**; and **b. 45UR4iP₄G**.

The system **45UR4iP₄P**, Figure 6.32a, shows a resistive part at low frequency after 5 days of immersion, with a slight decrease of low frequency impedance value to less than 100 Gohm cm². After two more days of testing, 7 days in total, the low frequency resistive part

is associated with stronger decrease of the low frequency impedance value of more than one order of magnitude, reaching 6 Gohm cm². Increase of the immersion time continues to register continuous degradation and after 40 days of immersion, another order of magnitude decrease occurs, reaching 300 Mohm cm².

After 40 days of immersion, the curve format for the system **45UR4iP₄P** suggests that the water is reaching the metallic substrate. From this point on, strong degradation occurs and after 75 days of immersion, the decrease of the low frequency impedance value reaches 3 Mohm cm². This is a decrease of four orders of magnitude, relatively to the initial value, representing strong degradation.

The evolution of the system **45UR4iP₄G**, Figure 6.32b, shows similar behaviour during the tests, but the system resistance to immersion is higher than for **45UR4iP₄P** system. Slower degradation of the barrier properties takes place. In this case, after 15 days of testing the initial capacitive behaviour is still apparent for full frequency range tested, with low frequency impedance value comparable with the **45UR4iP₄P** system after only 5 days of immersion, value just under the 100 Gohm cm². Only after 30 days of immersion does the resistive part clearly appears, together with low frequency impedance value showing one order of magnitude decrease. The low frequency impedance reaches 10 Gohm cm², which is similar to system **45UR4iP₄P** after 7 days of immersion only. Further immersion also leads to an increase of the resistive part, but always later than for the **45UR4iP₄P** system. After 80 days of immersion the low frequency impedance value reaches 10 Mohm cm², three orders of magnitude lower than the initial value, however, this is still one order of magnitude higher than for the **45UR4iP₄P** system after 75 days of immersion. The curve format suggests that the water is in contact with the metallic substrate.

The Bode plots for the systems prepared using similar plasma polymerization process, stage 4 but with the **E** coil coating appear in Figure 6.33. The results refer to the systems prepared in the two electrode locations of the plasma reactor. In this case, the tests were performed at ambient temperature.

The two **R** plasma reactor locations at initial immersion (1 hour line), show similar low frequency impedance value, higher than 10 Gohm cm², which is also comparable with unmodified **E** coil coating of Figure 5.2. The value is lower when compared with **U** systems, as already shown in Figure 5.1. Capacitive behaviour for full frequency range occurs for the system **ER4iP₄G**. This is representative of coating systems with high barrier properties. The system **ER4iP₄P** already show signs of the resistive part but the low frequency impedance, value is also representative of good coating system. ^{112;113;125}

The system **ER4iP₄P**, Figure 6.33a, shows faster decrease of performance during the immersion tests, which corresponds to lower stability under immersion. After 1 day of immersion, the low frequency impedance is near 10 Gohm cm². After 9 days of immersion tests, the low frequency impedance decreases three orders of magnitude to 50 Mohm cm². The curve format and the low frequency impedance results suggest that the water have reached the metallic substrate, with degradation of the coating barrier properties.

The system **ER4iP₄G**, Figure 6.33b, also shows degradation of the barrier properties during immersion. The full capacitive behaviour is lost after 2 days of immersion, showing

the low frequency resistive part. However, only after 55 days of immersion the low frequency impedance value is identical to the value of system **ER4iP₄P** after 1 day of immersion, near 10 Gohm cm². After 70 days of immersion, the low frequency impedance decreases further reaching 3 Gohm cm², one order of magnitude decrease.

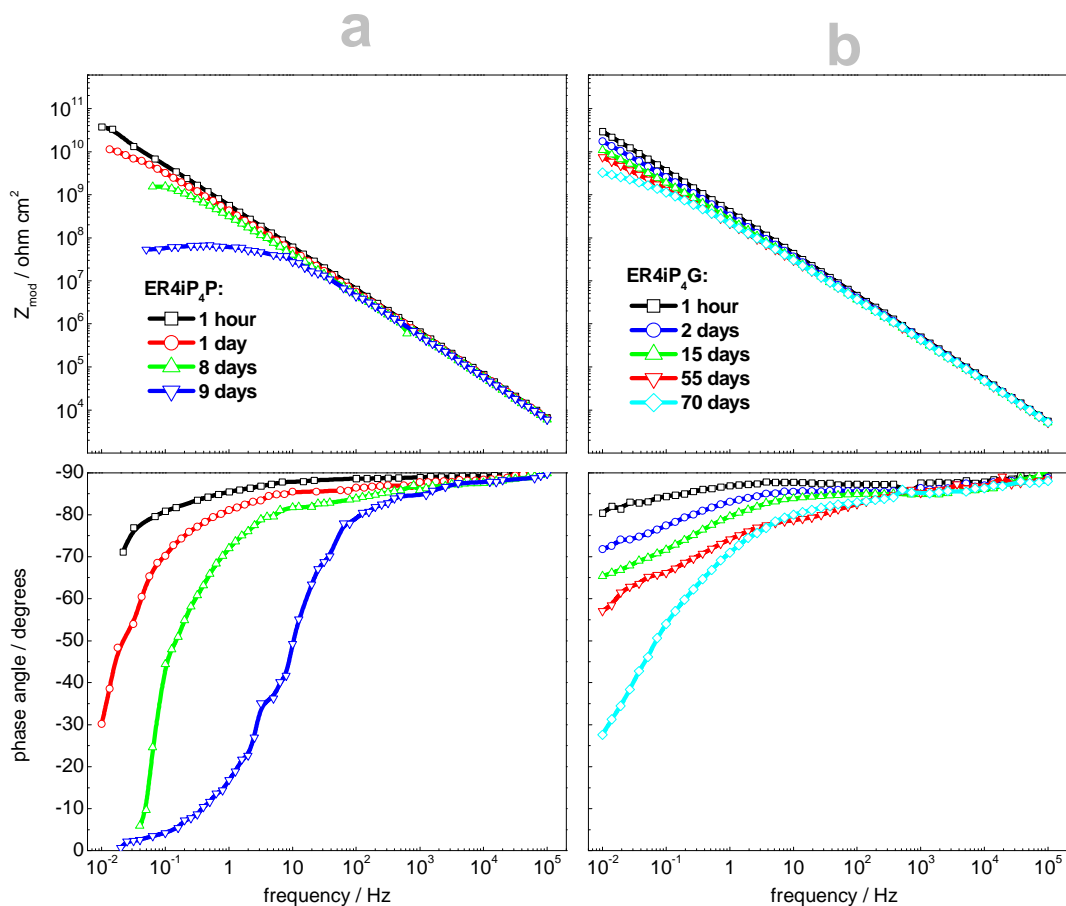


Figure 6.33 Bode plots obtained during the immersion tests for the systems: **a. ER4iP₄P**; and **b. ER4iP₄G**.

6.3.4. Characterization of the Systems Obtained in Stages **3** and **4**

Further characterization of the systems prepared using the plasma polymerization stages **3** and **4** will be carried out jointly in order to make comparisons easier.

i. Numerical Fitting of EIS Data

The numerical fitting of the impedance results offers quantitative information about the systems evolution during immersion. The results reflect the behaviour during immersion of the systems prepared using the stages **3** and **4**, with the conditions described in Table 4.7. The extracted parameters are related with the degradation processes occurring.

The estimated parameters C_{coat} and R_{por} obtained using equivalent circuits for the plasma activated **U** and **E** systems are in the Figure 6.34. The plasma polymerized **E** systems show two time constants, similar to unmodified **E** coil coating. In this case, the equivalent circuit **b** of Figure 5.3 is used. The high frequency process corresponds to experimental arrangement interferences.¹⁷⁷⁻¹⁸² Further explanation of the procedure appears in point 5.2.1. The low frequency represents the coating degradation due to water and ions absorption. For plasma polymerized **U** systems equivalent circuit **a** is used, correspondent to the only process occurring. The parameters evolution during immersion is dependent of the testing temperature, coil coating used, stage and electrode location.

For the **U** systems, the unmodified **U** coil coating shows the lowest C_{coat} values, followed by the **45U** coil coating, Figure 6.34a. These have C_{coat} values always lower than the plasma polymerized systems.

The plasma polymerized **U** systems tested at higher temperature, systems **45UR4iP₄G** and **45UR4iP₄P**, have the highest C_{coat} values during immersion. This is the result of increase of the degradation rate observed when the temperature of testing is increased. For these two systems, the highest C_{coat} appears for the system prepared in the **P** electrode location. The systems **UR3eP₅G** and **UR3eP₅P** have slower initial increase of C_{coat} value than the previous systems, but again, the plasma polymerization using the **P** electrode shows higher C_{coat} value.

The R_{por} values for the plasma polymerized **U** systems have identical value initially, but during immersion also reflect the testing conditions used, Figure 6.34c.

The systems **45UR4iP₄P** and **45UR4iP₄G** show a strong decrease of R_{por} parameter immediately from the beginning of the immersion tests. This occurs due to higher degradation rate related with the higher testing temperature used. The systems **UR3eP₅P** and **UR3eP₅G** show smaller decrease, which occurs after longer immersion period. The R_{por} decrease has relation with the paint degradation and respective decrease of barrier effect with consequent water and ions absorption.^{32;121;174}

For the stages **3** and **4**, higher and faster degradation occurs when the **P** electrode location is used during the plasma polymerization.

For the plasma polymerized **E** systems, the C_{coat} values are higher, Figure 6.34b, and the behaviour during immersion is more unstable than similar procedure for plasma polymerized **U** systems. The C_{coat} values have initially strong increase followed by instability. The values are close to the value obtained for the unmodified **E** coil coating.

The R_{por} values obtained for the plasma polymerized **E** systems appear in Figure 6.34d. The evolution during immersion is dependent of the reactor location. The initial values

confirm the increased performance of the **ER3eP₅G** system and only after 60 days of immersion does the R_{por} values decrease and become similar to unmodified **E** coil coating. This suggests increase of performance after the plasma polymerization procedure leading to better barrier properties during immersion. The system **ER4iP₄G** R_{por} values are similar to unmodified **E** coil coating initially, but during immersion show faster decrease than **ER3eP₅G**. This behaviour suggests faster degradation of the system barrier properties.

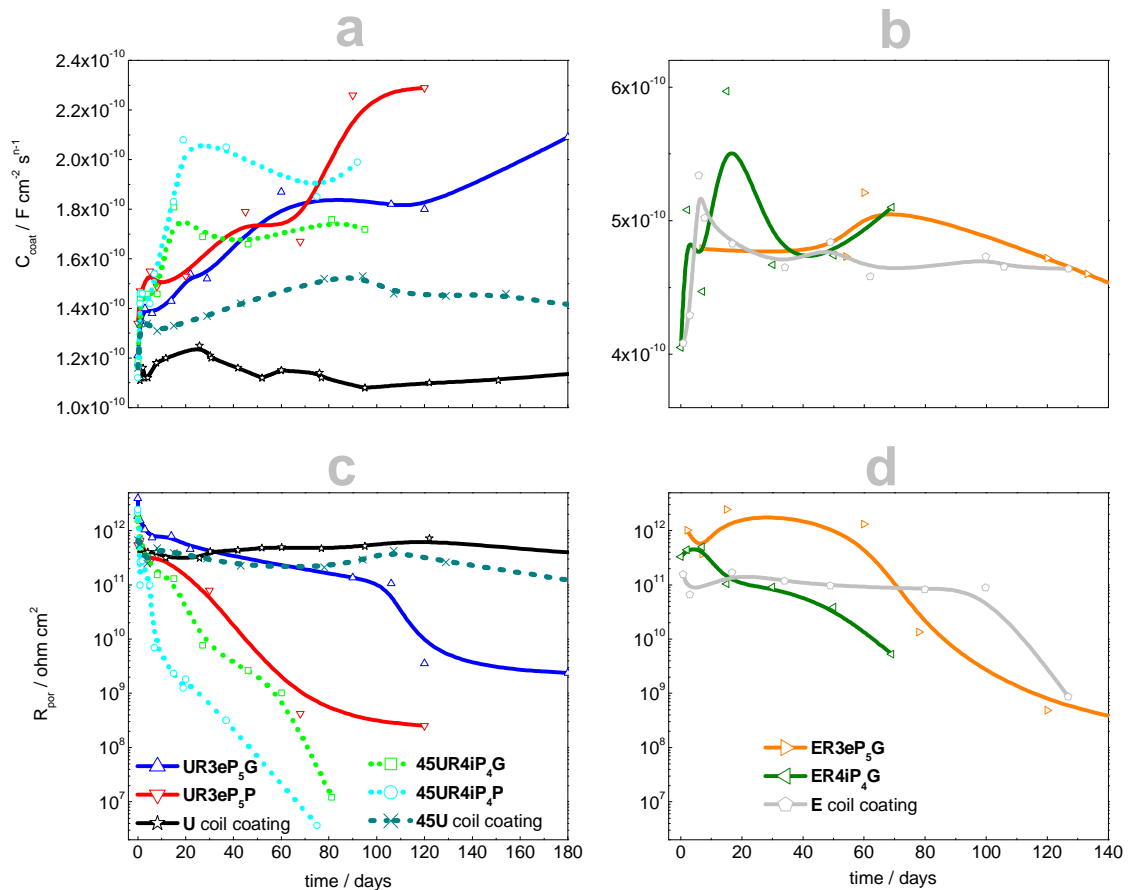


Figure 6.34 Evolution of the estimated parameters for the **R** plasma polymerization using **U** and **E** systems: **a.**, **c.** C_{coat} values; and **b.**, **d.** R_{por} values. The C_{coat} graphs have different scales adapted to the respective magnitude of the results.

The fitting results obtained for the **R** plasma polymerized **E** system using the **P** electrode, systems **ER3eP₅P** and **ER4iP₄P**, do not appear in Figure 6.34 since they have very poor performance associated with very fast degradation of the barrier properties. The respective estimated parameters have very unstable behaviour with very fast increase of C_{coat} and decrease of R_{por} . The Bode plots for these systems have a visible second time constant at low frequencies. The impedance value and the curve format of these Bode plots suggest

that active corrosion processes are occurring at the metal/paint interface. The **E** systems showed another high frequency process, previously described in point 5.2.1. This process moves even to higher frequencies when the low frequency time constant correspondent to the corrosion process appears, becoming outside the measured frequency range and disappearing from the spectra showed in Figure 6.31a.

ii. Water Uptake

The value of the capacitance of the coating systems permits to estimate the water uptake rate with the empirical relation of Brasher and Kingsbury,¹²⁸ using eq. 3.13 by following the procedure described in point 3.1.4. The water uptake plots for both **E** and **U** coil coatings, submitted to stages **3** and **4** using the two electrode locations, appear in Figure 6.35.

The water uptake and the saturation level reached are dependent of the stage used during the **R** plasma polymerization. The specimen location in the plasma reactor also influences the outcome. Similar very fast initial water uptake is observed for all the systems, characteristic behaviour of organic coatings.^{112;128;129}

The system **UR3eP₅P** has much higher water saturation level than all the other **U** plasma polymerized systems, suggesting that initially this system already has stronger degradation. The impedance data for this system also shows stronger and faster degradation during immersion, corroborating the stronger influence of the process.

The system **UR3eP₅G** has better performance and the saturation level obtained is very close to the **U** coil coating. These results agree with the verified higher barrier properties for the **UR3eP₅G** system.

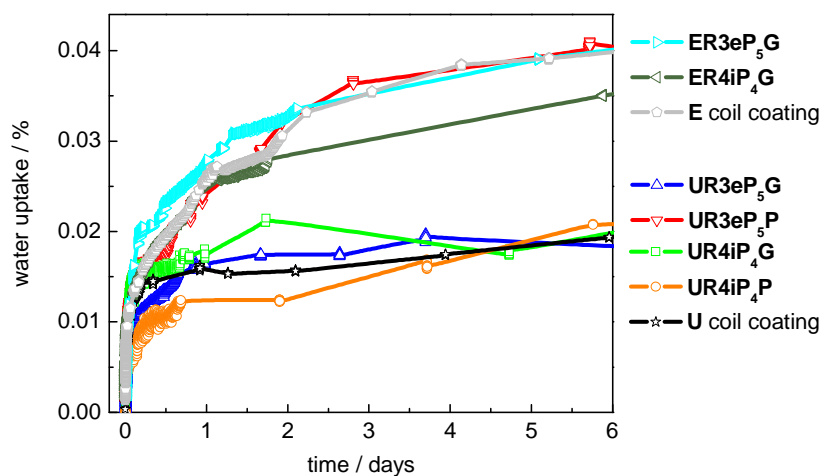


Figure 6.35 Water uptake plot for the plasma polymerized **E** and **U** systems using the **R** plasma reactor stage **3** and **4**.

Similar water saturation level, also similar to **U** coil coating, appears for the systems **UR4iP₄P** and **UR4iP₄G**. Initially, the system **UR4iP₄P** has even lower saturation level than **U** coil coating. However, after 4 days of immersion the saturation level increases to identical values.

The **R** plasma polymerized systems using the **E** coil coating have higher saturation level. The values are near the double of the values obtained for the plasma polymerized **U** systems. They also show a continuous raising trend during immersion. The absorption rate decreases after 3 to 4 days of immersion and the value becomes more constant. This value is similar to the value obtained for the **UR3eP₅P** system.

The system **ER4iP₄G** shows slightly lower saturation level, while the **ER3eP₅G** system shows coincident values with the unmodified **E** coil coating.

The water uptake values obtained for the systems prepared in the **P** electrode with **E** coil coating do not appear since they have very poor performance and unreliable results.

It is important to observe that during the plasma activation stage a relation between the impedance response and the location of the specimen inside the **R** plasma reactor was verified, point 6.3.1.i. The results suggested that the plasma activation performed in the **G** electrode have poorer performance than in the **P** electrode, i.e. the plasma activation step has higher influence on the **U** coil coating barrier properties when performed in the **G** electrode location. This also suggests that the differences of performance now verified (after the deposition of the plasma polymer film) show an inverse result. The systems with better performance are the ones prepared in the **G** electrode. These differences show that the film deposited on the activated surface can affect the performance of the whole system.

For the two stages (**3** and **4**) performed in the **R** plasma reactor, the systems showing higher performance are the ones prepared in the **G** electrode. This is noticed for the two coil coatings, **E** and **U** systems.

However, the system **ER3eP₅G** is the only system showing increase of performance, where the degradation occurs later than for the unmodified **E** coil coating. The plasma polymer films characterization results help to understand the degradation process involved.

iii. Structure

The plasma polymer films prepared in the **R** plasma reactor are silicon based that has enough elemental weight to provide contrast when imaged by TEM technique. However, the low thickness of the plasma polymer films prepared in the **R** plasma reactor brought difficulties to the TEM preparation and respective imaging. The different composition of the coil coating and of the plasma polymer film, which are visible under the transmission electron beam, are another reason for higher difficulties in the imaging process of the plasma polymerized **E** systems, since these areas have different molecular weight and thus different contrast levels.

The plasma polymerized **E** and **U** systems, showing acceptable TEM results appear in the micrographs of Figure 6.36, systems **UR4iP₄P** and **ER3eP₅G**. The preparation follows the procedure described in point 4.2.4. The other systems prepared in the **R** plasma reactor, following the same preparation procedure and submitted to TEM imaging, yielded micrographs that do not have good quality. These make impossible to gather reliable information.

The plasma polymer films generated are uniform, thin, compact and amorphous with thickness under 100 nm, without visible particles. Major differences between **E** and **U** plasma polymerized systems are noticed, which is related with the different structure of the coil coating used.

For the plasma polymerized **U** systems, micrograph **a**, only the plasma polymer film has enough contrast to be imaged, the **U** coil coating and the mounting resin are both transparent under the electron beam since they are carbon based components. In this case, the grey band crossing the micrograph represents the plasma polymer film. The gold layer deposited on the film surface, used to facilitate the imaging procedure, appears as small black dots.

For the plasma polymerized **E** systems, micrograph **b**, more information is available. The mounting resin used is the same and is transparent under TEM imaging. This is represented by the white region in the left side of the micrograph. The plasma polymer film is the gray zone labelled next to the **E** coil coating with the respective titanium based particles. The **E** coil coating shows internal pores. Each region is labelled. The different regions have different composition, confirmed by high resolution EDS. The pores found for the **E** coil coating are potential pathways for water and ions penetration during the immersion tests, which will lead to degradation of the metallic substrate.

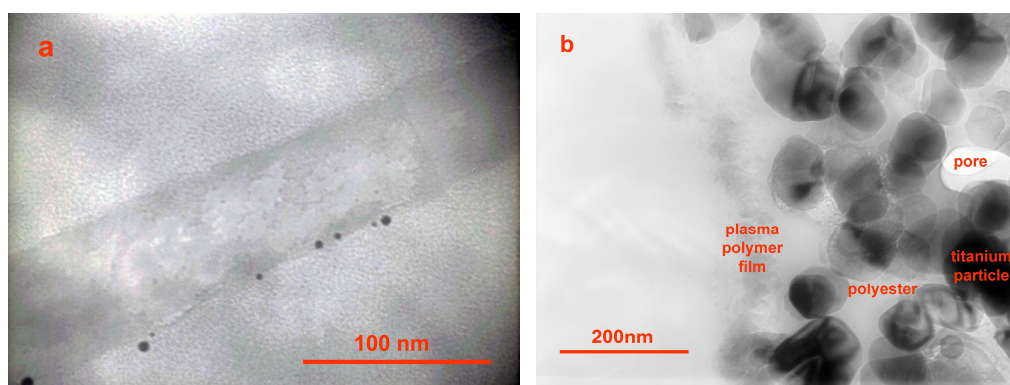


Figure 6.36 TEM micrographs of the plasma polymer films prepared in the **R** plasma reactor, systems: **a. UR4iP₄P**; and **b. ER3eP₅G**.

iv. Surface Characterization

The study of the new layer formed recurred to AFM for plasma polymerized **U** systems and SEM for the plasma polymerized **E** systems, in order to better observe the different visible features, similar to what was shown in point 5.3 for the unmodified coil coatings.

The surface morphology of the systems prepared by the plasma polymerization process with the stages **3** and **4** using the **R** plasma reactor before any testing, obtained using AFM, appears in Figure 6.37. The surface R_a and h parameters, calculated from the images using the procedure described in point 4.2.5, are in the respective images.

Similar particulate surface morphology appears for all the prepared systems, however, the surface morphology parameters are dependent of the stage used. The particle size is dependent on the electrode used, but also related with the stage used during the plasma polymerization.

The system **UR3eP₅G**, image **a**, shows the smallest surface particles, near 50 nm diameter, while the system **UR3eP₅P**, image **b**, has the biggest particles, around 100 nm. The R_a and h parameters have higher variation in the system **UR3eP₅P**, compared with unmodified **U** coil coating in Figure 5.7.

The two systems **UR4iP₄G** and **UR4iP₄P**, in image **c** and **d** respectively, have similar particle size of 80 nm. The surface morphology, as showed from R_a and h parameters, does not change markedly although variations are found according to the electrode location used.

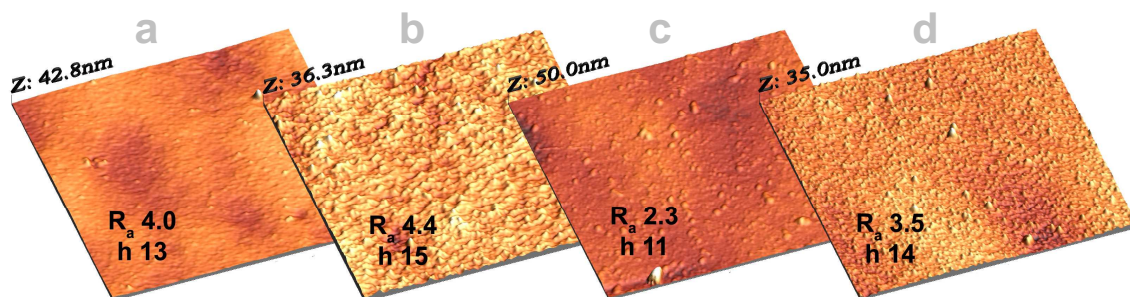
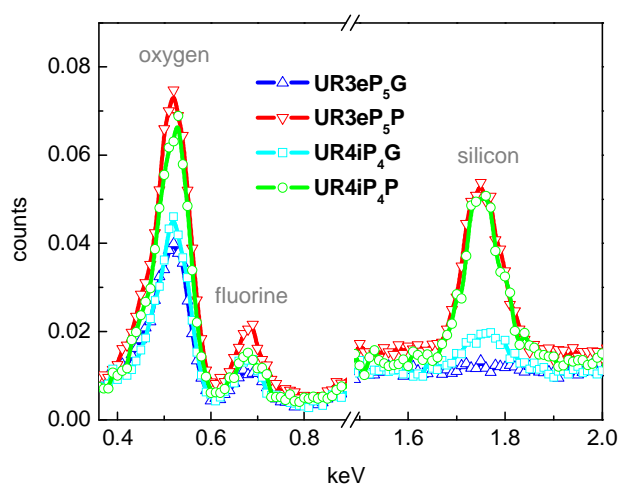


Figure 6.37 AFM 4x4 μm images with the surface morphology for the systems: **a. UR3eP₅G**; **b. UR3eP₅P**; **c. UR4iP₄G**; and **d. UR4iP₄P**. The values in nm of R_a and h are in the respective image.

EDS allowed to obtain the surface composition of the plasma polymerized systems prepared in **R** plasma reactor using the **U** coil coating, the results appear in Figure 6.38. In the table is the elements quantification for the systems prepared using the two electrode locations, values in at. %.

With the exception of the silicon element, the elements obtained remain unchanged after the plasma polymerization of the **U** systems using the **R** plasma reactor, compared with the unmodified **U** coil coating. The silicon element arises only from the plasma polymer layer. Different silicon content appears for the systems prepared in **P** and **G** electrode location. The content for the systems prepared in **P** electrode, systems **UR3eP₅P** and **UR4iP₄P**, is higher than for the systems prepared in **G** electrode, systems **UR3eP₅G** and **UR4iP₄G**. In the system **UR3eP₅G**, the fluorine element obtained is also different, showing increase of the content.



elemental quantification							
UR3eP₅G		UR3eP₅P		UR4iP₄G		UR4iP₄P	
fluorine	silicon	fluorine	silicon	fluorine	silicon	fluorine	silicon
69	0.4	47	0.6	47	0.4	46	0.7

Figure 6.38 Surface composition spectra of the **R** plasma polymerized **U** systems, quantification values in at. %.

The surface particle size and the content of the fluorine element show association with the plasma layer thickness. Similar effect was observed for the **M** plasma reactor, where a direct relation between surface particle size, the thickness of the plasma polymer layer and the decrease of fluorine content is noticed, point 6.2.2.ii.

The system **UR3eP₅G** shows the lowest particle size and the highest content of fluorine element. This suggests that the plasma polymer layer generated is the thinner.

The other **R** plasma polymerized systems all have lower content of fluorine element than unmodified **U** coil coating. The quantification of the fluorine element yields similar value for the three systems. This suggests thicker plasma polymer films, which are able to mask the

underneath fluorine signal. These three systems have surface particles with bigger size, which corroborates the higher thickness of the plasma polymer layer.

The systems **UR4iP₄G** and **UR4iP₄P** show 80 nm particles, suggesting identical thickness. The TEM image **a** of Figure 6.36 shows thickness of 80 nm for the system **UR4iP₄P**, corroborating the thickness value. The particles of the system **UR3eP₅P** are bigger near 100 nm, suggesting thickness of 100 nm for the plasma polymer layer.

The surface morphology of the plasma polymer film deposited in the **E** coil coating using the **R** plasma reactor was obtained with SEM technique. In Figure 6.39 are the SEM micrographs for the systems prepared using the two stages, before any immersion test. The surface morphology for the plasma polymerized **E** systems shows some differences dependent of the stage used and the two electrode locations of the **R** plasma reactor, **P** and **G**.

The system **ER3eP₅G** completely covers the surface pores of the **E** coil coating. In the system **ER3eP₅P**, variation of the **E** coil coating surface morphology occurs, forming surface agglomerates, but without covering the surface pores. In both these systems the titanium based particles, which are visible in the SEM micrographs, remain unchanged compared with the unmodified **E** coil coating of Figure 5.8.

The systems **ER4iP₄G** and **ER4iP₄P** also have some variation of the surface morphology. The variation is higher in the **G** electrode, but in both systems, the surface pores are still present and the titanium based particles unchanged.

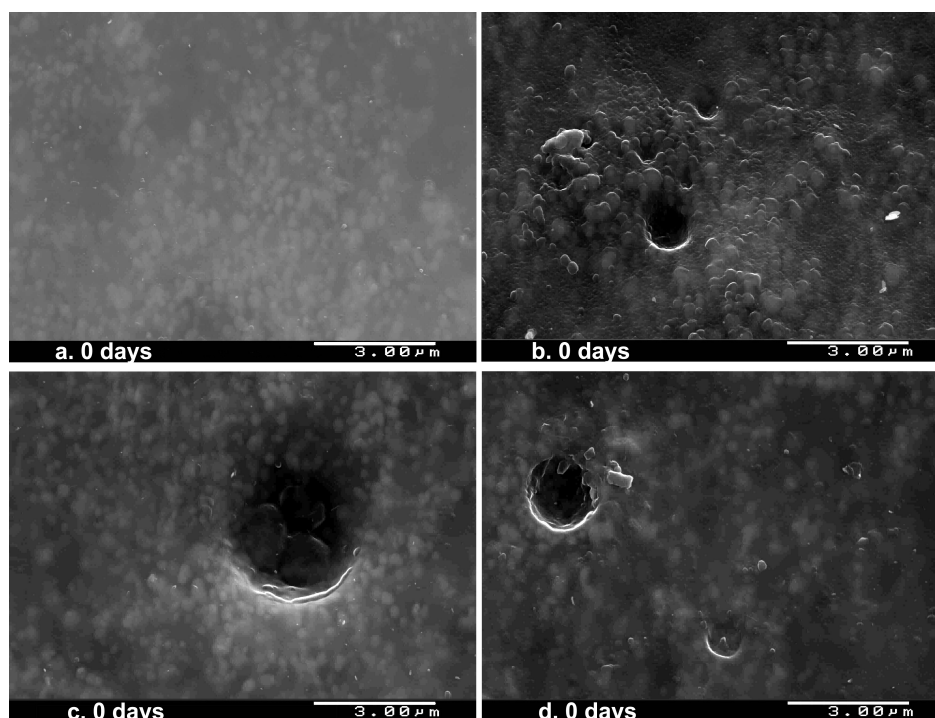
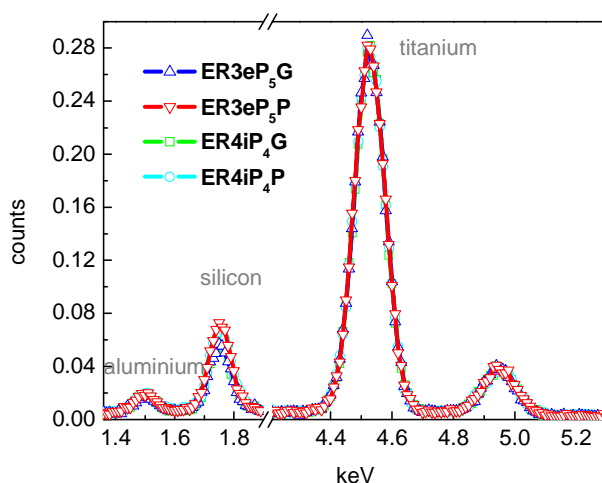


Figure 6.39 Surface morphology of the **R** plasma polymerized **E** systems: **a.** **ER3eP₅G**; **b.** **ER3eP₅P**; **c.** **ER4iP₄G**; and **d.** **ER4iP₄P**.

With EDS was possible to obtain the surface composition for the plasma polymerized **E** system. The results are in Figure 6.40. In the table are the content for the representative elements of the systems prepared using the two electrode locations of the **R** plasma reactor.

The constituent elements found for the unmodified **E** coil coating, Figure 5.9, are also present in the plasma polymerized **E** systems. An increase of silicon content occurs for all the systems. The increase is bigger for the systems **ER3eP₅P** and **ER4iP₄P**, prepared at **P** electrode, compared with **ER3eP₅G** and **ER4iP₄G** systems, prepared at the **G** electrode.

This increase of silicon content is similar to the increase verified for the plasma polymerized **U** systems. For this was necessary to subtract the silicon content obtained for the unmodified **E** coil coating alone (3 % shown in Figure 5.9) to the values obtained here. The variation calculated is 0.6 to 0.7 % increase of silicon content for the plasma polymerized **E** systems prepared in the **P** electrode and 0.4 to 0.5 % for **G** electrode.



elemental quantification					
ER3eP₅G			ER3eP₅P		
aluminium	silicon	titanium	aluminium	silicon	titanium
0.9	3.6	26	0.9	4.1	21
ER4iP₄G			ER4iP₄P		
aluminium	silicon	titanium	aluminium	silicon	titanium
1.0	3.5	24	1.2	4.1	21

Figure 6.40 Surface composition of the plasma polymerized **E** systems performed in the **R** plasma reactor, quantification values in at. %.

- Evolution of the Surface Properties

The surface morphology evolution determined by AFM, for the plasma polymerized **U** systems using the **R** plasma reactor, was performed doing measurements after different immersion periods. The images of Figure 6.41 present the evolution of the surface morphology of the plasma polymer film. The R_a and h values permit to follow the evolution for each system.

The two systems **UR3eP₅G** and **UR3eP₅P**, images **a** and **b** respectively, show similar surface morphology during immersion. The initial particulate surface morphology remains constant during long immersion periods and after 90 days of immersion continues to be present. The R_a and h values also show similar behaviour and remain without significant variation from initial values.

Between these two systems, the system **UR3eP₅G**, **G** electrode system, has higher stability of the R_a and h parameters, which suggests higher stability of the surface morphology during the immersion tests.

The systems **UR4iP₄G** and **UR4iP₄P**, images **c** and **d** respectively, have stronger variation of the surface morphology. The particulate surface morphology disappears during immersion and negative R_{sk} values are obtained. The negative R_{sk} values appear after 7 days for the system **UR4iP₄P** and after 30 days for **UR4iP₄G**. This suggests faster degradation for the system **UR4iP₄P**.

The composition evolution, of the **R** plasma polymerized **U** systems submitted to immersion tests, appears in Table 6.4. The table shows the element quantification results for the systems prepared in the two electrode locations of the **R** plasma reactor using the two stages. Of particular interest is the silicon content, which is the representative element of the plasma polymer layer. The fluorine element also has importance, since it is masked by the silicon based plasma polymer layer, meaning that an increase of fluorine element content represents a decrease of the masking effect and suggests dissolution of the plasma polymer layer.

The evolution of the composition is dependent of the electrode used for the plasma polymerization. The systems **UR3eP₅P** and **UR4iP₄P** maintain the content of the silicon and fluorine elements nearly constant during immersion.

The system **UR4iP₄G** shows decrease of the silicon content and increase of fluorine content. The values show vestigial sign of silicon after 7 days of immersion. These results suggest complete and fast dissolution of the plasma polymer film in the system **UR4iP₄G**. The system **UR3eP₅G** shows a reduction to half of the silicon element but only after 60 days of immersion. These results suggest only partial dissolution of the plasma polymer film for the system **UR3eP₅G**.

Thus, higher variation of the composition occurs when the plasma polymerization takes place in the **G** electrode, while the systems in the **P** electrode keep the composition more constant.

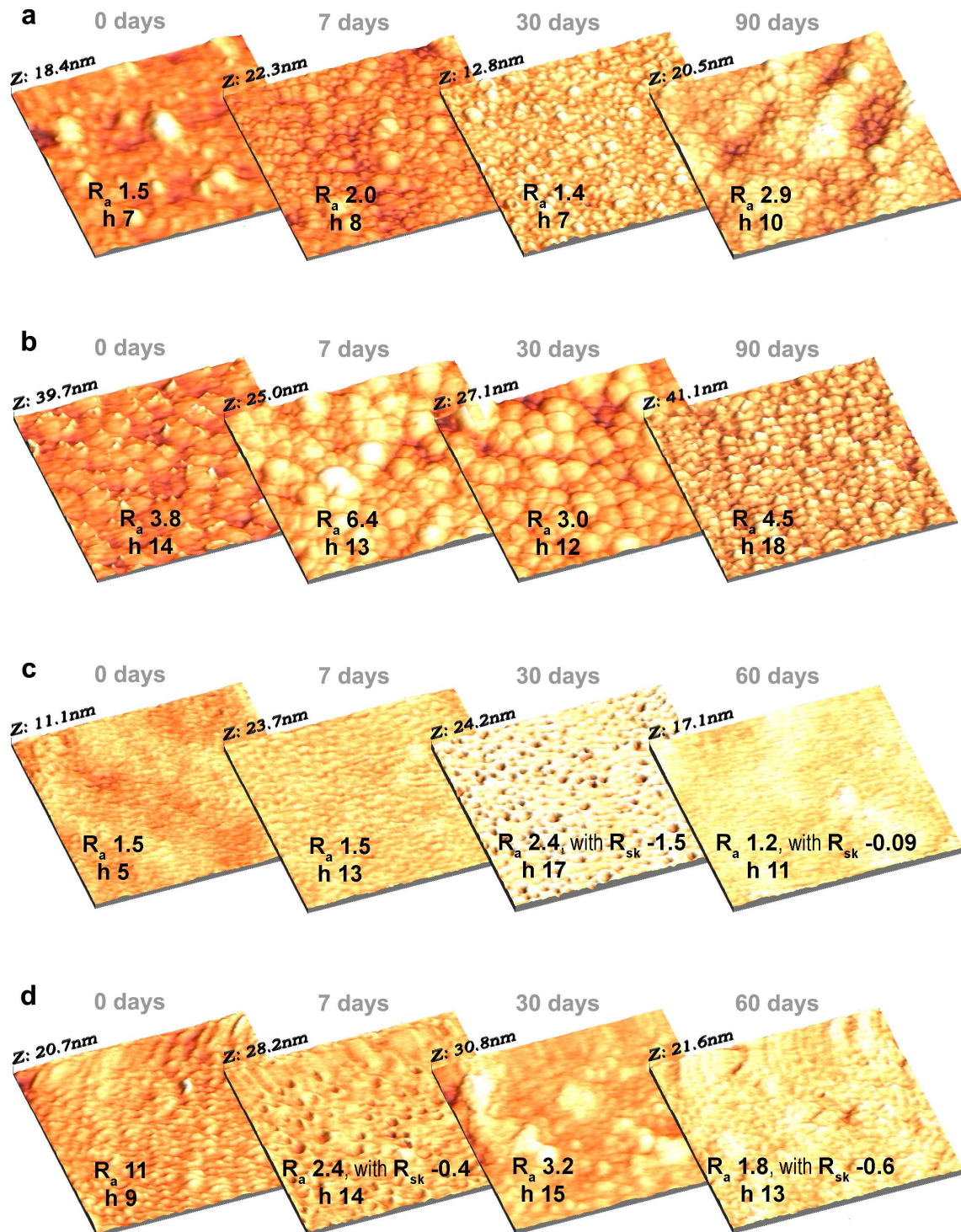


Figure 6.41 AFM $1 \times 1 \mu\text{m}$ images of the surface morphology evolution during immersion for the plasma polymerized **U** systems using the **R** plasma reactor: **a.** **UR3eP₅G**; **b.** **UR3eP₅P**; **c.** **UR4iP₄G**; and **d.** **UR4iP₄P**. The values in nm of R_a and h appear in the respective image.

Table 6.4 Composition evolution during immersion tests for the plasma polymerized **U** systems, values in at. %.

time (days)	UR3eP₅G		UR3eP₅P		UR4iP₄G		UR4iP₄P	
	fluorine	silicon	fluorine	silicon	fluorine	silicon	fluorine	silicon
0	69	0.4	47	0.6	47	0.4	46	0.7
7	54	0.3	44	0.6	56	0.05	53	0.7
30	48	0.4	46	0.7	56	0.04	50	0.5
60	55	0.2	45	0.7	58	0.04	51	0.6

The SEM micrographs of Figure 6.42, in the next two pages, show the surface morphology evolution with immersion of the plasma polymerized **E** systems, prepared using the two electrode locations during immersion.

Important surface variation is verified for the system **ER3eP₅G**, image **a**. The initial completely covered surface pores reappear after 7 days of immersion. Further immersion shows unchanged surface pores until 60 days of immersion.

The surface morphology evolution of the system **ER3eP₅P** is different, image **b**. Here, the surface agglomeration remains, but in some areas cracks appear together with parts showing surface layer removal.

The systems **ER4iP₄G** and **ER4iP₄P**, show surface degradation and formation of surface deposits for the first system, image **c**, while in the second, image **d**, surface degradation is also seen but without the formation of surface deposits. In these two systems, no cracks or areas with surface layer removal appear.

The surface composition evolution during immersion, obtained by EDS, of the plasma polymerized **E** systems using the **R** plasma reactor appears in Table 6.5.

During immersion, the systems **ER3eP₅G**, **ER3eP₅P** and **ER4iP₄G** have a continuous decrease trend of the silicon element content. This suggests dissolution of the plasma polymer film. After 60 days of immersion the silicon content for these three systems is similar to the silicon content of unmodified **E** coil coating, shown in Figure 5.9. This suggests complete dissolution of the plasma polymer film. Only the system **ER4iP₄P** maintains constant content of the silicon element during similar immersion period.

The surface results show that the plasma polymer film with the higher stability is the system **UR3eP₅P**, for **U** coil coating, and system **ER4iP₄P** for **E** coil coating. Both these systems show higher resistance to the immersion tests. However, these systems show the lowest barrier properties. This suggests that the formed plasma polymer film does not balance the negative influence of the plasma polymerization when the process is performed in the **P** electrode location.

The systems **UR3eP₅G** and **ER3eP₅G** show the best barrier properties, although the plasma polymer film suffers some degradation during immersion. These results suggest that the systems prepared in the **G** electrode location balance the plasma polymerization influence, sustaining their stability during long immersion periods.

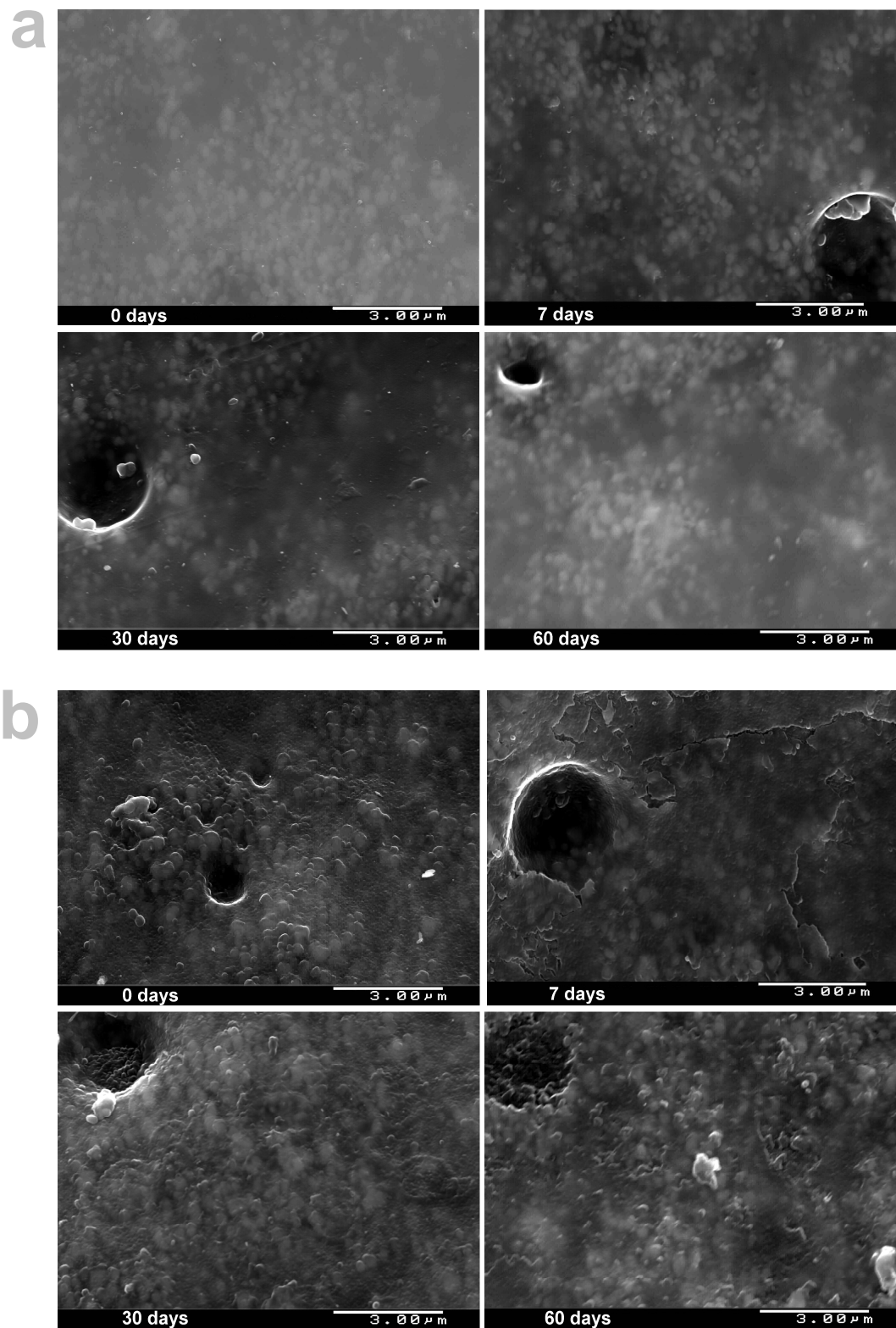


Figure 6.42 Surface morphology evolution during immersion tests for plasma polymerization of E systems using the R plasma reactor: **a.** ER3eP₅G; **b.** ER3eP₅P; **c.** ER4iP₄G; and **d.** ER4iP₄P.

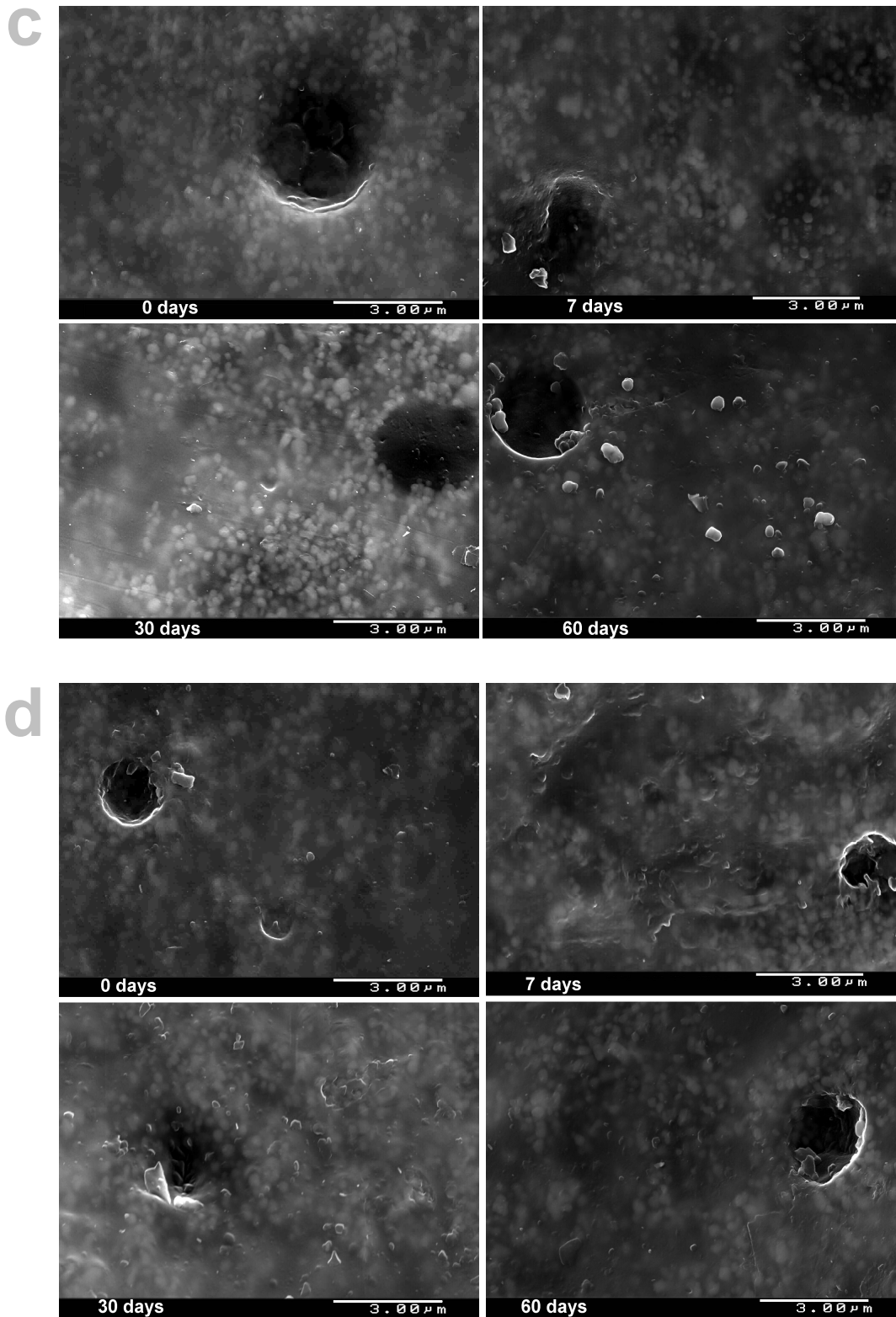


Figure 6.42 (cont.) Surface morphology evolution during immersion of plasma polymerized E systems using the R plasma reactor: a. ER3eP₅G; b. ER3eP₅P; c. ER4iP₄G; and d. ER4iP₄P.

Table 6.5 Composition evolution during immersion of the plasma polymerized **E** systems prepared in the **R** plasma reactor using the two electrode locations, values in at. %.

time (days)	ER3eP ₅ G			ER3eP ₅ P		
	aluminium	silicon	titanium	aluminium	silicon	titanium
0	1.0	3.6	26	0.9	4.1	21
7	1.0	3.4	25	0.8	3.7	23
30	1.0	3.4	25	0.9	3.7	21
60	0.9	2.9	20	0.8	2.7	26

time (days)	ER4iP ₄ G			ER4iP ₄ P		
	aluminium	silicon	titanium	aluminium	silicon	titanium
0	1.0	3.5	24	1.2	4.1	21
7	1.0	3.4	25	0.9	3.9	22
30	0.9	3.9	24	0.9	3.9	23
60	0.8	2.6	28	0.8	3.8	24

The tests on the plasma activated systems, presented in point 6.3.1, showed that stronger influence on the coil coating occurred when activation (stage **1**) takes place in the **G** electrode, showing faster degradation during immersion. However, after the plasma deposition step, these systems (the systems plasma polymerized in the **G** electrode) have the best performance. These results suggest that the plasma polymerization performed in the **G** electrode location following the plasma activation step generates a plasma polymer film that has the best properties, revealing to be the electrode location showing the best results.

v. Colour Coordinates

The CIE surface (x,y) reflection colour coordinates were measured for the plasma polymerized systems prepared in the **R** plasma reactor, Figure 6.43. The results obtained were compared with the CIE (x,y) colour coordinate of the respective unmodified coil coating used.

Only one CIE lab 1931 diagram with only one mark appears for the systems prepared in the **R** plasma reactor. This occurs since no variation of colour coordinates was obtained during the immersion tests, either for the different stage performed or for the two electrode location of the **R** plasma reactor. The colour coordinate appears in the centre of the CIE lab 1931 diagram, the white area, which is similar to the colour coordinate obtained for the unmodified **E** and **U** coil coatings.

The result has relation with the thickness of the plasma polymer film generated, which for these systems appears always lower than the minimal thickness necessary to induce interference with the systems colour, contrary to the **M** plasma polymerized **U** systems.

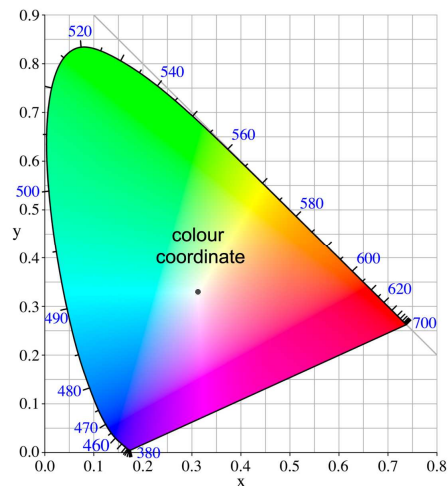


Figure 6.43 CIE chromaticity diagram (1931) coordinate for 2^o standard observer showing the (x,y) reflection colour coordinate for the plasma polymerized systems using the R plasma reactor.

6.4. Hollow Cathode Plasma Reactor

Although the H plasma reactor design permits continuous plasma polymerization process, for the sample preparation used in this work, performed in DOC facilities, the plasma polymerization used the static deposition arrangement. In this case, the set-up consists of two parallel metal substrates that form the hollow cathode. The advantage of the static deposition is to use a smaller size sample that allows fast exchange of samples and thus easier and faster coating development.

The plasma polymerization conditions used for the H plasma reactor are described in point 4.1.2.iii with the label used in Table 4.8.

6.4.1. EIS Results

The plasma polymerized system was tested using 0.5 M NaCl. The EIS results for the **UH2kP₆** system appear in Figure 6.44.

After immersion (1 hour), pure capacitive behaviour appears, with low frequency impedance value higher than 100 Gohm cm². The low frequency impedance value is comparable with the unmodified **U** coil coating of Figure 5.1, and representative of undamaged and defect free coating system that provide high protection to the metallic substrate.^{112;113;125}

The results show a decrease of the low frequency impedance after 8 days of immersion, together with the appearing of a low frequency resistive part. Increase of immersion time presents a noticeable drop of the low frequency impedance value and after 40 days of immersion one order of magnitude decrease appears, reaching 10 Gohm cm^2 . The curve format suggests that the water is in contact with the metallic substrate. ^{112;113;125}

Further increase of immersion time, 140 days (more than 4 months of immersion) does not show appreciable variation of the low frequency impedance value or of the curve format, suggesting constant performance during this period.

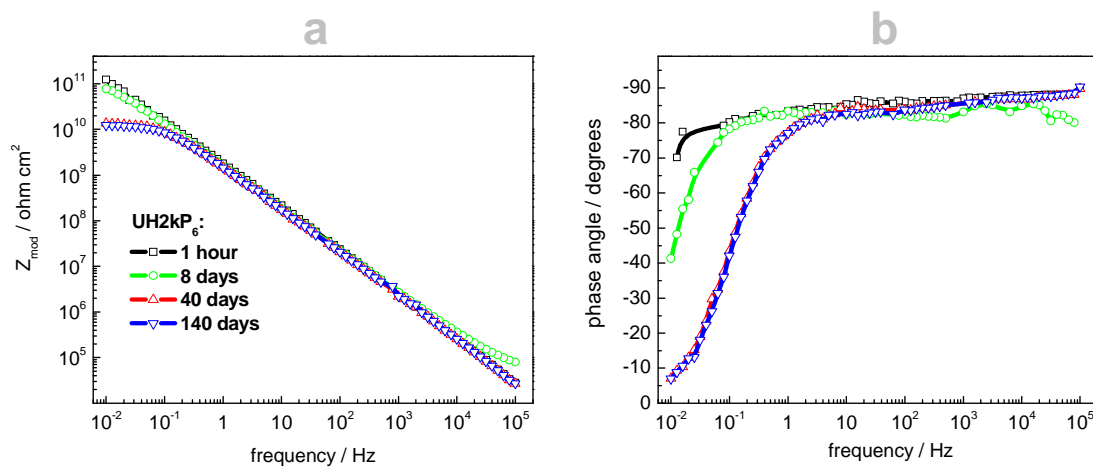


Figure 6.44 Impedance values evolution during immersion for the system UH2kP₆.

i. Numerical Fitting of EIS Data

The fitting was done using the electric circuit **a** of Figure 5.3, where R_{sol} is the electrolyte resistance, C_{coat} the coating capacitance and R_{por} the pore resistance.

In Figure 6.45 are the C_{coat} and R_{por} parameters evolution during immersion for the system UH2kP₆. The unmodified **U** coil coating results previously obtained serve as reference.

The initial instability of the system due to the fast processes occurring, surface pores and defects' filling up with water and ions, is higher for the system UH2kP₆ than for unmodified **U** coil coating. The coating capacitance, C_{coat} , is initially lower. However, after 15 days of immersion strong increase occurs, reaching identical value to the unmodified **U** coil coating. Further immersion does not show appreciable variation and the C_{coat} values remain unchanged.

The R_{por} value initially is unstable, rising and approaching the values of unmodified **U** coil coating. After 4 and until 10 days of immersion, accentuated decrease occurs attributed to

water and ions absorption, which are responsible by coating resistance decrease. Further immersion continues to show decrease of R_{por} value. The R_{por} decrease shows relation with the paint degradation and respective decrease of barrier effect, with consequent water and ions absorption.^{32;121;174} After 60 days of immersion, stabilization and even increase of the R_{por} value occurs.

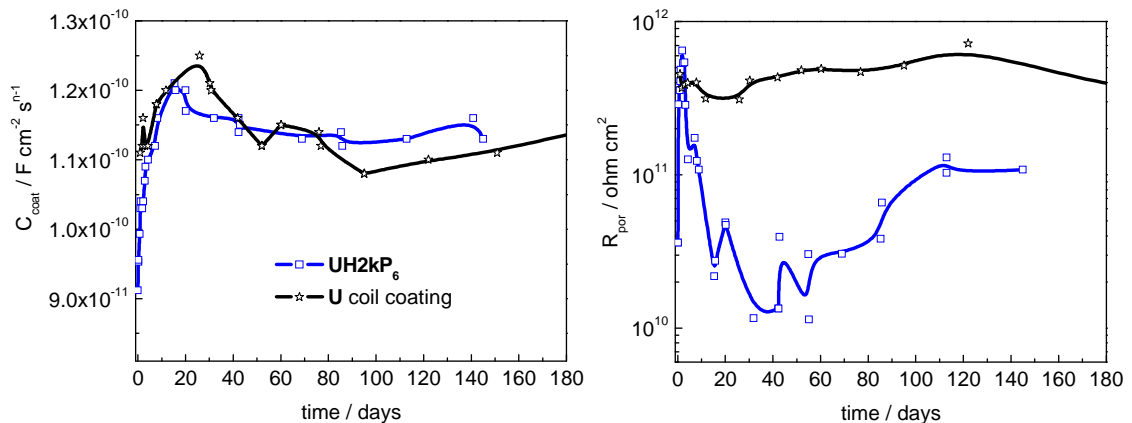


Figure 6.45 Evolution of C_{coat} and R_{por} parameters during immersion obtained by fitting the impedance results for the system **UH2kP₆**.

ii. Water Uptake

The variation of capacitance value permits the estimation of the system water uptake following the relationship of Brasher and Kingsbury,¹²⁸ using equation 3.13 with the procedure described in section 3.1.4. The results are in Figure 6.46.

The water uptake evolution for the system **UH2kP₆** appears different from previous plasma polymerized systems. Initial periods of immersion still show the fast water ingress, characteristic behaviour of organic coating systems.^{112;128;129} However, the water saturation level reached for the system **UH2kP₆** is lower, even lower than for unmodified **U** coil coating. This saturation level is unstable and shows continuous rising behaviour.

These results suggest that the **UH2kP₆** system has better barrier effect than the unmodified **U** coil coating. However, these water uptake results correspond only to the initial immersion time. The EIS results showed that higher degradation of the barrier ability during immersion for the system **UH2kP₆**.

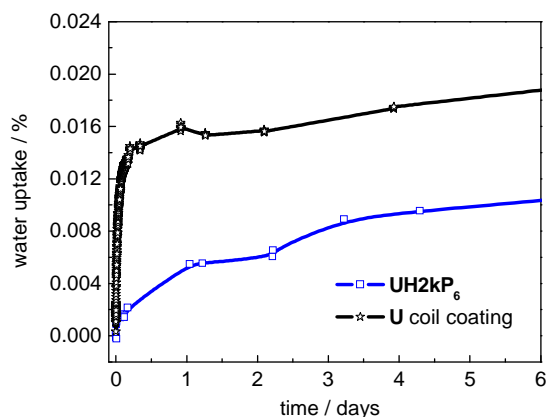


Figure 6.46 Water uptake evolution during immersion obtained from capacitance measurements, for the system **UH2kP₆**.

6.4.2. Plasma Polymer Film Characterization

i. Structure

The study of the structure of the plasma polymer film generated in the **H** plasma reactor was obtained with TEM. The plasma polymerization used TMS monomer, which is silicon based. This element has enough elemental weight for imaging by TEM following the procedure described in point 4.2.4 for sample preparation. The cross section micrograph of the plasma polymer film appears in Figure 6.47.

The structure of the plasma polymer film **UH2kP₆** is homogenous and amorphous with thickness of 410 nm showing particles with 60 nm diameter. In this case, the micrograph suggests that the particles are cylinders, with the 60 nm of diameter, crossing the full thickness of the plasma layer.

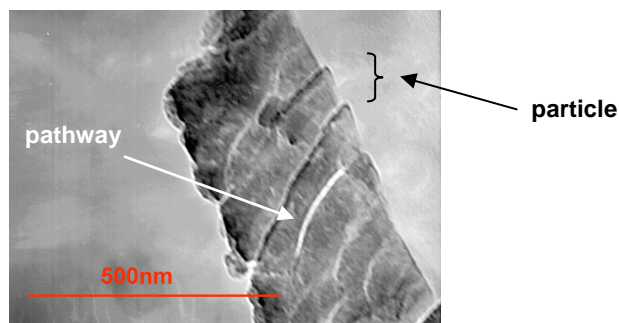


Figure 6.47 TEM cross-section micrograph of the system **UH2kP₆**.

ii. Surface Morphology

The AFM technique was used to study the system **UH2kP₆** surface morphology evolution during immersion, of the plasma polymer layer generated in the **H** plasma reactor. The R_a and h values calculated from the images, using the procedure described in point 4.2.5, appear in the respective images of Figure 6.48. The composition elemental quantification of the systems, acquired using EDS during immersion, appears in Table 6.6, values at. %.

The surface morphology obtained after the plasma polymerization but before immersion, appears in the Figure 6.48 with the label *0 days*. The system shows particulate surface morphology. The presence of negative R_{sk} suggests the presence of pores, attributed to the voids verified between the particles, which are visible in TEM micrograph of Figure 6.47. The surface granules diameter ranges from 40 to 70 nm, which agrees with the TEM micrograph particle size (corresponds to the cylinders diameter).

The initial composition of the **UH2kP₆** system shows carbon, chlorine, fluorine, oxygen and silicon elements. Similar to previous systems, the silicon arises only from the monomer and is the representative element of the plasma polymer film. The fluorine element content obtained is very low, when compared with the plasma polymer films prepared using the other plasma reactors, Table 6.1 and Table 6.4. The plasma polymer film higher thickness shows relation with this behaviour, since the noticed higher thickness leads to higher masking effect of the fluorine element EDS signal. The composition quantification shows higher silicon content than previous systems generated in the other plasma reactors, which corroborates higher masking effect.

During immersion, the surface morphology continues to show particles, maintaining similar diameter, however, the R_a and h parameters show that some variation occurs. A decrease of the values occurs during immersion and the R_{sk} changes to positive values. The composition results have a small decrease of fluorine element proportion after 7 days of immersion, which then also remains constant for longer immersion. The silicon element content is unchanged during immersion, Table 6.6.

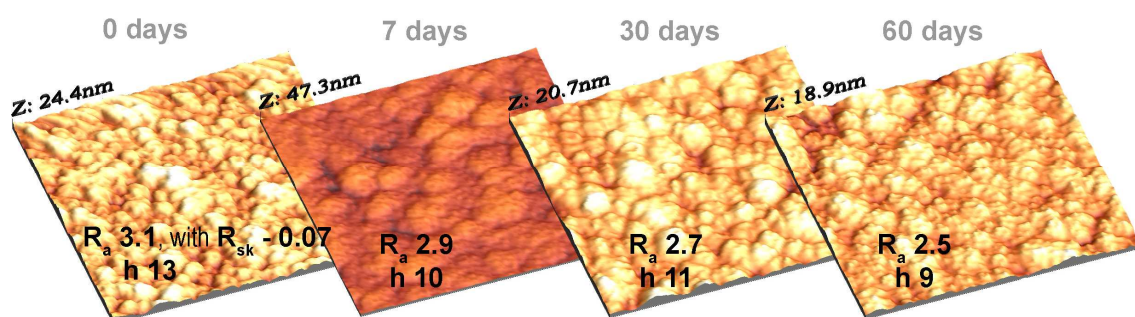


Figure 6.48 AFM $1 \times 1 \mu\text{m}$ images with the surface morphology evolution during immersion, for the system **UH2kP₆**, with the values in nm of R_a and h .

These results suggest that the plasma polymer film suffers modifications during immersion. The variation of R_{sk} values shows association with the surface voids, suggesting their blocking during immersion. The fluorine decrease suggests that the masking effect of the plasma polymer film increases during immersion and the constant silicon content is indication that dissolution of the plasma polymer film does not occur.

The results show that variation of the system **UH2kP₆** properties occurs during initial immersion period, however after longer immersion period the surface morphology stabilizes and remains constant.

Table 6.6 Surface composition evolution for the **UH2kP₆** system, quantification values in at. %.

time (days)	UH2kP₆	
	fluorine	silicon
0	29	3
7	21	3
30	21	3
60	22	3

Discussion

Section 7. Discussion

7.1. Introduction

Using the experimental results presented it is given here an overall analysis. The conditions tested were the two coil coating systems used, the plasma reactor, the combination of plasma polymerization steps, the reactor pressure, the plasma activation gas and time and the precursor mixture. These variables could affect the coating systems performance.

In this section, the correlation is made for each of the three plasma reactors. When the plasma polymerization conditions are similar, the results were associated for the different plasma reactors.

The systems degradation is assessed through the low frequency part of the EIS spectra, as described in point 3.1.3.iii, and one parameter to monitor the evolution of the degradation is the modulus of impedance at 0.1 Hz ($|Z|_{0.1 \text{ Hz}}$), taken from the experimental impedance measurements performed during immersion.

The unmodified coil coatings tested are very high performance paint systems and the initial impedance response refers to the coating capacitance. In this case, the low frequency part quantifies the systems barrier properties. Only after very long testing period does a resistive part appear that allows comparison of the level of coating degradation for the systems under study.

The systems modified by the plasma polymerization process show in general faster degradation in immersion. In these systems, the low frequency resistive part appears earlier. The resistive part arises from the influence of the plasma polymerization process on the barrier properties of the coil coating system that leads to an increase of water uptake. During immersion further increase of the system resistive part occurs. This increase is associated with decrease of the low frequency impedance value, which is dependent of the plasma polymerization process parameters tested.

For initial stages of immersion, the $|Z|_{0.1 \text{ Hz}}$ value corresponds to the coating capacitance that is influenced by the water and ions absorption. When higher degree of degradation appears, and the resistive part is formed, the $|Z|_{0.1 \text{ Hz}}$ corresponds to the coating resistance. Thus, $|Z|_{0.1 \text{ Hz}}$ is a good parameter to monitor the degradation and compare the performance of the plasma polymerized systems.

In such high performance systems, testing procedures that accelerate the degradation are necessary. These tests allow faster knowledge of the systems properties. Without such accelerated tests, the time to obtain the results becomes unacceptably long. Long term testing of the real performance is also important, permitting the relation between the experimental laboratorial results with the real world behaviour, however, not feasible for the PhD time frame.¹⁸⁸ One important point when performing accelerated tests is to verify that the degradation mechanisms are unchanged due to the testing conditions used.

In this work, the conditions of testing employed did not show variation of the degradation mechanism. Instead, increase of degradation rate occurs and important highlights concerning the influence of the plasma polymerization parameters could be gathered.

One good example is the EIS results for the systems **UM2eP₂** of Figure 6.7a and **45UM2gP₂** of Figure 6.9.

The system **45UM2gP₂** is tested at higher temperature and the plot format is identical to the one obtained for the system **UM2eP₂**. This suggests that these two systems have similar degradation mechanism. The high temperature tests permitted faster screening of the system performance, which was not possible at ambient temperature testing, system **UM2gP₂** shown in Figure 6.8b, allowing faster assessment of the system performance.

7.2. Coil Coating

The Figure 7.1 shows the $|Z|_{0.1 \text{ Hz}}$ evolution during immersion for the coil coatings without any plasma treatment - unmodified coil coatings. The two coil coatings are industrial high performance paints, showing high thickness, where strong variations of the properties due to degradation, at least for the relatively short immersion period, are not expected.

The **E** coil coating has poorer performance and the $|Z|_{0.1 \text{ Hz}}$ is lower since the beginning of the immersion tests, Figure 7.1. Immediately after immersion, the $|Z|_{0.1 \text{ Hz}}$ is under 4 Gohm cm^2 . This is near one order of magnitude lower than for the **U** coil coating, which shows $|Z|_{0.1 \text{ Hz}}$ higher than 10 Gohm cm^2 . Initial immersion shows a substantial drop of the $|Z|_{0.1 \text{ Hz}}$ value to less than 2 Gohm cm^2 . This initial decrease of impedance occurs related with initial absorption processes, filling up with electrolyte the surface pores and holidays present in the coating system. These pores are formed during the coil coating application and are visible in SEM images of Figure 5.8. The TEM image of Figure 6.36b shows that the holidays also exist internally.

Reaction of the coating components with electrolyte occurs, forming surface deposits during immersion, visible in the SEM images of Figure 5.8. These deposits can also occur in the coating internal pores and pathways, blocking the access to further water and ions. Dissolution of the internal deposits may also occur and the blocking effect lost.

The blocking/unblocking processes are responsible by some instability of the impedance values with progress of immersion tests. This period corresponds to the $|Z|_{0.1 \text{ Hz}}$ plateau obtained until the 90 days of immersion, where the values are not exactly stable but, instead, change slightly related with the blocking/unblocking processes. For longer immersion period, the blocking effect starts to decrease and the water absorption proceeds, leading to the steady decrease of the $|Z|_{0.1 \text{ Hz}}$ value observed. The Bode plot curve format of Figure 5.2 and the impedance value after 130 days of immersion suggest that the metallic substrate is in direct contact with the testing solution. This has strong effect in the impedance response, which after 130 days of immersion shows a $|Z|_{0.1 \text{ Hz}}$ value decrease of almost one order of magnitude, reaching 600 Mohm cm^2 . Nevertheless, the system shows constant composition during immersion (Figure 5.9) suggesting that the barrier properties decrease but the coating continues to be present, without corrosion of the metallic substrate.

For the **U** coil coating, the $|Z|_{0.1 \text{ Hz}}$ evolution is an almost straight line at the 10 Gohm cm^2 value during 300 days (10 months) of immersion, Figure 7.1. Acceleration of the **U** coil coating degradation, obtained with the increase of the testing temperature to 45° C, **45U** line in Figure 7.1, shows small decrease of the $|Z|_{0.1 \text{ Hz}}$ value for long immersion time. In this case, the value starts to decrease after 160 days (5 months) of immersion and after 330 days (11 months) reaches 6 Gohm cm^2 . The surface characterization results show that the system has constant surface properties, with the AFM images of Figure 5.7 showing very small variation of the surface morphology during immersion together with constant composition, shown in the table of Figure 5.9. These results are representative of a stable **U** coil coating during the immersion tests.

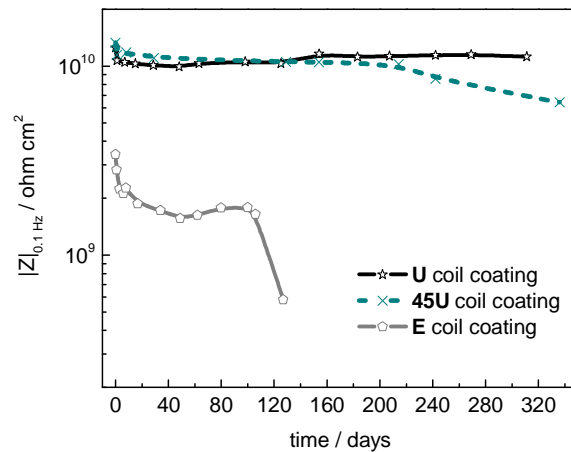


Figure 7.1 Evolution of the $|Z|_{0.1 \text{ Hz}}$ values during immersion tests for the unmodified **E** and **U** coil coatings.

The high anticorrosive protection found in **U** coil coating and lower protection (compared with **U** coil coating) offered by the **E** coil coating appear from the barrier effect of the coating, i.e. the paint capacity for delaying the aggressive species diffusion up to the metal/paint interface. The proposed degradation mechanism appears schematically in Figure 7.2.

In agreement with this scheme, it is assumed that the metal surface is effectively maintained isolated from the 0.5 M NaCl testing solution during the immersion test period for **U** system, scheme **a**. The pores and holidays of **E** coil coating decrease the barrier effect permitting that water and ions reach the metal surface, scheme **b**. However, visual inspection of the systems after the testing shows that neither of them shows destruction of the coating. Both also show no signs of swelling or detached parts.

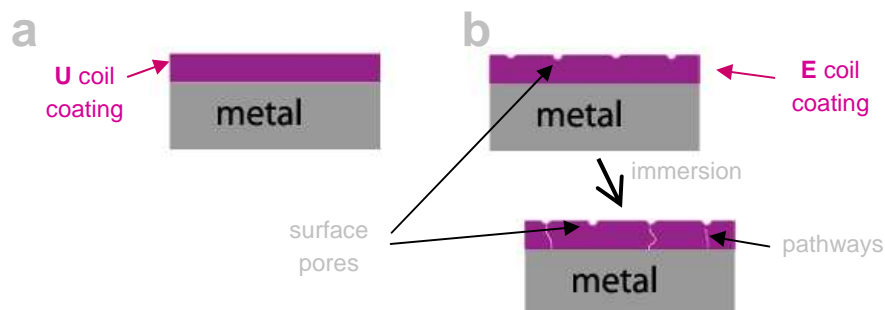


Figure 7.2 Degradation mechanism scheme for the unmodified coil coatings; **a. U**; and **b. E**.

7.3. Plasma Activation

The results show that important degradation of the coil coating occurs during the plasma activation step. The degradation is dependent of the plasma reactor and of the correspondent operation conditions appearing evident influence on the coil coating performance. The plasma activation step is used for cleaning and enhancement of the adhesion of the plasma polymer film. However, if the influence on the coil coating is in too high extent, degradation of the final performance of the systems occurs.

7.3.1. Activation Time and Carrier Gas

For the plasma activation stage performed in the **M** plasma reactor, the step duration and the carrier gas used were modified in order to test their influence in the coil coating barrier properties. The $|Z|_{0.1 \text{ Hz}}$ evolution of the plasma activated **U** systems using the **M** plasma reactor appears in Figure 7.3.

During the tests of the **M** plasma activated systems, the system **UM1dP₁** shows higher water uptake, Figure 6.3, together with high C_{coat} values, Figure 6.2, suggesting high degradation. This is in disagreement with the impedance results, Figure 6.1, and R_{por} behaviour, Figure 6.2, which suggest that the performance is maintained during immersion. The $|Z|_{0.1 \text{ Hz}}$ evolution also shows that the system has good behaviour, showing values close to the unmodified **U** coil coating.

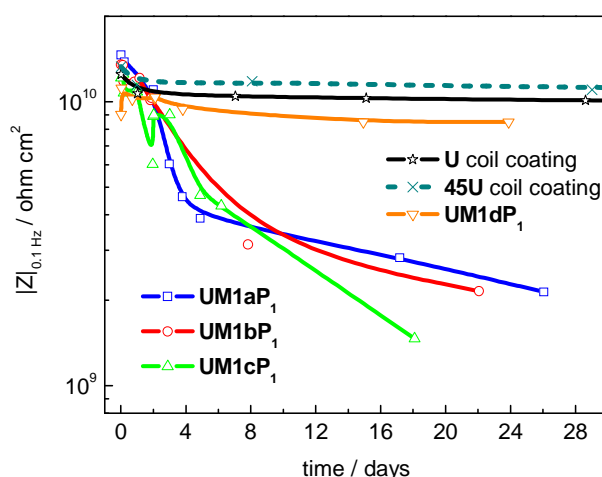


Figure 7.3 $|Z|_{0.1 \text{ Hz}}$ evolution during immersion of the plasma activated systems using the **M** plasma reactor.

As said in the beginning of this section, in point 7.1, the surface characterization can explain the results. During the plasma activation of the coil coating surface with argon, system **UM1dP₁**, hydrogen and low molecular weight compounds are removed from the surface layers.^{46;168} Since the coil coating is an organic base paint, these compounds are low molecular weight hydrocarbon compounds. This removal is responsible by variation of the surface morphology and by modification of the surface properties of the coil coating. The AFM parameters confirm that variation of the surface morphology occurs, Figure 6.4d. This variation of the surface properties may interfere with the C_{coat} values calculation, leading to the higher values noticed, which also influences the water uptake calculation, since the capacitance values are used to obtain the water uptake.

Upon contact with the testing solution new reactions may occur, changing once again the surface properties of the system **UM1dP₁**. This leads to further variation of the surface morphology that is noticed in Figure 6.5d. In this system, water can fill surface defects created but, since there are no complete pathways until the metallic surface, the ingress of water and ions continues to be limited by the barrier effect of the paint, i.e. the **U** coil coating barrier properties are not completely lost.

In Figure 7.4 is shown schematically the surface reactions that occur during the argon plasma activation. In the degradation scheme, the degradation of the plasma activation stage is represented as defects created in the coil coating surface.

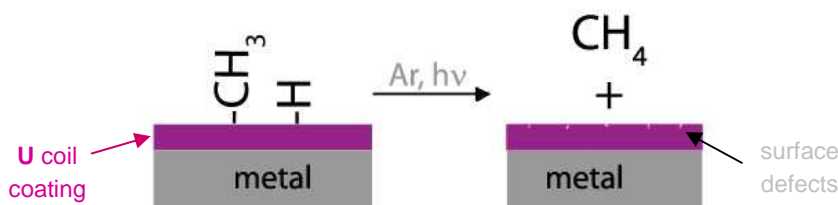


Figure 7.4 Degradation scheme of the plasma activation with argon, system **UM1dP₁**.

The same procedure but using oxygen (systems **UM1aP₁**, **UM1bP₁** and **UM1cP₁**), on the other hand, leads to higher and faster decrease of performance, as shown by pore resistance results of Figure 6.2. The $|Z|_{0.1 \text{ Hz}}$ shows that the degradation is continuous decreasing since the beginning of the immersion.

In this case, the surface characterization shows different influence, suggesting the formation of surface pores (negative R_{sk} values), images **a**, **b** and **c** in Figure 6.4. During immersion, the surface defects are maintained, images **a**, **b** and **c** in Figure 6.5. The plasma activation with oxygen consists of an oxidative step, where removal of organic components from the coating surface occurs. Surface enrichment with oxygen bonds is also obtained. New surface oxygenated carbon functionalities formed change the surface

interfacial properties.^{46,168} At the same time, pathways through the coating prolong the pores formed in the surface during immersion. These facilitate the ingress of electrolyte.

The scheme of Figure 7.5 shows the proposed activation mechanism for the surface reactions after oxygen plasma activation. In the scheme appear the pores and pathways across the coil coating representing the plasma activation influence.

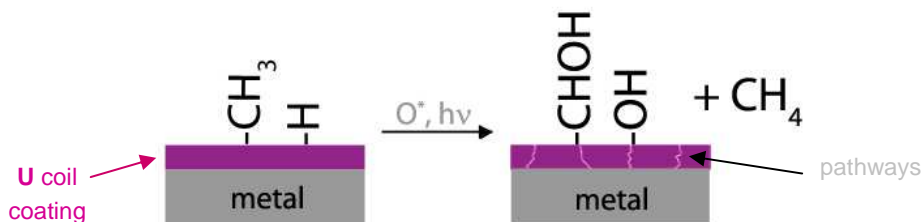


Figure 7.5 Degradation mechanism scheme for plasma activation with oxygen of the **U** systems.

The time of the plasma activation also has influence in the final properties. The results show that longer plasma activation with oxygen leads to higher degradation and consequently lower performance during immersion. This is clear in the $|Z|_{0.1 \text{ Hz}}$ evolution shown in Figure 7.3.

The results show that the two different gases produce different surface variation due to different surface reactions. However, plasma activation with argon shows milder influence, and consequently the destruction of the coil coating barrier effect is lower.

7.3.2. Electrode Location

The evolution of the $|Z|_{0.1 \text{ Hz}}$ during immersion, for the **R** plasma activated **E** and **U** systems, appears in Figure 7.6. For the **U** system, where comparison is possible, the values show that the process has quite lower influence on the barrier properties of the coil coating than similar step performed using the **M** plasma reactor. Degradation still occurs in the two **E** and **U** coil coatings used, dependent of the sample location inside the **R** plasma reactor.

The plasma activation of the **E** coil coating shows that the system **ER1hP₄P** has identical $|Z|_{0.1 \text{ Hz}}$ values to unmodified **E** coil coating. The system **ER1hP₄G** shows higher influence and during immersion has continuous faster decrease of $|Z|_{0.1 \text{ Hz}}$ values. After 20 days of immersion, the degradation is already very high, introducing interference to the EIS

measurements and producing unreliable results. The SEM micrographs of Figure 6.29a show new smaller surface pores after the plasma activation for the system **ER1hP₄G**. During immersion appear areas with complete removal of parts of the surface layer. For the system **ER1hP₄P** neither the smaller surface pores appear nor removal of parts from the surface layer occurs. Only surface scratches features appear during immersion. The numerical fitting of the impedance results show that the system **ER1hP₄P** has evolution during immersion similar to **E** coil coating, while the system **ER1hP₄G** has stronger decrease of performance during immersion, Figure 6.22d, in agreement with the $|Z|_{0.1 \text{ Hz}}$ evolution. In this second system, fast degradation occurs after 17 days of immersion. The Bode plot of Figure 6.20 at this time of immersion shows impedance values and curve format that suggest the existence of direct contact of water and ions with the metallic substrate.

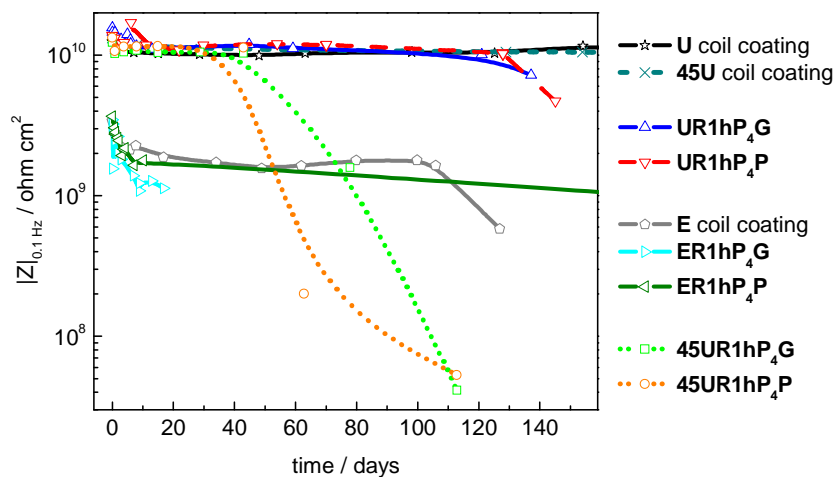


Figure 7.6 $|Z|_{0.1 \text{ Hz}}$ evolution during immersion of the plasma activated systems using the **R** plasma reactor.

The decrease of performance shows relation with the influence of the oxygen on the surface layers and with the presence of the surface pores of the **E** coil coating. Oxidation of the surface layers occurs, forming oxygen functionalities and pores/pathways, which decrease the barrier properties.

The degradation mechanism corresponds to the combination of the degradation mechanism for the unmodified **E** coil coating (Figure 7.2b), where the surface pores are the degradation factor, with the one for the plasma activation with oxygen (Figure 7.5), where the surface defects created during the plasma activation with oxygen are the degradation factor. The respective scheme showing the combination of these two degradation mechanisms for the plasma activated **E** systems appears in Figure 7.7. The plasma activation has stronger influence for the systems plasma activated in the **G** electrode.

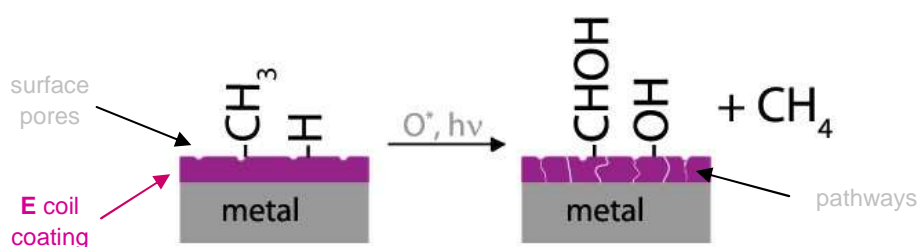


Figure 7.7 Degradation mechanism scheme for **R** plasma activation of **E** systems with oxygen.

Plasma activated **U** systems in **R** plasma reactor required high temperature immersion to produce detectable changes. At ambient temperature no variation of the properties occurs, producing identical response to the **U** coil coating until 120 days of immersion test. Only then, a small decrease of $|Z|_{0.1 \text{ Hz}}$ values appears, Figure 7.6.

Until 30 days of testing at higher temperature, systems **45UR1hP₄G** and **45UR1hP₄P**, show coincident $|Z|_{0.1 \text{ Hz}}$ evolution to unmodified **U** coil coating, Figure 7.6. Only after 40 days of immersion does a strong drop of $|Z|_{0.1 \text{ Hz}}$ appears, attributed to system degradation. The degradation continues and after 110 days of immersion at 45 °C, the $|Z|_{0.1 \text{ Hz}}$ values reach 3 Mohm cm² for the **G** electrode and 10 Mohm cm² for the **P** electrode. This is a significant decrease of impedance, suggesting that active corrosion processes on the metallic surface may soon appear.

The surface characterization of the systems **UR1hP₄G** and **UR1hP₄P**, AFM images of Figure 6.28, show negative R_{sk} values, which are representative of the formation of surface pores. The system **UR1hP₄G** has stronger surface morphology variation during immersion, showing also higher variation of the R_{sk} parameter.

The decrease of performance shows relation with the influence of the oxygen on the interfacial surface layers. The degradation mechanism is similar to the scheme of Figure 7.5, where oxygen functionalities are introduced in the surface. The degradation is stronger again when the specimen is treated in the **G** electrode location, similar to the plasma activated **E** systems.

7.4. Plasma Polymer Film Deposition

Evolution of the $|Z|_{0.1 \text{ Hz}}$ for the plasma polymerized systems shows that the plasma polymer film is able to annul the negative influence of the plasma activation step. The respective protection offered during immersion depends on the experimental conditions used during the plasma polymerization process. As a result, the performance of each system during immersion can be associated with the experimental conditions, the plasma polymerization steps and the coil coating to be treated.

For the **M** plasma reactor the pressure reduction and the oxygen availability during the process were tested. Both variables lead to variation of the systems performance. Modification of the precursor mixture also adds important surface characteristics, which influence the systems performance.

The **R** plasma reactor used always the same plasma polymerization experimental conditions, however the systems performance is dependent of the stage and of the electrode location used for the treatment. Both parameters influence the two coil coatings used, **U** and **E** systems.

In the **H** plasma reactor, TMS and oxygen precursor mixture was used for the treatment. In this case, the reactor was designed to test high rate continuous deposition, however, for easier handling of the specimens, the static deposition set-up was used instead.

7.4.1. Pressure, Oxygen Availability and Monomer

For the **M** plasma reactor the $|Z|_{0.1 \text{ Hz}}$ evolution during immersion of the plasma polymerized systems appears in Figure 7.8

The systems **UM2eP₂** and **UM2eP₃** were prepared using oxygen and HMDSO precursor mixture, at two plasma polymerization pressures, **P₂** and **P₃**. Both systems show continuous decrease of the $|Z|_{0.1 \text{ Hz}}$ values during immersion, with identical degradation rate until 80 days of immersion. From this point, the degradation rate increases for the system **UM2eP₂** and after 100 days of immersion shows $|Z|_{0.1 \text{ Hz}}$ values of 1 Gohm cm². The system **UM2eP₃** maintains the initial decrease rate during immersion and after 140 days, the $|Z|_{0.1 \text{ Hz}}$ reaches 5 Gohm cm².

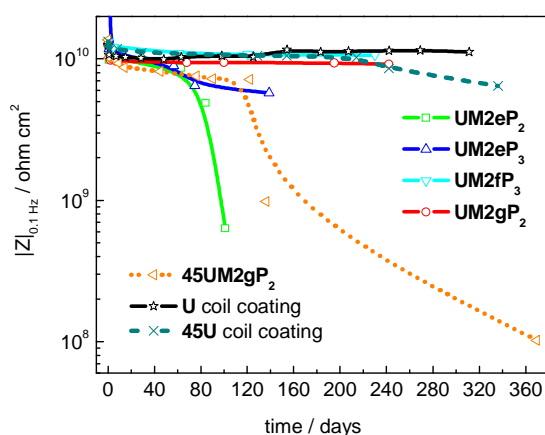


Figure 7.8 Evolution of the $|Z|_{0.1 \text{ Hz}}$ during immersion for the plasma polymerization performed in **M** plasma reactor.

The fitting procedure for these two systems, shown in Figure 6.10, corroborates the $|Z|_{0.1 \text{ Hz}}$ results, showing continuous degradation during the immersion tests. The structure and surface characterization results, shown in point 6.2.2.ii, clarify the mechanism responsible by the degradation. The TEM micrographs **a** and **b** of Figure 6.12 show similar particulate structure for these two systems, where are visible pathways between the particles constituting the plasma polymer layer. These pathways offer direct access to water and ions across the plasma polymer layer until the coil coating interface.

The AFM images of Figure 6.15**a** and **b** show that the plasma polymer layer is unstable during immersion. Moreover, the EDS results of Table 6.1 show a decrease of silica element proportion, which suggests dissolution of the plasma polymer layer during immersion. The dissolution of the plasma polymer film leaves exposed the **U** coil coating, which during the plasma activation step suffered degradation of their barrier properties. Now, without the protection of the plasma polymer layer, strong degradation occurs, which is responsible by the system degradation and steady decrease of $|Z|_{0.1 \text{ Hz}}$ values.

These surface characterization results show that the system **UM2eP₂** has always faster and stronger variation of the parameters and that the system **UM2eP₃** has higher resistance to dissolution. This is attributed to the decrease of the plasma polymerization pressure. According to this, the pressure used in the plasma polymerization has influence on the properties of the plasma polymer film produced. The Figure 7.9 shows schematically the proposed degradation mechanism for these two systems, **UM2eP₂** and **UM2eP₃**, prepared using HMDSO and oxygen precursor mixture.

The initial plasma activation step with oxygen leads to degradation of the coil coating, point 7.3.1. The plasma polymer film initially annuls this degradation, but during the immersion tests, dissolution of the plasma polymer film occurs. As soon as the dissolution of the plasma polymer film is complete, the degradation of the barrier properties increases, decreasing the systems performance.

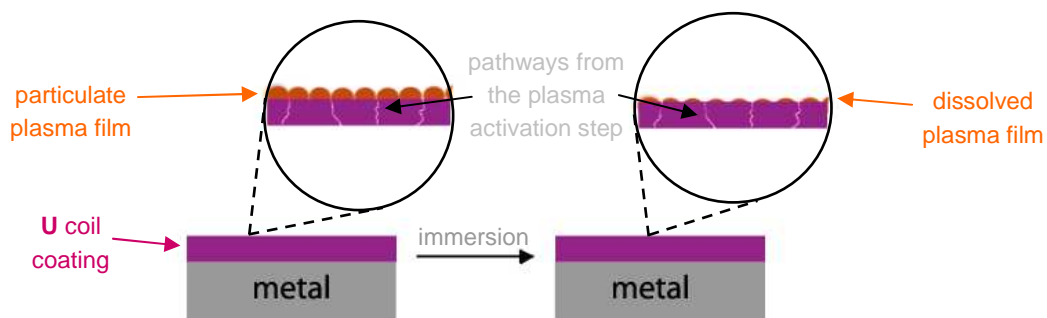


Figure 7.9 Degradation mechanism of the **M** plasma polymerization with HMDSO and oxygen.

Replacing the oxygen carrier gas by argon, system **UM2fP₃** prepared with HMDSO and argon precursor mixture, shows significant increase of performance. The $|Z|_{0.1 \text{ Hz}}$ plot shows constant values during immersion, which keeps very close to the unmodified **U** coil

coating, Figure 7.8. The characterization of the system shows that the structure of the plasma polymer film is compact without voids or particles, TEM micrograph **c** of Figure 6.12. Particulate surface morphology is obtained, as shown by the AFM image **c** of Figure 6.15. However, in this case, these particles are stable during immersion. Moreover, the silica content of the film remains unchanged during immersion, EDS results of Table 6.1. All together, these results suggest the formation of a stable and high performance system. The numerical fitting results for the system **UM2fP₃**, of Figure 6.10, also suggest high stability of the system, showing values close to the unmodified **U** coil coating.

In Figure 7.10 is proposed the degradation scheme for the system **UM2fP₃**. The plasma polymer film formed is stable during immersion and the absence of pathways in the plasma polymer layer limits the water ingress, decreasing the quantity of ions penetrating until the coil coating matrix. On the other hand, the plasma activation step, in this case, used argon that also has milder influence on the coil coating barrier properties, point 7.3.1. These two factors contribute to the system higher performance. Another stability factor is the lower plasma polymerization pressure, which also increases the systems performance.

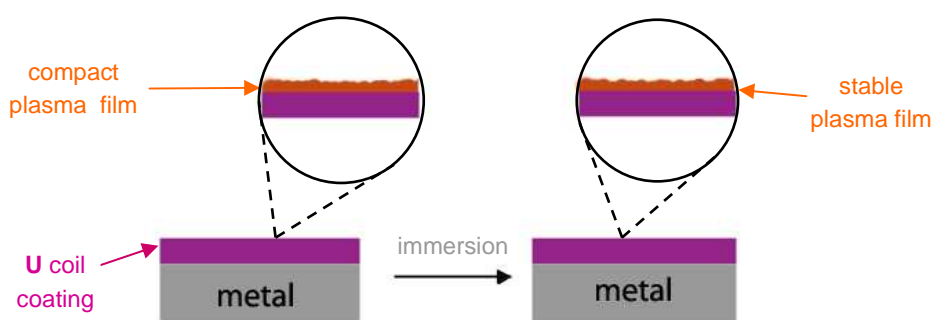


Figure 7.10 Degradation mechanism of the **M** plasma polymerized **U** system using HMDSO and argon precursor mixture.

The addition of HDFD monomer to the HMDSO and argon precursor mixture, system **UM2gP₂**, as said before, forms a hydrophobic surface.¹⁸⁷ The evolution of the $|Z|_{0.1 \text{ Hz}}$ values, in Figure 7.8, shows that the system has stable behaviour during immersion, comparable to the performance of the unmodified **U** coil coating. The characterization of this system shows that the plasma polymer film generated has compact structure without visible particles or voids, but with higher thickness, TEM micrograph **d** of Figure 6.12. The surface morphology results show that the plasma polymer film is stable during immersion but not particulate, AFM images **d** of Figure 6.15. Instead, the surface morphology suggests agglomeration of smaller particles. The plasma polymer stability during immersion is corroborated by the EDS results of Table 6.1, where stable element content is obtained. The proposed degradation scheme for this system is identical to the one in Figure 7.10.

An important remark from the results is that the plasma polymerization procedure performed in **M** plasma reactor could influence the coil coating, leading to degradation of their barrier properties. From the tested experimental parameters, the pressure reduction shows a small improvement of the systems performance. However, the replacement of oxygen carrier gas by argon leads to higher increase of performance. This is verified with the system **UM2fP₃**, which shows similar performance to unmodified **U** coil coating. The high performance is attributed to the combined effect of the pressure reduction with the decrease of oxygen availability (argon replaced oxygen) during the plasma polymerization process. The system **UM2gP₂** also shows good performance during immersion, however with lower barrier properties than system **UM2efP₃**. This can be attributed to the higher pressure used during the plasma polymerization.

7.4.2. Electrode Location and Steps Combination

The evolution of the $|Z|_{0.1 \text{ Hz}}$ values for the systems prepared in the **R** plasma reactor appears in Figure 7.11. The testing used the two coil coatings, **E** and **U**, both submitted to the plasma polymerization process on the two electrode location of the **R** plasma reactor, with oxygen and HMDSO precursor mixture.

The $|Z|_{0.1 \text{ Hz}}$ results for the plasma polymerization using the **E** coil coating shows initially almost one order of magnitude shift when compared with the plasma polymerized **U** systems. This is similar result to the unmodified coil coatings, point 7.2.

The plasma polymerized **E** systems using the **P** electrode, systems **ER3eP₅P** and **ER4iP₄P**, have very fast decrease of performance, Figure 7.11b. After only a few days of immersion, two orders of magnitude decrease of the $|Z|_{0.1 \text{ Hz}}$ values occurs, reaching 30 Mohm cm². The SEM images **b** and **d** of Figure 6.42, with the evolution of the surface morphology, show the removal of parts of the surface and formation of surface cracks during immersion. The EDS results corroborate the degradation and show variation of the composition, Table 6.5, with decrease of the silicon element (smaller decrease for the system **ER4iP₄P**). These results suggest that the adhesion of the plasma polymer film to the **E** coil coating is low, resulting in film detachment, which leaves the **E** coil coating uncovered and exposed to the testing environment.

The plasma polymerization of the **E** systems using the **G** electrode, systems **ER3eP₅G** and **ER4iP₄G**, have more stable behaviour during immersion, with evolution of $|Z|_{0.1 \text{ Hz}}$ values similar to the unmodified **E** coil coating, Figure 7.11b. During initial 60 days of immersion, the $|Z|_{0.1 \text{ Hz}}$ value of system **ER3eP₅G** is even higher than for unmodified **E** coil coating. This is attributed to improvement of the system performance obtained with the deposition of the plasma polymer layer. During further immersion, the values becomes lower but still close to unmodified **E** coil coating, reaching 500 Mohm cm² after 120 days (4 months) of immersion. The initial surface morphology of this system shows complete covering of the surface pores, Figure 6.39a. This corroborates the increase of $|Z|_{0.1 \text{ Hz}}$ value and respective

increase of performance. The surface pores reappear after 7 days of immersion but complete dissolution of the plasma polymer film is only noticed after 60 days of immersion, EDS composition results of Table 6.5. This corroborates the $|Z|_{0.1 \text{ Hz}}$ decrease behaviour, which after 60 days of immersion becomes lower than the correspondent unmodified **E** coil coating, following the plasma polymer film dissolution.

The system **ER4iP₄G** maintains the $|Z|_{0.1 \text{ Hz}}$ value similar to unmodified **E** coil coating, reaching 1 Gohm cm² after 70 days of immersion, similar to the value of system **ER3eP₅G** at that time of immersion. The surface morphology evolution for the system appears in Figure 6.42c. Here, surface deposits are formed after 60 days of immersion. The EDS composition results of Table 6.5, show similar decrease of the silicon element content during immersion to system **ER3eP₅G**, suggesting dissolution of the plasma polymer film.

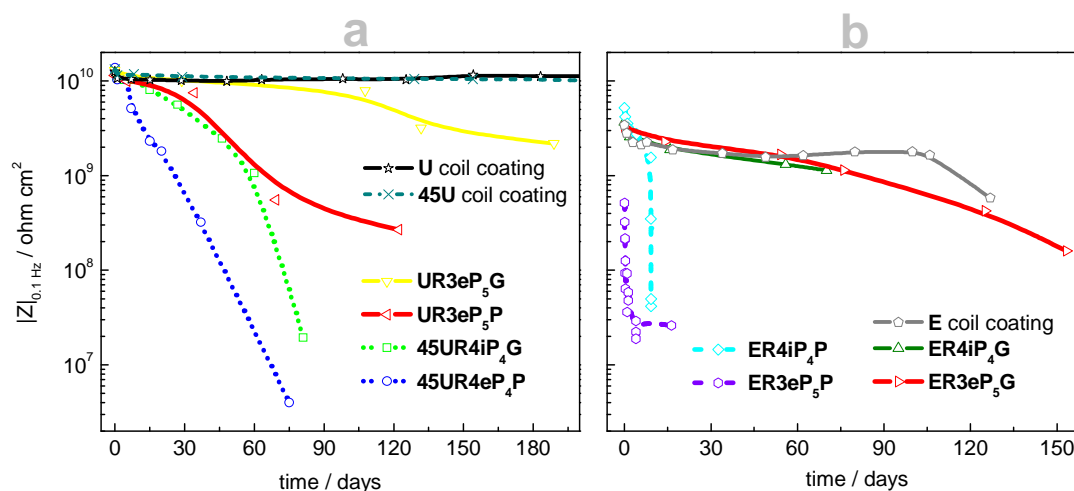


Figure 7.11 Evolution of the $|Z|_{0.1 \text{ Hz}}$ values during immersion for the plasma polymerized systems in R plasma reactor, using: **a.** U coil coating; and **b.** E coil coating.

All these systems, **ER3eP₅G**, **ER3eP₅P**, **ER4iP₄G** and **ER4iP₄P**, show surface degradation and composition variation. The partial dissolution leaves the **E** coil coating surface more prone to be reached by the testing environment. The systems **ER3eP₅G** and **ER3eP₅P** were submitted to the plasma activation step, which also leads to degradation of the barrier properties of the coil coating, as shown in point 7.3.2.

The general degradation mechanism is similar for all the plasma polymerized **E** systems and appears schematically in Figure 7.12.

The two systems prepared in **P** electrode show higher degradation, much faster than for unmodified **E** coil coating. The results show dissolution and detachment of surface layers that opens the way for water and ions absorption until the coil coating interface. The **E** coil coating pores are another degradation factor, increasing the degradation. The addition of these two degradation processes leads to very fast degradation during immersion. To the

behaviour of the system **ER3eP₅P**, also adds the influence of the plasma activation step, which increases further the degradation, as noticed in Figure 7.11b.

The degradation of the systems prepared in the **G** electrode show different evolution. Partial dissolution of the plasma polymer film also occurs during testing but the degradation rate is always slower than for the plasma polymerization performed in the **P** electrode. The results suggest that the plasma polymer film prepared in the **G** electrode is able to annul the influence of the plasma activation and the prepared systems maintain similar performance to the unmodified **E** coil coating. Thus, the degradation mechanism is similar to the one of Figure 7.12, but with slower degradation rate.

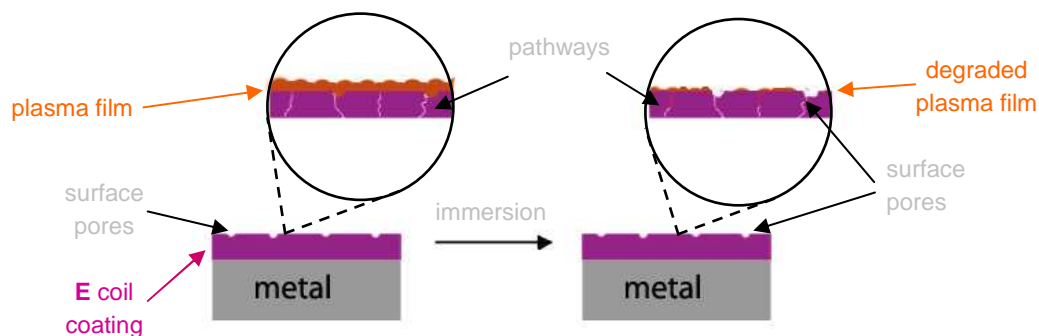


Figure 7.12 Degradation mechanism for the plasma polymerized **E** systems in the **R** plasma reactor using HMDSO and oxygen precursor mixture.

These systems show even slower degradation when the **3** stage is used (plasma activation, plasma deposition and plasma stabilization). Both systems **ER3eP₅P** and **ER3eP₅G** have better performance when compared with the systems **ER4iP₅P** and **ER4iP₅G** (systems without the initial plasma activation step). This gives indication of the necessity of the plasma activation step performed before the plasma deposition.

The results also suggest that the plasma polymerization performed in the **P** electrode has stronger effect to the **E** coil coating barrier properties. The degradation must arise from the plasma deposition step, since both systems **ER3eP₅P** and **ER4iP₅P** show similar degradation, however the system **ER4iP₄P** was not submitted to the plasma activation step. In this electrode location, the plasma polymer film generated is not able to annul the process influence. This has to be related with the higher influence of the polymerization process on the coil coating barrier properties together with worse properties of the generated plasma polymer film.

On the other hand, both systems submitted to the plasma polymerization in the **G** electrode location show better performance, even for the system **ER3eP₅G**, which **E** coil coating barrier properties were affected during the plasma activation step, as shown in point 7.3.2. In this electrode location, the plasma polymerization generates a plasma polymer film that is able to annul the influence of the plasma activation step, showing also good properties during immersion.

Plasma polymerization of the **U** coil coating using the **R** plasma reactor introduces similar alterations to the prepared systems. The process performed in the **P** electrode also shows different performance, systems **UR3eP₅P** and **45UR4iP₄P**, compared with **G** electrode systems. The $|Z|_{0.1 \text{ Hz}}$ values, shown in Figure 7.11a, for these **P** electrode systems have higher and faster decrease during the immersion tests. A decrease of 1.5 orders of magnitude to 300 Mohm cm² after 120 days of immersion occurs for the system **UR3eP₅P**, while the system **45UR4iP₄P** has more than 3 orders of magnitude decrease to 3 Mohm cm² after 75 days of immersion.

The TEM micrographs of the Figure 6.36 show that the plasma polymer films generated in the **R** plasma reactor are homogenous and compact with low thickness, less than 100 nm. The low thickness brought difficulties to the TEM preparation and respective imaging. For that reason, extrapolation of the thickness was performed using the particle size measured from the AFM results of Figure 6.37. The procedure appears described in page 125. It is obtained higher thickness for the system **UR3eP₅P**, followed by the systems **UR4iP₄G** and **UR4iP₄P** (which have similar thickness) and finally the system **UR3eP₅G**.

The surface characterization results show that the systems properties during immersion are also dependent of the stage used. The system **UR3eP₅P** shows small surface morphology variation, AFM image **b** of Figure 6.41b. Stronger variation is obtained for the system **UR4iP₄P**, Figure 6.41d, where negative R_{sk} values appear after 7 days of immersion. The EDS results of Table 6.4 show constant silicon content for both systems, suggesting that the plasma polymer film continues to be present during immersion. These results show that the plasma polymer film of the system **UR4iP₄P** suffers degradation during immersion, suggesting the formation of pathways until the coil coating interface, while the system **UR3eP₅P** seems to maintain constant surface properties.

The plasma polymerized **U** systems using the **R** plasma reactor and the **G** electrode have different evolution of the $|Z|_{0.1 \text{ Hz}}$, Figure 7.11a. The values for the system **45UR4iP₄G**, tested at 45° C, show slow initial decrease followed by strong drop, reaching 30 Mohm cm² after 80 days of immersion. The surface characterization of the system **UR4iP₄G** suggests that dissolution of the plasma polymer film occurs during the immersion tests. The EDS composition evolution of Table 6.4 corroborates the dissolution of the plasma polymer film, showing decrease of the silicon element content until vestigial values. The AFM images **c** of Figure 6.41 show negative R_{sk} after 30 days of immersion, which also suggests surface degradation. The system **UR3eP₅G** has different behaviour. In this case, the $|Z|_{0.1 \text{ Hz}}$ evolution follows the unmodified **U** coil coating until 50 days of immersion, showing then slow decrease rate. After 190 days of immersion (more than 6 months) one order of magnitude decrease to 3 Gohm cm² is obtained. The surface morphology of the plasma polymer remains stable during immersion, Figure 6.41a. However, the EDS results of Table 6.4 show a decrease of the silicon content to half the initial value, suggesting partial dissolution of the plasma polymer film during immersion.

The degradation mechanism has some differences for the **P** and **G** electrode location, since different processes occur. The scheme with the degradation mechanism for the systems prepared in the **G** electrode location appears in Figure 7.13. The systems tested

at higher temperature have acceleration of the degradation rate, but still show similar degradation mechanism.

Decrease of the coil coating barrier properties occurs during the plasma polymerization process performed on the **G** electrode location. Initially, the plasma polymer film formed is able to annul this degradation and the systems have degradation rate identical to the unmodified **U** coil coating. However, the plasma polymer film is unstable during immersion, showing dissolution. After dissolution of the plasma polymer film, the systems degradation rate increases, this leads to a decrease of performance compared with the unmodified **U** coil coating.

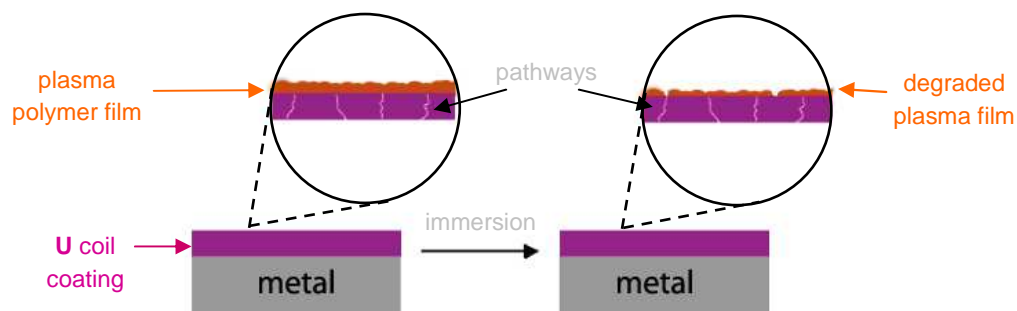


Figure 7.13 Degradation mechanism for the plasma polymerized **U** systems using the **R** plasma reactor with HMDSO and oxygen precursor mixture.

The systems prepared in the **P** electrode location generate stable plasma polymer film, which is corroborated by the surface characterization. However, these systems have weak barrier properties, showing faster decrease of performance than similar systems prepared in the **G** electrode. In the **P** electrode case, strong influence on the systems barrier properties occurs during the plasma deposition step, leading to degradation of the coil coating barrier properties. The deposited plasma polymer film is not able to annul this degradation, even if the plasma polymer film does not suffer complete dissolution. The degradation mechanism is similar to the scheme of Figure 7.13, but the degradation of the plasma polymer film in this case is milder.

The first important remark is that the results show higher influence on the coil coating barrier properties when the plasma activation step is performed in the **G** electrode. However, the plasma deposition performed in the same **G** electrode location generates systems that are able to annul the plasma activation influence. This occurs for both coil coatings used, **E** and **U** systems. These results also suggest that the plasma activation is important, introducing oxygenated species in the coil coating surface,^{46,168} which enhance the adhesion of the plasma polymer film to the coil coating. The systems degradation only starts after dissolution of the plasma polymer film.

The second important point is the combination of steps used. The systems showing better performance are the ones prepared using the stage **3** (plasma activation, plasma

deposition and plasma stabilization), which corresponds to the complete plasma polymerization process. This reinforces the necessity of the plasma activation step as adhesion promoter.

The final plasma stabilization step is also of great importance. Testing of the systems without the final stabilization showed fast degradation and film dissolution in both **E** and **U** coil coatings. A resume of the results for these systems prepared without the final plasma stabilization step is shown in the Appendix presented at the end on the work. The system has fast dissolution of the plasma polymer film, Table ii, associated with strong variation of the surface morphology, Figure i. These are both signs of bad behaviour of the plasma polymerized systems during immersion.

7.4.3. TMS Monomer

The $|Z|_{0.1 \text{ Hz}}$ values for the system **UH2kP₆**, shown in Figure 7.14, have initial higher drop than the other plasma polymerized systems, reaching 9 Gohm cm². Stable behaviour then follows this initial drop and the $|Z|_{0.1 \text{ Hz}}$ value remains unchanged until 120 days of immersion. After this immersion period, a second drop appears and the $|Z|_{0.1 \text{ Hz}}$ value reaches 6 Gohm cm².

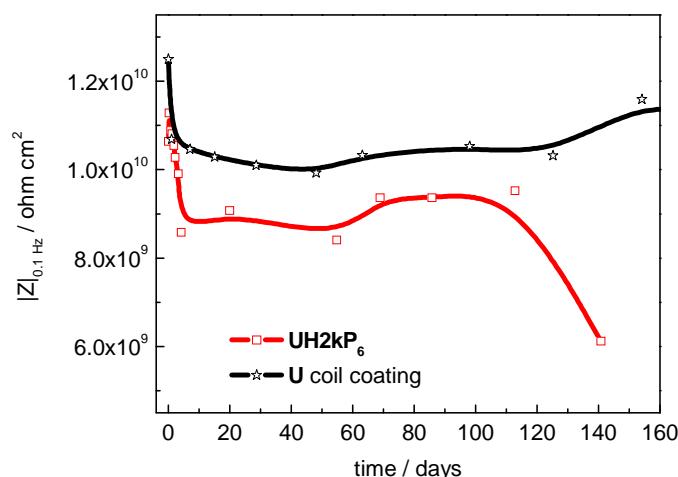


Figure 7.14 Evolution of $|Z|_{0.1 \text{ Hz}}$ values for the system **UH2kP₆**.

The system **UH2kP₆** has high thickness with 380 nm, showing individualized particles with pathways between them, TEM micrograph of Figure 6.47. This agrees with the particulate

surface morphology obtained on the AFM images of Figure 6.48, where the negative R_{sk} can be attributed to the pathways. The particulate surface morphology is maintained constant during the immersion tests, but the initial negative R_{sk} values change to positive. The system composition also remains unchanged during immersion, Table 6.6. These results suggest that the plasma polymer film formed is stable but with some surface variation during immersion.

The Bode plot evolution of Figure 6.44 shows a clear decrease of performance after 40 days of immersion. This decrease corresponds to water and ions absorption leading to coating degradation, which has influence on the impedance value. The R_{por} parameter reinforces that the system has a decrease of the initial barrier properties, showing strong decrease, Figure 6.45. The water uptake of Figure 6.46, suggests, however, that the system has even better performance than unmodified **U** coil coating, since the water saturation level for initial periods of immersion is lower. The values of water uptake show an increase tendency during further immersion. The data presented for the system **UH2kP₆** neither permits to obtain good explanation about the degradation mechanism nor about the system behaviour. Contradictory impedance response and surface results appear.

Formation of hydrophobic surface properties when using TMS monomer was previously reported.^{170;168} With this information a proposal for the system **UH2kP₆** contradictory results follows. The plasma polymerization process performed in **H** plasma reactor introduces degradation on the coil coating barrier properties. In this case, the plasma polymer film is not able to completely annul this influence and, as a result, the low frequency impedance values decrease initially. The hydrophobic nature of the plasma polymer film can delay the absorption process, decreasing the amount of absorbed water, which corresponds to the plateau verified on the $|Z|_{0.1 \text{ Hz}}$ evolution. Increase of immersion time decreases the hydrophobic nature of the surface and the absorption processes follows the normal course, accelerating the coating degradation, correspondent to the second drop of the $|Z|_{0.1 \text{ Hz}}$ values.

7.5. Reactor Comparison

The tested systems show that the plasma polymerization process has influence on the coil coated systems used, namely on the barrier properties and on the morphology and structure. Specific modifications of the parameters of each plasma reactor show lower influence or form plasma polymer films that are able to better balance the degradation. These experimental conditions are also responsible by the different systems surface properties.

The plasma polymerized systems prepared with the same precursor mixture and using the same coil coating are here discussed. The systems **UM2eP₃**, **UR3eP₅G** and **UR3eP₅P** use HMDSO and oxygen precursor mixture but refer only to **R** and **M** plasma reactors. Since

the idea is to compare all the three plasma reactors, the system **UH2kP₆** is also analysed, even if the system had been prepared with TMS and oxygen precursor mixture. The system **UM2fP₃**, prepared with HMDSO and argon, also appears, since this is one of the systems with the best performance. The $|Z|_{0.1 \text{ Hz}}$ evolution for these systems appears in Figure 7.15. The system **UR3eP₅P** was not included since has very poor performance with very fast decrease of the impedance values during immersion.

The systems **UM2eP₃** and **UR3eP₅G** have during the initial 50 days of immersion slower decrease of $|Z|_{0.1 \text{ Hz}}$ values, followed by faster and continuous decrease. The system **UM2eP₃** after 140 days of immersion has practically the same $|Z|_{0.1 \text{ Hz}}$ value than system **UH2kP₆** after similar immersion time, near 6 Gohm cm². The system **UR3eP₅G** shows lower $|Z|_{0.1 \text{ Hz}}$ value than the other two systems for the same immersion time. After 200 days of immersion reaches 2 Gohm cm², near one order of magnitude lower than initially.

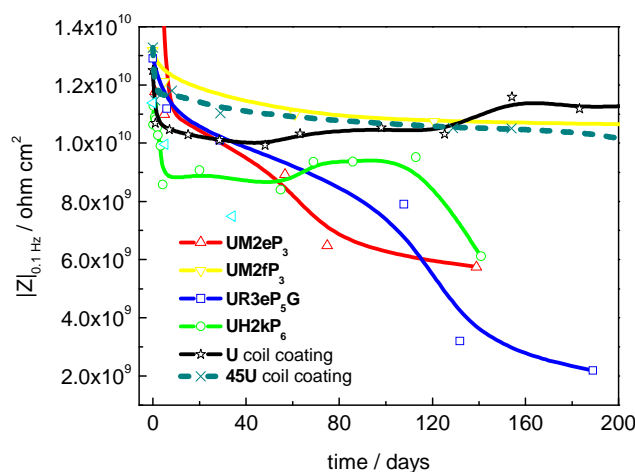


Figure 7.15 Evolution of $|Z|_{0.1 \text{ Hz}}$ for the plasma polymerization performed using HMDSO or TMS monomers: **M** vs. **R** vs. **H** plasma reactors.

These systems have different surface characteristics. The systems **UR3eP₅G** and **UM2fP₃** have compact structure, Figure 6.36 and Figure 6.12c respectively. The first system shows very low thickness, which was estimated using the AFM data of Figure 6.37a to be around 50 nm. The systems **UM2eP₃** and **UH2kP₆** show particulate structure with voids between the particles, TEM micrographs of Figure 6.12b and Figure 6.47 respectively. The first has thickness of 170 nm, while the second of 380 nm.

Particulate surface morphology is obtained for all these systems after the plasma polymerization procedure, together with similar silicon element content. During immersion, the surface particles suffer degradation and the silicon element proportion decreases for the systems **UR3eP₅G** (AFM images **a** of Figure 6.41 and Table 6.4) and **UM2eP₃** (AFM

images **b** of Figure 6.15 and Table 6.1). The system **UM2fP₃** maintains constant surface parameters (AFM image **c** of Figure 6.15 and Table 6.1). System **UH2kP₆** behaves differently. Maintains constant silicon content during immersion but the surface morphology, which initially shows negative R_{sk} values, maintains the particulate surface however changes the R_{sk} values to positive (Table 6.6 and AFM images of Figure 6.48).

The characterization results corroborate the $|Z|_{0.1 \text{ Hz}}$ evolution, showing higher variation of the parameters during immersion for the systems that have the higher degradation of the barrier properties during immersion.

These results suggest that good systems with high corrosion protection behaviour can be prepared, adding in the process important surface properties.¹ The systems barrier properties are controllable and dependent of the plasma polymerization parameters: pressure, carrier gas, combination of steps and reactor electrode location. These variables permit also to change the systems surface properties. The precursor mixture is another important factor since specific surface properties directly depend of the chosen monomers.

It is important to highlight the influence of the plasma activation step. The highest influence occurs for the **M** plasma reactor especially if using oxygen in the step. The plasma activation performed in the **R** plasma reactor, also used oxygen gas, but the influence appears dependent of the **R** plasma reactor electrode used, higher when using the **G** electrode. The two systems **UM2eP₃** and **UR3eP₅G**, which show higher degradation during the activation step, have similar behaviour and identical decrease of the barrier properties during immersion, Figure 7.13. The decrease of performance in these systems only starts when the dissolution of the plasma polymer layer is noticed and therefore shows relation with the influence of the plasma activation step performed prior to the plasma deposition.

The system **UH2kP₆** also shows similar degradation rate to the systems **UM2eP₃** and **UR3eP₅P**. Here the degradation mechanism is different. In this case, the plasma polymer layer remains stable during the immersion tests. Further tests would be necessary to fully understand the degradation mechanism in this case.

Argon activation also influenced the barrier properties of the coil coating, however, with lower degree. Moreover, the generated plasma polymer film using argon carrier gas is compact and stable during immersion, exactly as intended with the process. The systems stability is very high, maintaining long term protection during the immersion tests.

7.6. Estimation of Economical Aspects

To complement the study of the plasma polymer films deposited in the coil coating, estimation of the economical aspects was carried out¹ to calculate the financial impact caused by the introduction of the plasma polymerization process in the coil coating production line.

Estimation of economical aspects used the data generated from the hollow cathode reactor, using basic calculations of the consumption of monomer, argon and oxygen gases as well as electric power, derived from a series of high rate deposition experiments. The highest rate observed was 60 nm s^{-1} for a static deposition experiment on a silicon wafer, using monomer flux of TMS at 625 sccm with argon and oxygen fluxes set to 500 sccm and 5000 sccm, respectively. The power input is 2.5 kW.

The calculations on which the economical estimation is based are carried out using an annual plant throughput of 200,000 tons of coil coated steel. The deposition system design consists of five deposition loops, in order to achieve layer thickness of 150 nm, while maintaining a constant plant speed compared to the current plant. In Table 7.1 and Table 7.2 appear the estimations considering the use of TMS and HMDSO as monomer gas.

Assumptions:

- The coating setup consists in the strip hollow cathode principle.
- The conversion of the monomer and its transfer as polymer film to the coil coating is 100% (achieved with an optimised hollow cathode set-up).
- The coating thickness expected is 150 nm.
- The cost of TMS as monomer gas is € 100 per kg, and for HMDSO as alternative gas is € 5 per kg.
- The investment cost is € 10,000,000, (depreciation: 10 years, therefore cost per year is € 1,000,000).
- The consumption of gases and power increases linearly with the steel strip width.
- Production capacity of 200,000 tonnes per year is kept constant, therefore is necessary the installation of five deposition loops.

From the tables, it is evident that the monomer cost plays the biggest role in these calculations. This aspect becomes even more important since higher deposition rates appear for HMDSO as monomer component.

Table 7.1 Estimated cost for the plasma deposition step using TMS monomer.

	quantity	costs per year	costs per ton
running costs			
monomer (TMS)	26,600 sccm	€ 11 100 000	€ 55,50
other gases (argon, oxygen)	234,000 sccm	€ 237 000	€ 1,19
electricity (generators)	106 kW	€ 40 500	€ 0,20
electricity (vacuum pumps)	1100 kW	€ 319 000	€ 1,60
supplies (pump oil, lube, compressed air)	-	€ 50 000	€ 0,25
SUM running costs		€ 11 746 500	€ 58,74
investment costs			
deposition equipment	-	€ 1 000 000	€ 5,00
plant modification	-	€ 500 000	€ 2,50
monomer storage facility	-	€ 500 000	€ 2,50
SUM investment costs		€ 2 000 000	€ 10,00
additional costs			
special maintenance	500 hours	€ 35 000	€ 0,18
research & development	0,5 man-year	€ 126 000	€ 0,63
SUM additional costs		€ 161 000	€ 0,81
total costs		€ 13 907 500	€ 69,54

Table 7.2 Estimated cost for the plasma deposition step using HMDSO monomer.

	quantity	costs per year	costs per ton
running costs			
monomer (HMDSO)	7,655 sccm	€ 155 000	€ 0,78
other gases (argon, oxygen)	43,380 sccm	€ 27 000	€ 0,14
electricity (generators)	77kW	€22 500	€ 0,11
electricity (vacuum pumps)	1100 kW	€ 240 000	€ 1,20
supplies (pump oil, lube, compressed air)	-	€ 50 000	€ 0,25
SUM running costs		€ 494 500	€ 2,41
investment costs			
deposition equipment	-	€ 1 000 000	€ 5,00
plant modification	-	€ 500 000	€ 2,50
monomer storage facility	-	€ 500 000	€ 2,50
SUM investment costs		€ 2 000 000	€ 10,00
additional costs			
special maintenance	500 hours	€ 35 000	€ 0,18
research & development	0,5 man-year	€ 126 000	€ 0,63
SUM additional costs		€ 161 000	€ 0,81
total costs		€ 2 655 500	€ 13,28

Conclusions

Section 8. Conclusions

The aim of the ECSC project 7210-PR/383, ¹ in which this work was originated, was to improve scratch resistance, clean easiness, anti-fingerprint properties and colour control of coil coatings by the deposition of a thin plasma polymer film. The results presented in this thesis deal with the influence of the plasma polymerization conditions on the coil coating barrier properties that are related to paint degradation and at a latter stage corrosion of the metallic substrate. Summary of the most important conclusions appears here.

Several techniques were used to study the plasma deposited film and obtain both the surface and barrier properties of the coated systems.

- Electrochemical impedance spectroscopy assessed the coating capacitance (C_{coat}) and the coating pore resistance (R_{por}). The coating water uptake was determined from impedance measurements at constant frequency. All these parameters

allowed the analysis of the systems' performance in terms of their barrier properties. These parameters showed good reproducibility and correlated well with the systems' degradation. The results permitted to study specific variations of the plasma polymerization process and the influence of these on the coil coating properties.

- Transmission electron microscopy showed important details of the plasma polymer layer revealing their structure and thickness variation due to modifications of the plasma process parameters. The success of the technique was achieved after development of a proper methodology for sample preparation.
- Scanning electron microscopy showed the surface morphology of the systems before and after the immersion tests. Only the polyester systems were analysed since the electron beam energy destroyed the polyurethane systems.
- For the polyurethane systems, atomic force microscopy was used to study the systems surface morphology. The arithmetic roughness and the average height permitted to quantify the surface variation during testing.
- The surface elemental composition calculated from energy-dispersive x-ray spectroscopy showed the representative elements of the plasma polymer film. Their semi-quantification permitted to verify their stability during the tests.
- CIE colour coordinates, obtained by surface reflection of the plasma polymerized systems, were also analysed. The observed colour changes correlate with the plasma polymerization conditions and with the film stability in the testing environment.

Correlation of the surface morphology, composition data and structure information with impedance results help to clarify the degradation mechanisms of the systems during testing. This procedure showed how the plasma polymerization process influences the coil coatings properties.

The plasma activation step proved to be important. This step was used to clean the surface promoting the adhesion of the plasma polymer film to the coil coating. However, simultaneously damage of the coil coating barrier properties arises since the coil coating surface is directly exposed to the plasma conditions.

- Activation using the microwave plasma reactor leads to an increase of the surface roughness influencing the barrier properties of the coil coating. The barrier properties strongly decrease when the plasma activation uses oxygen, forming surface oxygenated bonds. Plasma activation with argon leads to smaller variation of these properties. In the latter one occurs abstraction of hydrogen atoms and removal of low molecular weight species from the coil coating surface.
- Activation using the radio frequency plasma reactor also increases the surface roughness, but in much lower extent. The negative influence on the coil coating

barrier properties was particularly important when the specimens were treated in the grounded electrode. For the specimens in the powered electrode, on the other hand, no significant variation of the barrier properties occurs.

The activation step precedes the deposition of the plasma polymer film. The **plasma deposition step**, when performed correctly, is able to annul the negative influence of the plasma activation stage. When this occurs, the coil coatings could gain improved surface properties, like scratch resistance and surface hydrophobicity, maintaining the original barrier properties.

- For the microwave plasma reactor, two important process variables are mandatory to increase the long term performance of the systems. The first is the use of relatively lower pressure during plasma polymerization. This leads to the decrease of the particle size and of the film thickness, which increases the film stability during immersion. The second is the use of argon carrier gas rather than oxygen, since smaller particles and thinner layers with compact structure are generated. These conditions together lead to very high stability of the plasma polymerized systems during immersion.
- Plasma polymerization on the radio frequency plasma reactor using the grounded electrode location generated thin, compact and stable plasma polymer films, which maintain the original barrier properties. The use of the powered electrode location, on the other hand, strongly influenced the protection properties. Here, stable plasma polymer films were formed. However, lower barrier properties for all the systems prepared in this electrode location were obtained.
- Another important variable for the radio frequency plasma reactor is the combination of steps during the process. The results show that the greatest performance is achieved using the combination of plasma activation, plasma deposition and plasma stabilization steps – stage **3**. This gives always better performance systems for both electrode locations, although the **G** electrode location has better long term performance.
- Plasma polymerization in hollow cathode plasma reactor simulates continuous deposition. The generated plasma polymer film is thick, particulate and stable during immersion. However, a negative influence on the protection properties of the systems appears, decreasing their performance. Further testing would be necessary to optimize this procedure.

With the present work it was shown that it is possible to carry out the plasma polymerization process on coil coated metal without damaging the barrier properties of the coating and without altering its colour. However, the experimental conditions should be criteriously chosen.

Based on this it was possible in this ECSC project to deposit polymerized films that have improved the scratch resistance and/or anti-fingerprint properties without diminishing the weathering resistance. Nevertheless, that is out of this thesis scope.

The financial impact caused by the introduction of the plasma polymerization process on the coil coating production line was analysed for the hollow cathode reactor. The results suggest that the differences in cost for two of the monomers used depend mainly on the chemicals (precursors) price, since the other costs are identical.

Section 9. Future Work

Some suggestions for future work appear here in two groups. The first concerns work started in the frame of this work but not completed. The second group presents proposals considered the natural continuation of the present work.

- Work Started but Not Completed

- Surface Chemical Groups

The plasma polymer films have different surface chemical groups depending on the precursor mixture and on the polymerization conditions. Most of the surface properties show dependence of these chemical groups. Study of their evolution during immersion

permits to verify the stability of the produced surface properties of the respective plasma polymer layer when exposed to the testing conditions.

Several attempts performed to obtain information concerning the chemical surface groups using infrared spectroscopy methods were performed. A first attempt used attenuated total reflection infrared spectroscopy (ATR-IR), but problems with the intensity of the used radiation limited the results obtained. High intensity led to overlapping peaks from the coil coating with the peaks from the plasma polymer film, whereas lower intensity does not give enough information to resolve the plasma polymer film peaks.

Only by the end of PhD, Raman spectroscopy and infrared spectroscopy were tried showing promising results and permitting to individualise the peaks attributed to the plasma polymer film and to the coil coating. This work should continue.

- Exposure to High Temperature

EIS measurements with samples exposed to higher temperature, showed to be an interesting way to accelerate the degradation rate of the systems, providing faster screening of the performance. The correlation with results obtained at ambient temperature can provide faster knowledge of the systems degradation. In the course of this work, some problems of reproducibility were encountered and only one temperature was investigated, 45° C. Continuation should include higher and lower temperatures, e.g. 30, 45 and 55° C. The possibility of introducing lower temperature than the environment is also considered.

- Continuation of the Work

- Natural and Accelerated Weathering Tests

Many coil coatings serve in the outdoor. For this reason, the plasma polymer films capability of increasing their weathering resistance is important. Natural exposition and accelerated weathering of the systems should be used. Examples are different testing environments, wet/dry immersion cycles, ultraviolet radiation and high temperature immersion tests.

- Formability tests

Formability tests are an important aspect of the coil coating systems, since they are formed to their final shape after the application of the coil coating. The influence of the formability on the plasma polymerized systems is, therefore, a very important subject of investigation.

- Surface Properties

Contact angle measurements after the plasma polymerization process is another interesting test to verify the systems surface properties. The contact angle evolution, during weathering, permits to find relations between the surface nature, hydrophobicity and the degradation processes.

- Composition

Auger electron spectroscopy and X-ray photoelectron spectroscopy would introduce surface composition maps of the plasma polymer films surface. The composition evolution during immersion can help to confirm the degradation mechanisms. These techniques used with sputtering provide composition profile giving further characterization of the plasma polymer films.

References

- 1 G. Grundmeier, N. Saemann, B. Strauss, B. Lindner, R. Valle, T. English, D.B. Hammond, M. Ferreira, M. Zheludkevich, *Tailored thin plasma polymers for surface engineering of coil-coated steel*, **2007**, n° 22432, L.EN, Publisher: European Commission, Luxembourg: EUR ISSN 1018-5593;
- 2 W.F. Smith, *Principles of Materials Science and Engineering* 3rd ed. New York: McGraw-Hill, **1996**, ISBN 0-07-114717-9;
- 3 W.D. Callister, Jr., *Fundamentals of Materials Science and Engineering: an interactive E. text*, Chichester: John Wiley, **2001**, ISBN 0-471-39551-X;
- 4 L. L. Sheir, R. A. Jarman, G. T. Burstein, *Corrosion*, 3rd ed. Oxford: Butterworth-Heinemann, **2002**: ISBN 0750610778;
- 5 NACE, *Corrosion basics*. Houston (Texas): National Association of Corrosion Engineers, **1984**: ISBN 0915567014;

-
- 6 C.G. Munger, *Corrosion protection by protective coatings*; 2nd ed. Houston (TX): National Association of Corrosion Engineers, cop. **1999**: ISBN 1575900882;
- 7 G.P. Bierwagen, *Progress in Organic Coatings* 28 (**1996**) 43;
- 8 N.D. Tomashov, *Theory and Protection of Metals: The Science of Corrosion*, The Macmillan Company, New York **1966**;
- 9 D.A. Jones, *Principles and Prevention of Corrosion*, 2nd ed. Upper Saddle River (NJ): Prentice Hall, **1996**: ISBN 0133599930;
- 10 H. Kaesche, *Corrosion of Metals*, Springer Verlag, **2003**: ISBN 3540006265;
- 11 M.G. Fontana, *Corrosion Engineering*, 3rd ed. New York: McGraw-Hill, **1986**: ISBN 0070214638;
- 12 H.H. Uhlig, *Uhlig's Corrosion Handbook*, 2nd Edition by R. Winston Revie, John Wiley & Sons, **2005**: ISBN: 9780471784944;
- 13 E. D. Verink, *The basics*, Houston (TX): National Association of Corrosion Engineers, **1994**: ISBN 1877914622;
- 14 J. Morgan, *Cathodic protection*, 2nd ed. Houston (TX): National Association of Corrosion Engineers, **1993**: ISBN 0915567288;
- 15 B.M. Rosales, A.R. Di Sarli, O. Rincón, *Progress in Organic Coatings* 50 (**2004**) 105;
- 16 C. Corfias, N. Pébère, C. Lacabanne, *Corrosion Science* 41 (**1999**) 1539;
- 17 L. Fedrizzi, F. Deflorian, G. Boni, P.L. Bonora, E. Pasini, *Progress in Organic Coatings* 29 (**1996**) 89;
- 18 F. Deflorian, L. Fedrizzi, S. Rossi, *Corrosion Science* 42 (**2000**) 1283;
- 19 R.B. Heimann, *Plasma-spray Coating: principles and applications*, Weinheim: VCH, **1996**: ISBN 3527294309;
- 20 Jr. Z.W. Wicks, F.N. Jones, S.P. Pappas, *Organic Coatings: science and technology*. New York: John Wiley, cop. **1992-1994**: ISBN 0471614068 (vol. 1). ISBN 0-471-59893-3 (vol. 2);
- 21 I. Suzuki, *Corrosion Resistant Coating Technology*, New York: Marcel Dekker, **1989**: ISBN 0824781600;
- 22 *Official Journal of the European Union* 31.12.1994, L 365, 1;
- 23 *Official Journal of the European Union* 21.10.2000, L 269, 34;
- 24 *Official Journal of the European Union* 13.2.2003, L 37, 19;
- 25 M. Delucchi, A. Barbucci, G. Cerisola, *Electrochimica Acta* 44 (**1999**) 4297;
- 26 A.C. Bastos, C. Ostwald, L. Engl, G. Grundmeier, A.M. Simões, *Electrochimica Acta* 49 (**2004**) 3947;
- 27 R.M. Souto, L. Fernández-Mérida, S. González, D.J. Scantlebury, *Corrosion Science* 48 (**2006**) 1182;
- 28 M.F. Montemor, A.M. Simões, M.G.S. Ferreira, B. Williams, H. Edwards, *Progress in Organic Coatings* 38 (**2000**) 17;
- 29 S. Maeda, *Progress in Organic Coatings* 28 (**1996**) 227;

- 30 R.M. Souto, M.L. Llorente, L. Fernandez-Merida, *Progress in Organic Coatings* 53 (2005) 71;
- 31 Becker Industrial Coatings, 30-08-2008, < <http://www.beckers-bic.com/BIC/bicweb.nsf/key/CoilCoatings> >;
- 32 S. Rossi, F. Deflorian, J. Fiorenza, *Surface and Coatings Technology* 201 (2007) 7416;
- 33 Y. Kim, J. Lee, Q. Ji, J.E. McGrath, *Polymer* 43 (2002) 7161;
- 34 B. Mailhot, K. Komvopoulos, B. Ward, Y. Tian, G. A. Somorjai, *Journal of Applied Physics* 89 (2001) 5712;
- 35 Y. Deslandes, G. Pleizier, D. Alexander, P. Santerre, *Polymer* 39 (1998) 2361;
- 36 M. Korhonen, P. Starck, B. Löfgren, *Journal of Applied Polymer Science* 87 (2003) 2016;
- 37 J.M. Sanchez-Amaya, R.M. Osuna, M. Bethencourt, F.J. Botana, *Progress in Organic Coatings* 60 (2007) 248;
- 38 K.A. Wood, *Progress in Organic Coatings* 43 (2001) 207;
- 39 V. Barranco, P. Thiemann, H.K. Yasuda, M. Stratmann, G. Grundmeier, *Applied Surface Science* 229 (2004) 87;
- 40 G. Grundmeier, P. Thiemann, J. Carpentier, V. Barranco, *Surface and Coating Technology* 174-175 (2003) 996;
- 41 C.-M. Chan, T.-M. Ko, H. Hiraoka, *Surface Science Reports* 24 (1996) 1;
- 42 S. Vaswani, J. Koskinen, D.W. Hess, *Surface and Coatings Technology* 195 (2005) 121;
- 43 L. Tonks, I Langmuir, *Physical Review* 33 (1929) 195;
- 44 J.L. Shohet, *The plasma state*, New York: Academic Press, 1971. ISBN: 9780126405507;
- 45 L. Rayleigh, *Philosophical Transactions* 11 (1906) 117;
- 46 N. Shirtcliffe, P. Thiemann, M. Stratmann, G. Grundmeier, *Surface and Coatings Technology* 142-144 (2001) 1121;
- 47 F.F. Shi, *Surface and Coatings Technology* 82 (1996) 1;
- 48 S. Gaur and G. Vergason, *Society of Vacuum Coaters* 505 (2000) 267;
- 49 G. Borcia, C.A. Anderson, N.M.D. Brown, *Applied Surface Science* 221 (2004) 203;
- 50 G. Borcia, C.A. Anderson, N.M.D. Brown, *Applied Surface Science* 225 (2004) 186;
- 51 H. Yasuda, Q. Yu, *Plasma Chemistry and Plasma Processing* 24 (2004) 325;
- 52 M.V. Jacob, C.D. Easton, G.S. Woods, C.C. Berndt, *Thin Solid Films* 516 (2008) 3884;
- 53 G. Grundmeier, M. Stratmann, *Materials and Corrosion* 49 (1998) 150;
- 54 S. Veprek, M. Venugopalan, *Plasma Chemistry* 3, Springer-Verlag Berlin Heidelberg New York, 1980. ISBN 3-540-10166-7;
- 55 G. Odian, *Principles of polymerization*, 4th ed. Hoboken (NJ): Wiley - Interscience, 2004. ISBN 0471274003;
- 56 G. Padron-Wells, B.C. Jarvis, A.K. Jindal, M.J. Goeckner, *Colloids and Surfaces B: Biointerfaces* 68 (2009) 163;

-
- 57 S.H. Cho, Z.T. Park, J.G. Kim, J.H. Boo, *Surface and Coatings Technology* 174-175 (2003) 1111;
- 58 J. Wiedemair, B. Balu, J. Moon, D.W. Hess, B. Mizaikoff, C. Kranz, *Analytical Chemistry* 80 (2008) 5260;
- 59 H. Biederman, D. Slavínská, *Surface and Coatings Technology* 125 (2000) 371;
- 60 M.C. Kim, S.H. Cho, J.G. Han, B.Y. Hong, Y.J. Kim, S.H. Yang, J.-H. Boo, *Surface and Coatings Technology* 169-170 (2003) 595;
- 61 A.J. Beck, F.R. Jones, R.D. Short, *Journal of the Chemical Society, Faraday Transactions* 94 (1998) 559;
- 62 H. Yasuda, T. Hsu, *Journal of Polymer Science - Polymer Chemistry Edition* 15 (1977) 81;
- 63 C. Mühlhan, St. Weidner, J. Friedrich, H. Nowack, *Surface and Coatings Technology* 116-119 (1999) 783;
- 64 C. Tu, Y. Wang, C. Li, K. Lee, J. Huang, J. Lai, *European Polymer Journal* 41 (2005) 2343;
- 65 J. Barz, M. Haupt, U. Vohrer, H. Hilgers, C. Oehr, *Surface and Coatings Technology* 200 (2005) 453;
- 66 W.L.E. Magalhães, M.F. de Souza, *Surface and Coatings Technology* 155 (2002) 11;
- 67 D. Hegemann, H. Brunner, C. Oehr, *Plasmas and Polymers* 6 (2001) 221;
- 68 T. Aumann, D. Theirich, J. Engemann, *Surface and Coatings Technology* 142-144 (2001) 169;
- 69 E. Braca, J.M. Kenny, D. Korzec, J. Engemann, *Thin Solid Films* 394 (2001) 30;
- 70 P. Favia, M. Creatore, F. Palumbo, V. Colaprico, R. d'Agostino, *Surface and Coatings Technology* 142-144 (2001) 1;
- 71 A. Raffaele-Addamo, E. Selli, R. Barni, C. Riccardi, F. Orsini, G. Poletti, L. Meda, M.R. Massafra, B. Marcandalli, *Applied Surface Science* 252 (2006) 2265;
- 72 R. Li, L. Ye, Y. Mai, *Composites Part A* 28A (1997) 73;
- 73 T.F. Wang, T.J. Lin, D.J. Yang, J.A. Antonelli, H.K. Yasuda, *Progress in Organic Coatings* 28 (1996) 291;
- 74 H.K. Yasuda, T.F. Wang, D.L. Cho, T.J. Lin, J.A. Antonelli, *Progress in Organic Coatings* 30 (1997) 31;
- 75 E. Angelini, S. Grassini, F. Rosalbino, F. Fracassi, R. d'Asgotino, *Progress in Organic Coatings* 46 (2003) 107;
- 76 Y. Chen, K. Kiushi, K. Chinone, M. Eguchi and Y. Momose, *Journal of Adhesion Science and Technology* 15 (2001) 371;
- 77 E. Angelini, R. d'Asgotino, F. Fracassi, S. Grassini and F. Rosalbino, *Surface and Interface Analysis* 34 (2002) 155;
- 78 C. Vautrin-UI, C. Boisse-Laporte, N. Benissad, A. Chausse, P. Leprince, R. Messina, *Progress in Organic Coatings* 38 (2000) 9;
- 79 H. Biederman, V. Stelmashuk, I. Kholodkov, A. Choukourov, D. Slavínská, *Surface and Coatings Technology* 174-175 (2003) 27;

- 80 E. Vassallo, A. Cremona, L. Laguardia, E. Mesto, *Surface and Coatings Technology* 200 (2006) 3035;
- 81 Y.B. Guo, F.C. Hong, *Diamond and Related Materials* 12 (2003) 946;
- 82 D. Hegemann, H. Brunner, C. Oehr, *Nuclear Instruments and Methods in Physics Research Section A: Accelerators, Spectrometers, Detectors and Associated Equipment* 208 (2003) 281;
- 83 D. Korzec, D. Theirich, F. Werner, K. Traub, J. Engemann, *Surface and Coatings Technology* 74-75 (1995) 67;
- 84 A. Hozuni, O. Takai, *Thin Solid Films* 303 (1997) 222;
- 85 H. Jiang, J.T. Grant, K. Eyink, S. Tullis, J. Enlow, T.J. Bunning, *Polymer* 46 (2005) 8178;
- 86 J.T. Grant, H. Jiang, S. Tullis, W.E. Johnson, K. Eyink, P. Fleitz, T.J. Bunning, *Vacuum* 80 (2005) 12;
- 87 E.M. Johnson, S.J. Clarson, H. Jiang, W. Su, J.T. Grant, T.J. Bunning, *Polymer* 42 (2001) 7215;
- 88 M. Yang, K. Chen, S. Hsu, T. Wu, *Surface and Coatings Technology* 123 (2000) 204;
- 89 K. Ortner, T. Jung, C.P. Klages, B. Linder, B. Strauss, N. Sämman, *Surface and Coatings Technology* 200 (2005) 976;
- 90 O. Takai, V. Anita, N. Saito, *Surface and Coatings Technology* 200 (2005) 1106;
- 91 F. Benítez, E. Martínez, J. Esteve, *Thin Solid Films* 377-378 (2000) 109;
- 92 D. Hegemann, U. Vohrer, C. Oehr, R. Riedel, *Surface and Coatings Technology* 116-119 (1999) 1033;
- 93 G. Fedosenko, A. Schwabedissen, D. Korzec, J. Engemann, *Surface and Coatings Technology* 142-144 (2001) 693;
- 94 V. Baranauskas, A.C. Peterlevitz, H.J. Ceragioli, A.L.S. Souto, S.F. Durrant, *Thin Solid Films* 398-399 (2001) 255;
- 95 G. Fedosenko, J. Engemann, D. Korzec, *Surface and Coatings Technology* 133-134 (2000) 535;
- 96 W. Albrecht, J. Schauer, T. Weigel, A. Lendlein, *Journal of Membrane Science* 269 (2006) 49;
- 97 M. Stefecka, D. Korzec, M. Siry, Y. Imahori, M. Kando, *Science and Technology of Advanced Materials* 2 (2001) 587;
- 98 X. Feng, J. Zhang, H. Xie, Q. Hu, Q. Huang, W. Liu, *Surface and Coatings Technology* 171 (2003) 96;
- 99 J. Thome, A. Holländer, W. Jaeger, I. Trick, C. Oehr, *Surface and Coatings Technology* 174-175 (2003) 584;
- 100 P.K. Chu, J.Y. Chen, L.P. Wang, N.Huang, *Materials Science and Engineering Reports* 36 (2002) 143;
- 101 P. Favia, R. d'Agostino, *Surface and Coatings Technology* 98 (1998) 1102;
- 102 A. Pfuch, R. Cihar, *Surface and Coatings Technology* 183 (2004) 134;

-
- 103 Y.Y. Xu, T. Muramatsu, M. Taniyama, T. Aoki, Y. Hatanaka, *Thin Solid Films* 368 (2000) 181;
- 104 Z. Hubicka, G. Pribil, R.J. Soukup, N.J. Ianno, *Surface and Coatings Technology* 160 (2002) 114;
- 105 C. Boisse-Laporte, O. Leroy, L. de Poucques, B. Agius, J. Bretagne, M.C. Hugon, L. Teule-Gay, *Surface and Coatings Technology* 179 (2004) 176;
- 106 C.M. Chan, T.M. Ko, H. Hiraoka, *Surface Science Reports* 24 (1996) 1;
- 107 Y. Leterrier, *Progress in Materials Science* 48 (2003) 1;
- 108 A. Choukourov, H. Biederman, D. Slavinska, M. Trchova, A. Hollander, *Surface and Coatings Technology* 174-175 (2003) 863;
- 109 R.M. France, R.D. Short, *Journal of the Chemical Society, Faraday Transactions* 93 (1997) 3173;
- 110 R. Claude, M. Moisan, Z. Zakrzewski, *Applied Physics Letters* 50 (1987) 1797;
- 111 J. Fang, H. Chen, X. Yu, *Journal of Applied Polymer Science* 80 (2001) 1434;
- 112 A. Amirudin, D. Thierry, *Progress in Organic Coatings* 26 (1995) 1;
- 113 J.N. Murray, *Progress in Organic Coatings* 30 (1997) 225;
- 114 J.N. Murray, *Progress in Organic Coatings* 30 (1997) 255;
- 115 J.N. Murray, *Progress in Organic Coatings* 31 (1997) 351;
- 116 S. Rossi, F. Deflorian, L. Fontanari, A. Cambuzzi, P.L. Bonora, *Progress in Organic Coatings* 52 (2005) 288;
- 117 J.R. Macdonald, *Impedance Spectroscopy*, Wiley, New York US, 1987;
- 118 D. Loveday, P. Peterson, B. Rodgers, *JCT CoatingsTech* 1 (2004) 46;
- 119 D. Loveday, P. Peterson, B. Rodgers, *JCT CoatingsTech* 1 (2004) 88;
- 120 D. Loveday, P. Peterson, B. Rodgers, *JCT CoatingsTech* 2 (2004) 22;
- 121 W. Strunz, C.A. Shiller, J. Vogelsang, *Electrochimica Acta* 51 (2006) 1437;
- 122 D.D. Macdonald, M. Urquidi-Macdonald, *Journal of the Electrochemical Society* 132 (1985) 2316;
- 123 E. Barsoukov, J.R. Macdonald, *Impedance Spectroscopy Theory, Experiment, and Applications*, 2nd ed, John Willey, 2005. ISBN: 0471647497;
- 124 G.W. Walter, *Corrosion Science* 26 (1986) 681;
- 125 O. Ferraz, E. Cavalcanti, A.R. Di Sarli, *Progress in Organic Coatings* 37 (1995) 1267;
- 126 J.M. McIntyre, H.Q. Pham, *Progress in Organic Coatings* 27 (1996) 201;
- 127 E. Akbarinezhad, M. Bahremandi, H.R. Faridi, F. Rezaei, *Corrosion Science* 51 (2009) 356;
- 128 D.M. Brasher, A.H. Kingsbury, *Journal of Applied Chemistry* 4 (1954) 62;
- 129 R.G. Duarte, A.S. Castela, M.G.S. Ferreira, *Progress in Organic Coatings* 65 (2009) 197
- 130 S.A. Lindqvist, *Corrosion* 41 (1985) 69;
- 131 E.P.M.V. Westing, G.M. Ferrari, J.H.W.D. Wit, *Corrosion Science* 36 (1994) 957

- 132 M.M. Wind, H.J.W. Lenderink, *Progress in Organic Coatings* 28 (1996) 239;
- 133 S. Duval, M. Keddad, M. Sfaira, A. Sghiri, H. Takenouti, *Journal of the Electrochemical Society* 149 (2002) B520
- 134 F. Deflorian, L. Fedrizzi, S. Rossi, F. Buratti, P.L. Bonora, *Progress in Organic Coatings* 39 (2000) 9
- 135 C.L. Pen, C. Lacabanne, N. Pébère, *Progress in Organic Coatings* 39 (2000) 167;
- 136 N.G. McCrum, ; B.E. Read, G. Williams, *Anelastic and dielectric effects in polymeric solids*, New York : Dover Publications, 1991. ISBN 0-486-66752-9;
- 137 Y. Camberlin, M. Glotin, M. Keddad, F. Ropital, H. Takenouti, *Progress in Organic Coatings* 39 (2000) 15;
- 138 A.S. Castela, A.M. Simões, *Corrosion Science* 45 (2003) 1631;
- 139 A.S. Castela, A.M. Simões, *Corrosion Science* 45 (2003) 1647;
- 140 A.S. Castela, A.M. Simões, *Progress in Organic Coatings* 46 (2003) 55
- 141 J. Goldstein, D. Newbury, D. Joy, C. Lyman, P. Echlin, E. Lifshin, L. Sawyer, J. Michael, *Scanning electron microscopy and X-ray microanalysis*, 3rd ed. New York: Kluwer Academic, cop. 2003. ISBN 0306472929;
- 142 J.I. Goldstein, *Scanning electron microscopy and X-ray microanalysis: a text for biologists, materials scientists, and geologists*, 2nd ed. New York: Plenum, 1992. ISBN 0306441756;
- 143 C.E. Lyman, D.E. Newbury, J.I. Goldstein, D.B. Williams, A.D. Romig, Jr.J.T. Armstrong, P. Echlin, C.E. Fiori, D.C. Joy E. Lifshin, K.P. Peters, *Scanning electron microscopy, X-ray microanalysis, and analytical electron microscopy: a laboratory workbook*. New York: Plenum, 1990. ISBN 0306435918;
- 144 L. Reimer, *Transmission Electron Microscopy: physics of image formation and microanalysis*, 4th ed. Berlin: Springer, cop. 1997. ISBN 3-540-62568-2;
- 145 D.B. Williams, C.B. Carter, *Transmission Electron Microscopy: a textbook for materials science*. New York: Plenum, cop. 1996 4 vol. ISBN 0-306-45324-X;
- 146 P.R. Buseck, J.M. Cowley, L. Eyring, *High-Resolution Transmission Electron Microscopy and Associated Techniques*, New York: Oxford University Press, 1992. ISBN 0-19-507262-6;
- 147 H.H. Rose, *Science and Technology of Advanced Materials* 9 (2008) 014107;
- 148 F. Giessibl, *Reviews of Modern Physics* 75 (2003) 949;
- 149 F. Walther, W.M. Heckl, R.W. Stark, *Applied Surface Science* 254 (2008) 7290;
- 150 A. Méndez-Vilas, J.M. Bruque, M.L. González-Martín, *Ultramicroscopy* 107 (2007) 617;
- 151 F. El Feninat, S. Elouatik, T.H. Ellis, E. Sacher, I. Stangel, *Applied Surface Science* 183 (2001) 205;
- 152 Q. Zhong, D. Innis, K. Kjoller, V.B. Elings, *Surface Science Letter* 290 (1993) L688;
- 153 Y. Roiter, S. Minko, *Journal of the American Chemical Society* 127 (2005) 15688;
- 154 P. Hinterdorfer, Y.F. Dufrêne, *Nature Methods* 3 (2006) 5;

-
- 155 P.M. Hoffmann, A. Oral, R.A. Grimble, H.Ö. Özer, S. Jeffery, J.B. Pethica, *Proceedings of the Royal Society A* 457 (2001) 1161;
- 156 B.K. Agarwal, *X-Ray spectroscopy: an introduction*, Berlin, Springer, 1979. ISBN 3540092684;
- 157 S. Huefner, *Photoelectron Spectroscopy: principles and applications*, 2nd ed. Berlin, Springer, cop. 1996. ISBN 3-540-60875-3;
- 158 B. Fortner, T.E. Meyer, *Number by colours: a guide to using colour to understand technical data*. New York: Springer, 1996. ISBN 0-387-94685-3;
- 159 IS&T NIP16 Conference, Vancouver, Canada, 2000 16-20;
- 160 I. Newton, *Opticks or, a Treatise of the reflexions, refractions, inflexions and colours of light. Also two treatises of the species and magnitude of curvilinear figures*, London, 1704;
- 161 T. Young, *Philosophical Transactions of the Royal Society of London* 92 (1802) 12;
- 162 W.D. Wright, *Transactions of the Optical Society* 30 (1928) 141;
- 163 J. Guild, *Philosophical Transactions of the Royal Society of London* A230 (1931) 149;
- 164 R.W. Hunt, *Measuring colour*, 3rd ed, Fountain Press, England, 1998. ISBN 0-86343-387-1;
- 165 T. Smith, J. Guild, *Transactions of the Optical Society* 33 (1931-1932) 73;
- 166 A. C. Harris and I. L. Weatherall, *Journal of the Royal Society of New Zealand* 20 (1990) 3;
- 167 EN 10130:2006, *Cold rolled low carbon steel flat products for cold forming. Technical delivery conditions*.
- 168 T.H. Chung, M.S. Kang, C.J. Chung, Y. Kim, *Current Applied Physics* 9 (2009) 598.
- 169 N. Benissad, C. Boisse-Laporte, C. Vallée, A. Granier, A. Goullet, *Surface and Coatings Technology* 116-119 (1999) 868;
- 170 Y. Inoue, H. Sugimura, O. Takai, *Thin Solid Films* 345 (1999) 90;
- 171 Q. Yu, C.E. Moffitt, D.M. Wieliczka, J. Deffeyes, H. Yasuda, *Progress in Organic Coatings* 44 (2002) 37
- 172 I. Horcas, R. Fernandez, J.M. Gomez-Rodriguez, J.Colchero, J. Gomez-Herrero, A.M. Baro, *Review of Scientific Instruments*, 78 (2007) 013705;
- 173 C.G. Oliveira, M.G.S. Ferreira, *Corrosion Science* 45 (2003) 123;
- 174 C.G. Oliveira, M.G.S. Ferreira, *Corrosion Science* 45 (2003) 139;
- 175 L. Fedrizzi, A. Bergo, M. Fanicchia, *Electrochimica Acta* 51 (2006) 1864;
- 176 F. Deflorian, S. Rossi, *Electrochimica Acta* 51 (2006) 1736;
- 177 D.W. Davison, R.H.Cole, *The Journal of Chemical Physics* 18 (1950) 1417;
- 178 D.W. Davison, R.H.Cole, *The Journal of Chemical Physics* 19 (1951) 1484;
- 179 J.R. Macdonald, *The Journal of Chemical Physics* 22 (1954) 1317;
- 180 J.R. Macdonald, *The Journal of Chemical Physics* 58 (1973) 4982;
- 181 J.R. Macdonald, *The Journal of Chemical Physics* 61 (1974) 3977;
- 182 J.R. Macdonald, D.R. Franceschetti, *The Journal of Chemical Physics*, 68 (1978) 1614;

- 183 A.S. Castela, *Propriedades e Comportamento Anticorrosivo de Revestimentos Orgânicos*, in Tese de Doutoramento em Engenharia Química, Universidade Técnica de Lisboa, **2002**: Lisboa.
- 184 J.B. Jorcin, M.E. Orazem, N. Pébère, B. Tribollet, *Electrochimica Acta* 51 (**2006**) 1473;
- 185 M.S. Abouzari, F. Berkemeier, G. Schmitz, D. Wilmer, *Solid State Ionics* 180 (**2009**) 922:
- 186 D. Theirich, K.P. Ningel, J. Engemann, *Surface and Coatings Technology* 86-87 (**1996**) 628;
- 187 A. Hozuni, O. Takai, *Thin Solid Films* 303 (**1997**) 222;
- 188 F. Deflorian, S. Rossi, M. Fedel, *Corrosion Science* 50 (**2008**) 2360;

Appendix - Activation and Deposition (R)

One more partial plasma polymerization treatment was used with the **R** plasma reactor, in order to understand the influence of the plasma stabilization step. This was performed using the sequence: plasma activation step and the plasma deposition step, i.e. plasma polymerization procedure without the final stabilization step (stage **2** accordingly with Table 4.1). The procedure used similar conditions to the ones described in point 4.1.2.ii, however the combination of time of the process, carrier gas employed and precursor mixture used is not contemplated in the Table 4.2. For this reason was attributed the letter **j** to this new combination. The pressure during the plasma polymerization corresponds to **P₅**, according with Table 4.3.

For the deposition, the two **P** and **G** electrode locations were used but the treatment was only performed on the **U** coil coating. A summary of the conditions used during the plasma polymerization treatment with the respective label is shown in Table a.

Table a Systems prepared at **G** and **P** electrode location of **R** plasma reactor, with the respective label correspondence.

coil coating	stage	precursor mixture	pressure (mbar)	label
Polyurethane U	plasma deposition 2	HMDSO and O ₂ j	0.03 P ₅	UR2jP₅G UR2jP₅P

- Systems Characterization

The results for the systems treated with the sequence plasma activation and plasma deposition (stage **2**) are here analysed.

The value of the capacitance of the coating systems permits to estimate the water uptake rate with the empirical relation of Brasher and Kingsbury,¹²⁸ using eq. 3.13 by following the procedure described in point 3.1.4. The water uptake plots for the systems **UR2jP₅P** and **UR2jP₅G** appear in Figure a. The systems **UR3eP₅P** and **UR3eP₅G** water uptake are also in the same figure for comparison.

Similar very fast initial water uptake is observed for all the systems, characteristic behaviour of organic coatings.^{112;128;129} The water uptake and the saturation level reached are dependent of the stage used during the **R** plasma polymerization. The specimen location in the plasma reactor also appears to have strong influence on the systems behaviour.

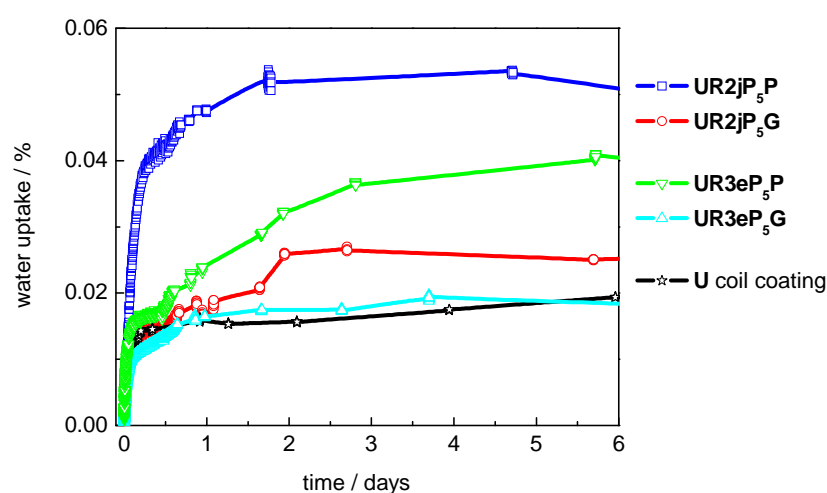


Figure a Water uptake plot for the plasma polymerized **U** systems using the **R** plasma reactor.

The system **UR2jP₅P** has higher water saturation level, even higher than system **UR3eP₅P**, suggesting that initially already has stronger degradation. The system **UR2jP₅G** has better performance but the saturation level obtained is still higher than for the system **UR3eP₅G** and unmodified **U** coil coating.

The Figure b, AFM images in page 222, shows the surface morphology evolution of the same systems, **UR2jP₅G** and **UR2jP₅P**. After the plasma deposition, AFM images with the label *0 days*, particulate surface morphology is obtained, similar to the other plasma polymerized systems using **R** plasma reactor, point 6.3.4. The particles present in the AFM images have 50 nm diameter for the system **UR2jP₅G** and 90 nm for the system **UR2jP₅P**. The EDS measurements performed for the same systems show the presence of the silicon element, Table b**Error! Reference source not found.**. This is the representative element of the plasma polymer film.

Table b Composition evolution during the immersion tests of the systems **UR2jP₅G** and **UR2jP₅P**.

time (days)	UR2jP₅G		UR2jP₅P	
	fluorine	silicon	fluorine	silicon
0	49	0.3	55	0.7
7	50	0.2	55	0.1
30	43	0.2	45	0.1
60	59	0.1	47	0.1

During immersion, the surface morphology has some variation, showing a small variation of the R_a and h values. The silicon content has higher variation, showing content decrease for both systems. The system **UR2jP₅G** shows continuous decrease of the silicon content until vestigial values, which are reached only after 60 days of immersion. The system **UR2jP₅P** shows a drop of the silicon content immediately after 7 days of immersion. These results suggest that the plasma polymer film is removed during immersion

These results show that degradation of the produced systems occurred during the immersion tests. It is also noticed a difference between the two electrodes location, being the **G** location the one with slower degradation and thus better performance. Their performance is, however, worse than the systems **UR3eP₅G** and **UR3eP₅P**.

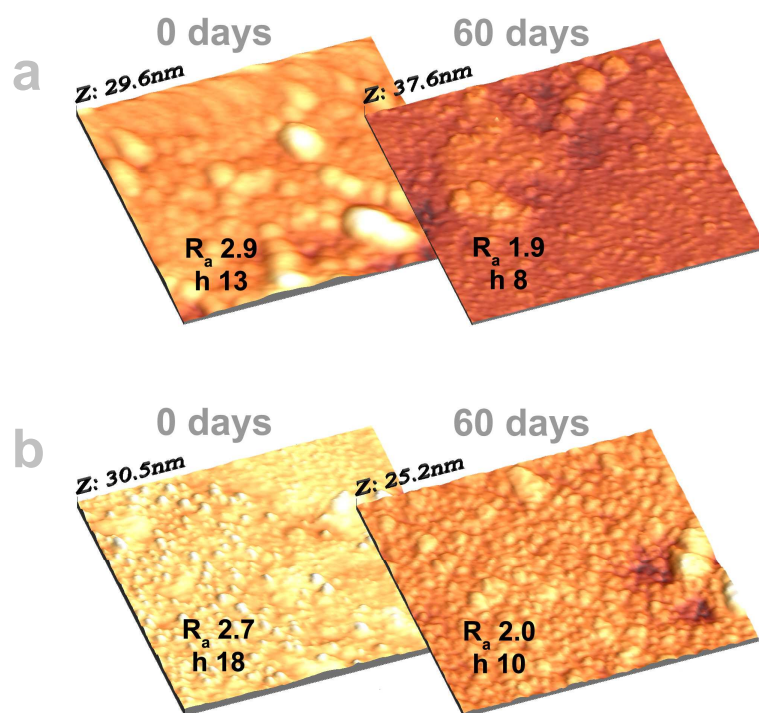


Figure b AFM $1 \times 1 \mu\text{m}$ images with the surface morphology evolution during immersion for the systems **a.** UR2jP₅P and **b.** UR2jP₅G. The R_a and h values in nm are in the correspondent image.

